technische universität
dortmund

Creating a modifiable heteroleptic Pd(II) Metallo-Cage System

Thesis for receiving the degree of “Doctor rerum naturalium”

TU Dortmund

Fakultät für Chemie und Chemische Biologie

Robin Rudolf

from Datteln, Germany

07.07.2021

Für Papa

• **I have the high ground!** •

Obi-Wan Kenobi

Examiner: Prof. Dr. Guido H. Clever

Coexaminer: JProf. Dr. Sebastian Henke

Faculty of Chemistry and Chemical Biology,
TU Dortmund University,
Otto-Hahn-Straße 6, 44227 Dortmund

Submission Date: 07.07.2021

Eidesstattliche Versicherung (Affidavit)

Name, Vorname
(Surname, first name)

Matrikel-Nr.
(Enrolment number)

Belehrung:

Wer vorsätzlich gegen eine die Täuschung über Prüfungsleistungen betreffende Regelung einer Hochschulprüfungsordnung verstößt, handelt ordnungswidrig. Die Ordnungswidrigkeit kann mit einer Geldbuße von bis zu 50.000,00 € geahndet werden. Zuständige Verwaltungsbehörde für die Verfolgung und Ahndung von Ordnungswidrigkeiten ist der Kanzler/die Kanzlerin der Technischen Universität Dortmund. Im Falle eines mehrfachen oder sonstigen schwerwiegenden Täuschungsversuches kann der Prüfling zudem exmatrikuliert werden, § 63 Abs. 5 Hochschulgesetz NRW.

Die Abgabe einer falschen Versicherung an Eides statt ist strafbar.

Wer vorsätzlich eine falsche Versicherung an Eides statt abgibt, kann mit einer Freiheitsstrafe bis zu drei Jahren oder mit Geldstrafe bestraft werden, § 156 StGB. Die fahrlässige Abgabe einer falschen Versicherung an Eides statt kann mit einer Freiheitsstrafe bis zu einem Jahr oder Geldstrafe bestraft werden, § 161 StGB.

Die oben stehende Belehrung habe ich zur Kenntnis genommen:

Official notification:

Any person who intentionally breaches any regulation of university examination regulations relating to deception in examination performance is acting improperly. This offence can be punished with a fine of up to EUR 50,000.00. The competent administrative authority for the pursuit and prosecution of offences of this type is the chancellor of the TU Dortmund University. In the case of multiple or other serious attempts at deception, the candidate can also be unenrolled, Section 63, paragraph 5 of the Universities Act of North Rhine-Westphalia.

The submission of a false affidavit is punishable.

Any person who intentionally submits a false affidavit can be punished with a prison sentence of up to three years or a fine, Section 156 of the Criminal Code. The negligent submission of a false affidavit can be punished with a prison sentence of up to one year or a fine, Section 161 of the Criminal Code.

I have taken note of the above official notification.

Ort, Datum
(Place, date)

Unterschrift
(Signature)

Titel der Dissertation:
(Title of the thesis):

Ich versichere hiermit an Eides statt, dass ich die vorliegende Dissertation mit dem Titel selbstständig und ohne unzulässige fremde Hilfe angefertigt habe. Ich habe keine anderen als die angegebenen Quellen und Hilfsmittel benutzt sowie wörtliche und sinngemäße Zitate kenntlich gemacht.
Die Arbeit hat in gegenwärtiger oder in einer anderen Fassung weder der TU Dortmund noch einer anderen Hochschule im Zusammenhang mit einer staatlichen oder akademischen Prüfung vorgelegen.

I hereby swear that I have completed the present dissertation independently and without inadmissible external support. I have not used any sources or tools other than those indicated and have identified literal and analogous quotations.

The thesis in its current version or another version has not been presented to the TU Dortmund University or another university in connection with a state or academic examination.*

*Please be aware that solely the German version of the affidavit ("Eidesstattliche Versicherung") for the PhD thesis is the official and legally binding version.

Ort, Datum
(Place, date)

Unterschrift
(Signature)

List of Publications and Conference Contributions

Publications

- "Identification of a Heteroleptic $Pd_6L_6L'_6$ Coordination Cage by Screening of a Virtual Combinatorial Library" S. Sudan, R. Li, S. Jansze, A. Platzek, R. Rudolf, G. H. Clever, F. Fadaei Tirani, R. Scopelliti, K. Severin, *J. Am. Chem. Soc.* **2021**, *143*, 1773-1778
- "Resolution of minor size differences in a family of heteroleptic coordination cages by trapped ion mobility ESI-MS" K. E. Ebbert, L. Schneider, A. Platzek, C. Drechsler, B. Chen, R. Rudolf, G. H. Clever, *Dalton Trans.*, **2019**, *48*, 11070-11075
- "Flexibility control in alkyl ether-functionalized pillared-layered MOFs by a Cu/Zn mixed metal approach", A. Schneemann, R. Rudolf, S. J. Baxter, P. Vervoorts, I. Hante, K. Khaletskaya, S. Henke, G. Kieslich, and R. A. Fischer, *Dalton Trans.*, **2019**, 48, 6564-6570
- "Linker Functionalization Triggers an Alternative 3D-Topology for Zinc-Isophthalate-4,4'-Bipyridine Frameworks", A. Schneemann, R. Rudolf, S. Henke, Y. Takahashi, H. Banh, I. Hante, C. Schneider, S. Noro, and R. A. Fischer, *Dalton Trans.*, **2017**, 46, 8198-8203
- "Influence of Co-adsorbates on CO_2 induced phase transition in functionalized pillared-layered metal–organic frameworks", A. Schneemann, Y. Takahashi, R. Rudolf, S. Noro, and R. A. Fischer, *J. Mater. Chem. A.,* **2016**, 4, 12963-12972

Conference Contributions

Poster, International Symposium on "Confinement-Controlled Chemistry", **2019**, *Bochum*, Germany

Poster, 10th Münster Symposium on Cooperative Effects in Chemistry, **2019**, *Münster*, Germany

Poster, SupraChem, **2019**, *Würzburg*, Germany

Poster, 14th Koordinationschemie-Treffen, **2018**, *Heidelberg*, Germany

Poster, Tag der Chemie, **2017**, *Dortmund*, Germany

Abstract

Supramolecular chemistry is the science of non-covalent interactions between at least two chemical units (e.g. ligands, metal complexes). Over the past decades, coordination driven self-assembly of organic ligands with metal cations led to a high number of discrete supramolecular nanostructures. [$M_n\mathbf{L}_{2n}$] type coordination cages based on square planar metal ions (e.g. Pd(II), Pt(II)) and so called banana-shaped ligands are one example with a high research activity over the last years. High symmetric supramolecular coordination structures with one type of ligand were already able to show potentials for applications in medicine, sensing or catalysis.

The combination of more than one kind of ligands to form a defined heteroleptic assembly is a relatively new subfield of supramolecular chemistry. Heteroleptic assemblies enable implementation of more than one function into a cage structure. However, simply mixing of two different bis-monodentate ligands in the presence of square planar metal cations is not trivial and can lead to narcissistic self-sorting or statistical mixtures of heteroleptic cages. To prevent this, rational design of the ligands leads to discrete heteroleptic assemblies. The Clever group introduced a method based on geometric shape-complementarity of the ligands to form a [$Pd_2\mathbf{L}^{\mathbf{A}}_{\mathbf{2}}\mathbf{L}^{\mathbf{P}}_{\mathbf{2}}$]-cage. Herein, this work uses this approach for the introduction of a novel and highly modifiable basic motif. Based on the archetype quinoline-based $\mathbf{L}^{\mathbf{A}}$ ligand, ligands $\mathbf{L}^{\mathbf{OMe}}$ and $\mathbf{L}^{\mathbf{OH}}$ are introduced. As first cages, [$Pd_2\mathbf{L}^{\mathbf{OMe}}_{\mathbf{4}}$] and [$Pd_2\mathbf{L}^{\mathbf{OH}}_{\mathbf{4}}$] with a similar strain and helical structure like the before reported [$Pd_2\mathbf{L}^{\mathbf{A}}_{\mathbf{4}}$] cages are formed. It is necessary to achieve these homoleptic cages, to transform them into heteroleptic structures with reduced strains in a novel [$Pd_2\mathbf{L}^{\mathbf{X}}_{\mathbf{2}}\mathbf{L}^{\mathbf{Y}}_{\mathbf{2}}$]-composition. Afterwards, pyridyl-based ligands $\mathbf{L}^{\mathbf{SC4}}$ and $\mathbf{L}^{\mathbf{SB}}$ are used to form heteroleptic assemblies. After these initial cage formations, a series of endohedrally modified [$Pd_2\mathbf{L}^{\mathbf{OMe}}_{\mathbf{2}}\mathbf{L}^{\mathbf{Y}}_{\mathbf{2}}$]-cages based on one topology are introduced. Additionally, a [$Pd_2\mathbf{L}^{\mathbf{OMe}}_{\mathbf{2}}\mathbf{L}^{\mathbf{X}}\mathbf{L}^{\mathbf{Z}}$]-cage is synthesised as a derivate of the experiences made with [$Pd_2\mathbf{L}^{\mathbf{OMe}}_{\mathbf{2}}\mathbf{L}^{\mathbf{Y}}_{\mathbf{2}}$]-cages. A further modification, an elongated ligand $\mathbf{L}^{\mathbf{LOMe}}$ is synthesized and a [$Pd_2\mathbf{L}^{\mathbf{LOMe}}_{\mathbf{4}}$]-cage is formed. Finally, in this work introduced cages of the [$Pd_2\mathbf{L}^{\mathbf{OMe}}_{\mathbf{2}}\mathbf{L}^{\mathbf{X}}_{\mathbf{2}}$]-type are used to investigate the influence of different endohedral modifications on guest uptake.

Zusammenfassung

Supramolekulare Chemie ist die Wissenschaft der nicht kovalenten Interaktionen zwischen mindestens zwei verschiedenen chemischen Einheiten (z.B. Liganden, Metallkomplexe). Über die letzten Jahrzehnte führte die Selbstassemblierung von organischen Liganden mit Metallkationen zu einer hohen Anzahl diskreter supramolekularer Nanostrukturen. [$M_n\mathbf{L}_{2n}$] Typ Koordinationskäfige welche auf quadratisch-planaren Metallionen (z.B. Pd(II), Pt(II)) und bananenförmigen Liganden basieren sind eine Variation dieser Strukturen mit einer hohen Forschungsaktivität in den letzten Jahren. Darauf basierende hochsymmetrische supramolekulare Koordinationsstrukturen mit einem Typ Ligand zeigten schon potenzielle Anwendungen in der Medizin, Sensorik oder in der Katalyse.

Die Kombination von mehr als einer Art Ligand, um eine definierte heteroleptische Assemblierung zu erzielen, ist ein neueres Feld der Chemie. Die Verwendung von verschiedenen Liganden in einer Käfigspezies ermöglicht die Implementierung von mehreren Funktionalitäten. Ein einfaches Mischen von zwei verschiedenen doppelt-einzahnigen Liganden, in der Gegenwart von quadratisch-planaren Kationen, kann zur narzisstische Selbstsortierung oder zu statistischen Mischungen von heteroleptischen Käfigen führen. Ein rationales Design der Liganden führt jedoch zu diskreten heteroleptischen Assemblierungen. Die Clever-Gruppe führte eine Methode basierend auf geometrischer Formkomplementarität ein um einen [$Pd_2\mathbf{L}^{\mathbf{A}}_2\mathbf{L}^{\mathbf{P}}_2$] Käfig zu formen. Die vorliegende Arbeit nutzt die eingeführte formkomplementäre Vorgehensweise zur Einführung einer neuartigen und modifizierbaren grundlegenden Struktur. Basierend auf dem archetypischen und auf Chinolin basierenden $\mathbf{L}^{\mathbf{A}}$ Liganden, wurden $\mathbf{L}^{\mathbf{OMe}}$ und $\mathbf{L}^{\mathbf{OH}}$ eingeführt. Als erstes wurden [$Pd_2\mathbf{L}^{\mathbf{OMe}}_4$] und [$Pd_2\mathbf{L}^{\mathbf{OH}}_4$] mit einer ähnlichen strukturellen Spannung und helikalen Struktur wie der schon berichtete [$Pd_2\mathbf{L}^{\mathbf{A}}_4$] Käfig synthetisiert. Es ist wichtig diese Käfige zu erhalten, um heteroleptische Strukturen mit einer vorteilhafteren reduzierten Spannung in einer neuartigen [$Pd_2\mathbf{L}^{\mathbf{X}}_2\mathbf{L}^{\mathbf{Y}}_2$] Zusammensetzung zu erreichen. Anschließend wurden Pyridinyl basierte $\mathbf{L}^{\mathbf{SC4}}$ und $\mathbf{L}^{\mathbf{SB}}$ Liganden genutzt, um neue heteroleptische Käfige zu formen. Nach diesen Käfigsynthesen wurde eine Serie von endohedral modifizierten [$Pd_2\mathbf{L}^{\mathbf{OMe}}_2\mathbf{L}^{\mathbf{Y}}_2$] Käfigen, basierend auf diesen Topologien, eingeführt. Zusätzlich wurde ein [$Pd_2\mathbf{L}^{\mathbf{OMe}}_2\mathbf{L}^{\mathbf{X}}\mathbf{L}^{\mathbf{Z}}$] Käfig aus den gemachten Erfahrungen mit den [$Pd_2\mathbf{L}^{\mathbf{OMe}}_2\mathbf{L}^{\mathbf{Y}}_2$] Käfigen synthetisiert. Eine weitere Modifizierung, ein verlängerter $\mathbf{L}^{\mathbf{LOMe}}$, wurde synthetisiert und ein [$Pd_2\mathbf{L}^{\mathbf{LOMe}}_4$] Käfig gebildet. Final wurden die eingeführten [$Pd_2\mathbf{L}^{\mathbf{OMe}}_2\mathbf{L}^{\mathbf{X}}_2$] Käfige auf ihre Wirt-Gast-Chemie untersucht.

TABLE OF CONTENT

1 Introduction

1.1 History of Supramolecular Chemistry

‘Chemistry beyond molecules.’ Many reports, theses and articles explaining supramolecular chemistry begin with this (here shortened) quote of 1987 Nobel prize laureate *Jean-Marie Lehn*.[1] These three words cannot better describe the fundamental interests and the topic of this emerging research field.

The above statement is justified by the historic long-time interest of chemistry as a science to investigate interactions between covalently connected atoms and effects on an intramolecular base. After a long period in which the focus was set on “single-molecule” chemistry, the research on molecule-molecule interactions was historically and thematically new as it started to be an own research topic. The more detailed and correct definition of supramolecular chemistry is the research on assemblies which are hold together by non-covalent interactions.[2] These non-covalent interactions include van-der-Waals forces, *π*-*π* stacking, hydrophobic effects, electrostatic interactions, hydrogen bonding, mechanical bonds and possible combinations of all these to form supramolecular species.[3–6] While covalent bonds can have a bond energy up to 1072 $kJ \cdot mol^{-1}$, non-covalent bond energies are much less strong and can be easily broken, making them reversible to allow dynamic behaviours for the supramolecular species (e.g. electrostatic interactions with 50-240 $kJ \cdot mol^{-1}$ as the strongest and van-der-Waals forces with less than 7 $kJ \cdot mol^{-1}$).[4]

Nature evolved a plethora of examples in billions of years of evolution, which humankind just discovered over the last decades. Life as we known it is based on DNA (deoxyribonucleic acid), composed of the four nucleobases, which are connected by a 2-deoxyribose-phosphate backbone to form a double helix, carrying the blueprint of proteins.[7] Hydrogen bonds between the complementary nucleobases and *π*-*π* stacking interactions between neighbouring nucleobases stabilize the secondary structure.[8] Proteins combine hydrophobic effects, metal coordination and electrostatic forces to form three-dimensional structures.[9] Enzymes are globular proteins that include a specific binding site, the enzyme pocket, for substrate molecules with specific shapes.[10] This encapsulation is called the lock-key principle, based on non-covalent binding of complementary guests. This concept initially described by *Herman Emil Fischer* (1894)

was expanded by the induced fit model by *Daniel E. Koshland Jr.* (1958), where the receptor undergoes conformational changes upon binding the substrate and ending up with a reaction and a subsequent release of the transformed product molecule. There are countless examples in nature showing the importance of supramolecular research to explore such processes and giving the inspiration for many research groups all over the world.

With an increase of available analytic methods for chemists, also the research on supramolecular chemistry increased the number of discoveries and inventions. Starting in the 1960s, the research of *Charles Pedersen*, *Jean-Marie Lehn*, and *Donald J. Cram* were a breakthrough in supramolecular science, affording them to be awarded with the 1987 Nobel prize in chemistry “for their development and use of molecules with structure-specific interactions of high selectivity." *Pedersen* synthesised the first crown ether in 1967 and *Lehn* the first cryptand in 1969, respectively (figure 1.1).[11,12] These compounds have a strong binding affinity for alkaline earth metals thanks to the lone pairs of the oxygen or nitrogen atoms which are oriented to the central pocket of the molecule.

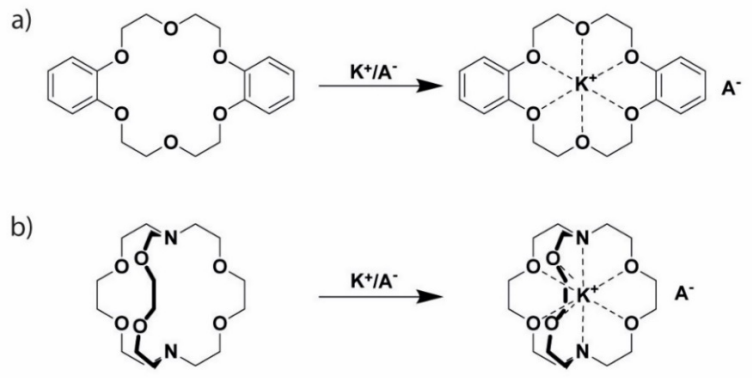

Figure 1.1 a) dibenzo-[18]crown-6 by *Pederson* and b) [2.2.2]cryptand by *Lehn* forming the respective potassium complexes.[11,12]

In 1979, *Cram* developed spherands, a class of molecules with an even stronger cation binding ability than crown ethers or cryptands due to the even more preorganized binding sites inside the molecules pocket.[13]

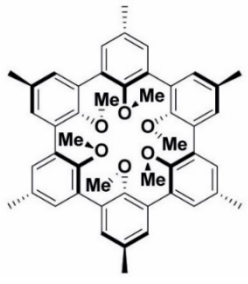

Figure 1.2 Spherand-6 by *Cram*.[13]

Being awarded with the Nobel prize in 1987, these scientists brought extensive advancement in the field of supramolecular chemistry, especially for the Host-Guest chemistry part, to become an independent and also cross-discipline of research with an increasing number and complexity of sub-areas.[14]

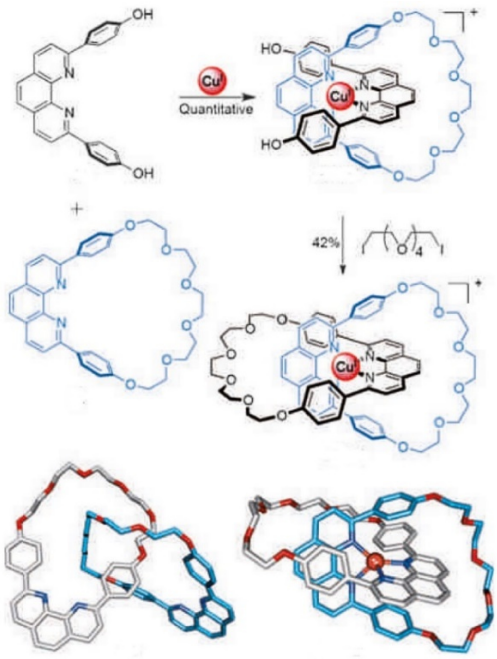

Figure 1.3 Metal template-mediated synthesis of a [2]catenane by Sauvage. Williamson ether macrocyclization of the tetrahedral coordination complex formed by coordination of a diphenol ligand and an already formed macrocycle.[15] © (2015) Wiley ‐ VCH Verlag GmbH & Co. KGaA, Weinheim. Reprinted with permission.

Only a few years before the first Nobel prize for supramolecular chemistry, *Jean-Pierre Sauvage* introduced another breakthrough method and easy way to synthesise catenanes (the first synthesis was actually reported by *Wassermann* in 1960 but with a more statistical approach and much smaller yield).[16–18] A catenane is a supramolecular structure consisting of at least two macrocycles which are interlocked within each other in a way that they cannot be separated without breaking a chemical bond. *Sauvage* used metal ions like copper as a template to bring in closer proximity the substrates, as shown in figure 1.3.[15,19,20]

With this novel strategy and further developments based on the same principle, it is now also possible to form higher ordered interlocked macrocyclic structures like Borromean rings[21], Tre- and Pentafoil knots[22] and the Solomon links[23,24], as shown in figure 1.4, with a high number of variants.[25] The ability of catenanes to rotate around each other, which can be detected by NMR (nuclear magnetic resonance) spectroscopy, gives the fundamental basis for building artificial molecular machines.[26,27]

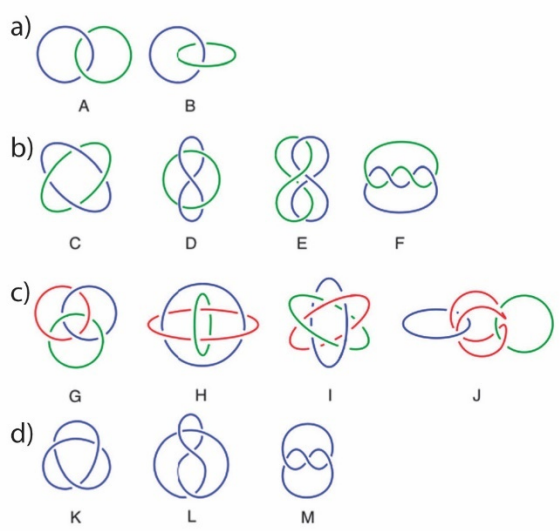

Figure 1.4 Schematic representation of possible three-dimensional interlocked ring structures a) Hopf link, b) Solomon links, c) Borromean rings, d) Trefoil knots. Adapted from ref.[25] with permission from The Royal Society of Chemistry.

Based on the catenane work, another class of supramolecular structures was developed, namely rotaxanes. These structures consist of at least one linear molecular unit which is enclosed by at least one macrocycle.[28] While the first example was reported by *Harrison* in 1967,[29] higher yields of rotaxanes could be achieved with the same synthetic strategy that led to higher yields for catenanes, using non-covalent interactions or metal coordination as passive or active templates, hydrogen bonds or hydrophobic effects.[30] In 1991, *J. Stoddard* showed the controlled motion of the macrocycle along the linear molecule by addition of bulky stopper functions at both end to prevent the macrocycle to leave (figure 1.5).[31,32] This so-called 'molecular shuttle' is seen as one prototype of molecular machines and switches.

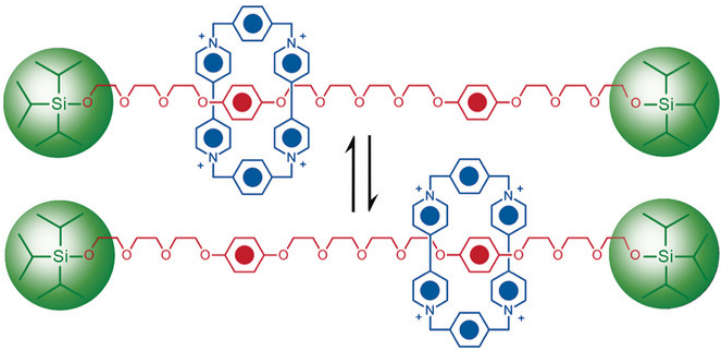

Figure 1.5 A [2]rotaxane, the 'molecular shuttle' introduced by Stoddard in 1991. The positive macrocyclic ring moves back and forth along the electron-rich linear molecular axis and between the hydroquinone recognition sites (1000 times/sec in acetone at room temperature).[32] © (2015) Wiley - VCH Verlag GmbH & Co. KGaA, Weinheim. Reprinted with permission.

In 2004, with the increasing knowledge and possibilities of analytic and synthetic methods, *Stoddard* introduced a 'molecular elevator' consisting of one molecular

platform with three macrocyclic rings attached and one unit consisting of three linear molecules connected to each other on one side and stoppers on the other ends. Variation of the pH value leads to a movement of this platform along the linear axis up and down, induced by crown ether functions switching between the cationic recognition sites.[33,34]

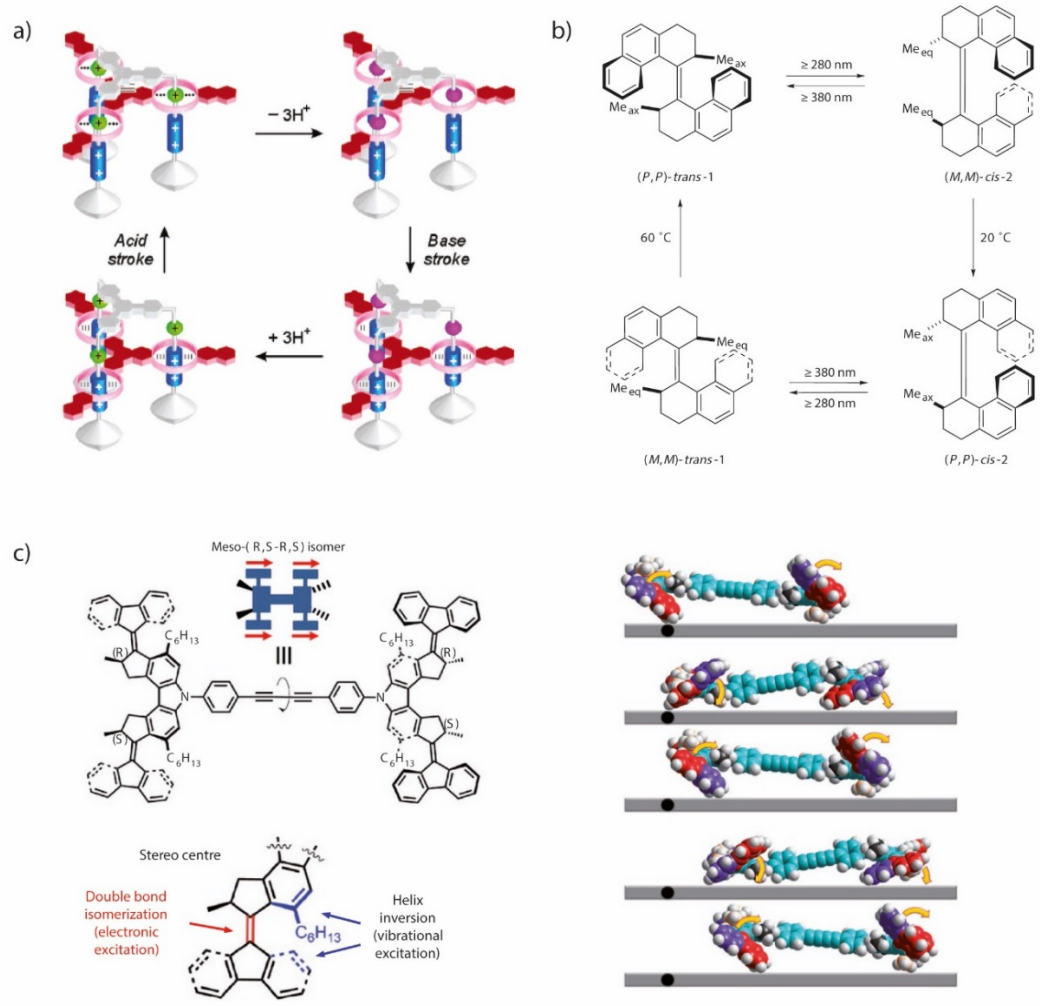

Figure 1.6 a) Simplified scheme of the movement cycle of the molecular elevator induced by acid/base addition. Adapted with permission from reference[34] (2006) American Chemical Society; b) Photochemical and thermal isomerization processes leading to a motion of Feringas 'molecular motor'. Adapted with permission from reference[35] © Springer Nature, American Chemistry Society. c) Structure of the molecular car with a detailed view of a single 'motor' and an illustration of the moving car. Adapted with permission from reference[36] © Springer Nature, American Chemistry Society.

The group of *Bernard Lucas Feringa* introduced a light-driven molecular motor in 1999.[35] This system consists of two paddle-like molecular units connected by an alkene moiety. The rotation of these paddles occurs by light irradiation and thermal isomerization. Further improvements of this principle led to the 'world's smallest car' of 1 nm length made from molecular machines which can move on a copper-surface (figure 1.6).

Due to their distinguished work on molecular machines *Sauvage*, *Stoddard* and *Feringa* were awarded with the Nobel prize in chemistry for the design and synthesis of the reported supramolecular structures in 2016. This indicates once again the high impact of supramolecular chemistry and highlights the work of all groups on different sub-areas of supramolecular chemistry and connections to biochemistry, materials sciences, medicine, and computational science showing the interdisciplinarity.[37,38]

1.2 Coordination-driven Self-assembly

A large number of artificial supramolecular structures is built by the coordination-driven self-assembly approach (also called metal-mediated self-assembly), based on highly reversible interactions.[39–41] Two different types of building blocks are needed for this kind of self-assembly.[42,43] First mentioned are transition metal complexes or 'naked' metal cations, which are brought into the self-assembly reaction with labile ligands. The second class of building blocks needed are electron pair donating organic ligands. As already mentioned in the previous chapter, the high reversibility of non-covalent and coordinative bonds often leads to dynamic supramolecular systems. In this case, the kinetically labile and relative weak metal-ligand coordination enables a so-called self-healing of different connected intermediates to reach an equilibrium with the thermodynamically favoured products.[44,45] The enthalpic contribution Δ*H* is mainly given by the formation of metal-ligand coordination bonds. The major entropic contribution Δ*S* is often given by the increase in entropy by released solvent molecules from the single components and the fewer needed solvent molecules for the solvation of a higher ordered species. These overall entropic and enthalpic contributions are usually the main driving forces behind coordination-driven self-assembly.

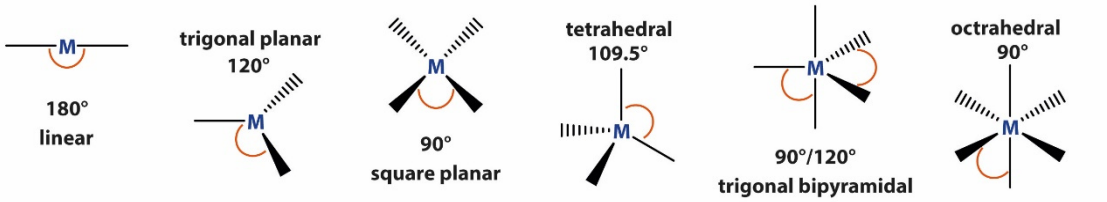

Figure 1.7 Possible coordination spheres of metal-ligand complexes.

Due to the modularity of available building blocks, a high diversity of geometrical structures can be obtained by metal cations (figure 1.7) with different coordination geometries and ligands distinctive in denticity, length, angle and sort of the coordinative groups of the ligand.[40] Possible structures are rings[46,47], knots and links[48,49], helicates[50–53], polyhedra[54,55] or spheres[56–60].

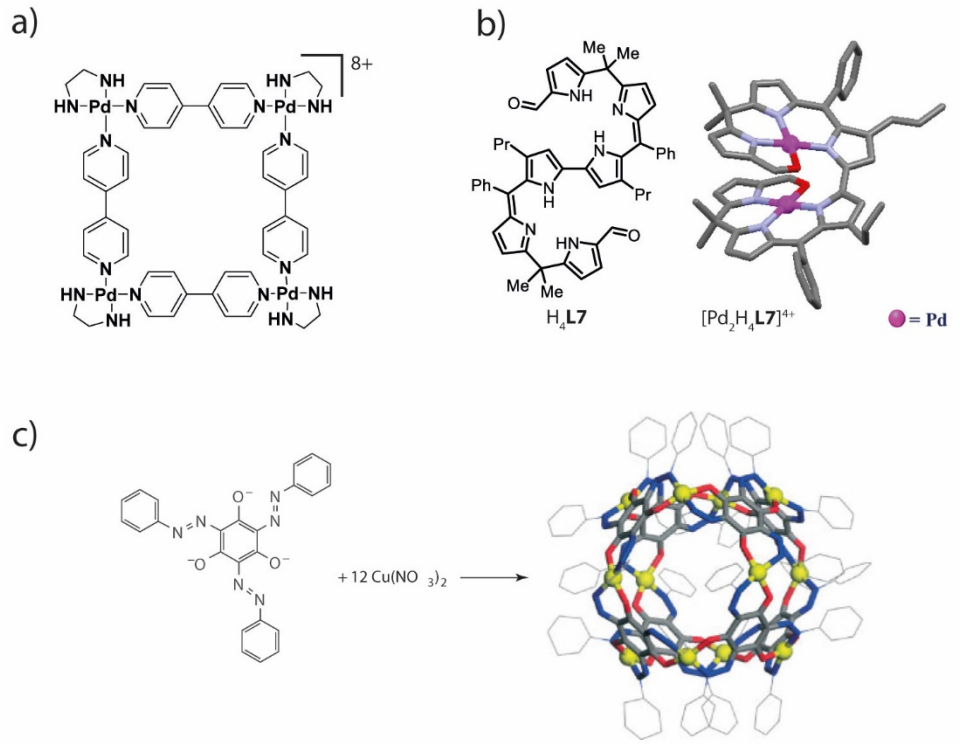

Figure 1.8 Some examples of coordination driven self-assemblies: a) Palladium-based ring-like structure of *Fujita*[46]; b) helicate reported by *Setsune*,[61] figure reprinted with permission from reference[62] © Springer Nature, American Chemistry Society; c) Schematic synthesis of a sphere synthesized by *Robson*,[56] figure reprinted with permission from reference[63], Copyright © 2012 John Wiley & Sons, Ltd.

Most research groups focus on certain metal and ligand geometries, giving a basic geometrical shape for purposeful comparative studies on these confined spaces.[39] $[M_nL_{2n}]$ type coordination cages based on square planar metal ions (*e.g.* Pd(II), Pt(II) or Cu(II))[64–66] and the so called banana-shaped ligands are one example with a high research activity a with a high research interest over the last years.[66,67] These symmetric banana-shaped ligands mostly consist of rigid and aromatic backbones which are connected to two terminal donor group functions. The length or property of such connections can be modified and different linkers can be used, such as single bonds, alkyne groups or flexible sp^3 subunits.[68] It is most important that the bonding vectors of both donor atoms can point in a common direction, leading to a possible formation of one coordination species instead of polymers, grids or mixtures of different species. Figure 1.9 explains the significance of the bend angle of the ligand to predict the resulting coordination cage geometry. The resulting species are mostly charged and therefore polar solvents like acetonitrile are preferably used.

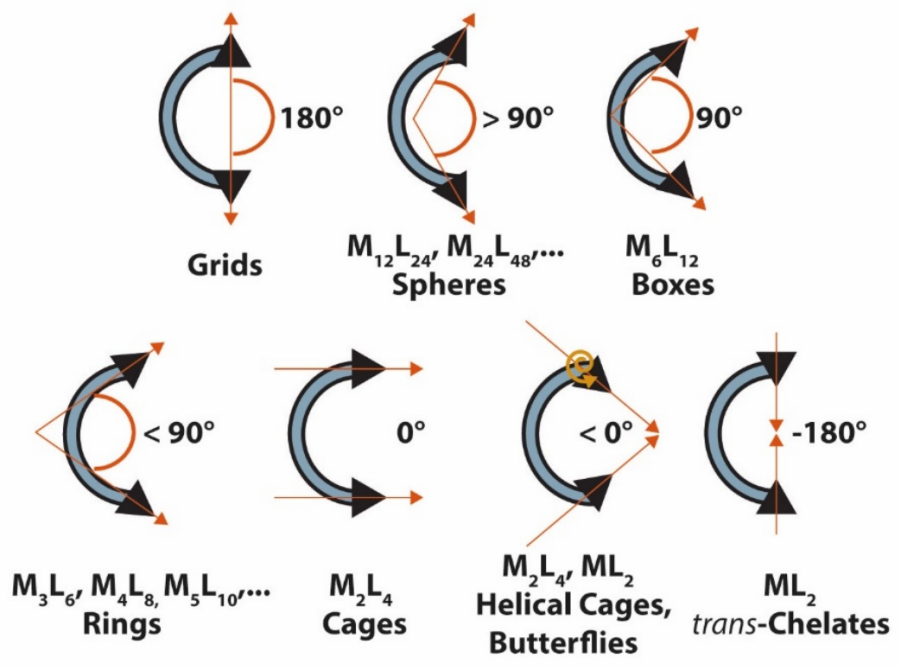

Figure 1.9 Schematic representation of donor group vectors of banana-shaped ligands leading to different classes of coordination species by combination with square planar metal ions.[39]

One class of the mentioned coordination species with a high interest by many research groups are coordination cages of the $[M_2\mathbf{L_4}]$-type with two cations (M = square planar d^8 Pd(II) or Pt(II) cations) bridged by four ligands (**L** = banana shaped ligands, including bis-monodentate ligands), occupying all coordination sites. Since the first reported $[M_2\mathbf{L_4}]$-type cage in 1998[69], the development of these structures made a great progress and a high number of different cages with some beautiful supramolecular peculiarities was reported (figure 1.10). The archetype supramolecular $[Pd_2\mathbf{L^1}_4]^{4+}$ cage of *Steel* was prepared by the reaction of a simple bis-monodentate pyridyl ligand $\mathbf{L}^1$ with $[PdI_2(pyridine)_2]$ as a metal source in the presence of Ag(I) cations, catching the iodide ligands of the precursor and delivering hexafluorophosphate counter ions from $AgPF_6$ for the positive charged cage. In the same year, *Steel* and *Atwood* reported a $[Cu_2\mathbf{L^2_4}(H_2O)_4]^{4+}$ cage, where two octahedral Cu(II) ions are connected by four $\mathbf{L}^2$ bis(amidomethyl)pyridyl ligands and additional four water molecules saturate the Cu(II) axial coordination positions.[70] As an insight in interpenetrated cage structures, figure 1.10 shows the double-cage $[Pd_4\mathbf{L^3_8}]^{8+}$ reported by *Clever* and co-workers in 2015.[71] In 2018, *Lützen* reported a rotaxane-like hexanuclear cage-in-ring structure $\{[Pd_2\mathbf{L^4_4}]@Pd_4\mathbf{L^4_8}]\}(BF_4)_{12}$.[72]

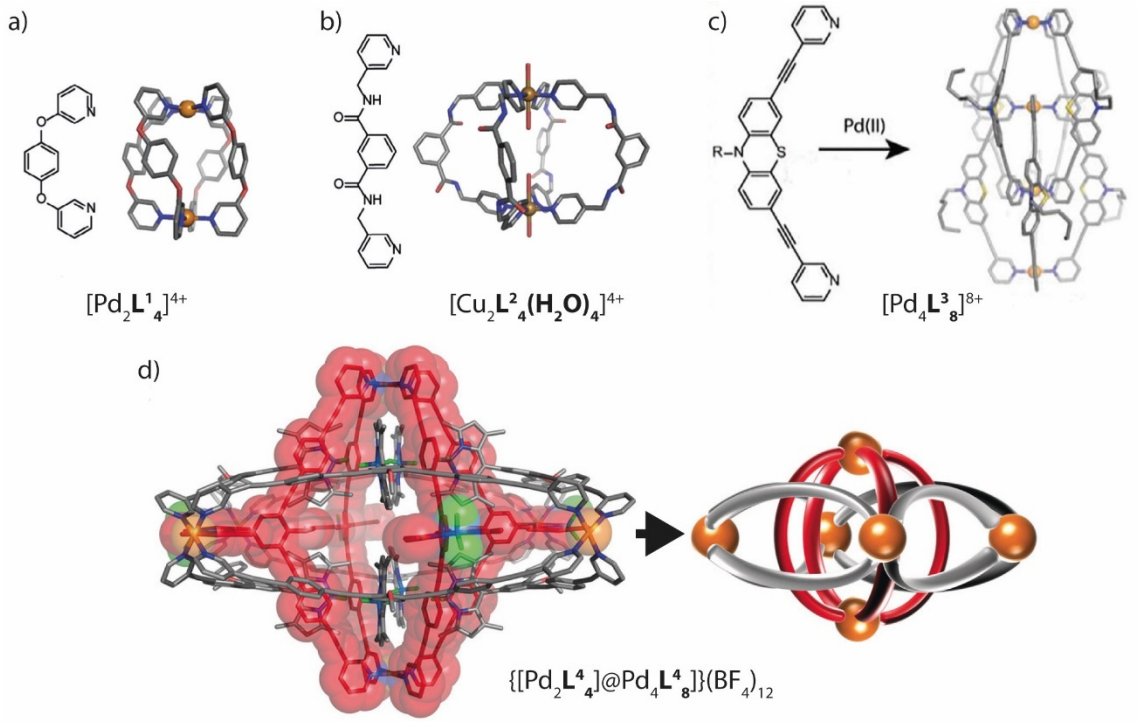

Figure 1.10 Examples for the development of $[M_nL_{2n}]$-type cages over time. a) First reported $[M_nL_{2n}]$-type cage of $[Pd_2L^1_4]^{4+}$-composition from *Steel* in 1998; b) Same year, $[Cu_2L^2_4(H_2O)_4]^{4+}$ cage reported by *Atwood* ; c) By *Clever* reported interpenetrated double cage $[Pd_2L^3_8]^{8+}$, 2015. a), b) and c) are adapted from reference[39] and reprinted with permission. © 2018 Elsevier B.V. All rights reserved.; d) Rotaxane-like cage-in-ring structure by *Lützen* $\{[Pd_2L^4_4]@Pd_4L^4_8]\}(BF_4)_{12}$, 2018. Adapted from reference[72] © (2018) Wiley - VCH Verlag GmbH & Co. KGaA, Weinheim. Reprinted with permission.

As notable from the last two structures, besides the bend angle and donor group vectors, other factors like counter ions, solvents or π-π stackings have an influence of the $[M_2L_4]$-type cage formation, leading to different species than a basic $[M_2L_4]$-cage. Surprises of the resulting structure against the expected one are always possible.

High symmetric supramolecular coordination structures were already able to show potential for applications in medicine,[73–77] sensing and separation,[78–88] catalysis enhancer,[89–97] and as stabilizators for reactive species.[98–100]

2 Creating a modifiable Heteroleptic System

2.1 Introduction

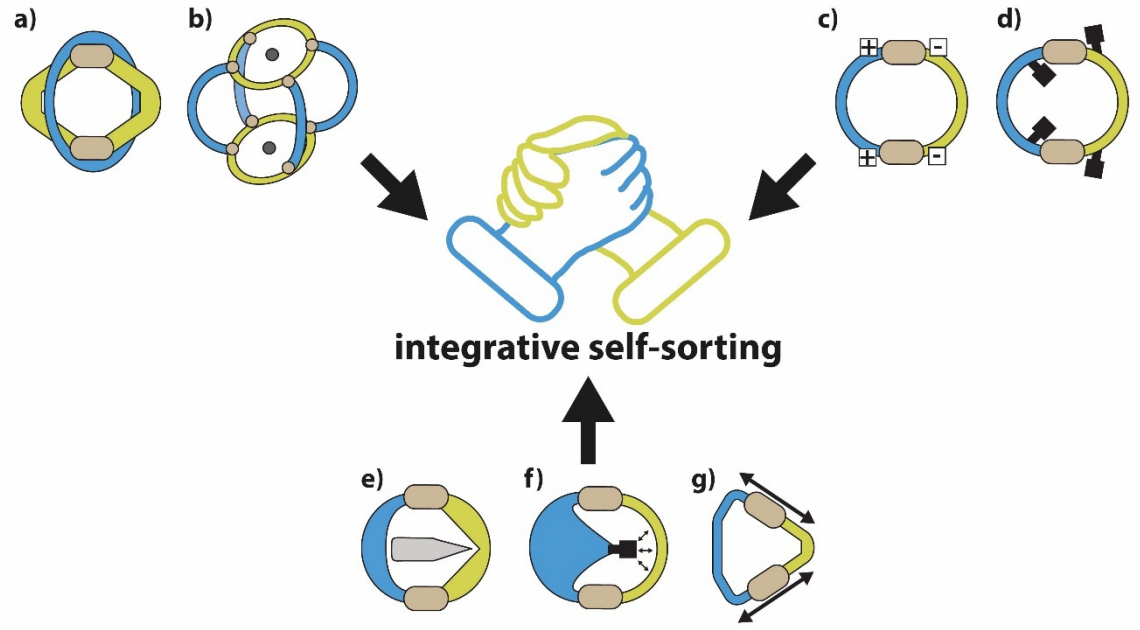

Figure 2.1 Overview of a) saturated metallo-macrocycles with additional ligands; b) metallo-cycles with bridging ligands at open coordination sites; c) charge separation by donor-site engineering; d) bulky substituents close to coordination sites; e) host-guest stabilisation by stabilizing effects; f) bulky steric endohedral modification of one ligand to force a heteroleptic assembly with 'space' giving ligand to form heteroleptic assemblies; g) shape complementary design to give heteroleptic structures.

Numerous homoleptic cages from the small $[M_2\mathbf{L_4}]$-cage to the $[Pd_{48}\mathbf{L_{96}}]$-Goldberg polyhedral of *Fujita* were reported over the last decades.[101–103] The combination of more than one kind of ligand to form a defined heteroleptic assembly is a relatively new field in comparison with homoleptic formations. Heteroleptic assemblies can lead to a possible implementation of more than one function based on the different ligands. This makes this kind of supramolecular assemblies an interesting research topic. Mixing two different bis-monodentate ligands in the presence of Pd(II) or Pt(II) cations would either lead to narcissistic self-sorting of two different homoleptic cages in one solution or to a statistical mixtures of heteroleptic cages. The achievement of one defined heteroleptic species by further highly demanding separation and purifications steps, would represent a non-elegant approach in the scientific field of supramolecular chemistry. To prevent

this, a rational designs of the ligand can lead directly to the desired heteroleptic assembly by integrative self-sorting methods (figure 2.1).[41] In the following sub-chapters, examples of defined self-sorted heteroleptic structures are shown.

2.1.1 Hierarchical assemblies

By using preformed hexa-aza macrocyclic Pd(II) complex **A** coordinated by the carboxylates donors of a tetra-anionic porphyrin ligand **B**, *Costas and Ribas* were able to form a $\mathbf{A_4B_2}$ tetragonal prismatic nanocage by a hierarchical assembly driven by charge separation and provided open coordination sides.[104] The macrocycles containing Pd(II) or Zn(II) as central atoms, make it possible to encapsulate anionic guests. Following up, *Costas and Ribas* elongated the hexa-aza macrocyclic Pd(II) complex, and the Zn(II)-centered porphyrin enables the uptake of ligands with further open coordination sites, making it possible to bind additional Zn, Cu or Fe.[105] An enantioselective hydroformylation by a Rh-Catalyst coordinated to a ligand encapsulated inside the same Zn(II) porphyrin based cage was shown in a work together with *Reek*.[106] The resulting supramolecular assembly showed high catalytic performance in the hydroformylation of styrene (figure 2.2).

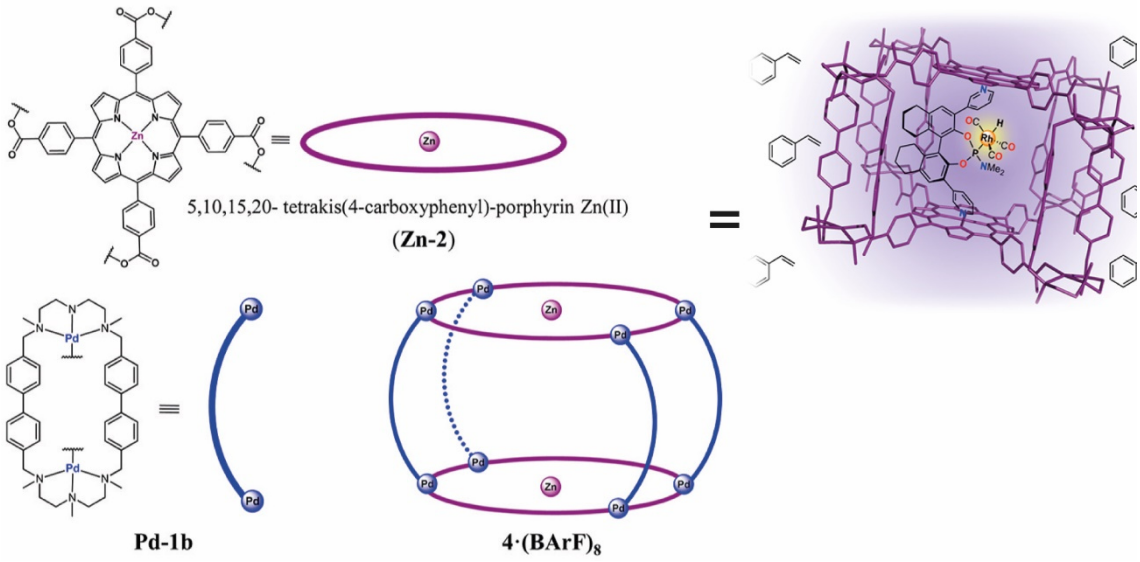

Figure 2.2 Supramolecular cage by hierarchical assembly of *Costas and Ribas* (left): tetra-anionic porphyrin ligand and a hexa-aza macrocyclic Pd(II) complex.[105] A work together with *Reek* leads to the catalytic active supramolecular species constating of the cage hosting an organic ligand coordinating to a Rhodium catalyst.[106] Adapted with permission from reference[106] Copyright © (2015) American Chemical Society.

2.1.2 Coordination-dependent Approaches

Cis-protected metal centres can be used for the assembly of heteroleptic cages. By charge separation between carboxylate and pyridine donors, *Stang* and co-workers were

able to introduce a series of heteroleptic supramolecular species.[107,108] The use of *cis*-protected $Pt(PEt_3)_2(OTf)_2$ metal building blocks (coordination-sphere engineering) in combination with tri- or tetradentate pyridine ligands and terephthalates led to the desired structures exploiting the preference to combine negatively charged carboxylates with one pyridine donor at each metal centre due to the favourable charge compensation (figure 2.3).

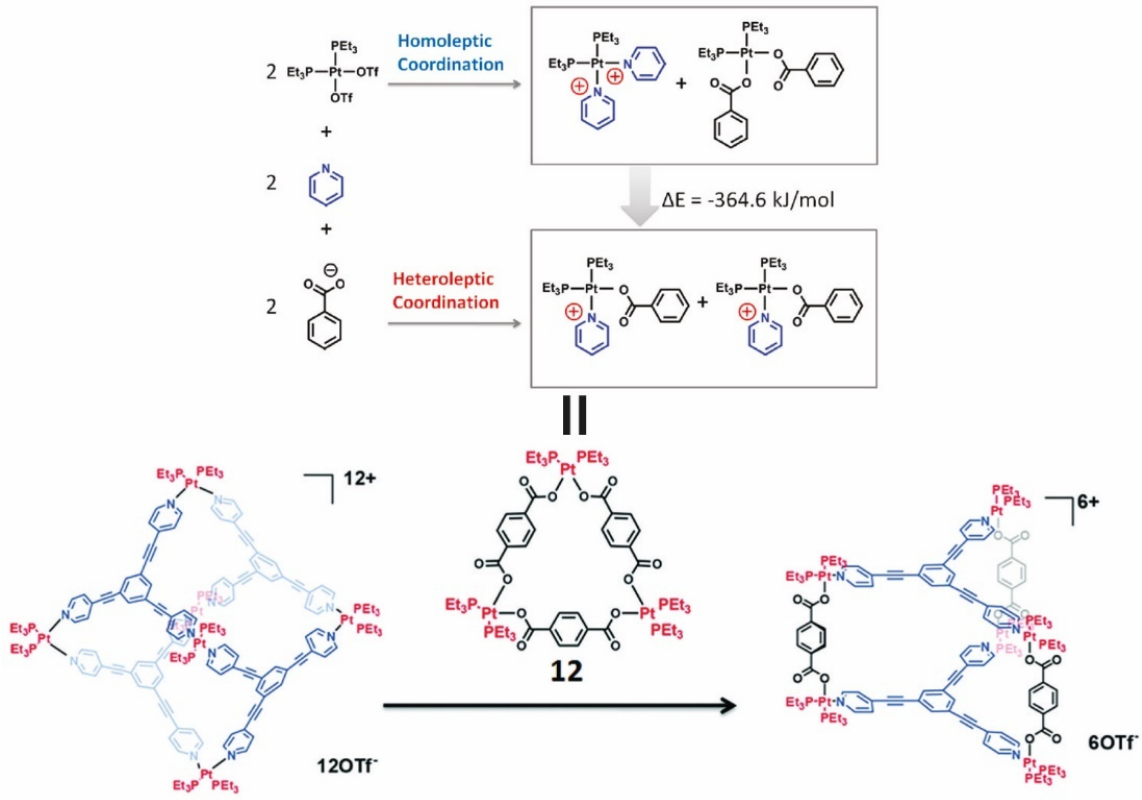

Figure 2.3 Selective self-assembly of *cis*-$Pt(PEt_3)_2(OTf)_2$ with carboxylates and pyridyl donor functions due to lower energy of the heteroleptic systems (above). Schematic example of the formation of a heteroleptic trigonal prism from a charged homoleptic tetrahedron combined with a neutral supramolecular triangle. Adapted with permission from reference[107] © (2015) American Chemical Society.

Bulky substituents near the coordination site can also lead to the formation of heteroleptic assemblies. Sterically demanding methyl groups in proximity to the coordination site by one ligand can lead to the desired structures, as showed by Fujita and co-workers (figure 2.4).[109] The Clever group introduced a similar approach, combining sterically demanding methyl groups in proximity to the coordination site with inside ($\mathbf{L^{Pi}}$) and outward ($\mathbf{L^{Ao}}$) the cavity pointing methyl groups of a $[Pd_2\mathbf{L^{Ao}}_2\mathbf{L^{Pi}}_2]$-cage.[110]

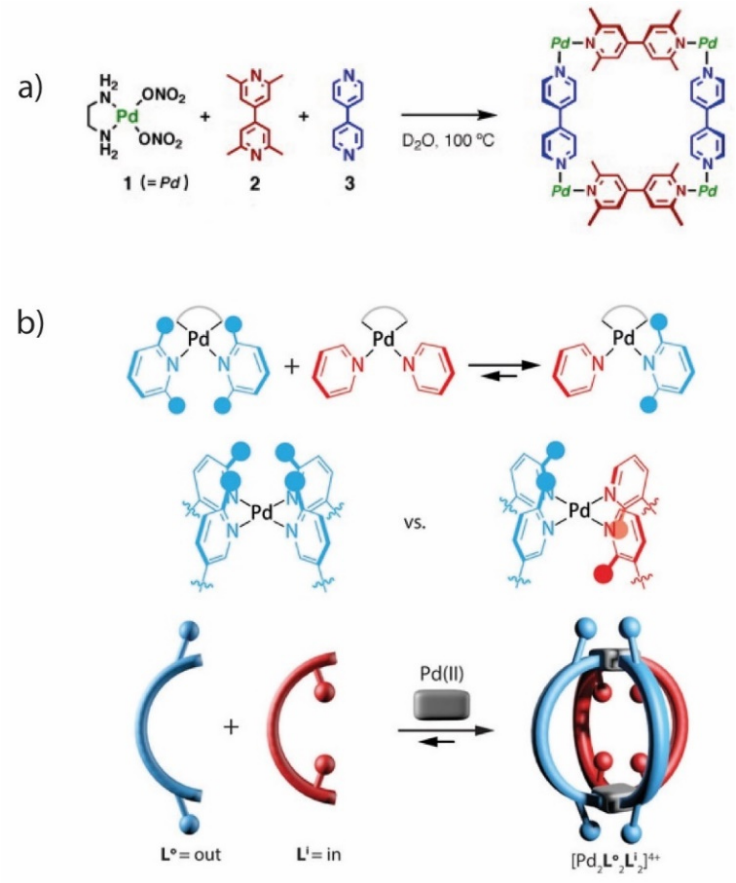

Figure 2.4 Bulky substituents close to coordination sites forcing the ligands to form heteroleptic coordination species. a) Example of Fujita and co-workers.[109] adapted from reference and reprinted with permission. © 2005 Elsevier B.V. All rights reserved; b) example of the Clever group.[110] Adapted with permission from reference[110] © 2018 John Wiley & Sons, Ltd.

2.1.3 Assembly-dependent Approaches

Besides the hierarchical assembly and modifications of coordination sites, assembly dependent approaches are another method to form selective heteroleptic cages. Guest molecules can template the heteroleptic cage formation, making the homoleptic cages less energetically favourable. Again, *Fujita* used *cis*-protected palladium (II) and combined it with two different tridendate pyridyl ligands.[111] This led to a mixture of homoleptic and heteroleptic cages. By the addition of different guests, this equilibrium could be triggered to form different ratios of homo- or heteroleptic cages. The combination of *cis*-protected Pt(II) with tris(pyridine)triazine and pyrazine led to a guest templated heteroleptic cage when large planar and aromatic guests are used.[112] *Yoshizawa* reported the synthesis of a heteroleptic cage by guest templation with fullerenes.[113] Two different ligands based on anthracene panels with phenylene or naphthalene backbones were prepared. The homoleptic Pd(II) cage (naphthalene backbone) with the bigger cavity was able to host C_{70} as well as diethyl malonate-

derivatized C_{60} fullerenes while the smaller cage (phenylene based ligands) was not able to be host these guests. Mixing both cages led to a static mixture of heteroleptic cages, but addition of C_{60} led to a reorganisation into heteroleptic *cis*-$[Pd_2L^1{}_2L^2{}_2]$ cage.

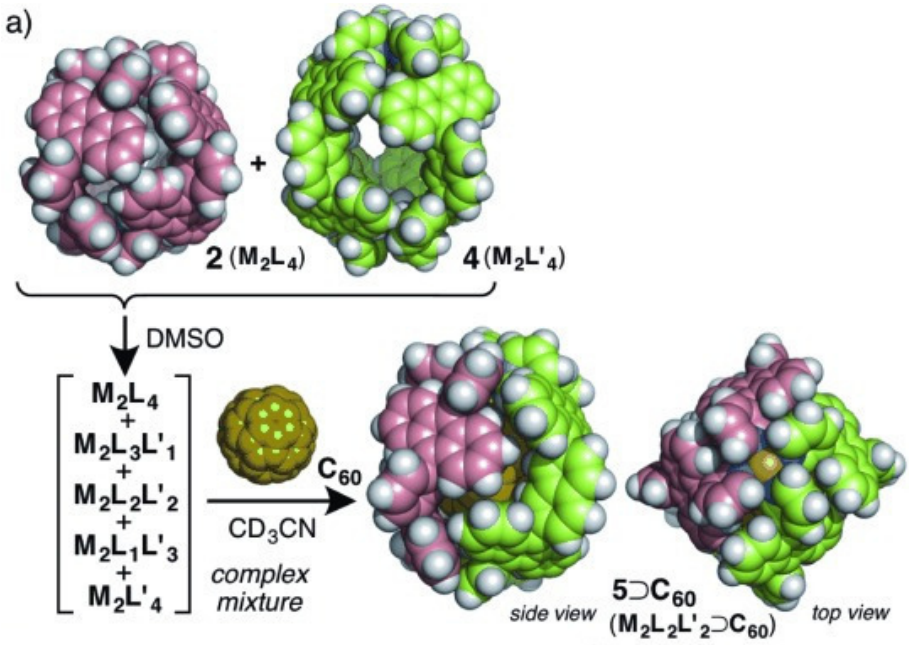

Figure 2.5 Reorganisation of two homoleptic Pd(II) cages to form a heteroleptic cage due to C_{60} guest templating. Adapted with permission from reference[113] © 2015 John Wiley & Sons, Ltd.

Another method to form defined heteroleptic species is the modification of the inward pointing side of a ligand with a bulky and sterically demanding functionality. This endohedral modification of ligands forces a heteroleptic assembly with less sterically demanding ligands to form heteroleptic assemblies. *Hooley* and co-workers reported the formation of heteroleptic cages including three different ligands with an increasing size of endohedral functions.[114] While the less sterically demanding ligands (**L^{8c}** unfunctionalized and **L^{8d}** with an **-NH$_2$** group) formed a statistical mixture of heteroleptic cages, the combination of the more steric demanding ligand (**L^{8a}** with trifluoroacetate function) led to the formation of $[Pd_2\mathbf{L^{8a}{}_2L^{8c}{}_2}]$-cage together with homoleptic $[Pd_2\mathbf{L^{8c}{}_4}]$- and no observed $[Pd_2\mathbf{L^{8a}{}_4}]$-cage (figure 2.6figure 1.1).

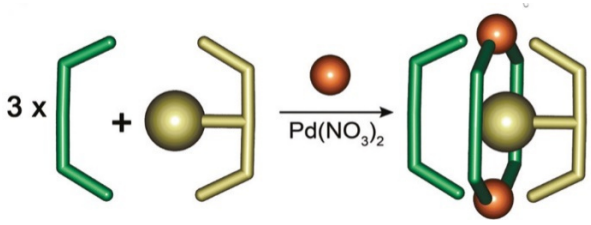

Figure 2.6 Schematic representation of the heteroleptic assembly induced by the combination of three 'space giving' ligands with one ligand functionalized with a bulky endohedral modification. Adapted with permission from reference[114] © (2011) American Chemical Society.

Nevertheless, when a guest molecule or bulky endohedral modification is needed to form heteroleptic cages, the cavity is already occupied and host-guest chemistry is limited, except the achieved host-guest complex is already useful in a certain way. An elegant method to achieve heteroleptic assemblies without the use of cavity space is to exploit the shape complementarity of the ligands. In 2014, *Fujita* and co-workers demonstrated the formation of a heteroleptic sphere using significant size differences of the ligands used.[115] The synthesised bis(pyridyl) benzene and extended bis-(pyridylethynylphenyl) benzene forms clean homoleptic cuboctahedral [$Pd_{12}\mathbf{L_{24}}$]-type spheres. By mixing the ligands in a 1:1:1 ratio with Pd(II), the desired [$Pd_{12}\mathbf{L_{12}L'_{12}}$]-sphere resulted in two isomers (figure 2.71).

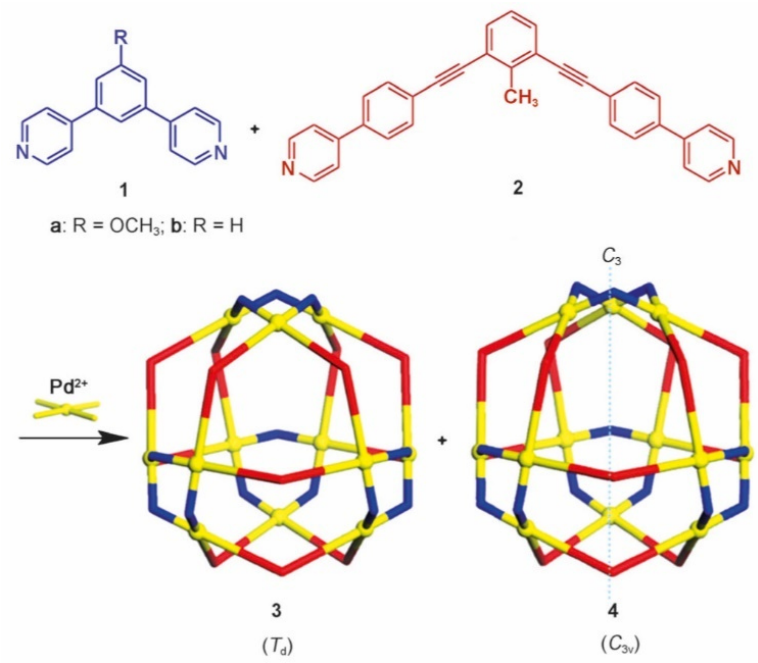

Figure 2.7 Schematic formation of the two isomers of the heteroleptic [$Pd_{12}L_{12}L'_{12}$]-sphere formed by shape complementary ligands.[115] © (2014) Wiley ‐ VCH Verlag GmbH & Co. KGaA, Weinheim. Reprinted with permission.

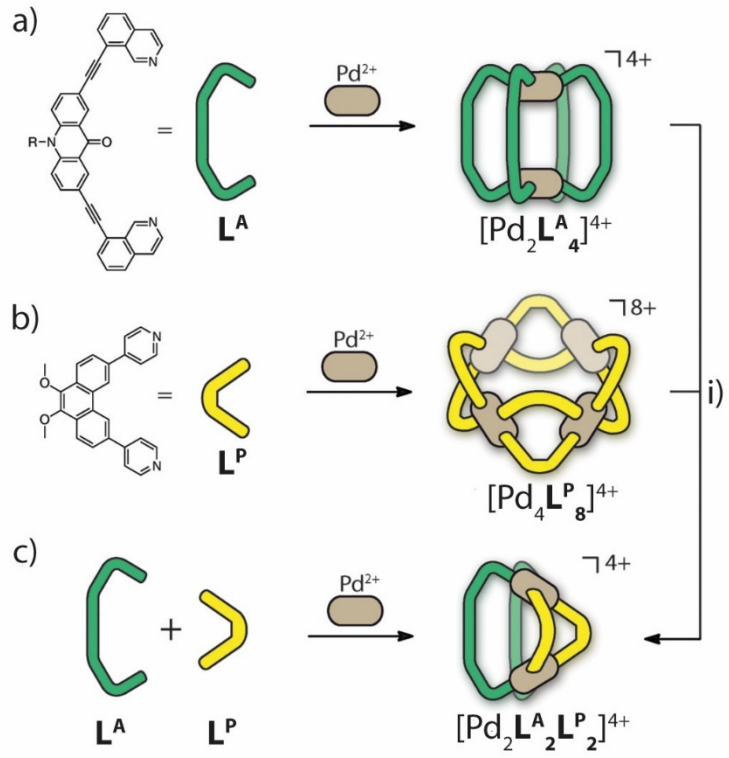

Figure 2.8 Schematic formation of homoleptic cages a) $[Pd_2L^A_4]^{4+}$ and b) $[Pd_2L^A_4]^{4+}$ from respective ligands; c) Combination of both ligands leads directly to $[Pd_2L^A_2L^P_2]^{4+}$; i) Mixing homoleptic assemblies $[Pd_2L^A_4]^{4+}$ and $[Pd_2L^A_4]^{4+}$ leads to the formation of $[Pd_2L^A_2L^P_2]^{4+}$. Adapted with permission from reference[116] © (2016) American Chemical Society.

The Clever group introduced a method based on geometric complementarity of the ligands to form heteroleptic assemblies.[116] A banana-shaped acridone-based ligand $\mathbf{L^A}$ with inward bent isoquinoline donors and a bend angle of θ = -120° was mixed with a banana-shaped phenanthrene-based ligand $\mathbf{L^P}$ with outward-bent pyridyl donor functions (θ = 60°) and Pd(II) in a 1:1:1 ratio. This combination resulted in the formation of a clean $[Pd_2\mathbf{L^A_2L^P_2}]$-cage in *cis*-conformation (figure 2.8). Also, mixing of the homoleptic species of $\mathbf{L^A}$ and $\mathbf{L^P}$ results in rearrangement to the single and stable heteroleptic products, making it the favourable thermodynamic minimum out of all possible ligand combinations. The geometric complementarity is characterized by the adoption of two rings inside a $[M_2\mathbf{L_4}]$-type cage, consisting of two ligands different in size and bend angle giving in coordinated form a planar donor groups to metal centre axis (directional bonding approach).[117–119] The formation of a heteroleptic $[Pd_2\mathbf{L^A_2L^P_2}]$-cage instead of the narcissistic self-sorting to homoleptic $[Pd_2\mathbf{L^A_4}]^{4+}$ and $[Pd_4\mathbf{L^P_8}]^{8+}$, would lead to an entropy increase as the number of supramolecular species would be higher. In addition, the homoleptic $[Pd_2\mathbf{L^A_4}]$-cage with its quinoline functions indicated a twisting to a helical species and a strain for the ligands, making it the driving force to form structures reducing the ligand strain, like the heteroleptic $[Pd_2\mathbf{L^A_2L^P_2}]$-cage. A further study expanded the systematic investigation of these heteroleptic assemblies.[120] A carbazole-based ligand

$\mathbf{L^C}$ with a bend angle of θ = -30° was mixed with both ligands $\mathbf{L^A}$ and $\mathbf{L^P}$, respectively. This led to the formation of two new heteroleptic cages in each case (figure 2.9). While $\mathbf{L^C}$ and $\mathbf{L^P}$ gave a *cis* conformation of $[Pd_2\mathbf{L^C}_2\mathbf{L^P}_2]$, the combination of $\mathbf{L^C}$ with $\mathbf{L^A}$ led to a novel topology of *trans*-$[Pd_2\mathbf{L^A}_2\mathbf{L^P}_2]^{4+}$ with both $\mathbf{L^A}$ ligands in a cavity-penetrating *anti*-conformation.

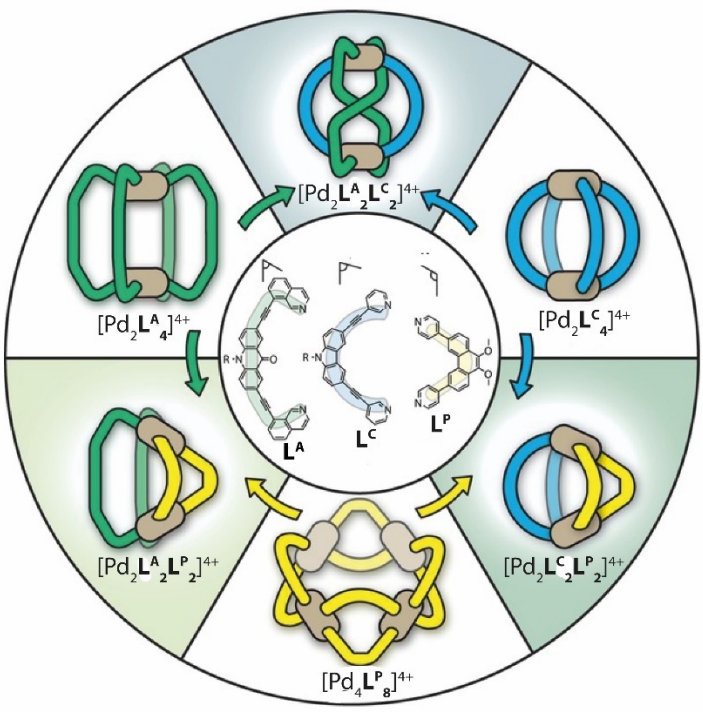

Figure 2.9 Schematic formation of possible combinations of ligands L^A, L^C and L^P and the respective homoleptic cages to form heteroleptic species upon mixing with each other.[120] © (2017) Wiley ‐ VCH Verlag GmbH & Co. KGaA, Weinheim. Reprinted with permission.

2.1.4 Host-Guest Chemistry

Most of the herein discussed supramolecular coordination species have a cavity allowing the molecule to be the host (**H**) for a smaller guest molecule (**G**) and forming a **HG**-complex. The host molecule cavity provides convergent binding sites (*e.g.* Lewis basic donor atoms or hydrogen bond donors) whereas the guest molecule provides divergent binding sites (*e.g.* Lewis acidic metal cations or hydrogen-bond acceptors).[121] Examples for host molecules are enzymes or the reported supramolecular coordination structures. A guest can in principle be every molecule small enough to fit into the cavity and to form weak non-covalent interactions. Importantly, the cavity needs to provide a defined space for non-covalent interactions of specific hosts and guests leading to reversible guest uptakes and releases. The **HG**-binding is characterized by the equilibrium between the free host and guest inside a solution with a **HG**-complex, defined in (1).

$$K_a = \frac{[\mathbf{HG}]}{[\mathbf{H}]\cdot[\mathbf{G}]} = \frac{k_1}{k_{-1}} \qquad (1)$$

K_a, the binding constant, expresses the thermodynamic stability of a specific **HG**-complex. A high binding constant correlates to a high concentration of the **HG**-complex in equilibrium. The binding constant can also be expressed by the ratio between the rate constant of the complexation and decomplexation, namely k_1 and k_{-1}, respectively. NMR, ITC or UV/VIS spectroscopy or many other methods giving quantitative analytics for the concentrations of involved molecules can be used to determine K_a.[122]

[$Pd_2\mathbf{L_4}$]-type cages are known for the encapsulation of anionic guests inside their cavity.[65,68,123,124] The archetype [$Pd_2\mathbf{L^A_2L^P_2}$]-cage, which is the template of this work reported [$Pd_2\mathbf{L^{OMe}_2L^{SX}_2}$]-type cages, was the first [$Pd_2\mathbf{L_4}$]-cage with a bent structure.[116] With the Pd(II) metal centres that can serve as anchors for charged anionic molecules this cage gave a shape-specific guest binding ability. By using a straight 2,7-naphtalene disulfate and a bent 2,6-naphtalene disulfate as guest molecules, the cage as a host was able to show a shape recognition on the level of host-guest binding (figure 2.10).

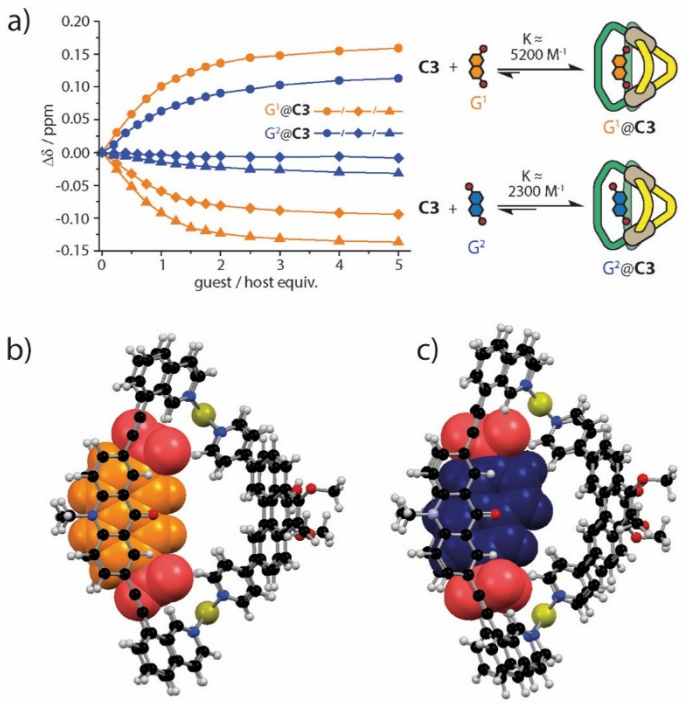

Figure 2.10 a) 1H NMR titration plot of the [$Pd_2L^A_2L^P_2$]-cage with 2,7-naphtalene disulfate and 2,6-naphtalene disulfate. DFT calculations shows the energy minimized structures of the HG-complex with b) 2,7-naphtalene disulfate@[$Pd_2L^A_2L^P_2$]$^{2+}$ and c) 2,6-naphtalene disulfate@[$Pd_2L^A_2L^P_2$]$^{2+}$. Adapted with permission from reference[116] © (2016) American Chemical Society.

2.2 Aim

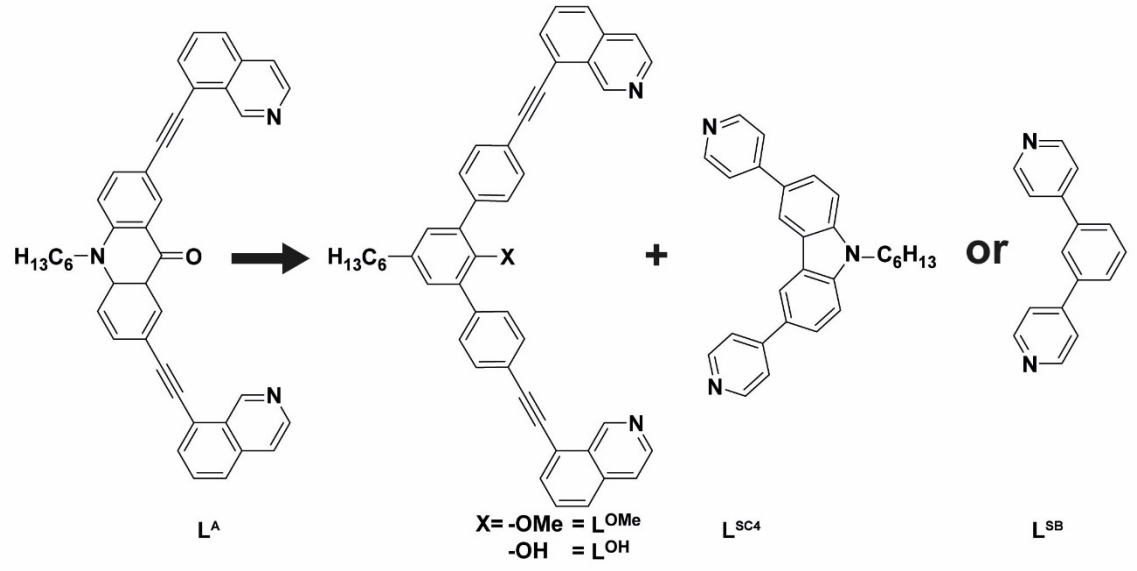

Figure 2.11 Starting point for the introduction of the new heteroleptic coordination cage with the archetype L^A ligand and modifiable new ligands L^{OMe} and L^{OH}. In addition the possible pyridyl ligands as counter-ligands inside a heteroleptic system, L^{SC4} and L^{SB}.

The ability to form pre-designed heteroleptic structures by the mentioned method of integrative self-sorting, gives the possibility to enlarge the availability of supramolecular structures for sensing and separation, catalysis, medical purposes, and stabilisation of reactive species. This is made possible by the implementation of multiple functions by different ligands of one supramolecular system. By having a highly modifiable basic motif forming a heteroleptic supramolecular coordination cage, comparative studies would be simplified, and the synthetic effort could be reduced. Herein, this work uses shape-complementary approach for the introduction of a highly modifiable basic motif. The before reported ligand $\mathbf{L^A}$ with its quinoline inward pointing donor function as the basic unit is replaced by ligands with highly changeable subunit, leading to the use of substituted phenyl-based backbones $\mathbf{L^{OMe}}$ (figure 2.11). It will be first investigated if the new ligands will form a homoleptic $[Pd_2\mathbf{L^{OMe}_4}]$ cage with a similar strain and helical structure like before reported $[Pd_2\mathbf{L^A_4}]^{4+}$, giving the main driving force to form heteroleptic structures with reduced strain in a $[Pd_2\mathbf{L^{OMe}_2L^X_2}]$-composition. Afterwards, pyridyl-based ligands $\mathbf{L^{SC4}}$ and $\mathbf{L^{SB}}$ are used to form the desired heteroleptic assemblies. After these initial findings, a series of endohedral modified cages with the same topology are introduced and possible influences of the modifications for the heteroleptic cage formation are investigated and lead to further supramolecular cages like a $[Pd_2\mathbf{L^{OMe}_2L^XL^Y}]$-type cage and an elongated $[Pd_2\mathbf{L^{LOMe}_4}](BF_4)_4$ system. Finally, in this

work introduced cages of the [$Pd_2\mathbf{L}^{\mathbf{OMe}}_{\mathbf{2}}\mathbf{L}^{\mathbf{X}}_{\mathbf{2}}$]-type are used to investigate the influence of different endohedral modifications on the guest uptake.

2.3 Ligands and corresponding homoleptic Cages with Quinoline Donor Functions

Ligand $\mathbf{L^{OMe}}$ ($\mathbf{L^{OMe}}$ = **L**igand **Me**thoxy (-**OMe**); 8,8'-((5'-hexyl-2'-methoxy-[1,1':3',1''-terphenyl]-4,4''-diyl)bis(ethyne-2,1-diyl))diisoquinoline) was prepared in overall 7 steps, starting with 4-hexylphenol to yield the ligand backbone in 2 steps (figure 2.12) and 8-bromoisoquinoline as the donor group for the "ligand arms" in 4 steps (figure 2.13). In the last synthetic step, $\mathbf{L^{OMe}}$ was accessed via a Suzuki-Miyaura Cross-Coupling.

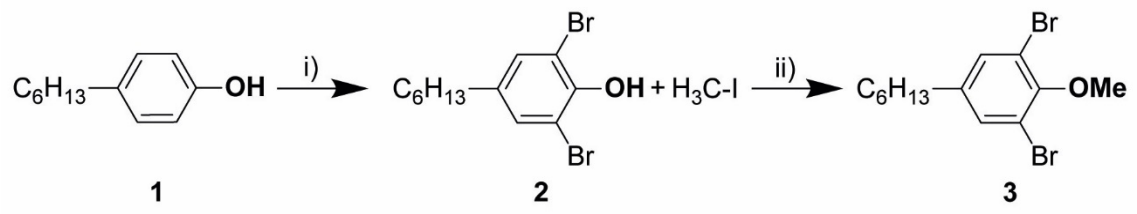

Figure 2.12 Synthesis of the ligand backbone. i) BTMA*Br_3, DCM/MeOH = 5:2, rt, 1 h; ii) K_2CO_3, acetone, reflux, 3 h.

4-hexylphenol (**1**) was brominated with BMTA*Br_3 (benzyltrimethylammonium-tribromid) to give 2,6-dibromo-4-hexylphenol (**2**) as a colourless oil in 99 % yield. Methylation with Iodomethane gave 1,3-dibromo-5-hexyl-2-methoxybenzene (**3**) as the backbone building block (97 % yield, highly viscous colourless oil). 8-bromoisoquinoline (**4**) was transformed to 8-((trimethylsilyl)ethynyl)isoquinoline (**5**) in a Sonogashira cross-coupling with ethynyltrimethylsilane to give a yield of 92 %. After deprotection (**6**, 99 %), the second Sonogashira cross-coupling with 1-bromo-4-iodobenzene gave 8-((4-bromophenyl)ethynyl)isoquinoline (**8**, 68 %). The reaction of **8** with bis(pinacol)diborane produced the pinacol ester 8-((4-(4,4,5,5-tetramethyl-1,3,2-dioxaborolan-2-yl)phenyl)ethynyl)isoquinoline (**9**) in 85 % yield. After preparing **3** and **9**, the final Suzuki-Miyaura cross-coupling (figure 2.14) took place to give $\mathbf{L^{OMe}}$ (50 %). The ligand was further purified by GPC to give $\mathbf{L^{OMe}}$ (For ^{1}H NMR of the ligand, see figure 2.15, further characterization of $\mathbf{L^{OMe}}$ see experimental section).

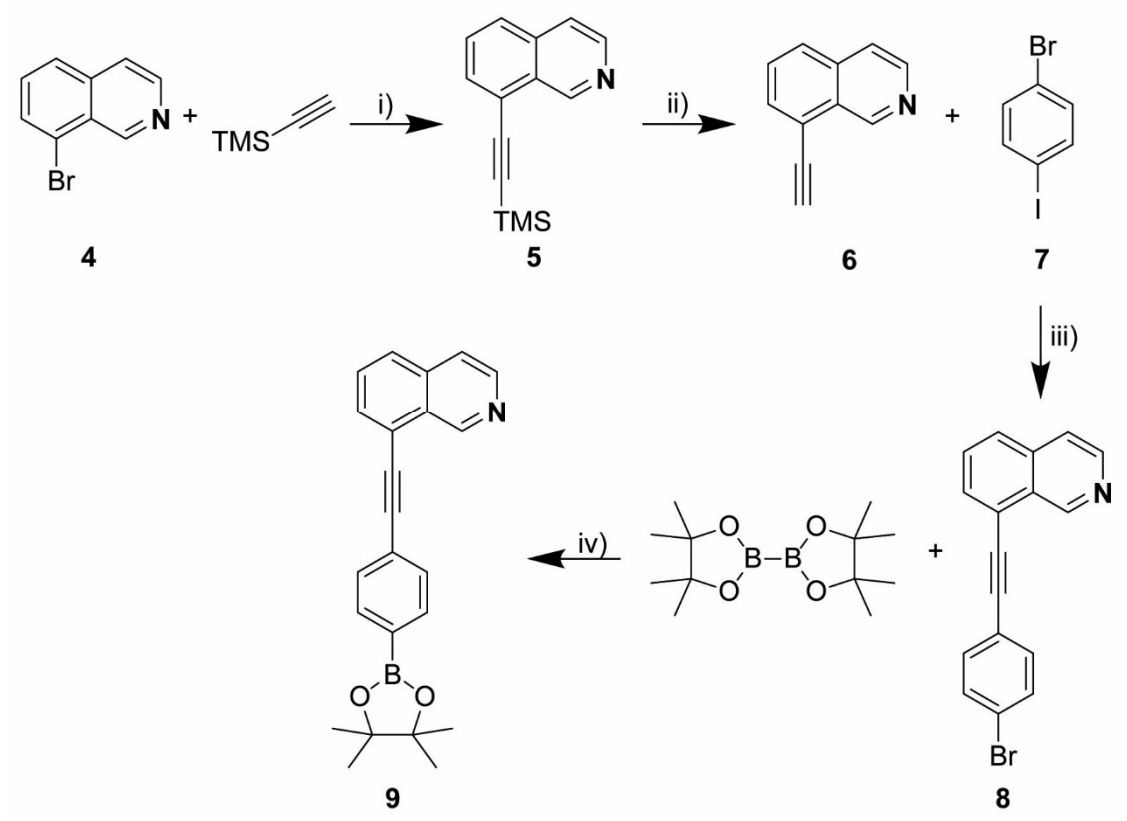

Figure 2.13 Synthesis of the ligand arm. i) $Pd(PPh_3)_2Cl_2$, CuI, Et_3N, THF, 65 °C, overnight; ii) K_2CO_3, MeOH, rt, 4 h; iii) $Pd(PPh_3)_2Cl_2$, CuI, Et_3N, THF, rt, overnight; iv) $Pd(dppf)Cl_2$, KOAc, DMF, 155 °C, 75 min.

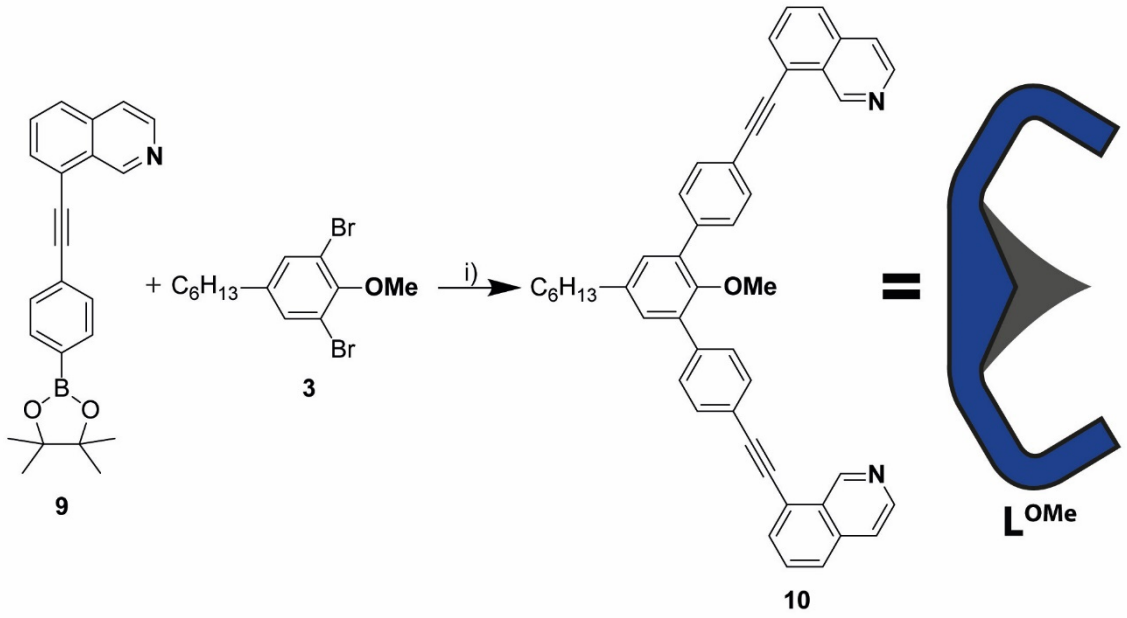

Figure 2.14 Suzuki-Miyaura cross-coupling of compound 8 and 3 to form ligand L^{OMe}. i) $Pd(PPh_3)_4$, K_2PO_4, 1,4-dioxane/H_2O = 3:1, 100 °C, overnight.

After successful synthesis of $\mathbf{L^{OMe}}$, it was used to prepare a $[Pd_2\mathbf{L_4}]$-type supramolecular coordination cage.

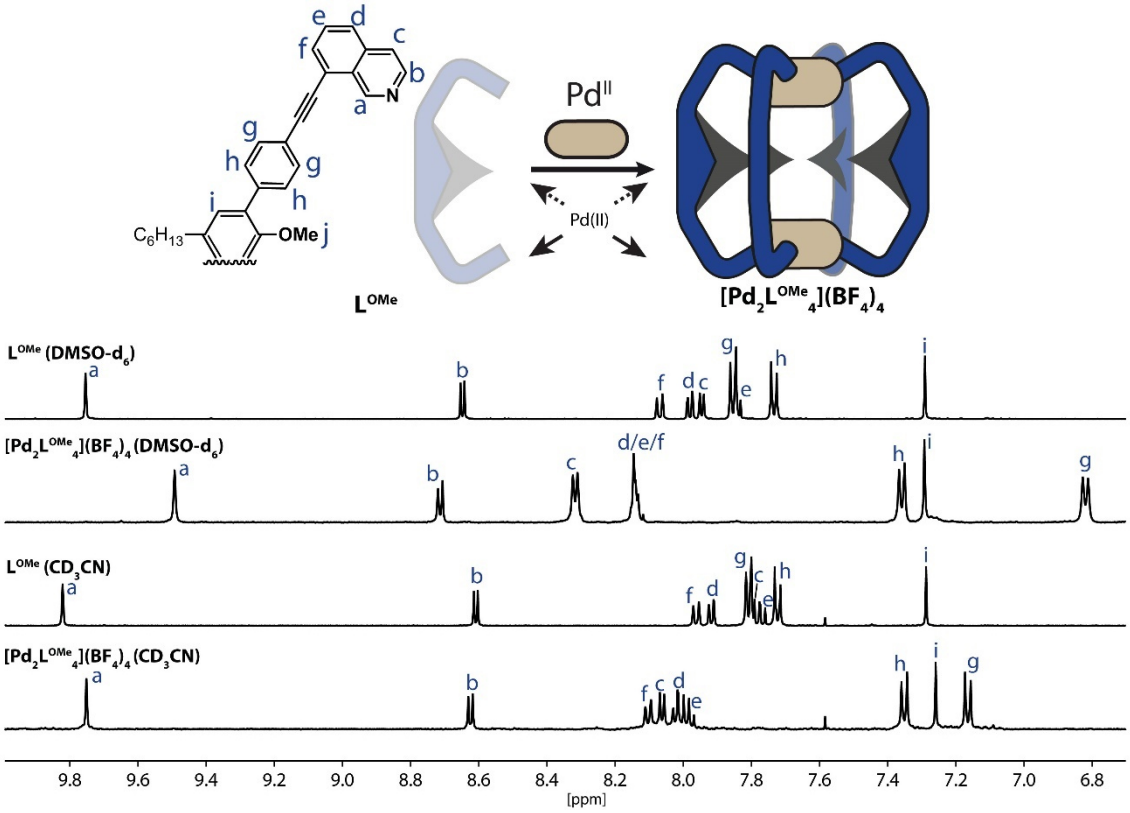

Figure 2.15 Schematic formation of the homoleptic $[Pd_2L^{OMe}_4](BF_4)_4$ cage and partial ^1H NMR spectra (500 MHz, 298 K, DMSO-d_6 and CD_3CN) of the free ligand L^{OMe} compared with the associated homoleptic cages.

In the following the standard preparation protocol for cage solutions inside an NMR tube is described[116]. The ligand was dissolved in deuterated acetonitrile or dimethyl sulfoxide (each 7 mM), respectively. 240 µl (1 eq,1.68 µmol) of the ligand stock solution was placed in an NMR tube together with 240 µl pure solvent. Afterwards, 60 µl (0.5 eq, 0.8 µmol) of a 15 mM tetrakis(acetonitrile)palladium(II) tetrafluoroborate stock solution in the respective solvent was added and the tube was sealed. After thorough mixing, the sample was heated for 2 h at 70 °C to give a 0.7 mM $[Pd_2\mathbf{L}^{\mathbf{OMe}}_4](BF_4)_4$ cage solution. To prove the formation of the expected cage, several analytic methods were used, starting with simple ^1H NMR (figure 2.15). $\mathbf{L}^{\mathbf{OMe}}$ shows in CD_3CN and DMSO-d_6 nine aromatic signals with a total count of 34 protons by signal integration. After addition of $[Pd(CH_3CN)_4](BF_4)_2$, all aromatic signals are shifted with constant signal integration, indicating a reaction with Pd^{2+} in a $Pd^{2+}/\mathbf{L}^{\mathbf{OMe}}$ ratio of 1:2 leading to one symmetric molecule for both solvents. The upfield shift of several protons suggests a shielding by π-systems of neighboured ligands. This indicates the desired twisting of the $[Pd_2\mathbf{L}^{\mathbf{OMe}}_4](BF_4)_4$ to a helical structure like seen before for the $[Pd_2\mathbf{L}^{\mathbf{A}}_4]$-cage and induce a strain to the system which can be the driving force for building heteroleptic assemblies.

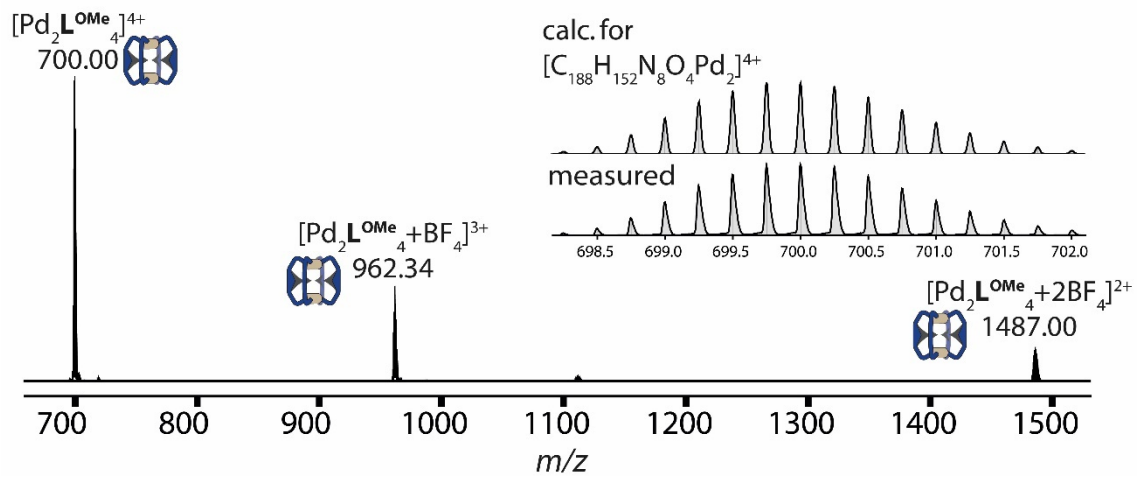

Figure 2.16 ESI mass spectrum of $[Pd_2L^{OMe}_4](BF_4)_4$ (DMSO-d_6 sample).

After the ^{1}H NMR spectrum indicated a well-defined ligand/palladium coordination, the sample was analysed by ESI-MS. Both CD_3CN and DMSO-d_6 samples show a clean mass spectrum with the main peaks at *m/z* = 700.00, 962.34 and 1487.00 corresponding to $[Pd_2\mathbf{L}^{\mathbf{OMe}}_{\mathbf{4}}]^{4+}$, $[Pd_2\mathbf{L}^{\mathbf{OMe}}_{\mathbf{4}}+BF_4]^{3+}$ and $[Pd_2\mathbf{L}^{\mathbf{OMe}}_{\mathbf{4}}+2BF_4]^{2+}$ as it is confirmed from the calculated isotope patterns (figure 2.16).

Additionally, a ^{1}H DOSY NMR spectrum in CD_3CN was measured to prove the formation of a one species. The measured spectrum (figure 2.17) shows a defined single species with a diffusion coefficient of $D = 5.217 \cdot 10^{-10}$ $m^2 \cdot s^{-1}$. To calculate the hydrodynamic radius, the Stokes-Einstein equation is used (Equation 2) with k_b = Boltzmann constant, T for temperature, η the dynamic viscosity of the respective solvent and r_H as the hydrodynamic radius.[125,126] The low concentration of the samples lead to the use of the dynamic viscosity for pure solvents, due to the negligible difference. In estimation a perfect spherical structure is assumed to avoid the need of a shape factor.

$$D = \frac{k_b T}{6\pi\eta r_H} \qquad (2)$$

From this a hydrodynamic radius for $[Pd_2\mathbf{L}^{\mathbf{OMe}}_{\mathbf{4}}](BF_4)_4$ in CD_3CN of r_H = 12.13 Å is calculated, being in the same range as for similar reported structures like the $[Pd_2\mathbf{L}^{\mathbf{A}}_{\mathbf{4}}]$-cage.[116]

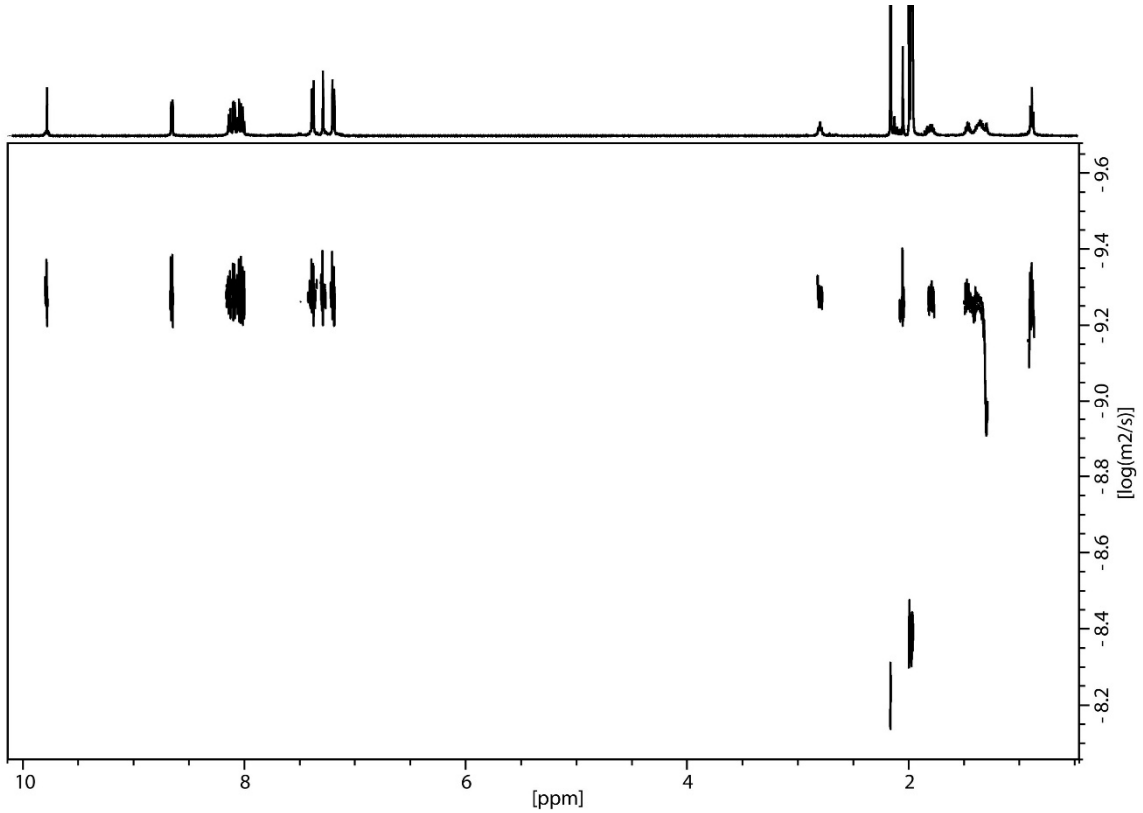

Figure 2.17 ^{1}H DOSY NMR (500 MHz, 298 K, CD_3CN) spectrum of homoleptic $[Pd_2L^{OMe}{}_4](BF_4)_4$ cage. One species with a diffusion coefficient of $D = 5.217 \cdot 10^{-10}$ $m^2 \cdot s^{-1}$.

Single crystal X-ray analysis further confirms the twisted ligand structure of $[Pd_2\mathbf{L}^{\mathbf{OMe}}{}_4]^{4+}$ (figure 2.18). The crystals, grown with slow vapor diffusion of ethyl acetate to a 0.7 mM $[Pd_2\mathbf{L}^{\mathbf{OMe}}{}_4]^{4+}$ cage solution in CD_3CN at 7 °C, were measured on a *Bruker D8 venture* diffractometer. Analysis of the solid-state structure shows a mixture of (P)- and (M)-$[Pd_2\mathbf{L}^{\mathbf{OMe}}{}_4]^{4+}$ conformers in one crystal, induced by the quinoline units orientating in one defined way for each isomer. The Pd•••Pd distance of 18.1 Å and a distance of the most distal protons of 24.2 Å is in a good agreement with the hydrodynamic radius by ^{1}H DOSY NMR measurement of r_H = 12.13 Å. The **-MeO•••OMe-** distances for neighboured oxygens are in a range of 3.5 Å up to 5.1 Å and 6.3 Å across the cavity. In general, the Methoxy groups are not sorted inside the cavity in a particular way. As seen from one single ligand inside the cage structure, the quinoline units pointing to different directions and all ligands units are distorted along the ligand axis to respond a strain induced by the cage formation.

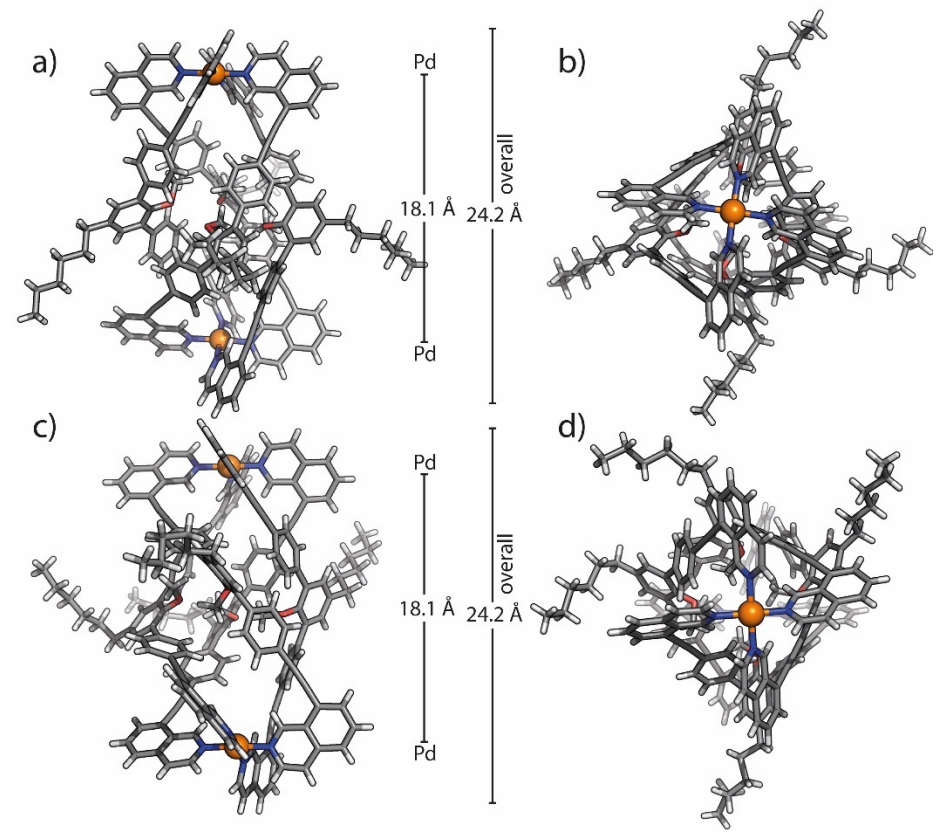

Figure 2.18 X-ray structures of two $[Pd_2L^{OMe}{}_4]^{4+}$ conformers inside the same crystal. a) side view of (P)-$[Pd_2L^{OMe}{}_4]^{4+}$; b) top view of (P)-$[Pd_2L^{OMe}{}_4]^{4+}$; c) side view of (M)-$[Pd_2L^{OMe}{}_4]^{4+}$; b) top view of (M)-$[Pd_2L^{OMe}{}_4]^{4+}$. Solvent molecules and BF_4^- counterions were omitted for clarity. Colour scheme: C = dark grey, H = light grey, O = red, N = blue, Pd = orange.

While signal H_a, H_b, H_e and H_i of $[Pd_2\mathbf{L}^{OMe}{}_4](BF_4)_4$ in CD_3CN are assignable with the signal integration, shape and shift on the ppm scale, the other signals are identified by 2D NMR. To assign the ^1H NMR signals of the formed cage, ^1H-^1H COSY and ^1H-^1H NOESY NMR experiments were performed for $[Pd_2\mathbf{L}^{OMe}{}_4](BF_4)_4$ in CD_3CN and DMSO-d_6. The pre-identified signal H_b shows a cross-peak with the adjacent proton H_c (^1H-^1H COSY NMR spectrum, figure 2.19) and H_e with H_f (bigger deshielding/downfield shift of h_f against H_d, due to alkyne group). The same cross-peaks are shown by ^1H-^1H NOESY NMR (figure 2.20). More interesting on this spectrum re the H_a-H_g and H_h-H_i cross-peaks to distinguish proton H_g and H_h.

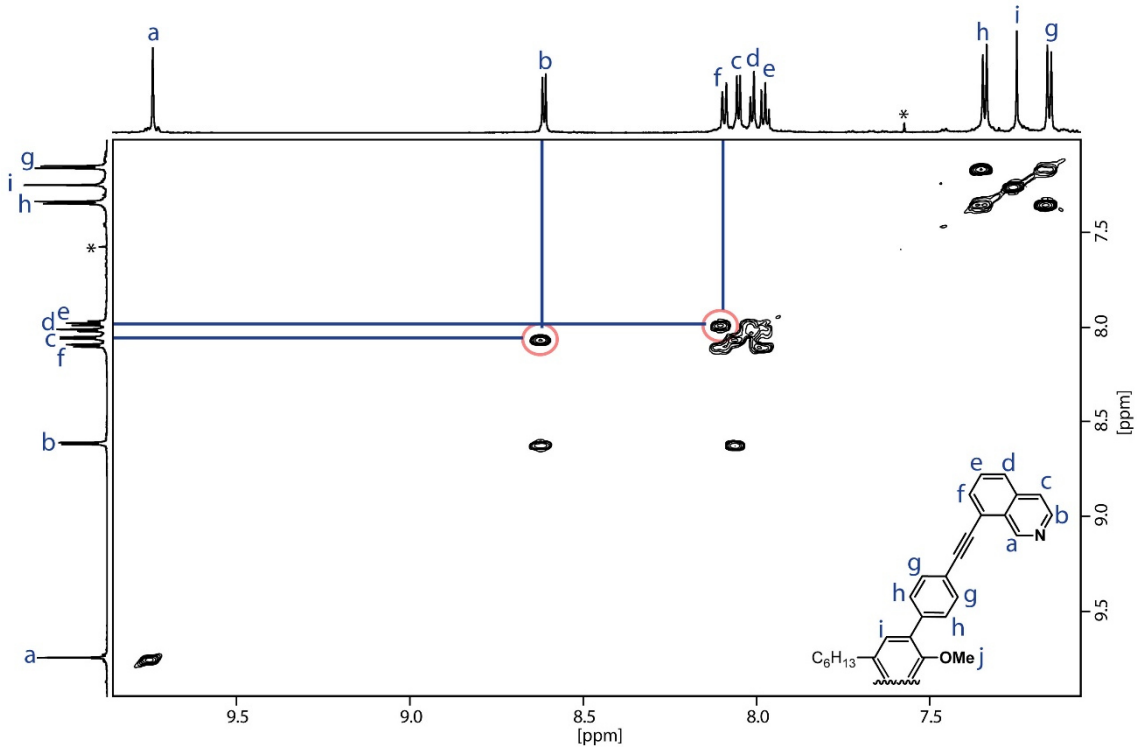

Figure 2.19 Partial ^{1}H-^{1}H COSY NMR (700 MHz, 298 K, CD_3CN) spectrum of homoleptic $[Pd_2L^{OMe}{}_4](BF_4)_4$ cage. Cross-peaks between L^{OMe} ligand protons are marked dark blue.

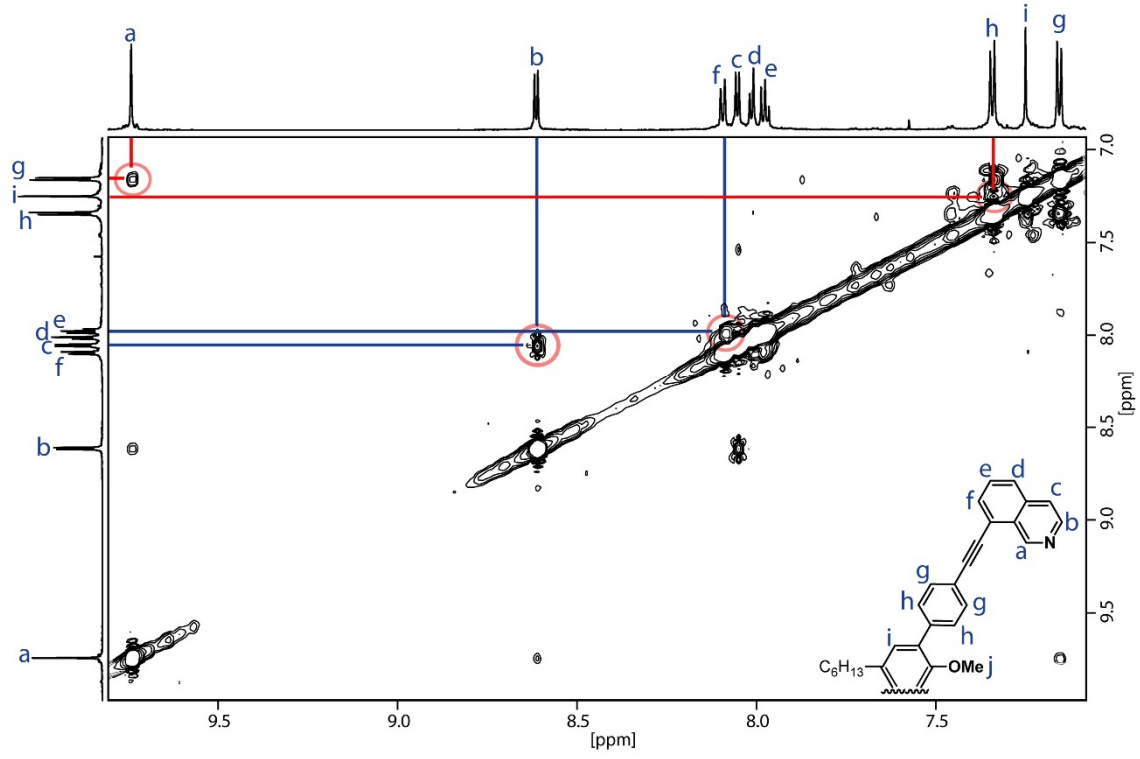

Figure 2.20 Partial ^{1}H-^{1}H NOESY NMR (700 MHz, 298 K, CD_3CN) spectrum of homoleptic $[Pd_2L^{OMe}{}_4](BF_4)_4$ cage. Cross-peaks between L^{OMe} ligand proton are marked dark blue; important H_a-H_g and H_i-H_h cross-peaks are marked with red.

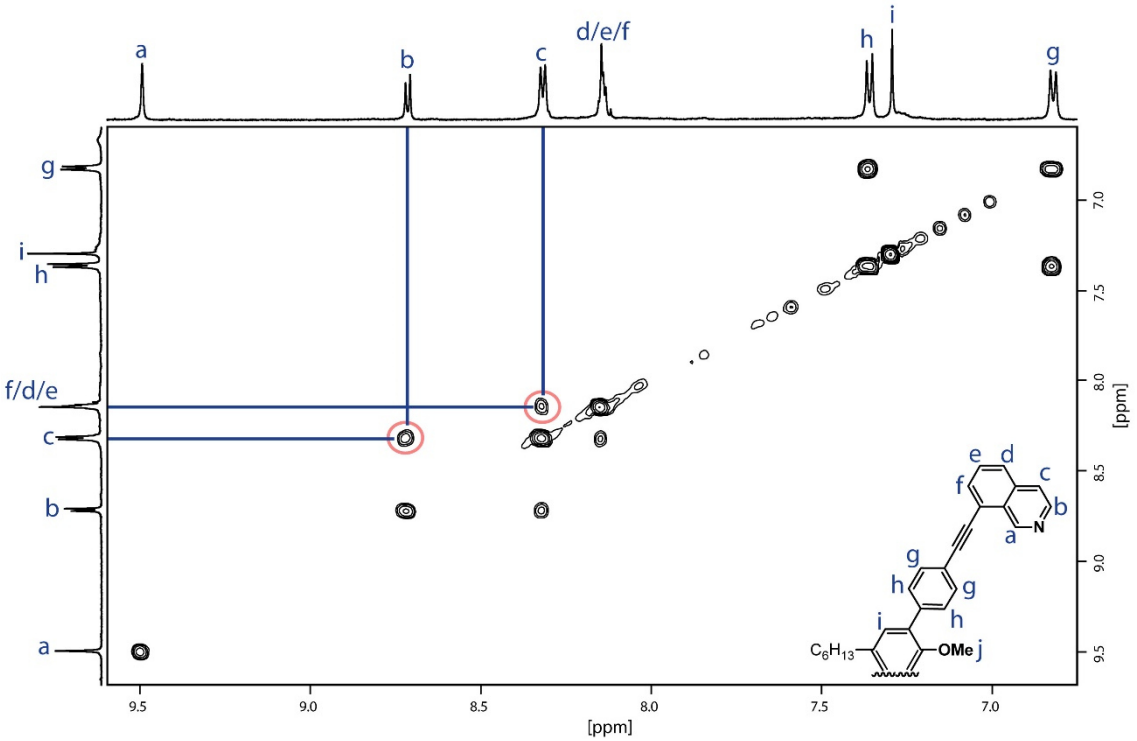

Figure 2.21 Partial ^{1}H-^{1}H COSY NMR (700 MHz, 298 K, DMSO-d_6) spectrum of homoleptic $[Pd_2L^{OMe}{}_4](BF_4)_4$ cage. Cross-peaks between L^{OMe} ligand protons are marked dark blue.

For the ^{1}H NMR spectrum of $[Pd_2\mathbf{L^{OMe}{}_4}](BF_4)_4$ in DMSO-d_6, it is also possible to assign protons H_a, H_b and H_i accounting for the signal shape and shift on ppm scale. ^{1}H-^{1}H COSY NMR spectrum (figure 2.21) indicates cross-peaks of H_b-H_c and H_c with the overlapping signals of $H_{d/e/f}$. Cross-peaks H_a-H_g and H_h-H_i in the ^{1}H-^{1}H NOESY NMR spectrum (labelled red, figure 2.22) indicates protons H_g and H_h.

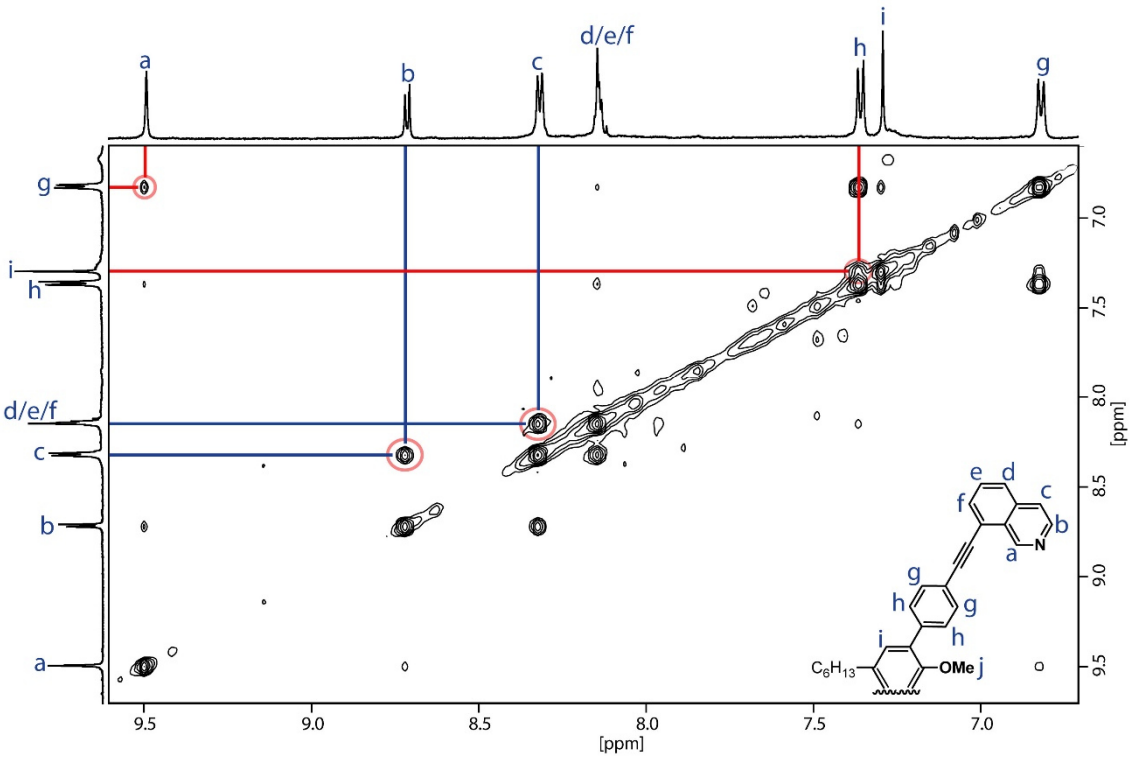

Figure 2.22 Partial ^{1}H-^{1}H NOESY NMR (700 MHz, 298 K, DMSO-d_6) spectrum of homoleptic $[Pd_2L^{OMe}_4](BF_4)_4$ cage. Cross-peaks between L^{OMe} ligand protons are marked dark blue; important H_i-H_h cross-peaks marked with red.

The ligand $\mathbf{L^{OH}}$ ($\mathbf{L^{OH}}$ = **L**igand Hydroxy (-**OH**); 5'-hexyl-4,4''-bis(isoquinolin-8-ylethynyl)-[1,1':3',1''-terphenyl]-2'-ol) was prepared in 8 steps. The synthesis followed the procedure for $\mathbf{L^{OMe}}$ with an additional deprotection of the methoxy group using BBr_3 (46 % Yield, figure 2.23). The ligand was further purified by GPC to give $\mathbf{L^{OH}}$ as a slightly yellow solid (for ^{1}H NMR spectrum, see figure 2.24, further characterization of $\mathbf{L^{OH}}$ see experimental section).

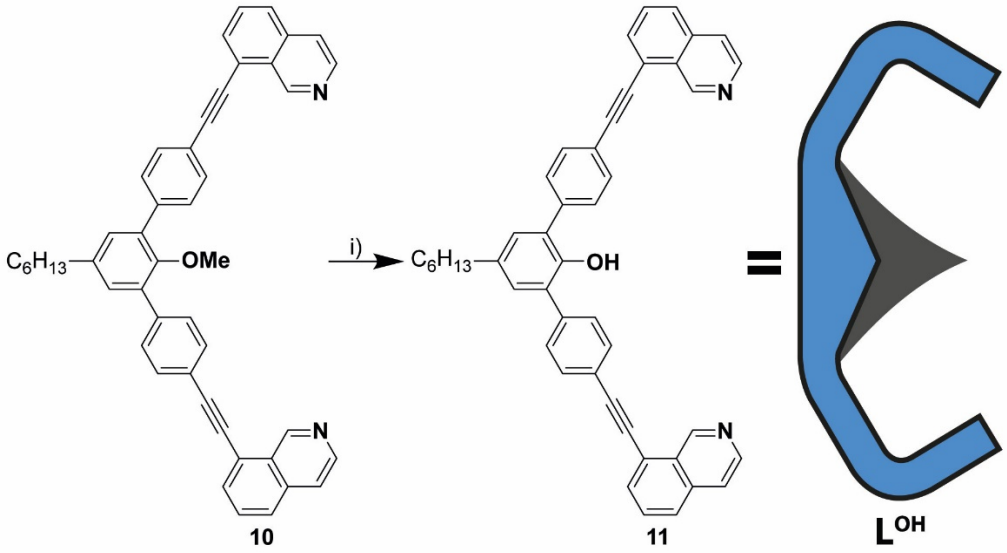

Figure 2.23 Deprotection of L^{OMe} to form L^{OH}. i) BBr_3, DCM, 0 °C, 2 d.

Cage solutions with $\mathbf{L^{OH}}$ were prepared at 0.7 mM $[Pd_2\mathbf{L^{OH}_4}](BF_4)_4$ in CD_3CN and DMSO-d_6 using the same procedure as for $[Pd_2\mathbf{L^{OMe}_4}](BF_4)_4$. While the ^1H NMR analysis for CD_3CN shows the formation of a well-defined species (figure 2.24), in DMSO-d_6 broadened and low resolved ^1H signals were observed, which was not further investigated. The signal integration is not changing after cage formation, indicating a reaction with Pd^{2+} in a $Pd^{2+}/\mathbf{L^{OMe}}$ ratio of 1:2 to a symmetric molecule. The upfield shift of several protons can be again explained by helical twist along the Pd-Pd axis, resulting in a strained structure with shielding π-systems from the neighbouring ligand.

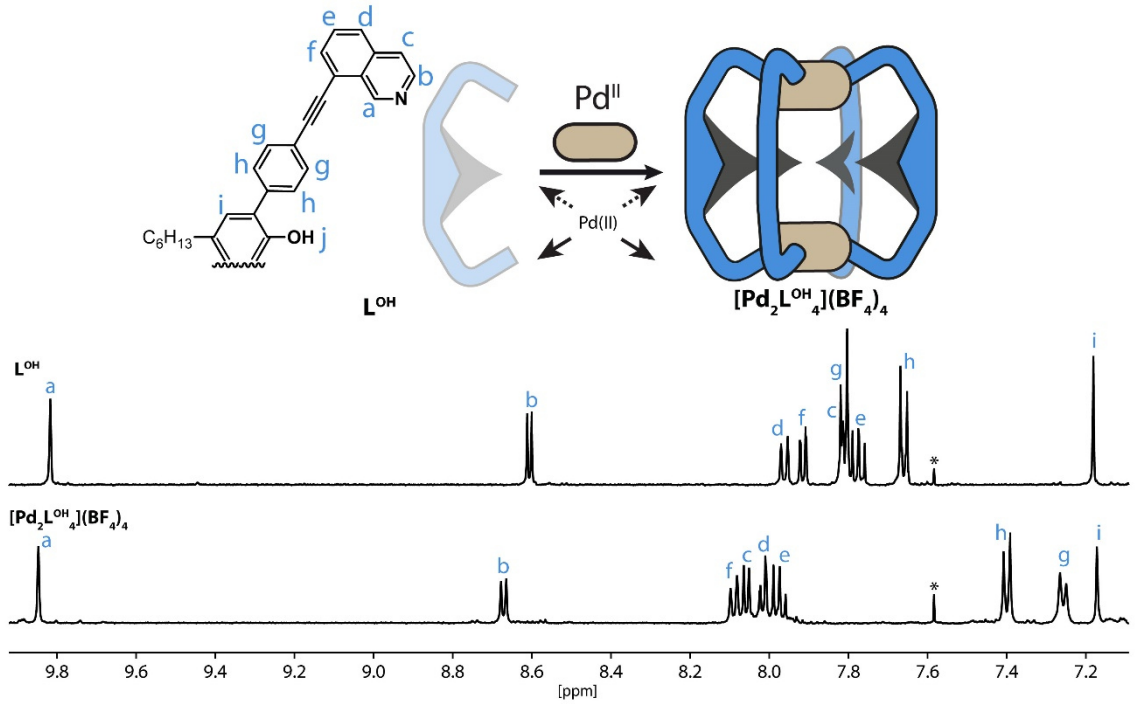

Figure 2.24 Schematic formation of the homoleptic $[Pd_2\mathbf{L^{OH}_4}](BF_4)_4$ cage and partial ^1H NMR spectra (500 MHz, 298 K, CD_3CN) of the free ligand $\mathbf{L^{OH}}$ compared with the associated homoleptic Cage.

For ESI-MS measurements with a *Bruker ESI-timsTOF* mass spectrometer, cage samples were diluted 1:10, leading to a slow decomposing. This caused a not clean mass spectrum of $[Pd_2\mathbf{L^{OH}_4}](BF_4)_4$ (figure 2.25). To circumvent this, samples were diluted and immediately injected into the ESI-MS device, now showing the prominent peaks $[Pd_2\mathbf{L^{OH}_4}]^{4+}$ with *m/z* = 685.7, $[Pd_2\mathbf{L^{OH}_4}+BF_4]^{3+}$ with *m/z* = 943.3 and $[Pd_2\mathbf{L^{OH}_4}+2BF_4]^{2+}$ with *m/z* = 1459.5 with matching calculated isotope patterns.

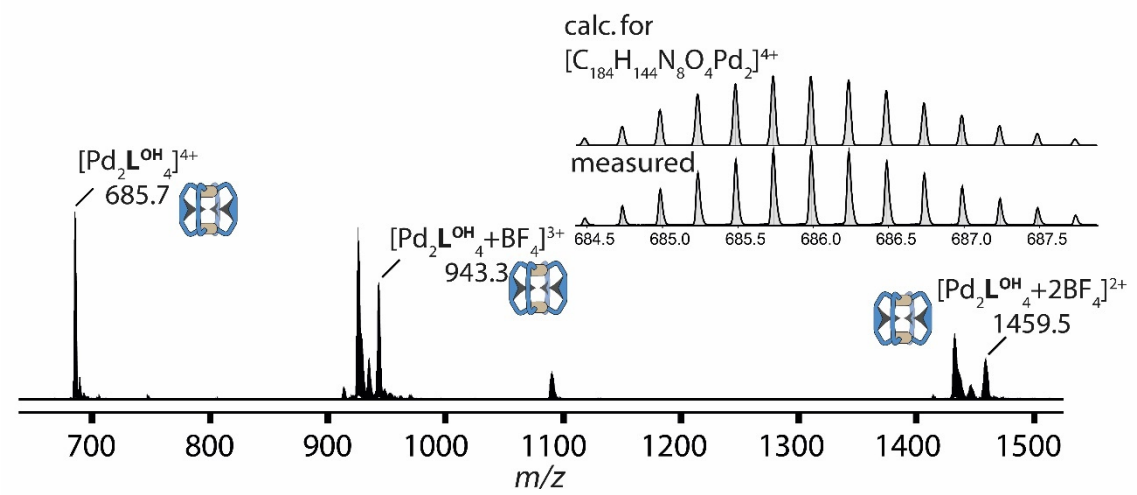

Figure 2.25 ESI mass spectrum of $[Pd_2L^{OH}_4](BF_4)_4$ (CD_3CN sample).

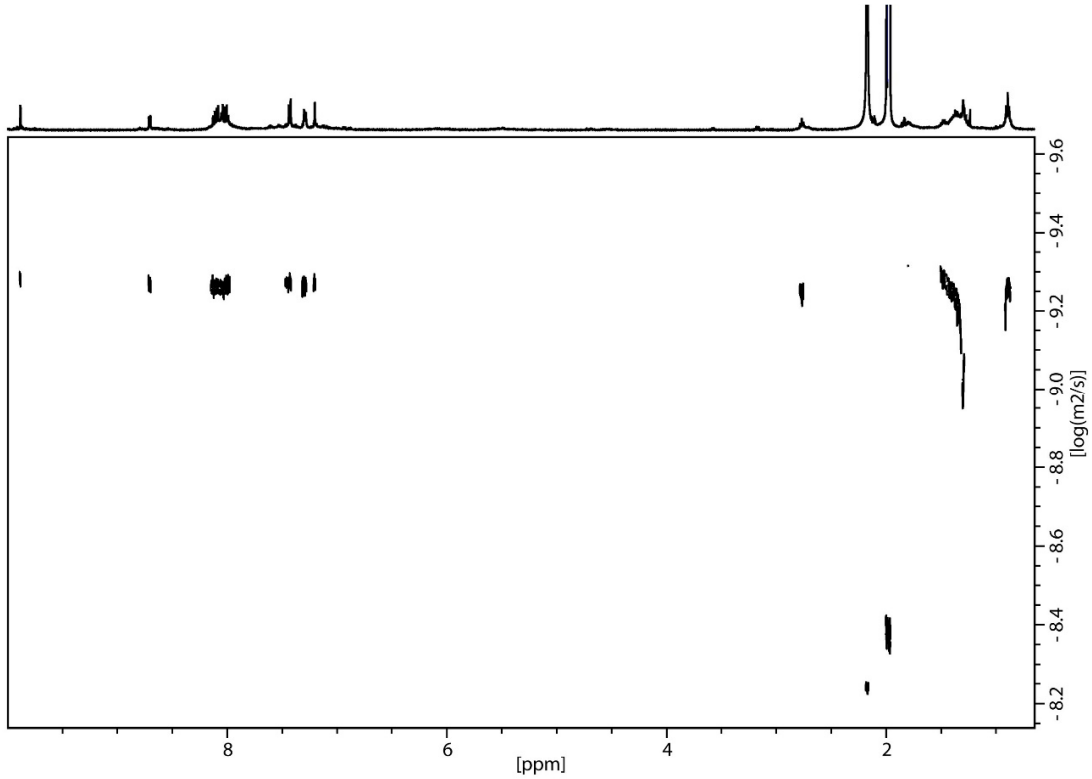

Figure 2.26 ^{1}H DOSY NMR (500 MHz, 298 K, CD_3CN) spectrum of homoleptic $[Pd_2L^{OH}_4](BF_4)_4$ cage.

To further confirm the existence of a single supramolecular coordination cage $[Pd_2\mathbf{L}^{\mathbf{OH}}_4](BF_4)_4$, a ^{1}H DOSY NMR spectrum was measured (figure 2.26)), showing a diffusion coefficient of D = 5.3844 • 10^{-10} $m^2 \cdot s^{-1}$. From this a hydrodynamic radius of r_H = 11.9 Å is calculated, being in the same range as $[Pd_2\mathbf{L}^{\mathbf{OMe}}_4](BF_4)_4$ in CD_3CN with r_H = 12.13 Å.

The ^{1}H NMR signals of $[Pd_2\mathbf{L}^{\mathbf{OH}}_4](BF_4)_4$ are assigned by ^{1}H-^{1}H COSY and ^{1}H-^{1}H NOESY NMR. Signals H_a, H_b, H_e and H_i are determined by shift, shape, and signal integration

and retroactive approved by 2D NMR techniques. The ^{1}H-^{1}H COSY NMR spectrum (figure 2.27) shows a cross-peak of H_c-H_b and H_e-H_f, with H_f instead over H_d chosen because of the more deshielding/downfield shift of the H_f neighbouring alkyne group. Exclusion leads to the assignment of proton H_d, while ^{1}H-^{1}H NOESY NMR enables the assignment of H_g and H_h due to the cross-peaks to proton H_a and H_i, respectively (labels red, figure 2.28).

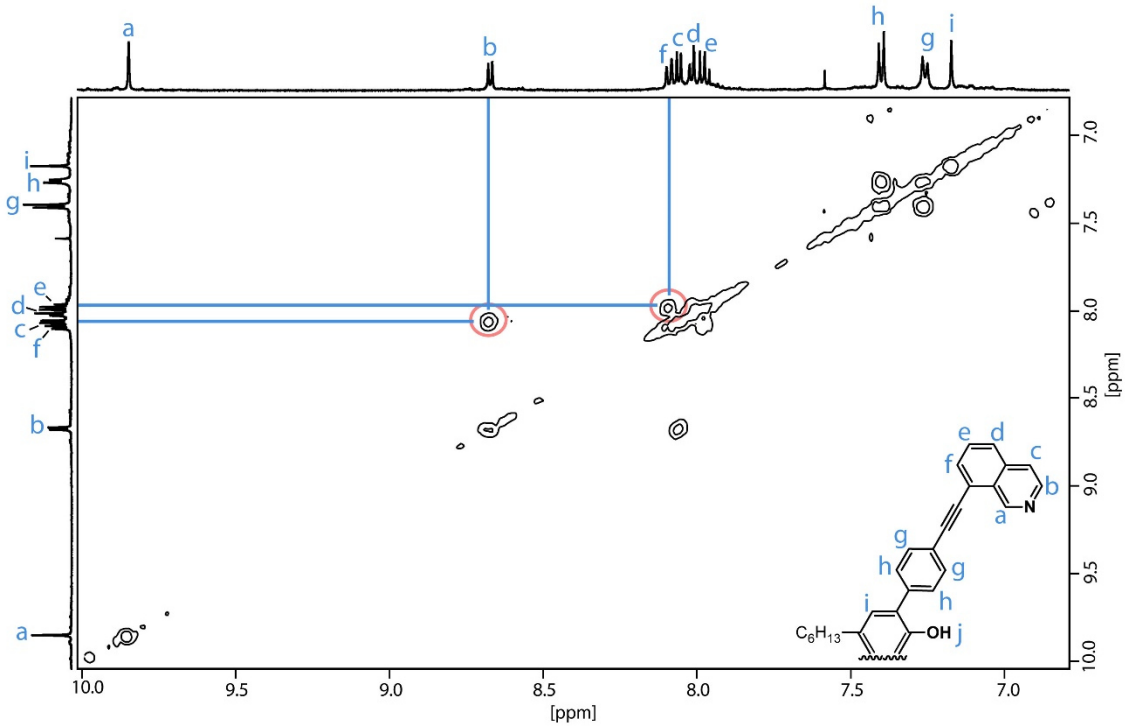

Figure 2.27 Partial ^{1}H-^{1}H COSY NMR (600 MHz, 298 K, CD_3CN) spectrum of homoleptic $[Pd_2L^{OH}_4](BF_4)_4$ cage. Cross-peaks between L^{OH} protons are marked light blue.

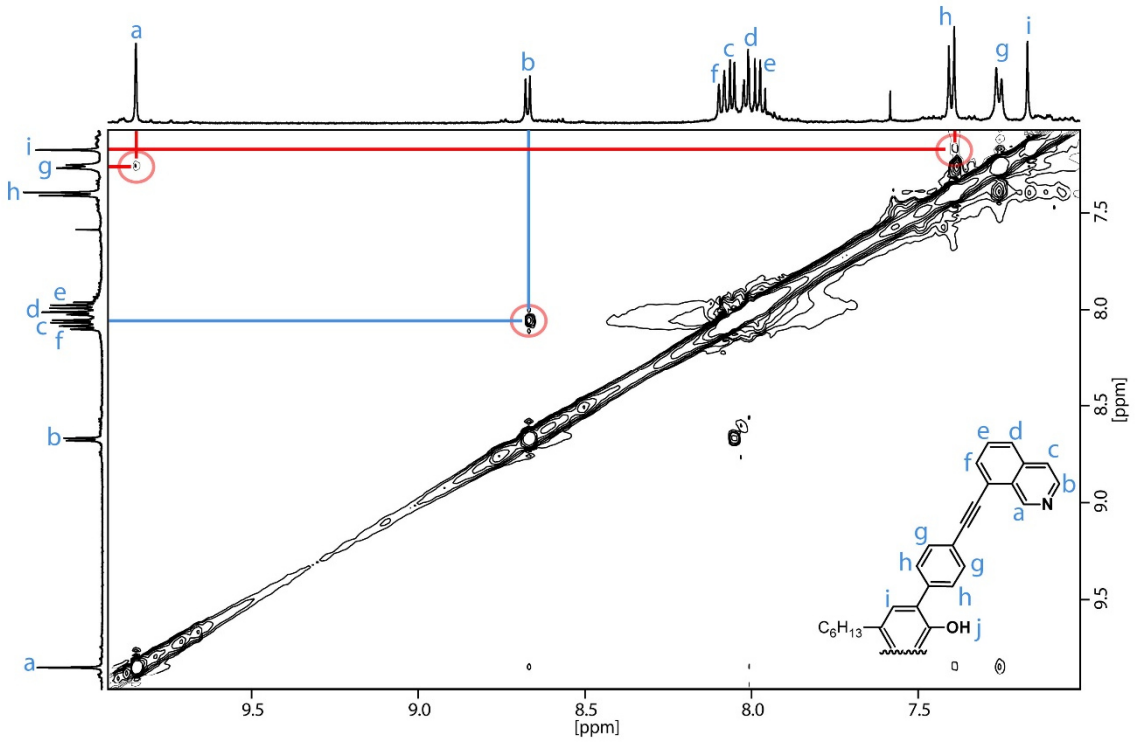

Figure 2.28 Partial ^{1}H-^{1}H NOESY NMR (600 MHz, 298 K, CD_3CN) spectrum of homoleptic $[Pd_2L^{OH}_4](BF_4)_4$ cage. Cross-peaks between L^{OH} protons are marked light blue; important H_a-H_g and H_i-H_h cross-peaks are marked with red.

2.4 A new $[Pd_2L^A_2L^B_2]$ System

After successful synthesis of $\mathbf{L^{OMe}}$ and $\mathbf{L^{OH}}$ (The following results are focused on $\mathbf{L^{OMe}}$ as it was better synthetically accessible) and the respective homoleptic cages $[Pd_2\mathbf{L^{OMe}_4}](BF_4)_4$ and $[Pd_2\mathbf{L^{OH}_4}](BF_4)_4$, the aim was to design heteroleptic cages based on shape complementarity. In a first attempt to synthesise a $[Pd_2\mathbf{L^{OMe}_2L^X_2}](BF_4)_4$ cage $\mathbf{L^{SC4}}$ ($\mathbf{L^{SC4}}$ = Ligand **S**hort **C**arbazole with **4** for the position of the nitrogen at the pyridine unit) was used. $\mathbf{L^{SC4}}$ was chosen in accordance to the shape complementarity approach and because of the already reported synthesis of the brominated precursor before coupling reaction (figure 2.29, Yield = 33 %) and a promising size and angle according to archetype systems by the Clever group.[116,127,128]

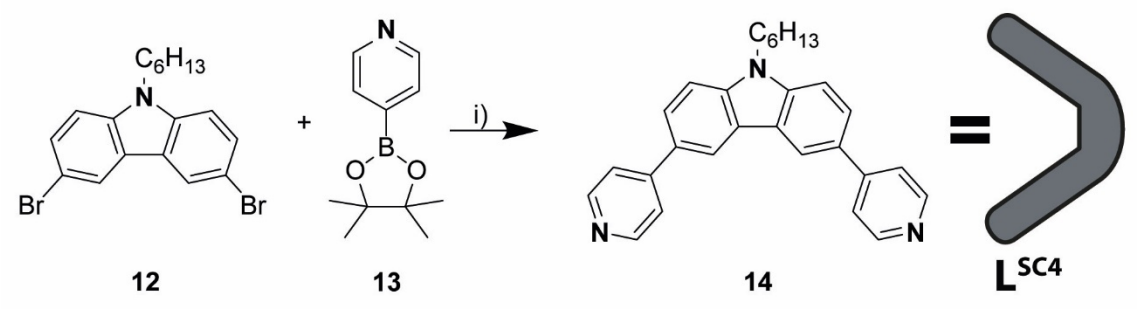

Figure 2.29 Suzuki-Miyaura cross-coupling to form L^{SC4}. i) $Pd(PPh_3)_4$, Na_2CO_3, DMF/water = 3:1, 100 °C, overnight.

For a 0.7 mM $[Pd_2\mathbf{L}^{OMe}{}_2\mathbf{L}^{SC4}{}_2](BF_4)_4$ solution, 7 mM stock solutions of $\mathbf{L}^{OMe}$ and $\mathbf{L}^{SC4}$ in CD_3CN or DMSO-d_6 were used, respectively. 120 µl of $\mathbf{L}^{OMe}$ and 120 µl of $\mathbf{L}^{SC4}$ were transferred inside an NMR tube. 240 µl solvent and 60 µl of a 15 mM $[Pd(CH_3CN)_4(BF_4)_2]$ were added and after mixing, the sealed NMR tubes were heated at 70 °C overnight. While the CD_3CN sample gave a cloudy suspension, the DMSO-d_6 remained clear and was further investigated by ^{1}H NMR spectroscopy (figure 2.30).

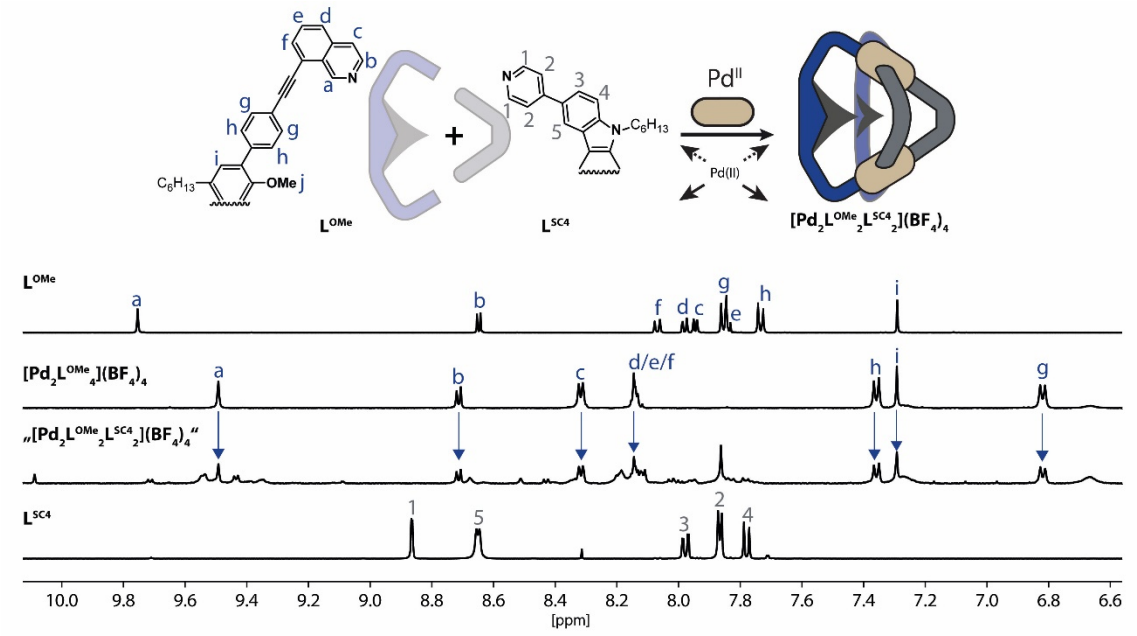

Figure 2.30 Schematic formation of the heteroleptic $[Pd_2\mathbf{L}^{OMe}{}_2\mathbf{L}^{SC}{}_2](BF_4)_4$ cage and comparison of the partial ^{1}H NMR spectra (500 MHz, 298 K, DMSO-d_6) of $[Pd_2\mathbf{L}^{OMe}{}_4](BF_4)_4$, $\mathbf{L}^{OMe}$, $\mathbf{L}^{SC4}$ and the resulting spectrum of the $[Pd_2\mathbf{L}^{OMe}{}_2\mathbf{L}^{SC}{}_2](BF_4)_4$ formation.

The spectrum shows clearly signals of the homoleptic $[Pd_2\mathbf{L}^{OMe}{}_4](BF_4)_4$ cage but in addition new and defined signals appeared. For further insights an ESI-MS spectrum was recorded (figure 2.31).

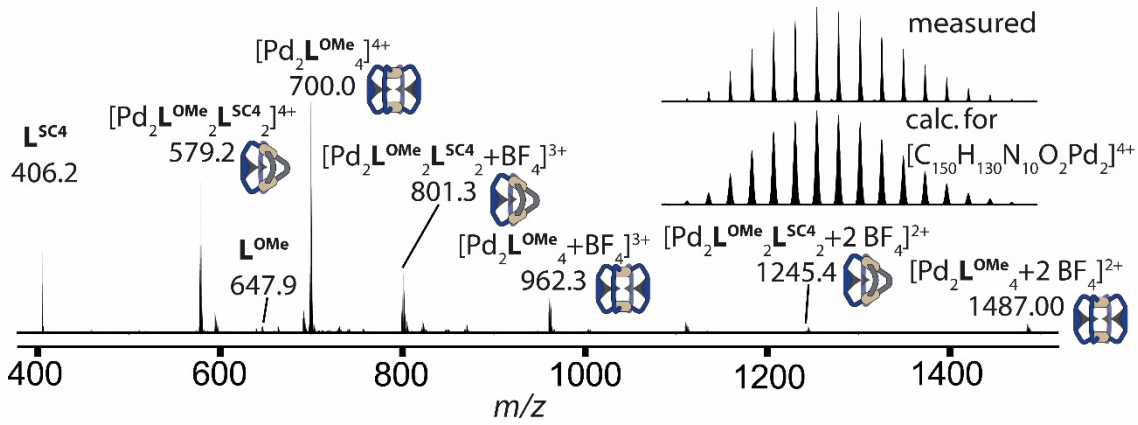

Figure 2.31 ESI mass spectrum of a $[Pd_2L^{OMe}{}_2L^{SC4}{}_2](BF_4)_4$ sample.

The mass spectrum shows a mixture of the already assigned and specific peaks of $[Pd_2L^{OMe}{}_4](BF_4)_4$ and additional ones of the desired $[Pd_2L^{OMe}{}_2L^{SC4}{}_2](BF_4)_4$ peaks with *m/z* = 579.2, 801.3, 1487.0 for $[Pd_2L^{OMe}{}_2L^{SC4}{}_2]^{4+}$, $[Pd_2L^{OMe}{}_2L^{SC4}{}_2+BF_4]^{3+}$ and $[Pd_2L^{OMe}{}_2L^{SC4}{}_2+2BF_4]^{2+}$ including fitting measured and calculated isotope patterns, respectively. Further experiments with extended heating time, additional equivalents of L^{SC4} or a different solvent unfortunately do not lead to the formation of one heteroleptic species.

Figure 2.32 shows a DFT-based geometric optimisation of the $[Pd_2L^{OMe}{}_2L^{SC4}{}_2]^{4+}$ structure with a Pd•••Pd distance of 14.6 Å and a distance between the most distal hydrogen atoms of 26.0 Å (BP86-D4/def2-SVP (def2-TZVP for Pd) as for all DFT calculations in this work). Calculation of trans-isomers were not performed during this work because of the previous results of the Clever group showing cis-isomers being the energetically favoured species.[116]

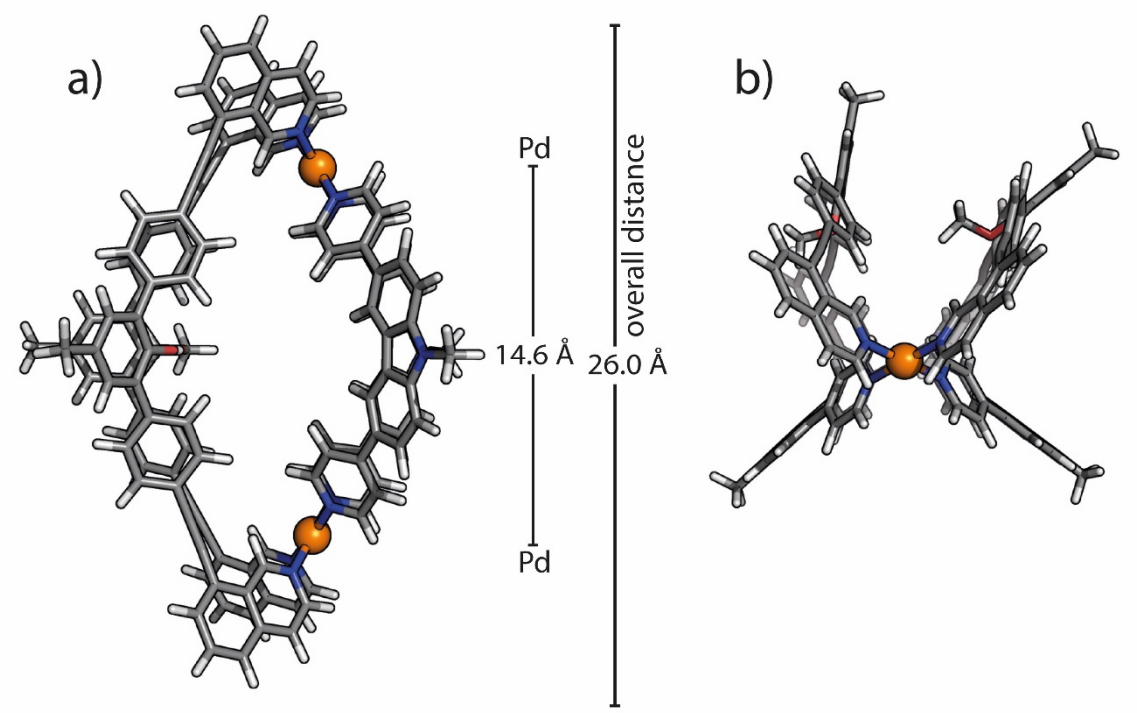

Figure 2.32 DFT (BP86-D4/def2-SVP (def2-TZVP for Pd)) geometric optimized structure of $[Pd_2L^{OMe}{}_2L^{SC4}{}_2]^{4+}$ in DMSO with a) top view and b) side view. Sidechains are scaled down to a methyl group to simplify the calculation. Colour scheme: C = dark grey, H = light grey, O = red, N = blue, Pd = orange.

While the combination of $\mathbf{L^{SC4}}$ with $\mathbf{L^{OMe}}$ did not lead to a clean formation of a single $[Pd_2\mathbf{L^{OMe}}_2\mathbf{L^{SC4}}_2](BF_4)_4$ cage, $\mathbf{L^{SB}}$ ($\mathbf{L^{SB}}$ = **L**igand **S**hort **B**enzene; 1,3-di(pyridin-4-yl)benzene) shows improved results. $\mathbf{L^{SB}}$ was already reported by *Fujita* and co-workers as a ligand and was used to form $[Pd_{12}\mathbf{L^{SB}}_{24}]$ supramolecular spheres.[129,130] The synthetic procedure is different to the reported. Starting from commercially available compounds, a Suzuki-Miyaura cross-coupling (figure 2.33) led to the ligand $\mathbf{L^{SB}}$ (77 % yield) which was further purified by GPC before used for cage formations.

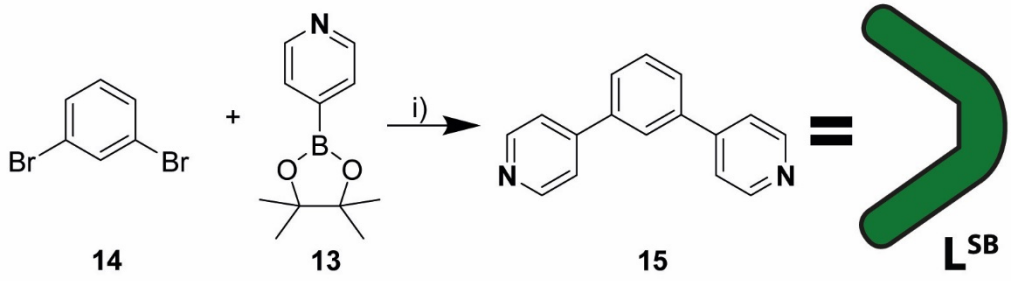

Figure 2.33 Synthesis of L^{SB}. i) $Pd(PPh_3)_4$, Na_2CO_3, 1,4-Dioxane, 100 °C, overnight.

The homoleptic $[Pd_{12}\mathbf{L^{SB}}_{24}](BF_4)_{24}$ coordination sphere in DMSO-d_6 was synthesised first (sphere synthesis, see experimental section). The ^{1}H NMR spectrum is in accordance with the reported spectrum from Fujita and co-workers (figure 2.34).

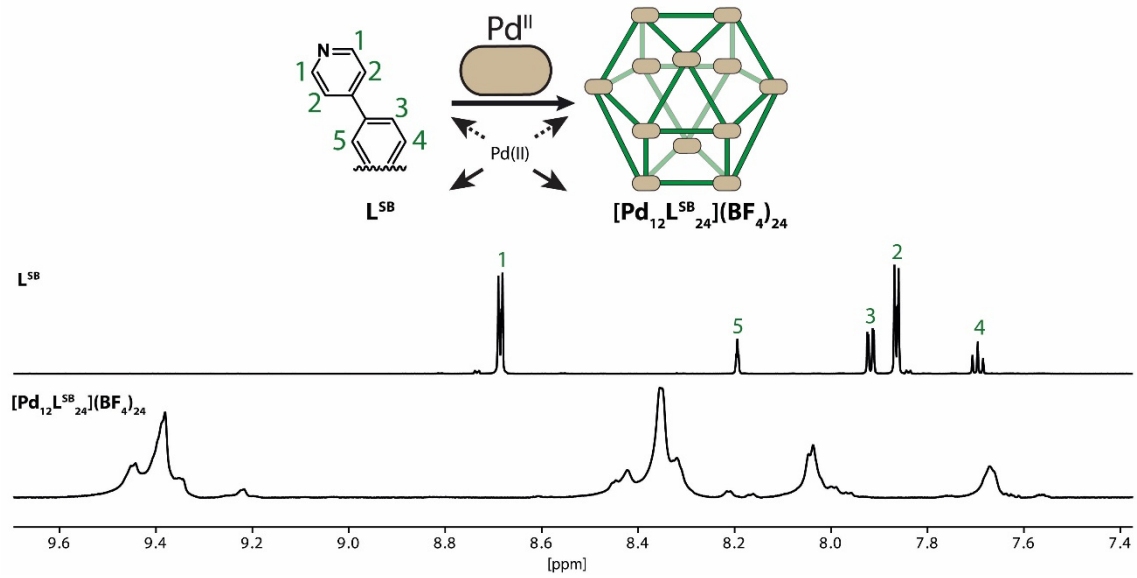

Figure 2.34 Schematic formation of the homoleptic $[Pd_{12}L^{SB}_{24}](BF_4)_{24}$ sphere and partial ^{1}H NMR spectra (500 MHz, 298 K, DMSO-d_6) of the free ligand L^{SB} with the associated sphere. Formation of the sphere leads to broadening of the ^{1}H signals.

Furthermore, an ^{1}H DOSY NMR spectrum (figure 2.35) experiment shows a single species with a diffusion coefficient of D = 4.743 · 10^{-10} $m^2 \cdot s^{-1}$ and a calculated hydrodynamic radius of r_H = 23.13 Å. These values are slightly bigger than reported and could be explained with different temperatures during the ^{1}H DOSY NMR measurements. Nevertheless, it indicates a single supramolecular species with double the size of the $[Pd_2\mathbf{L}^{\mathbf{OMe}}_{\mathbf{4}}](BF_4)_4$ and $[Pd_2\mathbf{L}^{\mathbf{OH}}_{\mathbf{4}}](BF_4)_4$ cages.

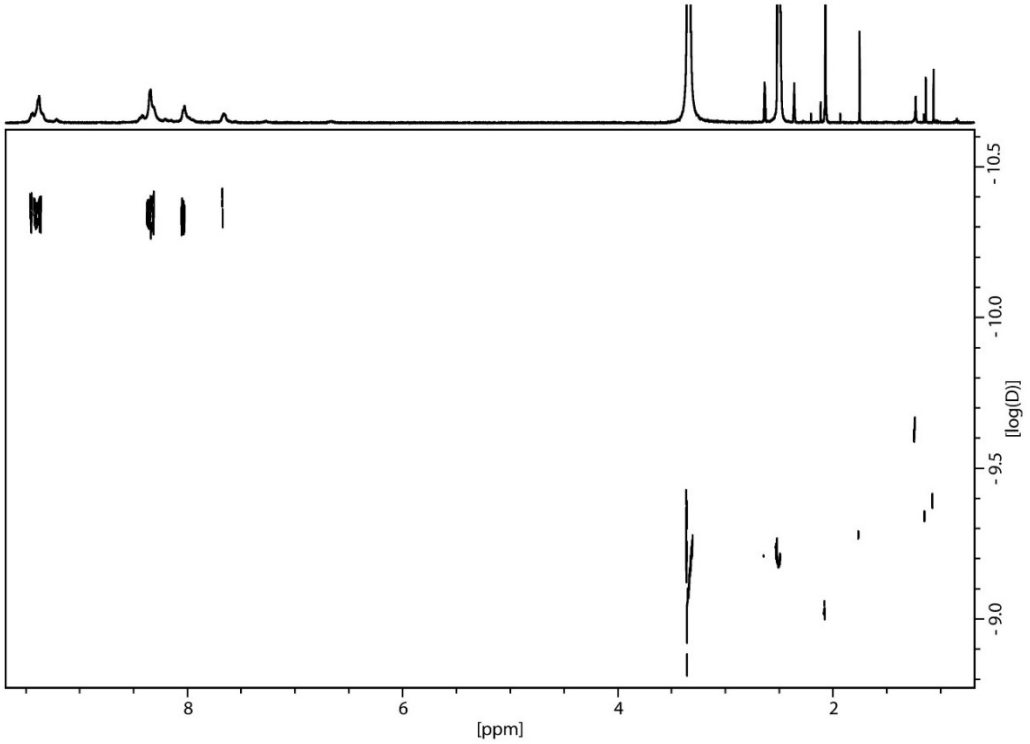

Figure 2.35 ^{1}H DOSY NMR (500 MHz, 298 K, DMSO-d_6) spectrum of the $[Pd_{12}\mathbf{L}^{\mathbf{SB}}_{\mathbf{24}}](BF_4)_{24}$ sphere.

After synthesis of $\mathbf{L}^{\mathbf{SB}}$ and the correspondent homoleptic $[Pd_{12}\mathbf{L}^{\mathbf{SB}}_{\mathbf{24}}](BF_4)_{24}$ sphere, the heteroleptic $[Pd_2\mathbf{L}^{\mathbf{OMe}}_{\mathbf{2}}\mathbf{L}^{\mathbf{SB}}_{\mathbf{2}}](BF_4)_4$ cage was formed. For a 0.7 mM cage solution, 120 µl of a 7 mM $\mathbf{L}^{\mathbf{OMe}}$ and 120 µl of a 7 mM $\mathbf{L}^{\mathbf{SB}}$ solution were mixed inside an NMR tube (with CD_3CN or DMSO-d_6 as solvent). 300 µl pure solvent and 60 µl of a 15 mM $[Pd(CH_3CN)_4(BF_4)_2]$ stock solution were added and the sealed NMR tube was carefully shaken and heated at 70 °C for 10 min to give a slightly yellow solution.

The ^{1}H NMR spectrum of the DMSO-d_6 sample shows a well-defined spectrum without the existence of $[Pd_2\mathbf{L}^{\mathbf{OMe}}_{\mathbf{4}}](BF_4)_4$ or $[Pd_{12}\mathbf{L}^{\mathbf{SB}}_{\mathbf{24}}](BF_4)_{24}$ (figure 2.36). Signal integration and signals form comparison lead to the conclusion that a symmetric heteroleptic coordination cage with a Pd/$\mathbf{L}^{\mathbf{OMe}}$/$\mathbf{L}^{\mathbf{SB}}$ ratio of 1:1:1 is formed. Several signals like the singlet corresponding to proton H_a shows a downfield shift which is in contrast with the other signals for the $[Pd_2\mathbf{L}^{\mathbf{OMe}}_{\mathbf{4}}](BF_4)_4$ and $[Pd_2\mathbf{L}^{\mathbf{OH}}_{\mathbf{4}}](BF_4)_4$ cages which shows an upfield shift instead. While as already discussed, the upfield shifts can indicate a twisting of the homoleptic cage structures which is proved by X-ray analysis. The downfield shift of the same ligands inside this new species could indicate a non-twisting of the $\mathbf{L}^{\mathbf{OMe}}$ ligand inside the supramolecular coordination cage. This is a possible additional indication of the formation of $[Pd_2\mathbf{L}^{\mathbf{OMe}}_{\mathbf{2}}\mathbf{L}^{\mathbf{SB}}_{\mathbf{2}}](BF_4)_4$, due to the driving force of building a $[Pd_2\mathbf{L}^{\mathbf{x}}_{\mathbf{2}}\mathbf{L}^{\mathbf{y}}_{\mathbf{2}}]$-cage over a homoleptic assembly by reducing strains for the ligands.

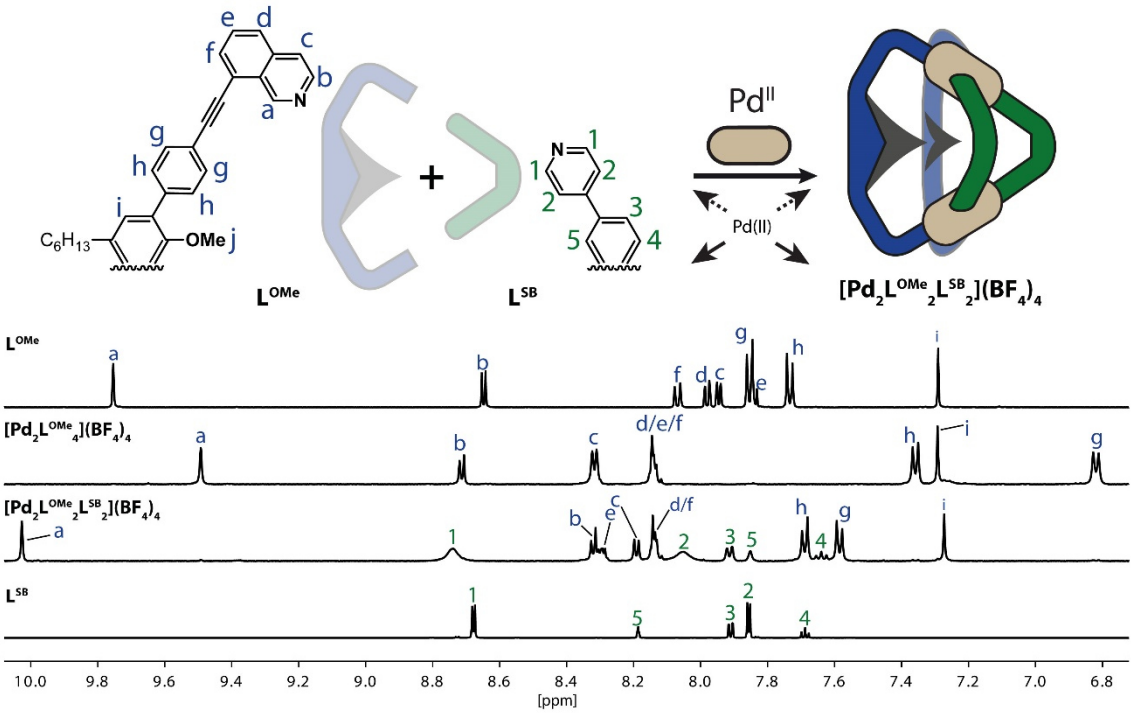

Figure 2.36 Schematic formation of the heteroleptic $[Pd_2L^{OMe}{}_2L^{SB}{}_2](BF_4)_4$ cage and comparison of the partial ^{1}H NMR spectra (500 MHz, 298 K, DMSO-d_6) of L^{OMe}, L^{SB}, $[Pd_2L^{OMe}{}_4](BF_4)_4$ and the respective heteroleptic cage.

The CD_3CN sample shows a mixture of $[Pd_2\mathbf{L^{OMe}{}_4}](BF_4)_4$ and a supposed heteroleptic $[Pd_2\mathbf{L^{OMe}{}_2L^{SB}{}_2}](BF_4)_4$ cage (figure 2.37). Longer heating, addition of more $\mathbf{L^{SB}}$ or fine tuning of the ligand-to-ligand ratio by ^{1}H NMR measurement did not lead to the formation of one clean heteroleptic coordination cage. It was therefore proceeded with analysis of the DMSO-d_6 sample, justified with the existence of one new heteroleptic coordination species. However, the choice of the used solvent has a great impact of the formation of the desired $[Pd_2\mathbf{L^X{}_2L^Y{}_2}]$-type cages in this work.

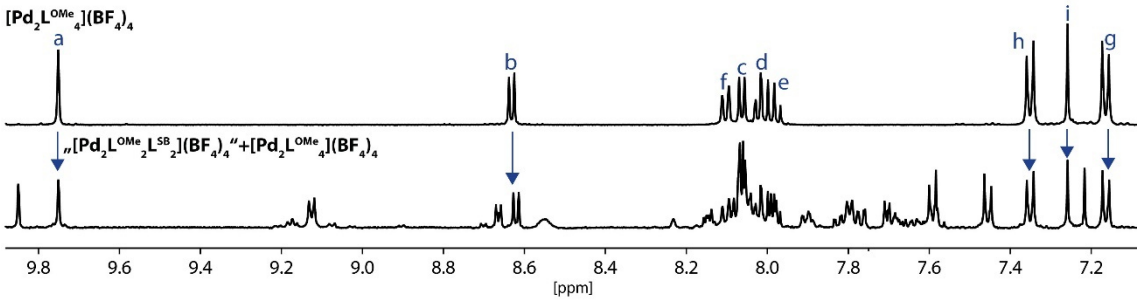

Figure 2.37 Partial ^{1}H NMR spectra (500 MHz, 298 K, CD_3CN) of $[Pd_2L^{OMe}{}_4](BF_4)_4$ and mixed Pd/L^{OMe}/L^{SB} in a 1:1:1 ratio to give a supposed $[Pd_2L^{OMe}{}_2L^{SB}{}_2](BF_4)_4$ cage with homoleptic $[Pd_2L^{OMe}{}_4](BF_4)_4$.

The ESI-MS spectrum for the DMSO-d_6 sample in figure 2.38 confirms the formation of the desired $[Pd_2\mathbf{L}^{\mathbf{OMe}}{}_2\mathbf{L}^{\mathbf{SB}}{}_2](BF_4)_4$ cage with *m/z* = 492.65 for $[Pd_2\mathbf{L}^{\mathbf{OMe}}{}_2\mathbf{L}^{\mathbf{SB}}{}_2]^{4+}$, *m/z* = 658.87 for $[Pd_2\mathbf{L}^{\mathbf{OMe}}{}_2\mathbf{L}^{\mathbf{SB}}{}_2{+}BF_4]^{3+}$ and *m/z* = 1072.31 for the $[Pd_2\mathbf{L}^{\mathbf{OMe}}{}_2\mathbf{L}^{\mathbf{SB}}{}_2{+}2BF_4]^{2+}$ species. The existence of homoleptic $[Pd_2\mathbf{L}^{\mathbf{OMe}}{}_4](BF_4)_4$ cage with *m/z* = 700.00 for $[Pd_2\mathbf{L}^{\mathbf{OMe}}{}_4]^{4+}$ and *m/z* = 962.34 for $[Pd_2\mathbf{L}^{\mathbf{OMe}}{}_4{+}BF_4]^{3+}$ can be explained with the dilution of the DMSO-d_6 sample in CD_3CN (1:10) before measuring at *Bruker ESI-timsTOF* mass spectrometer, resulting in the partial decomposition of the heteroleptic cage to a mixture with homoleptic species like for a pure CD_3CN sample reported before.

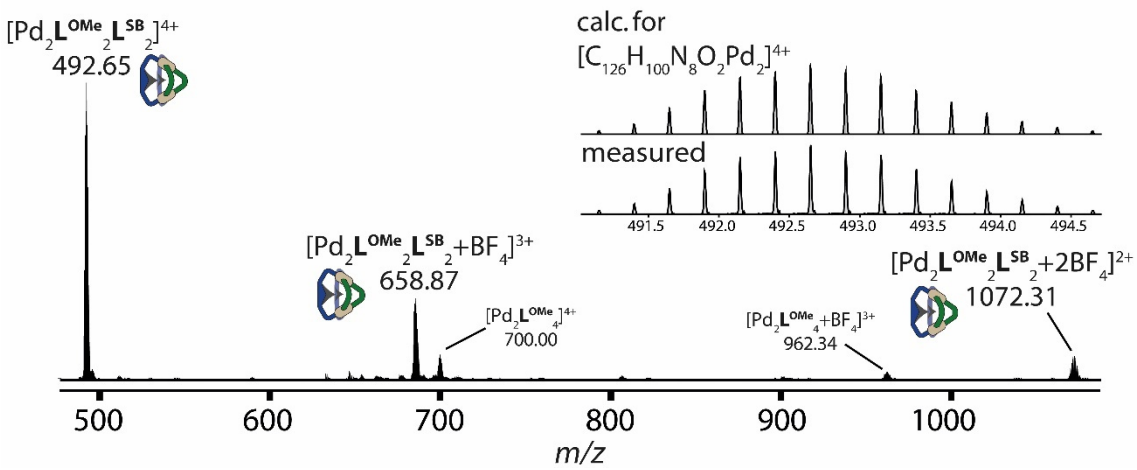

Figure 2.38 ESI mass spectrum of $[Pd_2\mathbf{L}^{\mathbf{OMe}}{}_2\mathbf{L}^{\mathbf{SB}}{}_2](BF_4)_4$.

Further confirmation for a single supramolecular coordination cage is given by ^{1}H DOSY NMR spectrum in figure 2.39 with a diffusion coefficient of D = 8.9421 • 10^{-11} $m^2 \cdot s^{-1}$ leading to a hydrodynamic radius of r_H = 12.37 Å. This is in the same range as $[Pd_2\mathbf{L}^{\mathbf{OMe}}{}_4](BF_4)_4$ with 12.13 Å and $[Pd_2\mathbf{L}^{\mathbf{OH}}{}_4](BF_4)_4$ with 12.13 Å.

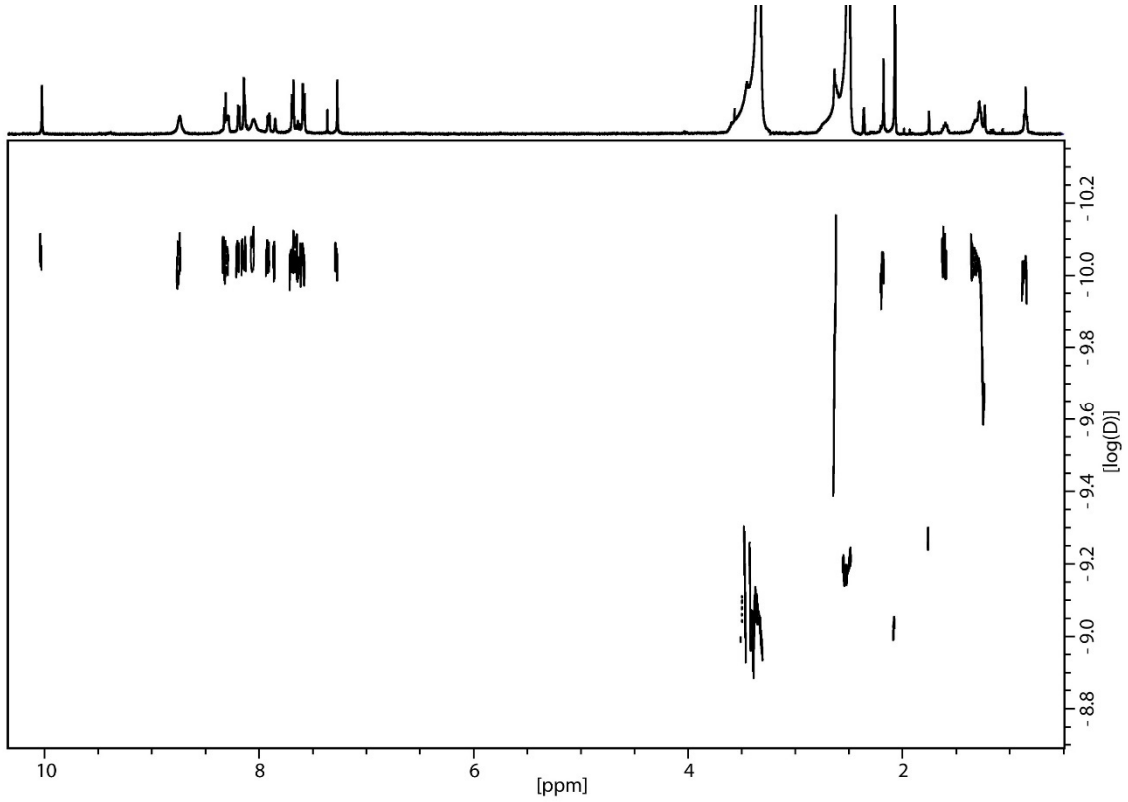

Figure 2.39 ^{1}H DOSY NMR (500 MHz, 298 K, DMSO-d_6) spectrum of the $[Pd_2L^{OMe}{}_2L^{SB}{}_2](BF_4)_4$ cage.

To address the ^{1}H signals of $[Pd_2\mathbf{L}^{\mathbf{OMe}}{}_2\mathbf{L}^{\mathbf{SB}}{}_2](BF_4)_4$ and of the following supramolecular species, 2D NMR experiments were measured at 25 °C or 70 °C: This can course sharpening and better separation of ^{1}H signals.

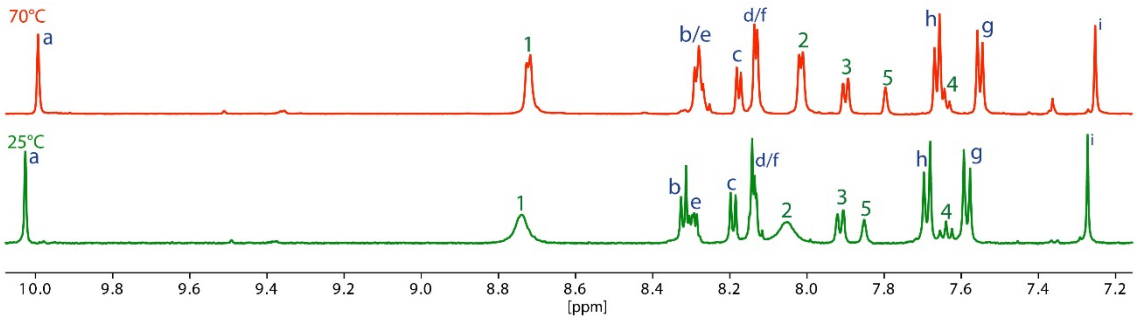

Figure 2.40 ^{1}H NMR spectra (500 MHz, DMSO-d_6) of $[Pd_2L^{OMe}{}_2L^{SB}{}_2](BF_4)_4$ at 298 K (25 °C, green) and 343 K (70 °C, red).

Proton resonances of H_a and H_i of ligand $\mathbf{L}^{\mathbf{OMe}}$ and H_1 and H_4 for ligand $\mathbf{L}^{\mathbf{SB}}$ could be assigned from the ^{1}H NMR by signal integration, shape and shift and were further confirmed by 2D NMR experiments. In the 2D spectra, ligand cross-peaks of $\mathbf{L}^{\mathbf{OMe}}$ proton signals are coloured dark blue and for $\mathbf{L}^{\mathbf{SB}}$ dark green, while red marks interligand cross-peaks between $\mathbf{L}^{\mathbf{OMe}}$ and $\mathbf{L}^{\mathbf{SB}}$ protons. ^{1}H-^{1}H COSY NMR in figure 2.41 shows a cross-

peak between H_1-H_2 and H_4-H_3 for signals dedicated to $\mathbf{L^{SB}}$. ^{1}H-^{1}H NOESY NMR spectrum in figure 2.42 confirm this, additionally with cross-peaks of H_2-H_1 and H_3-H_5.

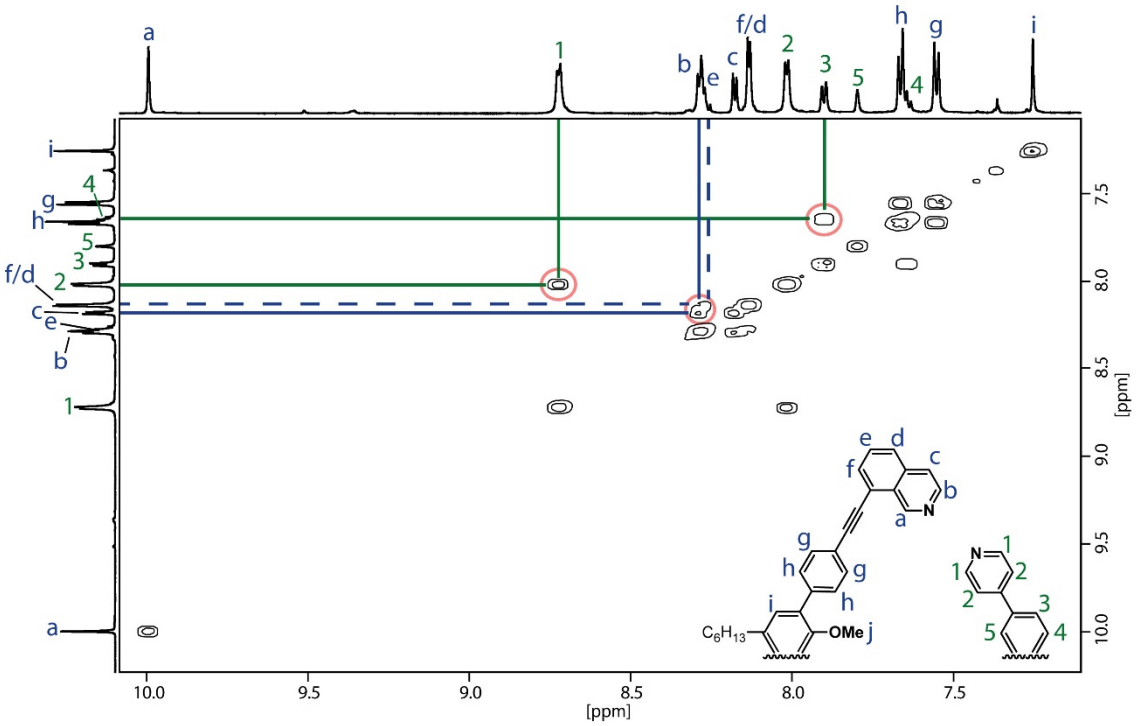

Figure 2.41 Partial ^{1}H-^{1}H COSY NMR (600 MHz, 343 K, DMSO-d_6) spectrum of the $[Pd_2L^{OMe}{}_2L^{SB}{}_2](BF_4)_4$ cage. Cross-peaks between L^{OMe} protons are marked dark blue; cross-peaks between L^{SB} protons are marked dark green.

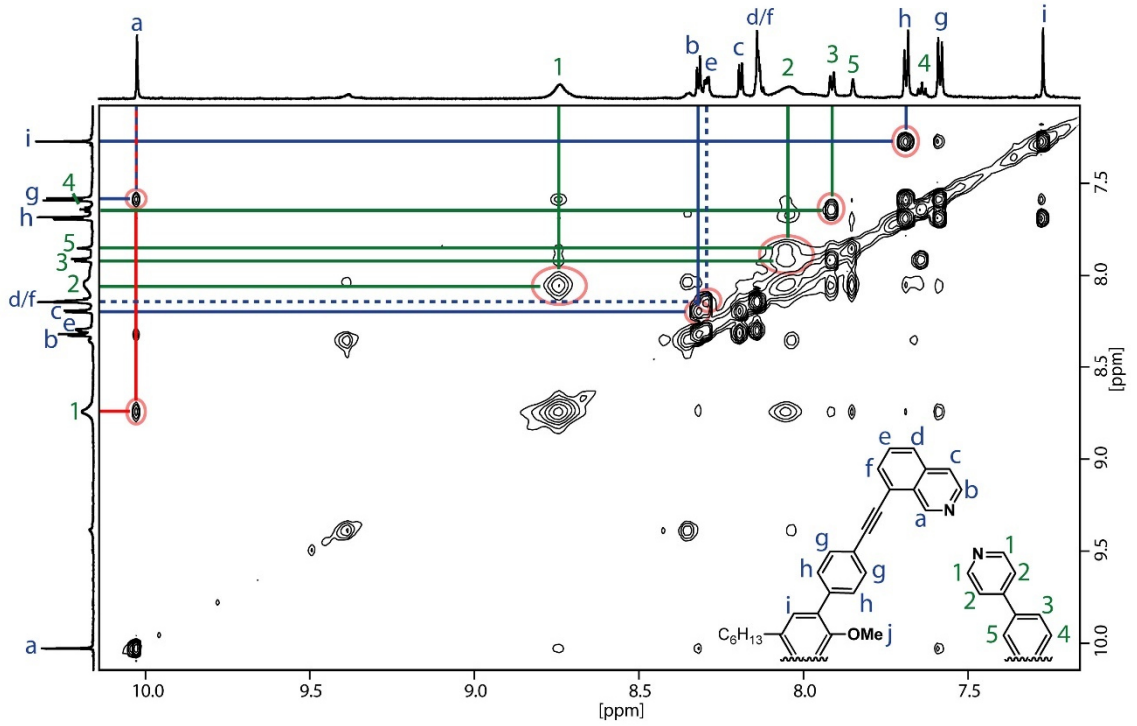

Figure 2.42 Partial ^{1}H-^{1}H NOESY NMR (700 MHz, 298 K, DMSO-d_6) spectrum of the $[Pd_2L^{OMe}{}_2L^{SB}{}_2](BF_4)_4$ cage. Cross-peaks between L^{OMe} protons are marked dark blue; cross-peaks between L^{SB} protons are marked dark green; interligand cross-peaks with red.

$\mathbf{L^{OMe}}$ proton assigment starts with cross-peaks of H_a-H_g and H_i-H_h. Shape and signal integration lead to a possible assigment of H_e and $H_{d/f}$, due to an additional ^{1}H-^{1}H NOESY NMR cross-peaks of these signals. Also, a weak ^{1}H-^{1}H COSY NMR cross-peak is visible. The remaining protons H_b and H_c are confirmed by ^{1}H-^{1}H COSY/NOESY NMR cross-peaks. Interligand cross-peak of H_a with H_1 completes the proton assignment.

As the crystallization of $[Pd_2\mathbf{L^{OMe}_2L^{SB}_2}](BF_4)_4$ was not successful, a DFT-based geometric optimisation was performed, giving an three-dimensional visual impression of the structure in figure 2.43.

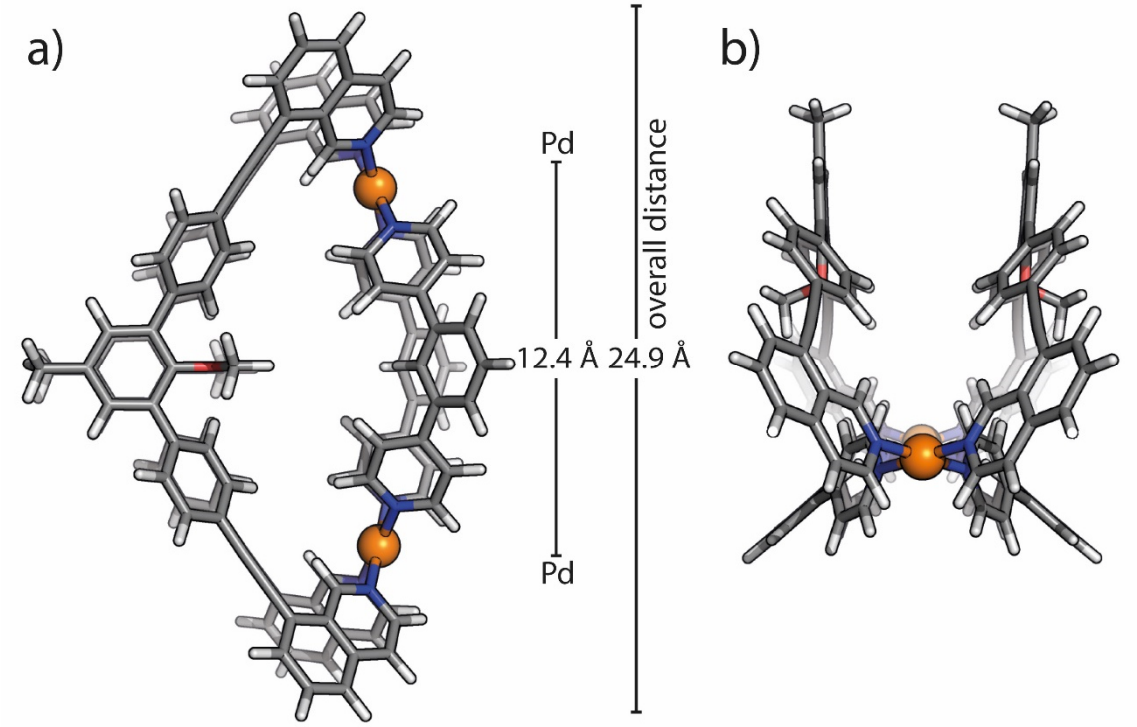

Figure 2.43 DFT (BP86-D4/def2-SVP (def2-TZVP for Pd)) calculated structure of $[Pd_2L^{OMe}_2L^{SB}_2]^{4+}$ in DMSO with a) top view and b) side view. Sidechains are scaled down to a methyl group to simplify the calculation. Colour scheme: C = dark grey, H = light grey, O = red, N = blue, Pd = orange.

The Pd•••Pd distance is calculated with 12.4 Å and the distance of the most distal hydrogen atoms is given with 24.9 Å. This is comparable in size with the hydrodynamic radius calculated from the ^{1}H DOSY NMR experiment with of r_H = 12.37 Å. Both ligands undergo a distortion of a possible planar conformation, leading to a twist along the ligand axis inside the cage.

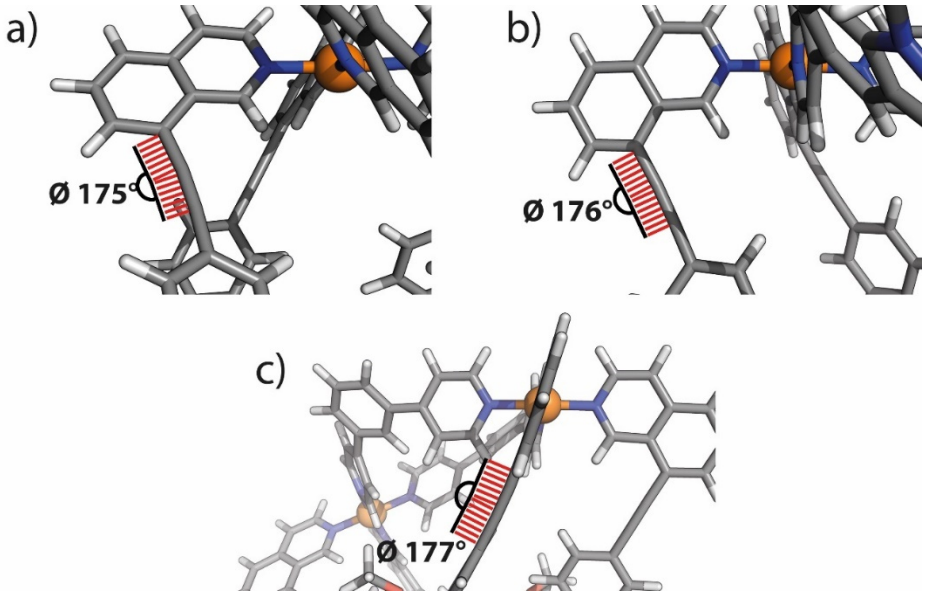

Figure 2.44 DFT (BP86-D4/def2-SVP (def2-TZVP for Pd)) optimized geometric structures for a) $[Pd_2L^{OMe}{}_4]^{4+}$ b) $[Pd_2L^{OMe}{}_2L^{SC4}{}_2]^{4+}$and c) $[Pd_2L^{OMe}{}_2L^{SB}{}_2]^{4+}$ zoomed on an alkyne groups to show the respective bending apart from the ideal 180° angle. Colour scheme: C = dark grey, H = light grey, O = red, N = blue, Pd = orange.

Beside the influence of the solvent, which will be addressed in further studies, the given strain of the homoleptic assembly is reduced by the formation of a heteroleptic $[Pd_2\mathbf{L}^{OMe}{}_2\mathbf{L}^{SB}{}_2]$-cage instead of a $[Pd_2\mathbf{L}^{OMe}{}_2\mathbf{L}^{SC4}{}_2]$-cage. Measured alkyne angles for the DFT models of $[Pd_2\mathbf{L}^{OMe}{}_4]^{4+}$ with Ø175° (figure 3.16, experimental section), $[Pd_2\mathbf{L}^{OMe}{}_2\mathbf{L}^{SB}{}_2]^{4+}$ with Ø176° and Ø177° for $[Pd_2\mathbf{L}^{OMe}{}_2\mathbf{L}^{SC4}{}_2]^{4+}$ (figure 2.32) show for all species a difference to the ideal 180° of linear alkynes. With a less strained angle for $[Pd_2\mathbf{L}^{OMe}{}_2\mathbf{L}^{SB}{}_2]^{4+}$ it is more favourable to form the heteroleptic assembly than the homoleptic $[Pd_2\mathbf{L}^{OMe}{}_4]$-cage. Figure 2.45 compares the bend angle of θ = -120° for $\mathbf{L}^{OMe}$ with the bending angles of $\mathbf{L}^{SC4}$ with θ = 90° and $\mathbf{L}^{SB}$ with θ = 120°. Besides the bend angle, also the shorter N•••N distance of $\mathbf{L}^{SB}$ could influence the better $[Pd_2\mathbf{L}^{OMe}{}_2\mathbf{L}^{SB}{}_2]$-cage formation. PM6 calculation of $\mathbf{L}^{SB}$ and $\mathbf{L}^{SC4}$ leads to N•••N distances of 9.9 Å and 12.1 Å, respectively. The bend angle of θ = 90° combined with the N•••N distances and the rigid carbazole backbone could give the $[Pd_2\mathbf{L}^{OMe}{}_2\mathbf{L}^{SC4}{}_2]$-cage further strain compared to the strain of the $[Pd_2\mathbf{L}^{OMe}{}_4]$-cage, leading to an equilibrium of energetically close structures where none is favourable over the other. Combination of $\mathbf{L}^{OMe}$ and $\mathbf{L}^{SB}$ leads to a system perfect in shape complementarity due to bend angles, N•••N distances and the ability of both ligands to distort along the ligand axis as seen in the DFT based geometric optimisation of $[Pd_2\mathbf{L}^{OMe}{}_2\mathbf{L}^{SB}{}_2]^{4+}$ to overcome unfavourable conformeric conditions.

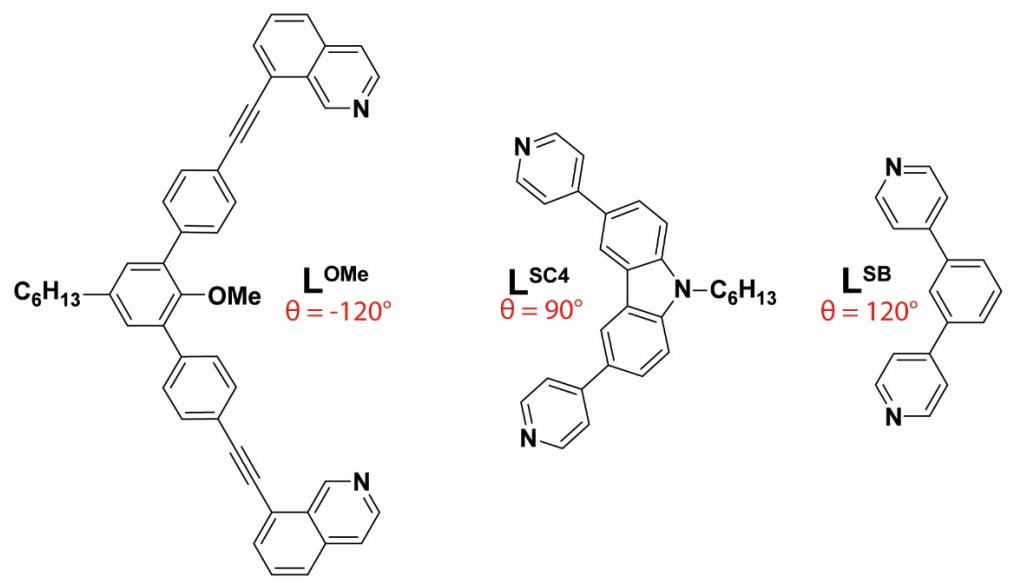

Figure 2.45 Structures of the used ligands with the respective bend angles.

2.5 Implementation of different endohedral Modifications

After successful introduction of the $[Pd_2\mathbf{L}^{\mathbf{OMe}}{}_2\mathbf{L}^{\mathbf{SB}}{}_2](BF_4)_4$ system, the system is further modified in order to show the variability of this basic shape. While the synthesis of $\mathbf{L}^{\mathbf{OMe}}$ takes more effort with 7 synthesis steps, $\mathbf{L}^{\mathbf{SB}}$ is a one-step synthesis starting from the commercially available starting materials.

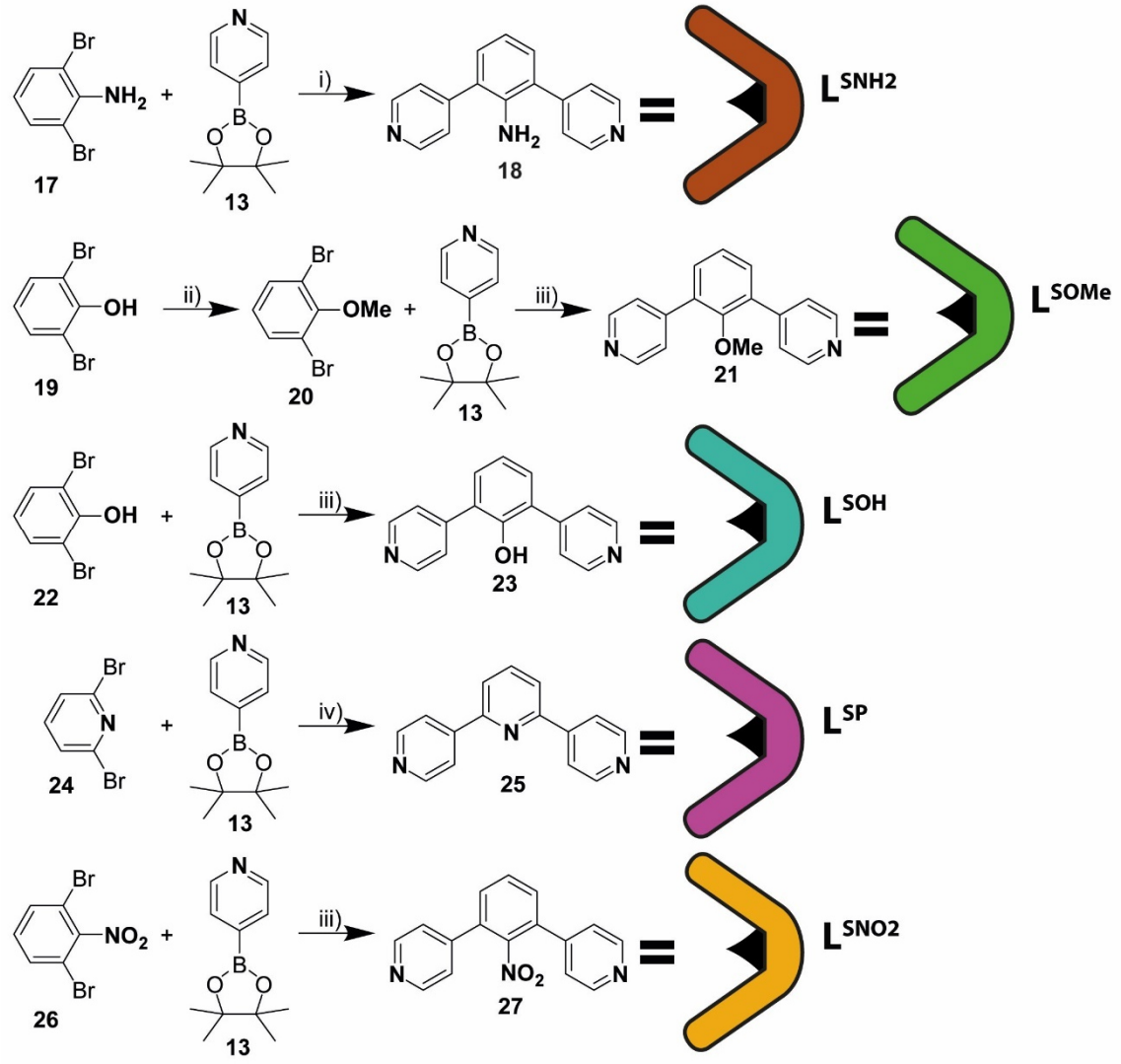

Figure 2.46 Synthesis and representing coloured figures of L^{SNH2} (brown), L^{SOMe} (green) L^{SOH} (turquoise), L^{SP} (violet) and L^{SNO2} (yellow). Synthesis steps: i) $Pd(PPh_3)_4$, Na_2CO_3, 1,4-dioxane/water = 4:1, 100 °C, overnight; ii) 6 eq iodomethane, K_2CO_3, reflux, 5 h; iii) $Pd(PPh_3)_4$, K_3PO_4, DMF/water = 3:1, 100 °C, overnight; iv) $Pd(PPh_3)_4$, Na_2CO_3, 1,4-dioxane, 100 °C, overnight.

Due to less synthetic effort, this ligand is modified instead of $\mathbf{L}^{\mathbf{OMe}}$ to show the robustness and limits of the heteroleptic system in forming different cages based on the same topologic motif. The benzene backbone is substituted by aniline, methoxybenzene,

phenol, additional pyridyl, and nitrobenzene to give the in figure 2.46 mentioned ligands, synthesised under slightly different conditions such as solvent or salt for the Suzuki-Miyaura cross-coupling.

L^{SNH2} (**L^{SNH2}** = **L**igand **S**hort with **-NH_2** group, 2,6-di(pyridin-4-yl)aniline) was synthesised by coupling of 2,6-dibromoaniline with 4-(4,4,5,5-tetramethyl-1,3,2-dioxaborolan-2-yl)pyridine with a yield of 90 %. Starting with 2,6-dibromophenol, the hydroxy group was reacted with iodomethane to give 1,3-dibromo-2-methoxybenzene (37 % yield), which was finally coupled with 4-(4,4,5,5-tetramethyl-1,3,2-dioxaborolan-2-yl) pyridine to give **L^{OMe}** (**L^{SOMe}** = **L**igand **S**hort with **Methoxy** group; 4,4'-(2-methoxy-1,3-phenylene) dipyridine) with a yield of 53 %. 2,6-dibromophenol, 2,6-dibromopyridine and 1,3-dibromo-2-nitrobenzene were coupled with the already mentioned boronic pinacol ester to give **L^{SOH}**, **L^{SP}**, **L^{SNO2}** with 36 %, 63 %, 56 % yield, respectively (**L^{SOH}** = **L**igand **S**hort with **-OH** group (2,6-di(pyridin-4-yl) phenol); **L^{SP}** **L**igand **S**hort with additional **P**yridine group (4,2':6',4''-terpyridine); **L^{SNO2}** = **L**igand **S**hort with **-NO_2** group (4,4'-(2-nitro-1,3-phenylene)dipyridine). Before further use, all materials were purified by GPC.

L^{SNH2} was already reported and used to form heteroleptic platinum metallacycles,[131] **L^{SOH}** was prepared as an intermediate with a final structure leading to a [Pd_{12}**L_{24}**]-sphere,[132] **L^{SP}** was used to form heteroleptic platinum rhomboids, triangles, triangular bipyramid[108] and a [Pd_9**L_{18}**]-complex.[133] In this work, all ligands are used to form homoleptic species in DMSO-d_6 like it is already done for **L^{SB}**, which gives the described [Pd_{12}**L^{SB}_{24}**]$(BF4)_{24}$ sphere. Since no [Pd_{12}**L_{24}**] spheres for **L^{SNH2}**, **L^{SOMe}**, **L^{SOH}** and **L^{SNO2}** were reported, comparison with before measured ^{1}H NMR spectra are not possible. Nevertheless, ^{1}H DOSY NMR measurements lead to the formation of a single species for **L^{SNH2}** or **L^{SOH}** when reacted with 0.5 eq Pd(II), with a $D = 4.2330 \cdot 10^{-11}$ $m^2 \cdot s^{-1}$ and $D = 4.6387 \cdot 10^{-11}$ $m^2 \cdot s^{-1}$ leading to hydrodynamic radii of r_H = 25.91 Å and r_H = 23.65 Å. As already introduced in the precious section, the hydrodynamic radius measured for [Pd_{12}**L^{SB}_{24}**]$(BF_4)_{24}$ is r_H = 23.13 Å. By similarity, this indicates the formation of [Pd_{12}**L^{SNH2}_{24}**]$(BF4)_{24}$ and [Pd_{12}**L^{SOH}_{24}**]$(BF_4)_{24}$, respectively. **L^{SOMe}** plus 0.5 eq Pd(II) shows the formation of two species by ^{1}H DOSY NMR experiment with $D = 4.2330 \cdot 10^{-11}$ $m^2 \cdot s^{-1}$ and $D = 4.6387 \cdot 10^{-11}$ $m^2 \cdot s^{-1}$. For the first mentioned diffusion coefficient r_H = 24.85 Å is calculated, an indication for a possible [Pd_{12}**L^{SOMe}_{24}**]$(BF_4)_{24}$ sphere. The second included species with a r_H = 7.41 Å and $D = 1.4795 \cdot 10^{-10}$ $m^2 \cdot s^{-1}$ is even smaller than the reported [Pd_2**L_4**] or [Pd_2**$L^{OMe}_2L^Y_2$**] cages. A possible ring-like structure or a fragment of the bigger species could be an explanation. **L^{SP}** with 0.5 eq Pd(II) forms a species with $D = 5.3795 \cdot 10^{-10}$ $m^2 \cdot s^{-1}$ leading to a r_H = of 20.39 Å, smaller than the suggested [Pd_{12}**L_{24}**]-spheres. The bend angle of **L^{SP}** is smaller due to the pyridyl backbone instead

of a substituted benzene ring as a basic structure element. This suggests literature reported smaller complexes like $[Pd_8\mathbf{L}^{\mathbf{SP}}_{\mathbf{16}}]$- or $[Pd_9\mathbf{L}^{\mathbf{SP}}_{\mathbf{18}}]$-type in one mixture. Interestingly, in this work only one species could be indicated by ^{1}H DOSY NMR. This difference of the homoleptic structure needs to be reminded when it comes to the discussion of the $[Pd_2\mathbf{L}^{\mathbf{OMe}}_{\mathbf{2}}\mathbf{L}^{\mathbf{SP}}_{\mathbf{2}}](BF_4)$ cage. To this additionally, $\mathbf{L}^{\mathbf{SNO2}}$ + 0.5 eq Pd(II) forms a mixture of two species with $D = 8.6560 \cdot 10^{-11}$ m^2·s^{-1} and $D = 1.2513 \cdot 10^{-11}$ m^2·s^{-1}, giving a mixture of r_H = 12.67 Å and r_H = 8.77 Å, respectively.

The formation of the heteroleptic cages is similar to $[Pd_2\mathbf{L}^{\mathbf{OMe}}_{\mathbf{2}}\mathbf{L}^{\mathbf{SB}}_{\mathbf{2}}](BF_4)_4$ and is taking place in DMSO-d_6. 120 µl of a 7 mM stock solution of $\mathbf{L}^{\mathbf{OMe}}$ was mixed with 120 µl of a 7 mM stock solution of $\mathbf{L}^{\mathbf{SNH2}}$, $\mathbf{L}^{\mathbf{OMe}}$, $\mathbf{L}^{\mathbf{SOH}}$, $\mathbf{L}^{\mathbf{SP}}$, $\mathbf{L}^{\mathbf{SNO2}}$, respectively. After addition of 60 µl of a 15 mM $[Pd(CH_3CN)_4(BF_4)_2]$ stock solution, 300 µl pure solvent was added and the combined solutions were heated in an NMR tube at 70 °C for 10 min to give slightly yellow 0.7 mM solutions. Formation of $[Pd_2\mathbf{L}^{\mathbf{OMe}}_{\mathbf{2}}\mathbf{L}^{\mathbf{SNH2}}_{\mathbf{2}}](BF_4)_4$ and $[Pd_2\mathbf{L}^{\mathbf{OMe}}_{\mathbf{2}}\mathbf{L}^{\mathbf{SP}}_{\mathbf{2}}](BF_4)_4$ were additionally carried out in CD_3CN and analysed by ^{1}H NMR, resulting in a mixture of different species including $[Pd_2\mathbf{L}^{\mathbf{OMe}}_{\mathbf{4}}](BF_4)_4$ as seen for $[Pd_2\mathbf{L}^{\mathbf{OMe}}_{\mathbf{2}}\mathbf{L}^{\mathbf{SB}}_{\mathbf{2}}](BF_4)_4$ in CD_3CN. Again, longer heating, adding more $\mathbf{L}^{\mathbf{SB}}$ or fine tuning of the ligand-to-ligand ratio by ^{1}H NMR did not lead to clean single species in CD_3CN. This led to the focus on DMSO-d_6 as the only used solvent.

A well-defined ^{1}H NMR spectrum of $[Pd_2\mathbf{L}^{\mathbf{OMe}}_{\mathbf{2}}\mathbf{L}^{\mathbf{SNH2}}_{\mathbf{2}}](BF_4)_4$ in DMSO-d_6 is shown in figure 2.47 without the existence on any homoleptic species. A comparison of the signal integration of the free ligands with the new species indicate a symmetric heteroleptic coordination molecule with a Pd to ligand ratio of 1:2, including a 1:1 ratio of $\mathbf{L}^{\mathbf{OMe}}$ to $\mathbf{L}^{\mathbf{SNH2}}$.

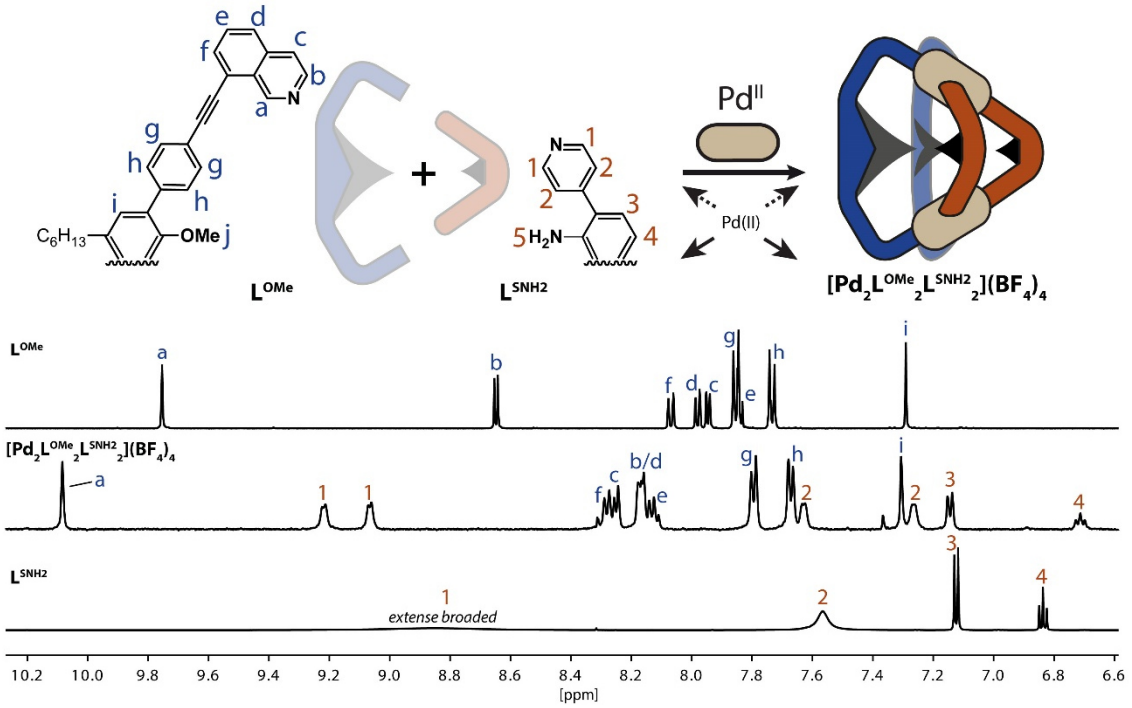

Figure 2.47 Schematic formation of the heteroleptic $[Pd_2L^{OMe}{}_2L^{SNH2}{}_2](BF_4)_4$ cage and comparison of the partial ^1H NMR spectra (500 MHz, 298 K, DMSO-d_6) of the free ligands L^{OMe} and L^{SNH2} with the respective heteroleptic cage.

Again, several signals like H_a show a downfield shift instead of a upfield shift like seen in $[Pd_2L^{OMe}{}_4](BF_4)_4$ and $[Pd_2L^{OH}{}_4](BF_4)_4$. This indicates a less strained structure with larger distances between the L^{OMe} π systems in contrast to the helical homoleptic cage.

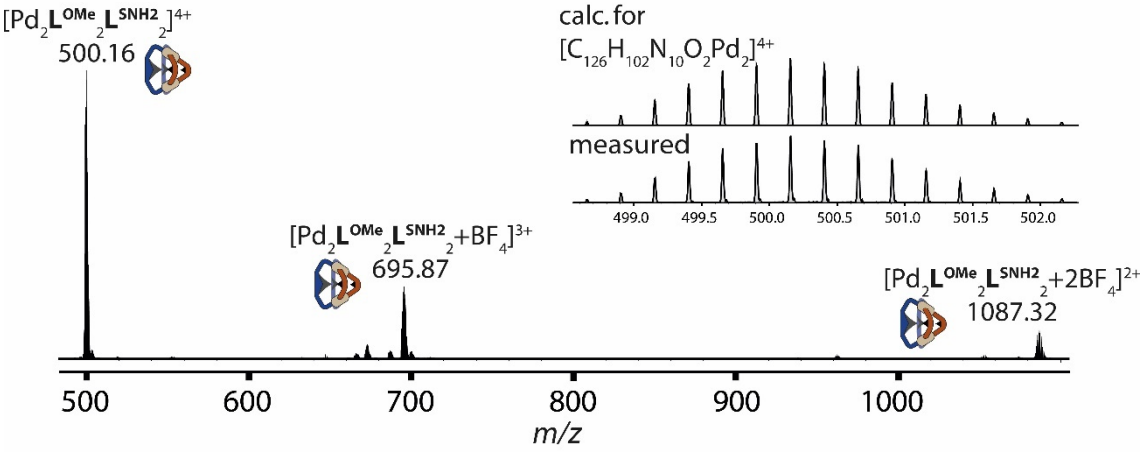

Figure 2.48 ESI mass spectrum of a $[Pd_2L^{OMe}{}_2L^{SNH2}{}_2](BF_4)_4$ sample.

The existence of $[Pd_2L^{OMe}{}_2L^{SNH2}{}_2](BF_4)_4$ is additionally proven by ESI-MS. The spectra in figure 2.48 displays $[Pd_2L^{OMe}{}_2L^{SNH2}{}_2]^{4+}$ with *m/z* = 500.16, $[Pd_2L^{OMe}{}_2L^{SNH2}{}_2+BF_4]^{3+}$ with *m/z* = 695.87 and $[Pd_2L^{OMe}{}_2L^{SNH2}{}_2+2BF_4]^{2+}$ with *m/z* = 1087.32. No additional species can be identified, showing the $[Pd_2L^{OMe}{}_2L^{SNH2}{}_2](BF_4)_4$ cage is longer stable against dilution in

acetonitrile then $[Pd_2\mathbf{L}^{\mathbf{OMe}}{}_2\mathbf{L}^{\mathbf{SB}}{}_2](BF_4)_4$ in a comparable experiment time at *Bruker ESI-timsTOF*.

^{1}H DOSY NMR spectrum (figure 2.49) further confirm $[Pd_2\mathbf{L}^{\mathbf{OMe}}{}_2\mathbf{L}^{\mathbf{SNH2}}{}_2](BF_4)_4$ with a diffusion coefficient of D = 8.9785 $\cdot 10^{-11}$ $m^2 \cdot s^{-1}$, leading by a calculation with the Stokes-Einstein equation to a hydrodynamic radius of r_H = 12.21 Å. This is in the same magnitude like $[Pd_2\mathbf{L}^{\mathbf{OMe}}{}_2\mathbf{L}^{\mathbf{SB}}{}_2](BF_4)_4$ with r_H = 12.37 Å.

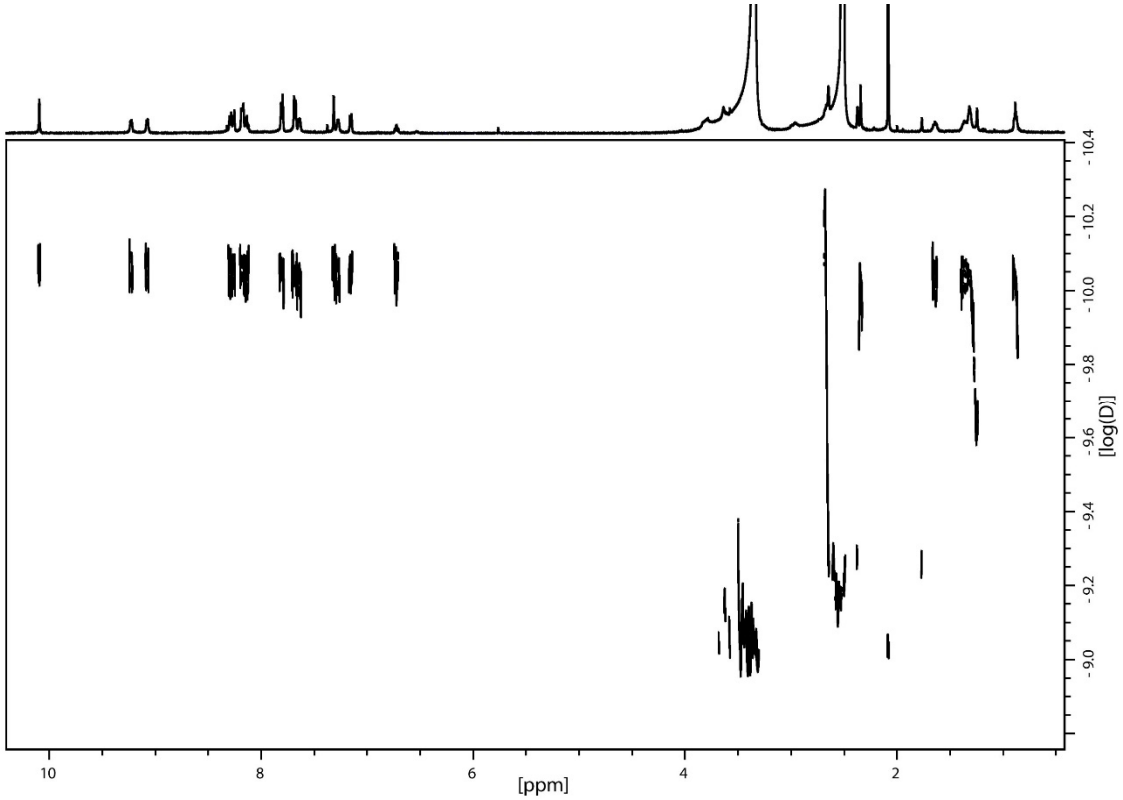

Figure 2.49 ^{1}H DOSY NMR (500 MHz, 298 K, DMSO-d_6) spectrum of the $[Pd_2\mathbf{L}^{\mathbf{OMe}}{}_2\mathbf{L}^{\mathbf{SNH2}}{}_2](BF_4)_4$ cage.

As already mentioned, the total count of signal protons in the ^{1}H NMR spectrum is fitting to the $[Pd_2\mathbf{L}^{\mathbf{OMe}}{}_2\mathbf{L}^{\mathbf{SNH2}}{}_2](BF_4)_4$ cage. Interestingly, the signal integration does not fit, with two additional signals than expected for a $[Pd_2\mathbf{L}^{\mathbf{OMe}}{}_2\mathbf{L}^{\mathbf{SNH2}}{}_2]$-cage. First assigned signals and by 2D NMR techniques retrospectively confirmed proton signals are H_a, H_e and H_i for $\mathbf{L}^{\mathbf{OMe}}$ and H_4 for $\mathbf{L}^{\mathbf{SNH2}}$ because of shape, shift and signal integration. Starting with ^{1}H-^{1}H COSY NMR spectrum in figure 2.51, cross-peak of H_e with H_f is indicated by assuming a higher downfield shift for H_f over H_d, reasoned on a stronger deshielding of the neighboured alkyne group. Overlayed signal attributed to $H_{c/d}$ with cross-peak to H_b and H_e complete the feasible signal attribution by ^{1}H-^{1}H COSY NMR for $\mathbf{L}^{\mathbf{OMe}}$ for this cage. $\mathbf{L}^{\mathbf{SNH2}}$ proton signal H_4 shows a cross-peak to H_3. With attributed the most signals of $\mathbf{L}^{\mathbf{OMe}}$, only distinction of is H_g/H_h missing, signals at 9.22 ppm and 9.06 ppm were attributed to

H_1, showing cross-peaks to protons of H_2. The total signal integration of signals labelled H_1 (8) and signals labelled H_2 (8) fits to this assignment.

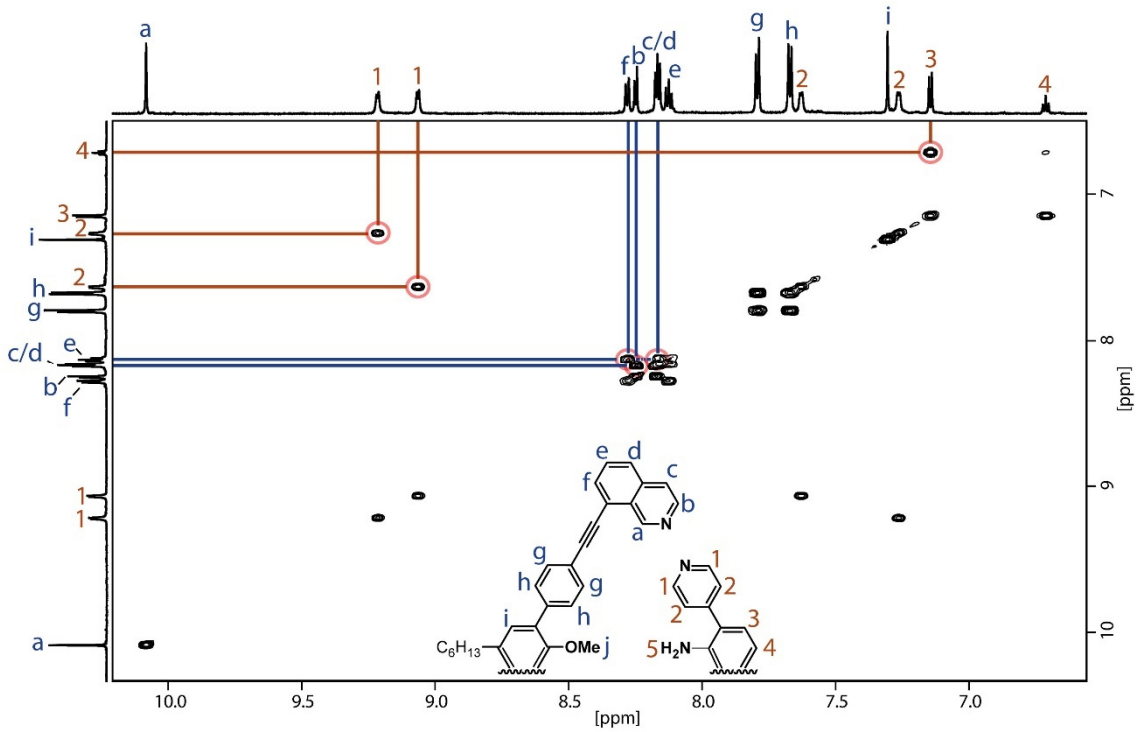

Figure 2.50 Partial ^{1}H-^{1}H COSY NMR (600 MHz, 298 K, DMSO-d_6) spectrum of the $[Pd_2L^{OMe}{}_2L^{SNH2}{}_2](BF_4)_4$ cage. Cross-peaks between L^{OMe} protons are marked dark blue; cross-peaks between L^{SNH2} protons are marked brown.

^{1}H-^{1}H NOESY NMR experiment (figure 2.51) further reveals the vicinity of H_1-H_2. In addition, the position of H_2 is confirmed by a cross-peak to H_3. The ^{1}H-^{1}H NOESY NMR confirms all addressed $\mathbf{L^{OMe}}$ with additional H_g/H_h proton distinction by cross-peaks of H_g-H_a and H_h-H_i. Interligand cross-peaks between H_1-H_a and H_1-H_b agreed with the proton assignment. The **-NH_2** group (*5*) at 3.62 ppm shows consistently cross-peaks with the H_2 protons in figure 2.52.

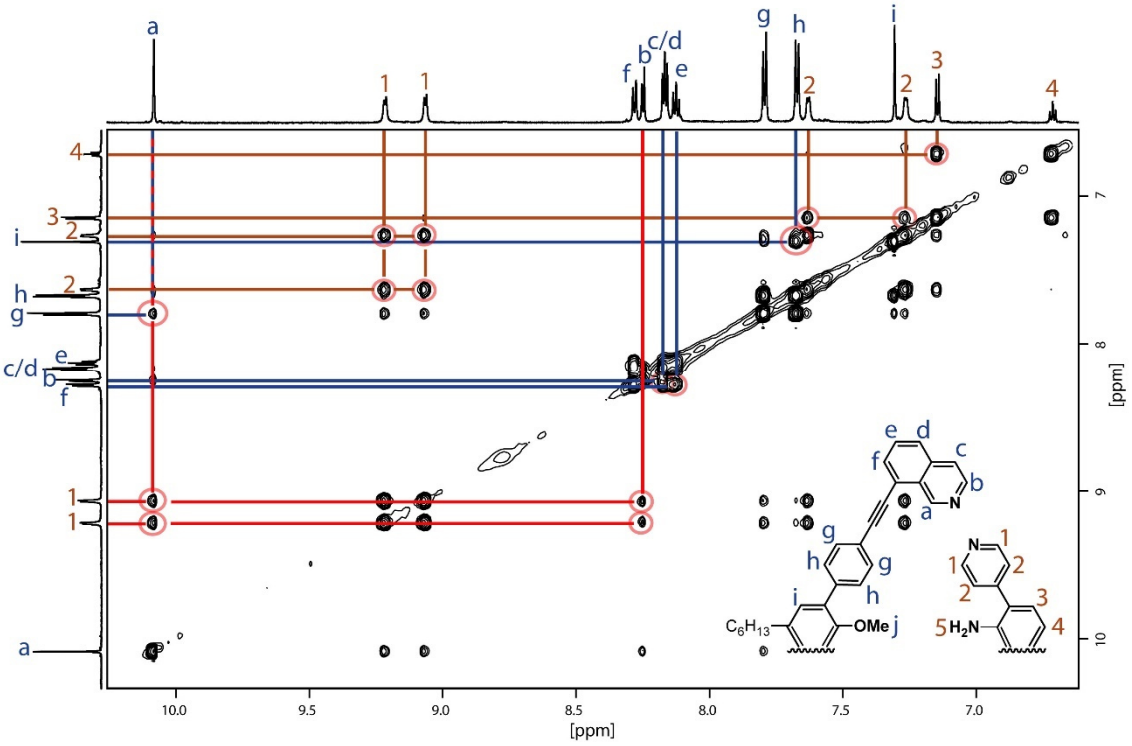

Figure 2.51 Partial ^{1}H-^{1}H NOESY NMR (700 MHz, 298 K, DMSO-d$_6$) spectrum of the [Pd$_2$L$^{OMe}_2$L$^{SNH2}_2$](BF$_4$)$_4$ cage. Cross-peaks between L^{OMe} protons are marked dark blue; cross-peaks between L^{SNH2} protons are marked brown; interligand cross-peaks with red.

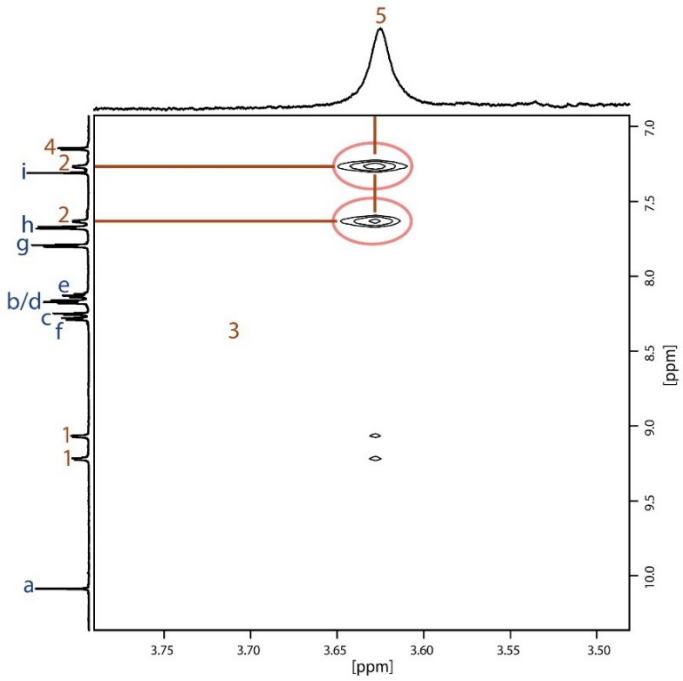

Figure 2.52 Partial ^{1}H-^{1}H NOESY NMR (700 MHz, 298 K, DMSO-d$_6$) spectrum of the [Pd$_2$L$^{OMe}_2$L$^{SNH2}_2$](BF$_4$)$_4$ cage focused on the aromatic amine group of L^{SNH2}. Cross-peaks between L^{SNH2} protons are marked brown.

After addressing all signals by 2D NMR, the question was, why the H_1 and H_2 protons shows a strong splitting, while this is not observed for the other protons of **L^{SNH2}**. A

possible explanation is a restricted rotation of the pyridyl-phenyl-axis due to a steric hindrance from the **-NH_2** group, causing the splitting. To prove this, the temperature was elevated to 70 °C to allow a rotation of the pyridyl moiety (figure 2.53).

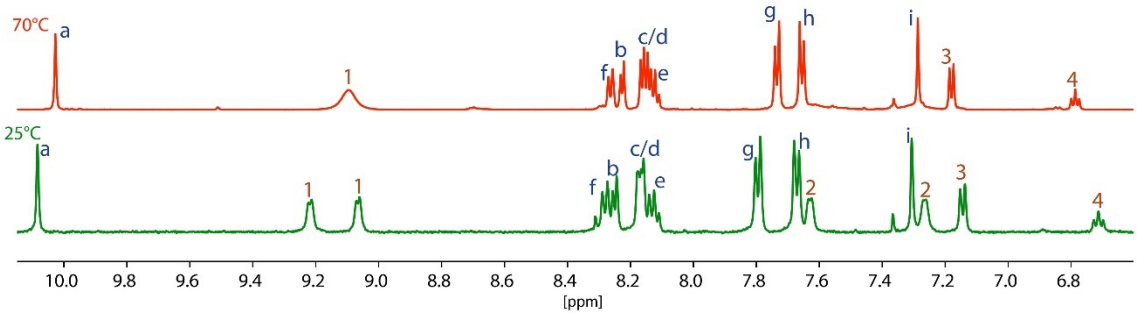

Figure 2.53 ^{1}H NMR spectra (500 MHz, DMSO-d_6) of $[Pd_2L^{OMe}{}_2L^{SNH2}{}_2](BF_4)_4$ at 298 K (25 °C, green) and 343 K (70 °C, red).

As expected, at 70 °C signals of H_1 merged to one broad signal, while signals of H_2 disappeared due to a strong broadening. Increase of the base of signals H_h and H_i point on the possible position of the ^{1}H signals of H_2. ^{1}H-^{1}H NOESY NMR at 70 °C further proved the identity of H_1, showing a cross-peak to H_a. Although strongly broadened, in the ^{1}H-^{1}H NOESY NMR cross-peaks between H_1 and H_2 still show a splitting of the H_2 protons. This shows that the heating of the sample does not overcome the steric hindrance, making the H_1 and H_2 protons magnetically non-equivalent and the signal H_1 at 70 °C is an overlapped signal of two signals.

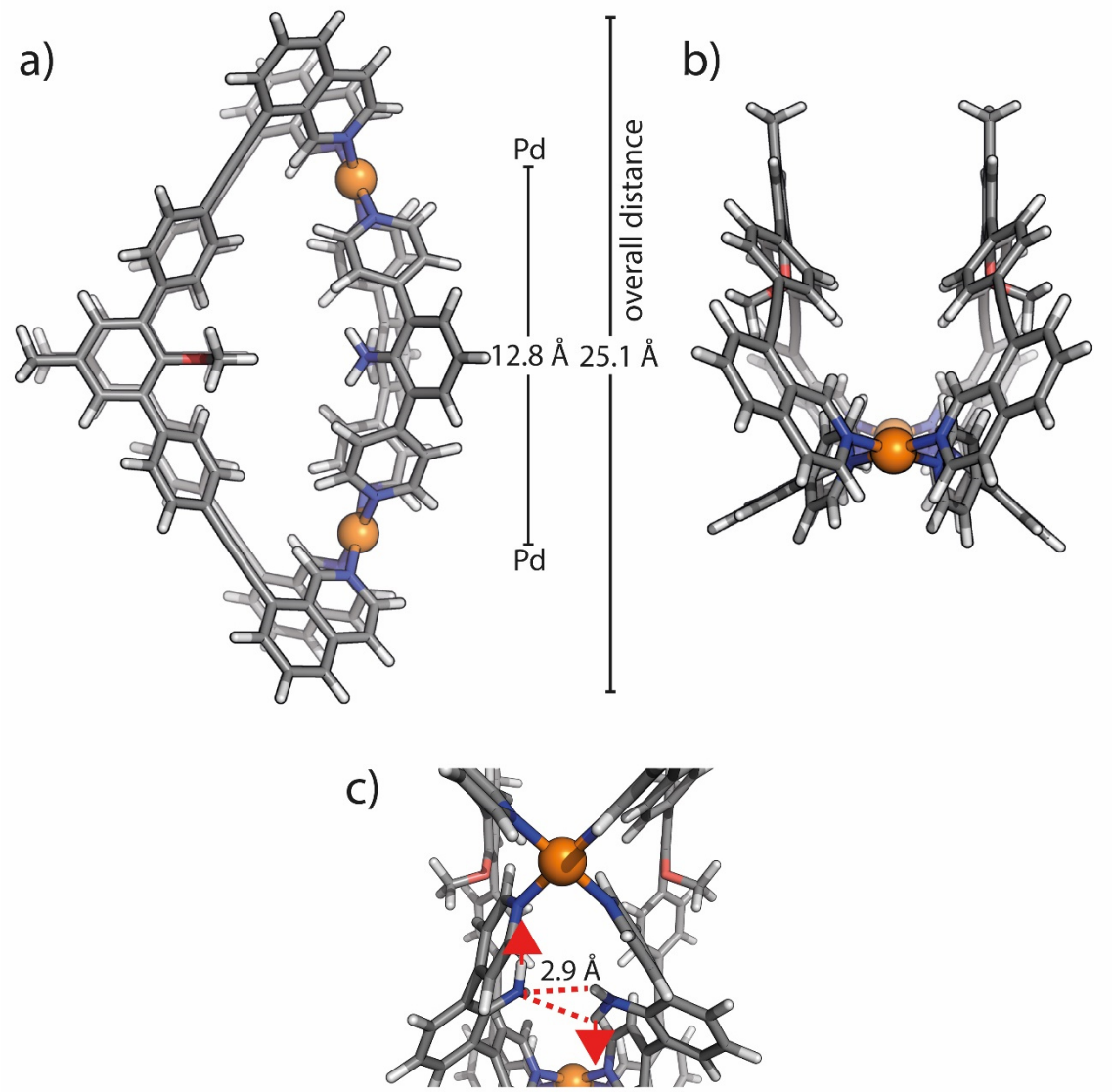

Figure 2.54 DFT (BP86-D4/def2-SVP (def2-TZVP for Pd)) calculated structure of $[Pd_2L^{OMe}{}_2L^{SNH2}{}_2]^{4+}$ in DMSO with a) top view and b) side view and c) closer view on the amine groups with marked 2.9 Å distance between one free electron pair of one L^{SNH2} ligand and 2 hydrogens of the other L^{SNH2} ligand. Sidechains are scaled down to a methyl group to simplify the calculation. Colour scheme: C = dark grey, H = light grey, O = red, N = blue, Pd = orange.

A DFT calculation gives an impression of the structural properties in the gas phase (figure 2.54), showing a Pd•••Pd distance with 12.8 Å (equating DFT model of $[Pd_2\mathbf{L}^{\mathbf{OMe}}{}_2\mathbf{L}^{\mathbf{SB}}{}_2]^{4+}$ with 12.4 Å) and a distance of the most distal hydrogen atoms with 25.1 Å (fits with the from ^{1}H DOSY NMR spectrum calculated hydrodynamic radius of r_H = 12.21 Å written before). The **-NH2•••NH2-** distance is with 2.9 Å in the range of hydrogen bonding.[134] This bonding inside the cavity prevents a fast moving between possible orientations of the backbones (relative to the NMR time scale). The formed hydrogen bond fixes the orientation of the **-NH_2** in a way which makes them block the free rotation of the pyridyl groups.

This hindered free rotation along the pyridyl-phenyl-axis leads finally to fixed positions of the pyridyls, leading to a magnetically inequivalent protons for ^{1}H NMR measurements. An additional indication of the existence and importance of hydrogen bonding inside $[Pd_2\mathbf{L}^{OMe}{}_2\mathbf{L}^{SNH2}{}_2](BF_4)_4$ is the comparison with $[Pd_2\mathbf{L}^{OMe}{}_2\mathbf{L}^{SOMe}{}_2](BF_4)_4$ including bulky but free rotatable **-OMe** groups, showing no splitting of the pyridyl protons (figure 2.56). Stabilizing hydrogen bonds within the cage could explain the higher stability of this heteroleptic cage upon dilution in acetonitrile prior to ESI-MS experiments compared to $[Pd_2\mathbf{L}^{OMe}{}_2\mathbf{L}^{SB}{}_2](BF_4)_4$.

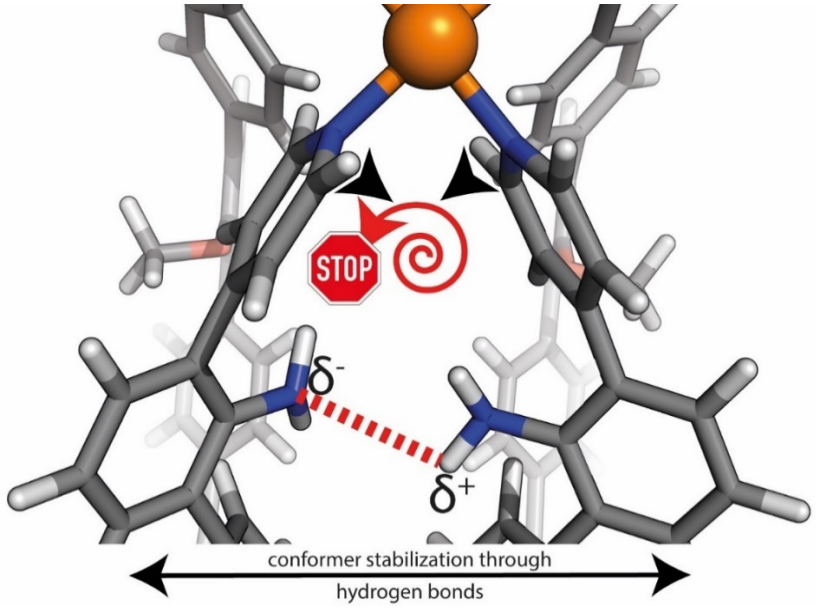

Figure 2.55 Graphic to illustrate the described effect of conformer stabilizing hydrogen bond between both -NH_2 groups to stop the free rotation of the pyridyls in $[Pd_2\mathbf{L}^{OMe}{}_2\mathbf{L}^{SNH2}{}_2](BF_4)_4$.

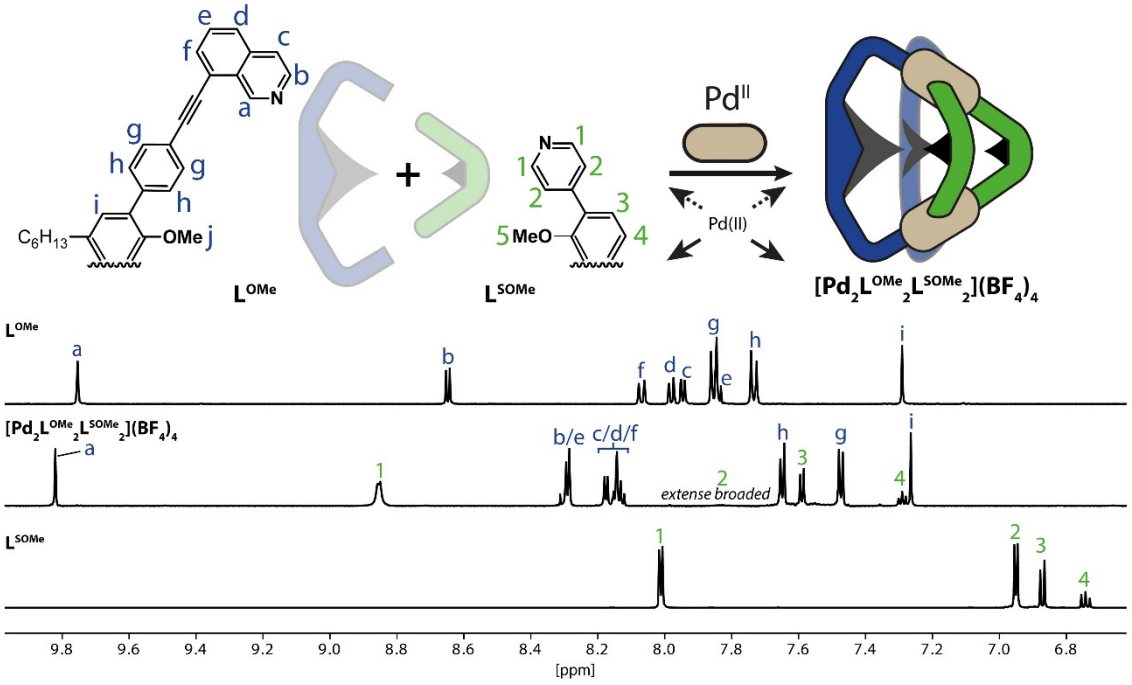

Figure 2.56 Schematic formation of the heteroleptic $[Pd_2L^{OMe}{}_2L^{SOMe}{}_2](BF_4)_4$ cage and comparison of the partial ^{1}H NMR spectra (500 MHz, 298 K, DMSO-d_6) of the free ligands L^{OMe} and L^{SOMe} with the respective heteroleptic cage.

For the $[Pd_2\mathbf{L}^{OMe}{}_2\mathbf{L}^{SOMe}{}_2](BF_4)$, the entire signal integration leads to a Pd/ligand ratio of 1:2 and a ratio for $\mathbf{L}^{OMe}$:$\mathbf{L}^{SB}$ of 1:1. Again a downfield shift compared to $[Pd_2\mathbf{L}^{OMe}{}_4](BF_4)_4$ is observed, dedicated to a lower twisting of the $\mathbf{L}^{OMe}$ ligands and a larger distance of the π-systems of the $\mathbf{L}^{OMe}$ ligands.

Figure 2.57 shows the ESI-MS spectrum of $[Pd_2\mathbf{L}^{OMe}{}_2\mathbf{L}^{SOMe}{}_2](BF_4)_4$, with *m/z* = 507.66 for $[Pd_2\mathbf{L}^{OMe}{}_2\mathbf{L}^{SOMe}{}_2]^{4+}$, *m/z* = 705.87 for $[Pd_2\mathbf{L}^{OMe}{}_2\mathbf{L}^{SOMe}{}_2{+}BF_4]^{3+}$ and *m/z* = 1102.32 for the $[Pd_2\mathbf{L}^{OMe}{}_2\mathbf{L}^{SOMe}{}_2{+}2BF_4]^{2+}$. A peak at *m/z* = 683.21 is attributed to $[Pd_2\mathbf{L}^{OMe}{}_2\mathbf{L}^{SOMe}{}_2{+}F]^{3+}$, showing a contamination of fluoride. This contamination is commonly observed when heating samples containing BF_4^-. This makes the placement of the counterion inside the cavity plausible with a repulsion of two guest including one F^-, visible in the nonexistence of a $[Pd_2\mathbf{L}^{OMe}{}_2\mathbf{L}^{SOMe}{}_2{+}F{+}BF_4]^{2+}$ species. Nevertheless, these are effects only visible in the gas phase and could be different in solution.

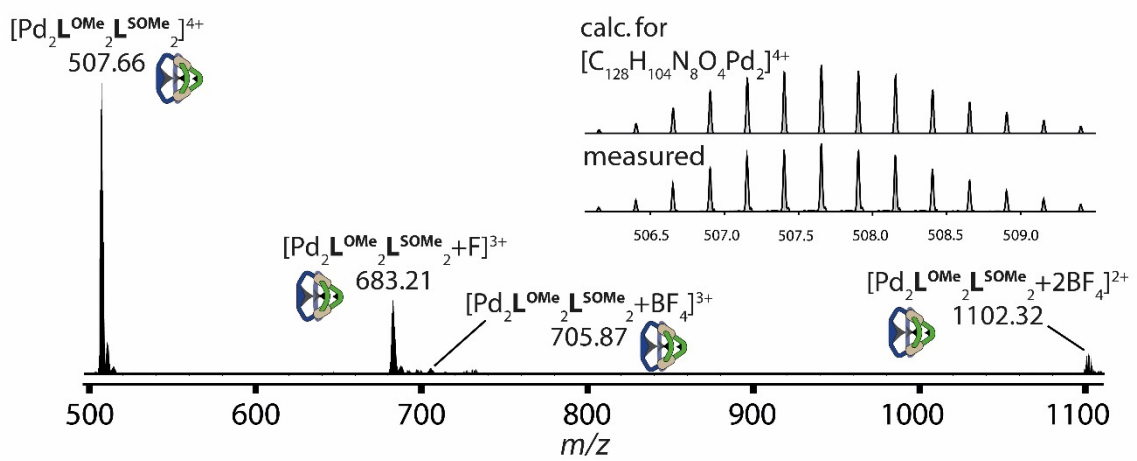

Figure 2.57 ESI mass spectrum of a $[Pd_2L^{OMe}{}_2L^{SOMe}{}_2](BF_4)_4$ sample.

From ^{1}H DOSY NMR measurement (figure 2.58) a single species is confirmed. A hydrodynamic radius of r_H = 11.9 Å is calculated with the Stokes-Einstein equation from a diffusion coefficient of D = 9.2053 · 10^{-11} $m^2 \cdot s^{-1}$ in agreement with the previously measured radii of $[Pd_2L^{OMe}{}_2L^{SB}{}_2](BF_4)_4$ and $[Pd_2L^{OMe}{}_2L^{SNH2}{}_2](BF_4)_4$ with r_H = 12.37 Å and r_H = 12.21 Å, respectively.

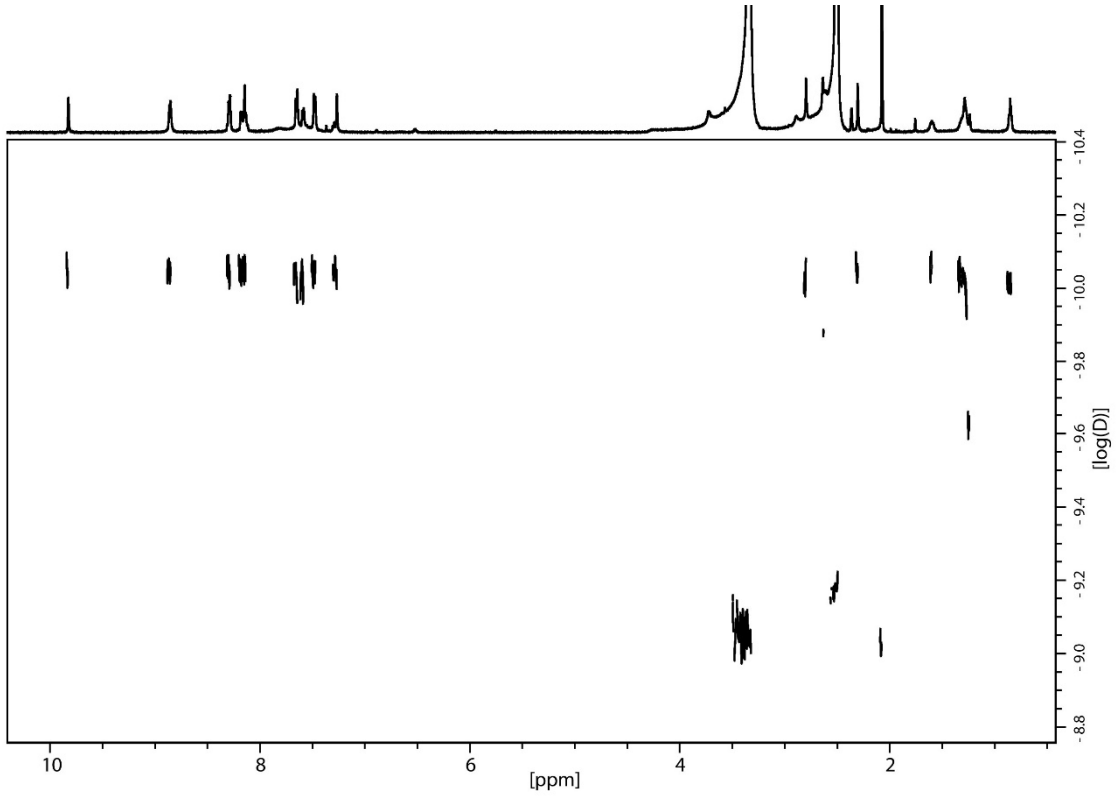

Figure 2.58 ^{1}H DOSY NMR (500 MHz, 298 K, DMSO-d_6) spectrum of the $[Pd_2L^{OMe}{}_2L^{SOMe}{}_2](BF_4)_4$ cage.

^{1}H-^{1}H COSY NMR experiment (figure 2.60) indicates the proximity of the first by size, shape, and signal integration estimated proton H_4 with H_3 (light green). Estimated signal

H_1 does not show a cross-peak to presumably proton H_2, due to the broadening of this signal. Unfortunately, it is also not possible to sharpen the signal shape by measuring at higher temperatures, an overlapping of signal H_2 with H_h is visible due to the broadening of the base of signal H_h, including a “shoulder” (figure 2.59).

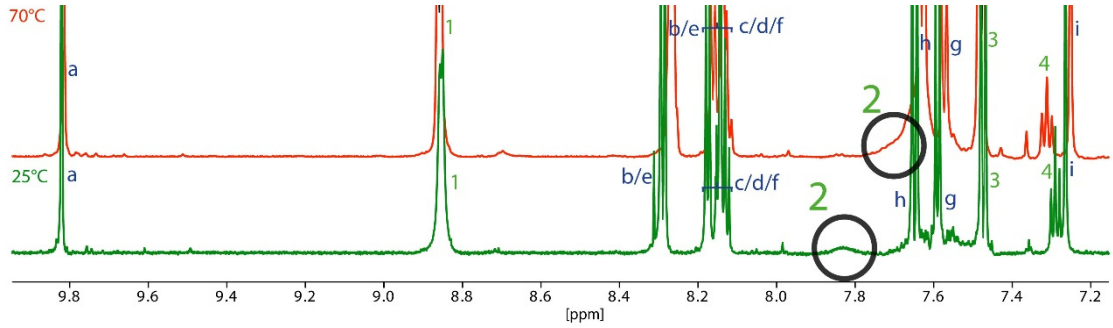

Figure 2.59 ^{1}H NMR spectra (500 MHz, DMSO-d_6) of $[Pd_2L^{OMe}{}_2L^{SOMe}{}_2](BF_4)_4$ at 298 K (25 °C, green) and 343 K (70 °C, red). Signal 2 of ligand L^{SOMe} broadened signal at 25 °C and Highfield shifted at 70 °C, underlaying signal h of L^{OMe}.

H_a and H_i of $\mathbf{L^{OMe}}$ inside $[Pd_2\mathbf{L^{OMe}}{}_2\mathbf{L^{SOMe}}{}_2](BF_4)_4$ are initially assigned according to size, shift and signal integration for H_a and H_i, while H_g and H_h are not distinguishable from each other. The remaining protons of $\mathbf{L^{OMe}}$ could not be assigned by ^{1}H-^{1}H COSY NMR, due to a strong overlap.

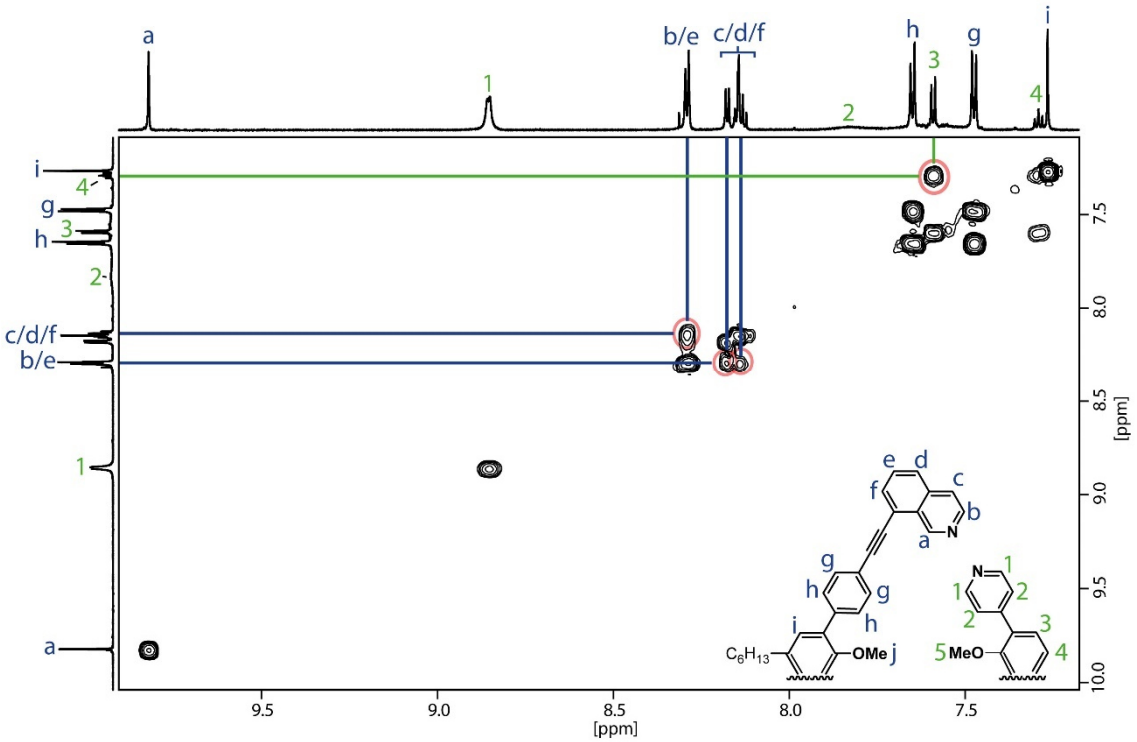

Figure 2.60 Partial ^{1}H-^{1}H COSY NMR (600 MHz, 298 K, DMSO-d_6) spectrum of the $[Pd_2L^{OMe}{}_2L^{SOMe}{}_2](BF_4)_4$ cage. Cross-peaks between L^{OMe} protons are marked dark blue; cross-peaks between L^{SOMe} protons are marked light green.

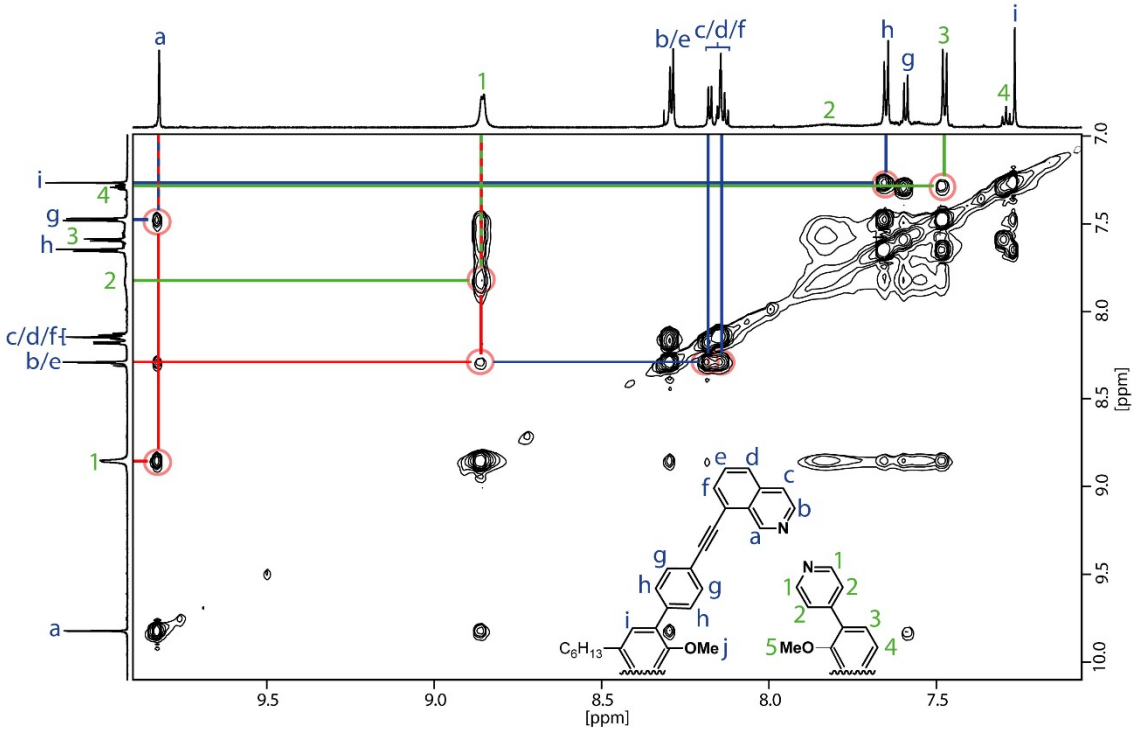

Figure 2.61 Partial ^{1}H-^{1}H NOESY NMR (700 MHz, 298 K, DMSO-d_6) spectrum of the $[Pd_2L^{OMe}{}_2L^{SOMe}{}_2](BF_4)_4$ cage. Cross-peaks between L^{OMe} protons are marked dark blue; cross-peaks between L^{SOMe} protons are marked light green; interligand cross-peaks with red.

From ^{1}H-^{1}H NOESY NMR (figure 2.61) experiments, cross-peaks of H_g and H_h with H_a and H_i, (dark blue) are identified, respectively. H_b is estimated from an inter-ligand cross-peak with H_1 (red lines). Determination of H_e by a cross-peak with a combined $H_{b/e}$ signal is estimated by signal integration and an additional cross-peak to $H_{c/d/f}$. This is only plausible by this combination of overlaying signals for the respective protons including a perfect count of proton number for $H_{c/d/f}$. In addition, H_1 shows a cross-peak to H_a and to a broadened H_2.

Figure 2.62 shows the geometric optimization (DFT calculation) of $[Pd_2\mathbf{L}^{OMe}{}_2\mathbf{L}^{SOMe}{}_2]^{4+}$ with a Pd•••Pd distance of 12.6 Å and a distance 25.5 Å between the two most distal protons, being in an agreement with ^{1}H DOSY NMR measurement showing a hydrodynamic radius of r_H = 11.9 Å.

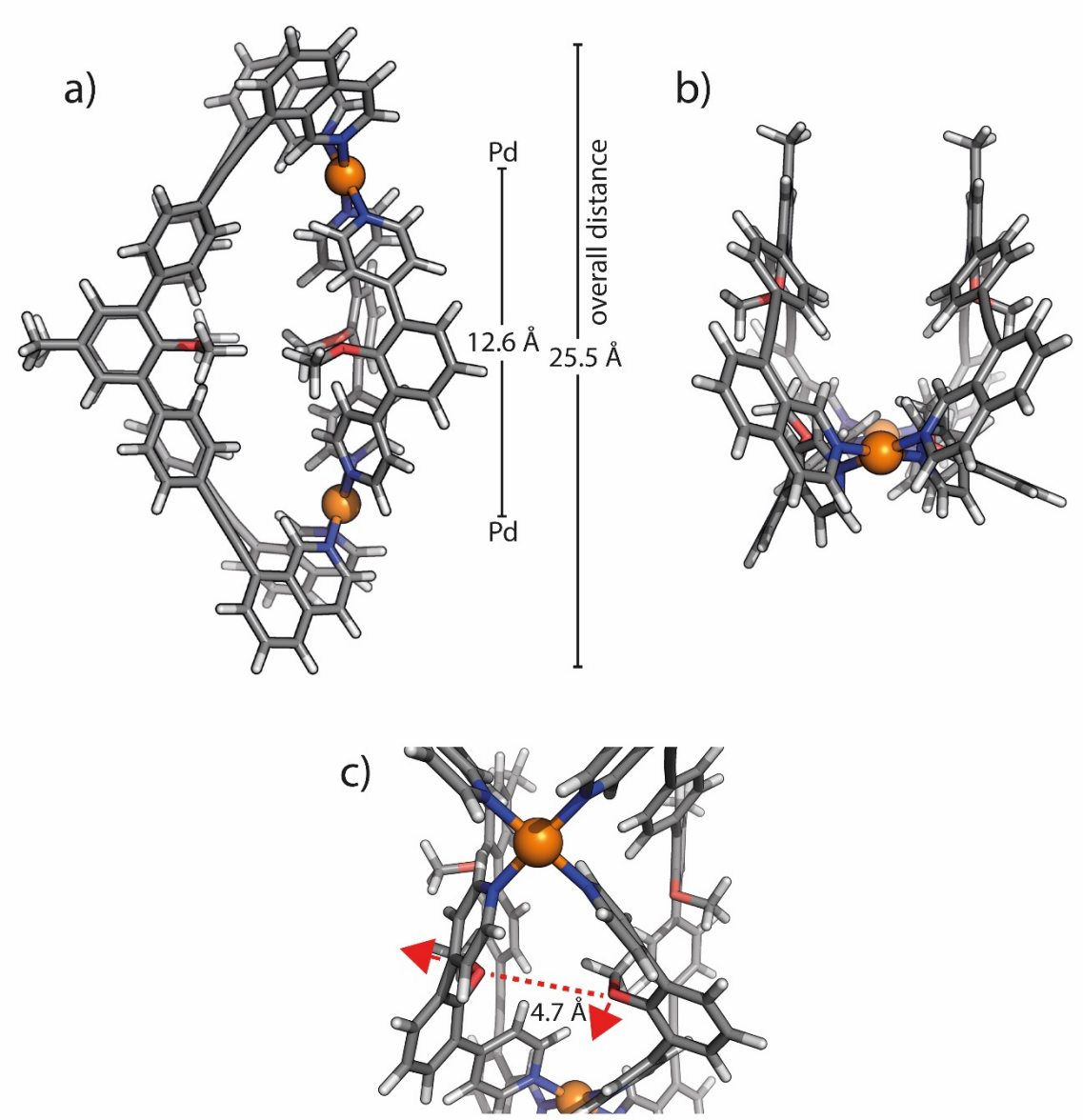

Figure 2.62 DFT (BP86-D4/def2-SVP (def2-TZVP for Pd)) calculated structure of $[Pd_2L^{OMe}{}_2L^{SOMe}{}_2]^{4+}$ in DMSO with a) top view, b) side view and c) closer view on the methoxy groups. Sidechains are scaled down to a methyl group to simplify the calculation. Colour scheme: C = dark grey, H = light grey, O = red, N = blue, Pd = orange.

The free rotatable **-OMe** groups seems to be in different position with only one group pointing inside the cavity, opposite to what is observed in the crystal structure for $[Pd_2\mathbf{L}^{\mathbf{OMe}}{}_4](BF_4)_4$, where all **-OMe** groups are pointing inside. Nevertheless, due to the freely rotatable nature of the **-OMe** groups, both groups could switch their position, changing back and forth the orientation of the phenyl group. This ends up in a fast movement, not notable on the NMR time scale. Otherwise, the magnetic characteristics of each $\mathbf{L}^{\mathbf{SOMe}}$ ligand would be different, ending up in a splitting of ^1H signals like seen before in $[Pd_2\mathbf{L}^{\mathbf{OMe}}{}_2\mathbf{L}^{\mathbf{SNH2}}{}_2](BF_4)_4$, where the **-NH$_2$** act like an blocker and orientate each $\mathbf{L}^{\mathbf{SNH2}}$ ligand in one (for the NMR time scale) fixed conformation inside the cage structure.

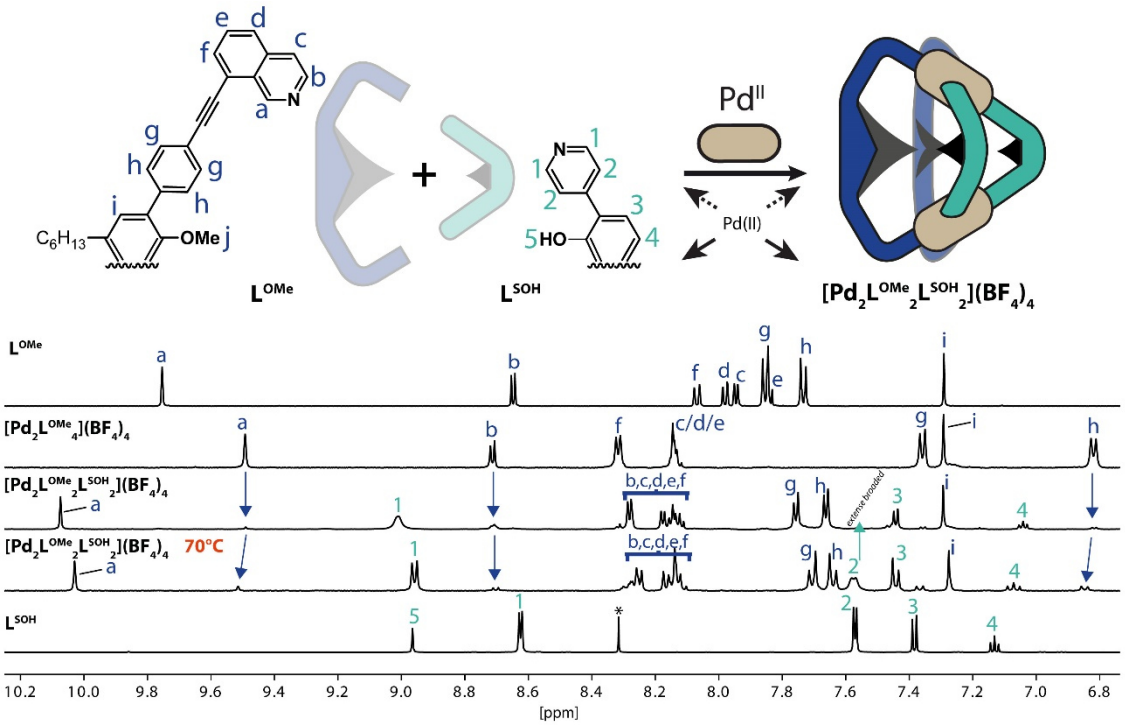

Figure 2.63 Schematic formation of the heteroleptic $[Pd_2L^{OMe}_2L^{SOH}_2](BF_4)_4$ cage and comparison of the partial ^{1}H NMR spectra (500 MHz, 298 K, DMSO-d_6) of the free ligands L^{OMe} and L^{SOH} with the homoleptic $[Pd_2L^{OMe}_4](BF_4)_4$ cage and additional comparison of the heteroleptic cage at 343 K (70 °C).

The ^{1}H NMR (figure 2.12) is well resolved and signal integration is matching to the formation of $[Pd_2\mathbf{L^{OMe}_2L^{SOH}_2}](BF_4)_4$ with a Pd/ligand ratio of 1:2 and a ratio of $\mathbf{L^{OMe}/L^{SOH}}$ of 1:1. Ass mentioned previously, in $[Pd_2\mathbf{L^{OMe}_4}](BF_4)_4$ signals of $\mathbf{L^{OMe}}$ are downfield shifted, indicating less twisting of the quinoline-based ligands in the heteroleptic cage. A small amount of $[Pd_2\mathbf{L^{OMe}_4}](BF_4)_4$ was found in every sample with ~3 % proportion according to ^{1}H NMR signal integration. Extended heating times, additional equivalents of $\mathbf{L^{SOH}}$ or fixing the ligand-to-ligand ratio 1:1 by ^{1}H NMR titration of ligand against ligand, showed no improvement, indicating an equilibrium induced by lone pair repulsions of the $\mathbf{L^{SOH}}$ ligands.

With the first impression of the ^{1}H NMR analysis, an ESI-MS measurement was performed (figure 2.64). As expected, $[Pd_2\mathbf{L^{OMe}_2L^{SOH}_2}]^{4+}$ with *m/z* = 500.65 and $[Pd_2\mathbf{L^{OMe}_2L^{SOH}_2}+2BF_4]^{2+}$ with *m/z* = 500.65 and respective isotopic pattern are existent besides a small peak for $[Pd_2\mathbf{L^{OMe}_4}]^{4+}$ at m/z = 700.00. A peak of $[Pd_2\mathbf{L^{OMe}_2L^{SOH}_2}+BF_4]^{3+}$ with a calculated *m/z* = 696.54 is completely missing.

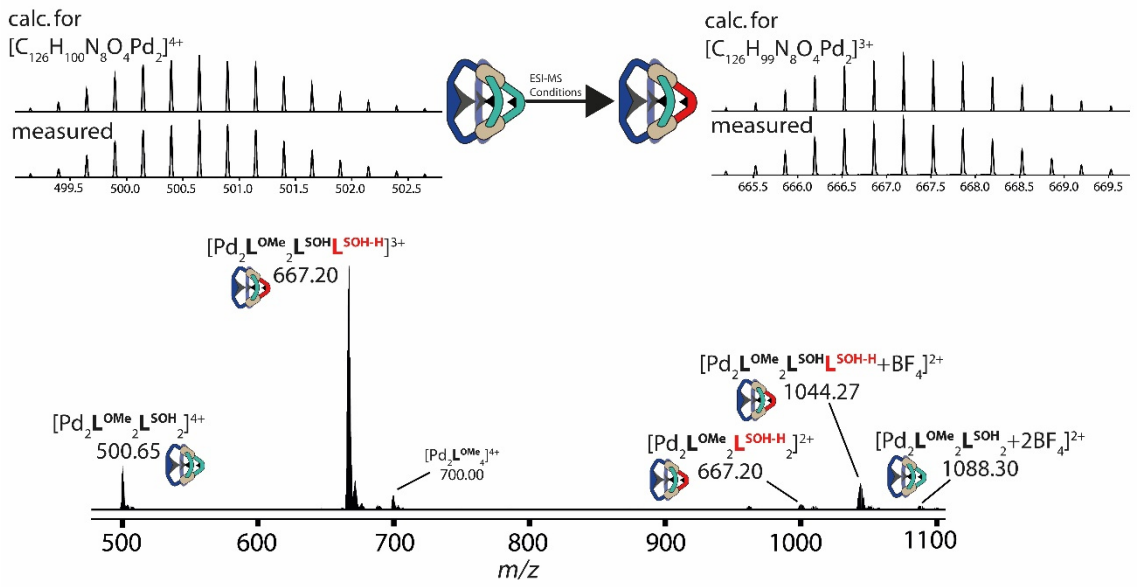

Figure 2.64 ESI mass spectrum of a $[Pd_2L^{OMe}{}_2L^{SOH}{}_2](BF_4)_4$ sample.

Interestingly the species $[Pd_2L^{OMe}{}_2L^{SOH}L^{SOH\text{-}H}]^{3+}$ ($L^{SOH\text{-}H}$ as an abbreviation for the deprotonated L^{SOH} ligand) with *m/z* = 667.20 shows the highest intensity, indicating a deprotonation of one phenol. This behaviour was not observed for the free ligand L^{SOH} or for L^{OH} and $[Pd_2L^{OH}{}_4](BF_4)_4$, respectively.

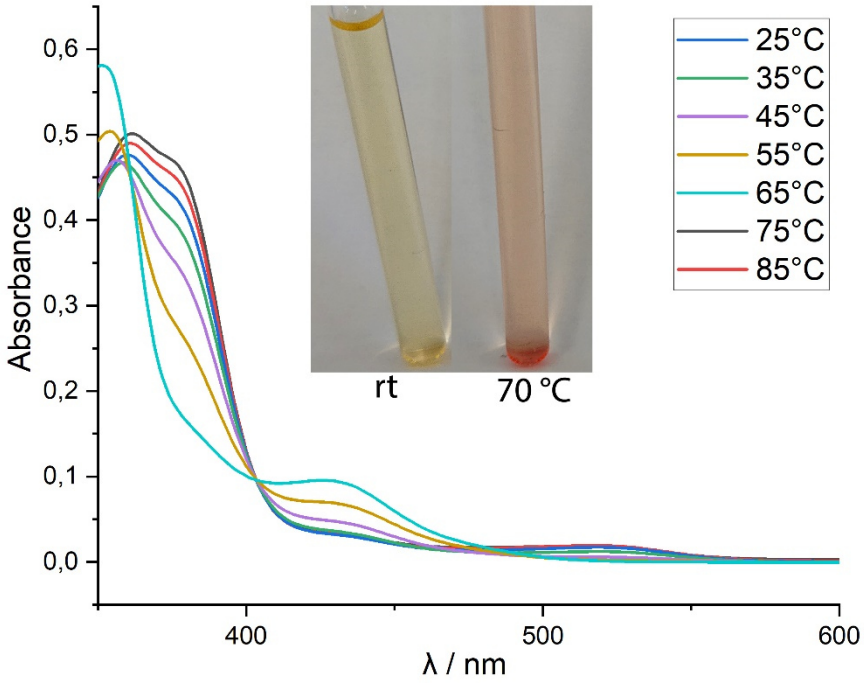

Figure 2.65 UV-VIS spectra of $[Pd_2L^{OMe}{}_2L^{SOH}{}_2](BF_4)_4$ in DMSO-d_6 with increasing temperature and pictures of NMR tubes with the sample at room temperature and 70 °C.

Additionally, a colour change of the cage solution from yellow to orange can be observed by heating from room temperature to 70 °C, respectively (figure 2.65). Figure 2.63 proves an intact cage species at higher temperature. As all other cages does not show this

behaviour, it is exclusively for $[Pd_2\mathbf{L}^{\mathbf{OMe}}{}_2\mathbf{L}^{\mathbf{SOH}}{}_2](BF_4)_4$ and should be in relation with the $\mathbf{L}^{\mathbf{SOH}}$ ligand. Heating a pure $\mathbf{L}^{\mathbf{SOH}}$ solution of the same ligand concentration does not lead to a colour change. UV-VIS spectra at different temperatures show an isosbestic point at 404 nm. This indicates the existence of a reaction but not exactly what happen. Further studies need to be done to may indicate a deprotonation of the phenol-based ligands.

^{1}H DOSY NMR measurement proves the presence of only one main species (figure 2.66). The measured values are in the same magnitude as the before reported heteroleptic cages with $D = 9.0274 \cdot 10^{-11}$ m^2·s^{-1} and a calculated r_H = 12.15 Å.

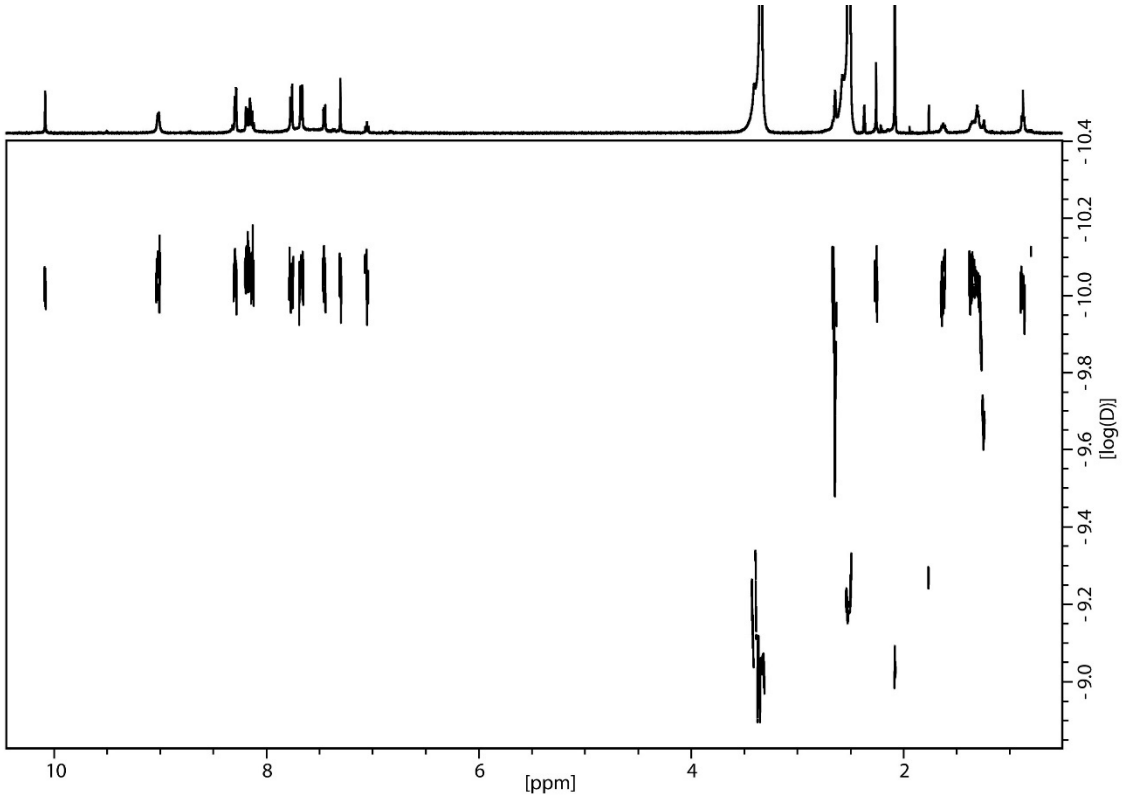

Figure 2.66 ^{1}H DOSY NMR (500 MHz, 298 K, DMSO-d$_6$) spectrum of the $[Pd_2\mathbf{L}^{\mathbf{OMe}}{}_2\mathbf{L}^{\mathbf{SOH}}{}_2](BF_4)_4$ cage.

To assign the ^{1}H signals, 2D NMR experiments were measured at 25 °C and 70 °C. Unfortunately, the signals H_b,H_c,H_d,H_e,H_f of $\mathbf{L}^{\mathbf{OMe}}$ are strongly overlapping. For the remaining signals, it is possible to assign them by shape, shift and signal integration. ^{1}H-^{1}H COSY NMR experiments at 70 °C (figure 2.67) shows H_1-H_2 and H_3-H_4 cross-peaks, although H_2 can only be observed at 70 °C. ^{1}H-^{1}H NOESY NMR at 25 °C (figure 2.68) and 70 °C (figure 2.69) reveal the proximity of H_2-H_3 and confirms additionally to ^{1}H-^{1}H COSY NMR H_1-H_2 and H_3-H_4. The distinction of H_g and H_h is enabled with H_g-H_a and H_h-H_i cross-peaks. An interligand cross-peaks is visible for H_a-H_1.

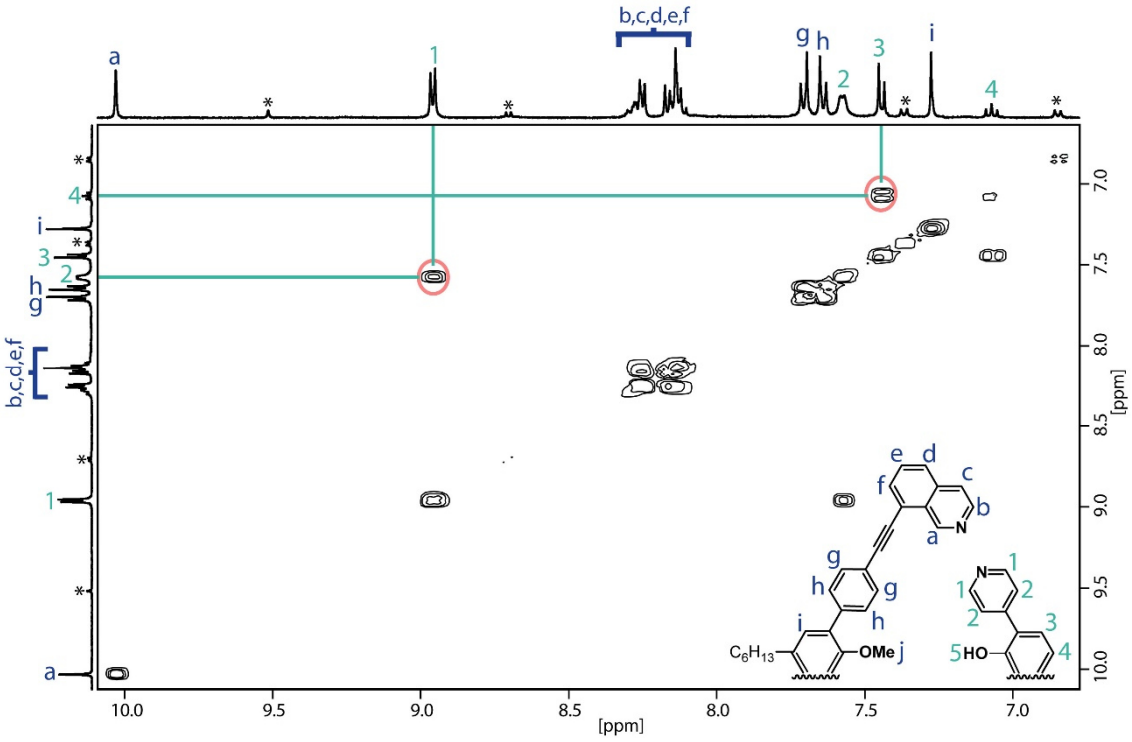

Figure 2.67 Partial ^{1}H-^{1}H COSY NMR (600 MHz, 343 K, DMSO-d$_6$) spectrum of the [Pd$_2$L$^{OMe}_2$L$^{SOH}_2$](BF$_4$)$_4$ cage. Cross-peaks between L^{SOH} protons are marked turquoise.

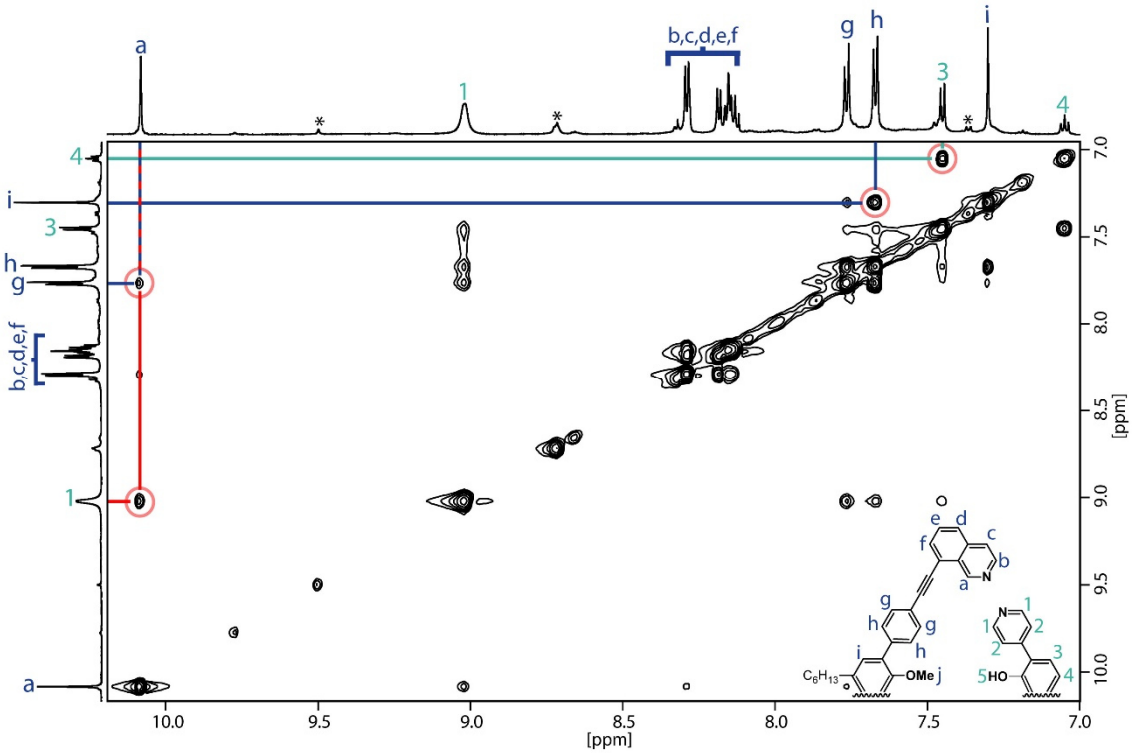

Figure 2.68 Partial ^{1}H-^{1}H NOESY NMR (600 MHz, 298 K, DMSO-d$_6$) spectrum of the [Pd$_2$L$^{OMe}_2$L$^{SOH}_2$](BF$_4$)$_4$ cage. Cross-peaks between L^{OMe} protons are marked dark blue; cross-peaks between L^{SOH} protons are marked turquoise; interligand cross-peaks with red.

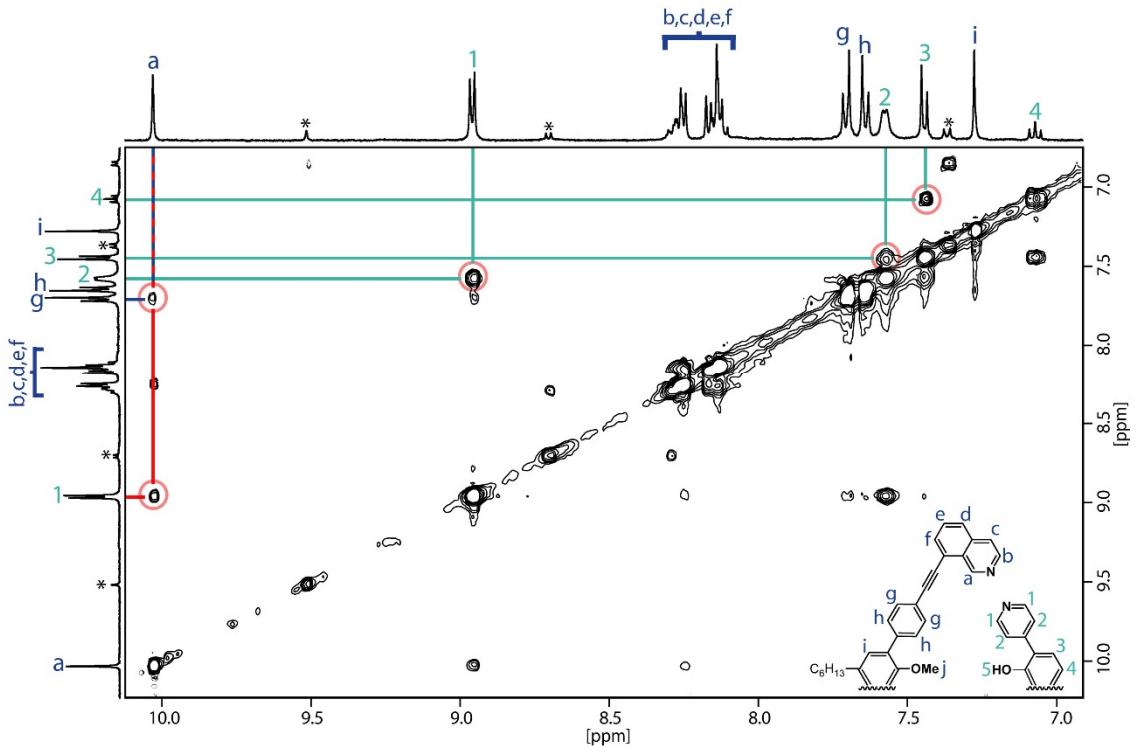

Figure 2.69 Partial ^{1}H-^{1}H NOESY NMR (400 MHz, 343 K, DMSO-d$_6$) spectrum of the [Pd$_2$L$^{OMe}_2$L$^{SOH}_2$](BF$_4$)$_4$ cage. Cross-peaks between L^{OMe} protons are marked dark blue; cross-peaks between L^{SOH} protons are marked turquoise; interligand cross-peaks with red.

Figure 2.70 shows a Pd•••Pd distance of 12.6 Å and a distance of 25.5 Å for the most distal protons of the DFT calculated optimized structure, similar to reported values for similar cages of the [Pd$_2$**L$^{OMe}_2$L$^{X}_2$**](BF$_4$)$_4$ type. A comparison with the ^{1}H DOSY NMR given r_H = 12.15 Å proves the size range of the calculation. The distance for **-OH•••OH-** is calculated with 3.8 Å and thus larger than the **-NH2•••NH2-** distance for [Pd$_2$**L$^{OMe}_2$L$^{SNH2}_2$**](BF$_4$)$_4$ with 2.9 Å. In agreement to these calculated distances, the hydrogen bonding for [Pd$_2$**L$^{OMe}_2$L$^{SOH}_2$**](BF$_4$)$_4$ would be weaker than for [Pd$_2$**L$^{OMe}_2$L$^{SNH2}_2$**](BF$_4$)$_4$.[134] The ^{1}H NMR spectrum, [Pd$_2$**L$^{OMe}_2$L$^{SOH}_2$**](BF$_4$)$_4$ shows no splitting of the ^{1}H pyridyl signals, showing a freely rotatable pyridyl-phenyl-axis axis. This is different to the postulated non rotatable pyridyl-phenyl-axis inside the [Pd$_2$**L$^{OMe}_2$L$^{SNH2}_2$**](BF$_4$)$_4$ cage, induced by hydrogen bonds of the **-NH$_2$** functions which stabilize two conformers of the **L^{SNH2}** ligands inside the cage structure by hindering a free pyridyl rotation (relative on NMR time scale).

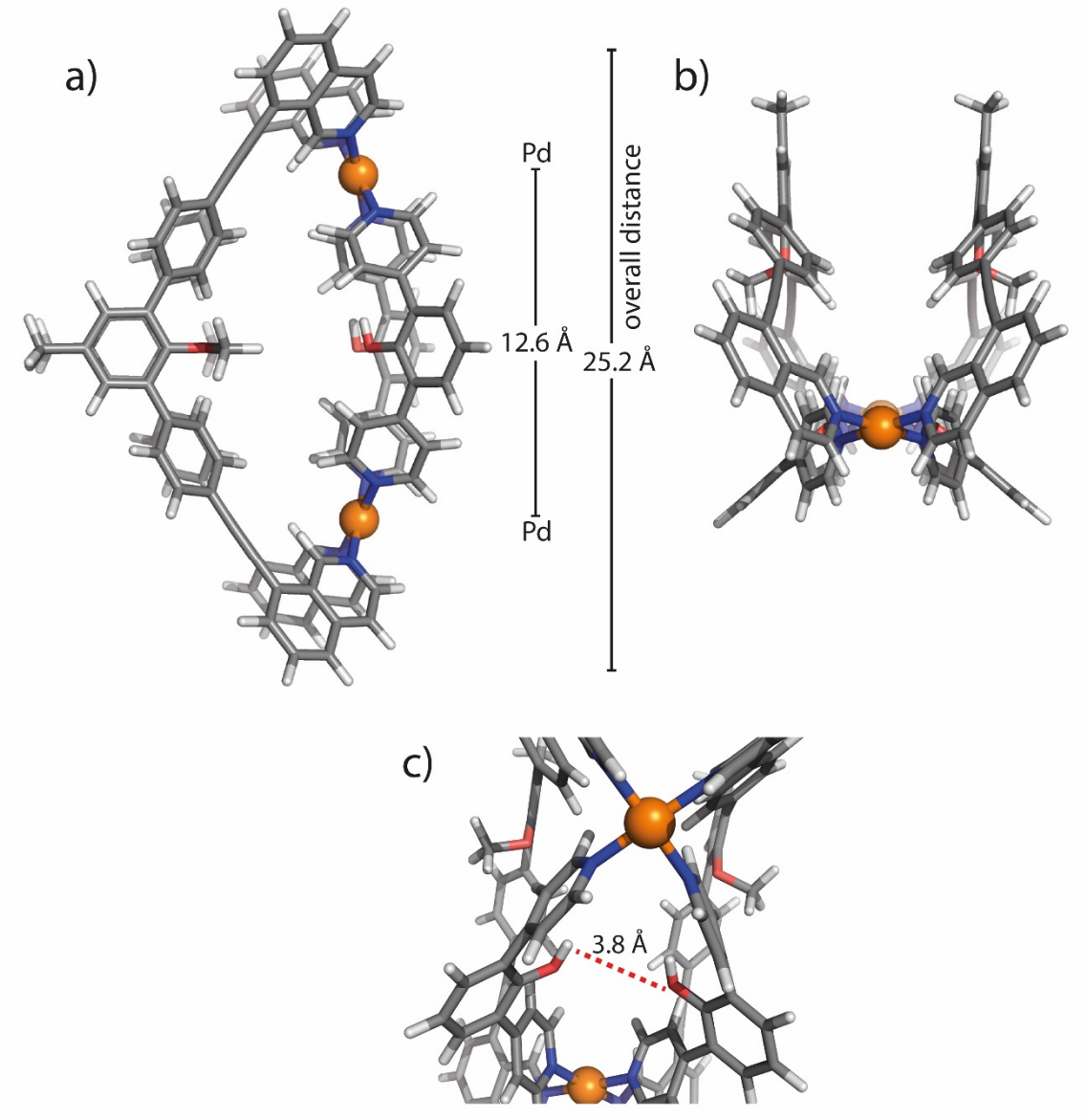

Figure 2.70 DFT (BP86-D4/def2-SVP (def2-TZVP for Pd)) optimized structure of $[Pd_2L^{OMe}{}_2L^{SOH}{}_2]^{4+}$ in DMSO with a) top view, b) side view and, c) closer view on the --OH groups. Sidechains are scaled down to a methyl group to simplify the calculation. Colour scheme: C = dark grey, H = light grey, O = red, N = blue, Pd = orange.

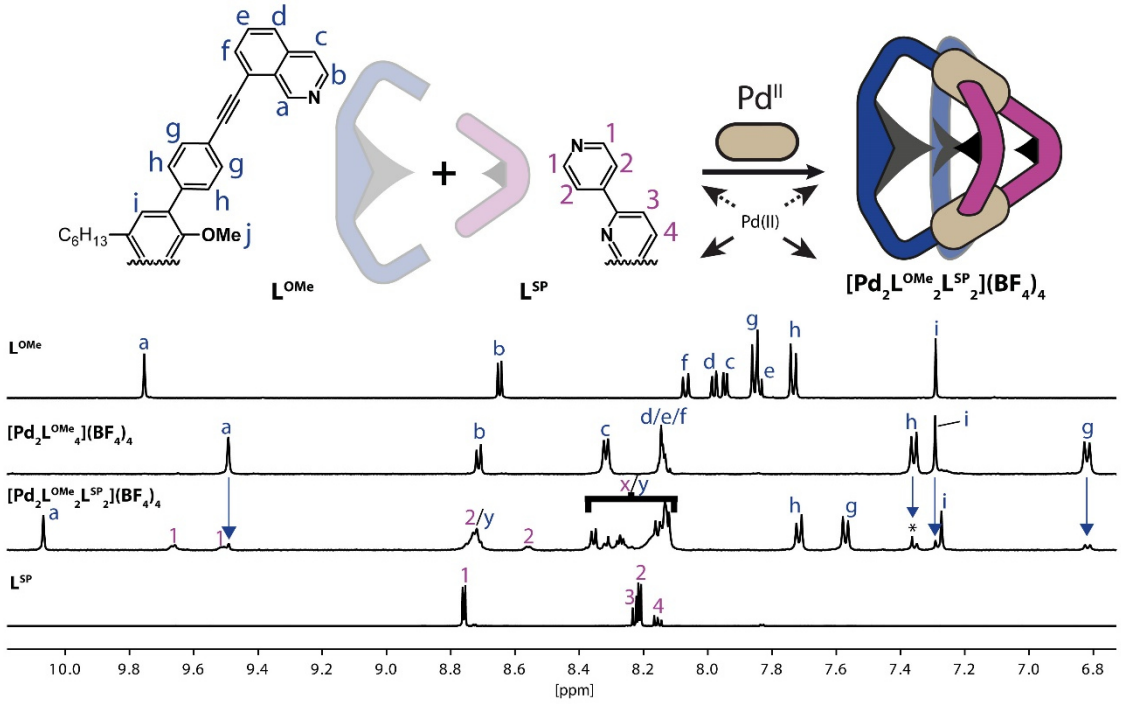

Figure 2.71 Schematic formation of the heteroleptic $[Pd_2L^{OMe}_2L^{SP}_2](BF_4)_4$ cage and comparison of the partial ^{1}H NMR spectra (500 MHz, 298 K, DMSO-d_6) of the free ligands L^{OMe} and L^{SP} with the respective heteroleptic cage.

Synthesis of $[Pd_2\mathbf{L}^{OMe}_2\mathbf{L}^{SP}_2](BF_4)_4$ (figure 2.71) shows the typical pattern for $\mathbf{L}^{OMe}$ ligand observed for all reported $[Pd_2\mathbf{L}^{OMe}_2\mathbf{L}^{X}_2]$-type cages. Moreover, multiple overlapped signals between the area 8.10 ppm-8.40 ppm and 8.68 ppm-8.77 ppm are observed. The overall signal integration does not fit perfectly for the overlapped areas. A reason for this could be the coexistence of the homoleptic cages $[Pd_2\mathbf{L}^{OMe}_4](BF_4)_4$ (~8 % by integration). The amount of such species could not be decreased by addition of more $\mathbf{L}^{SP}$, longer heating or ligand to ligand ratio tuning by ^{1}H NMR titration. ^{1}H NMR measurement at higher temperature was tried to achieve a better signal separation but could not achieve a better distinction (figure 2.72).

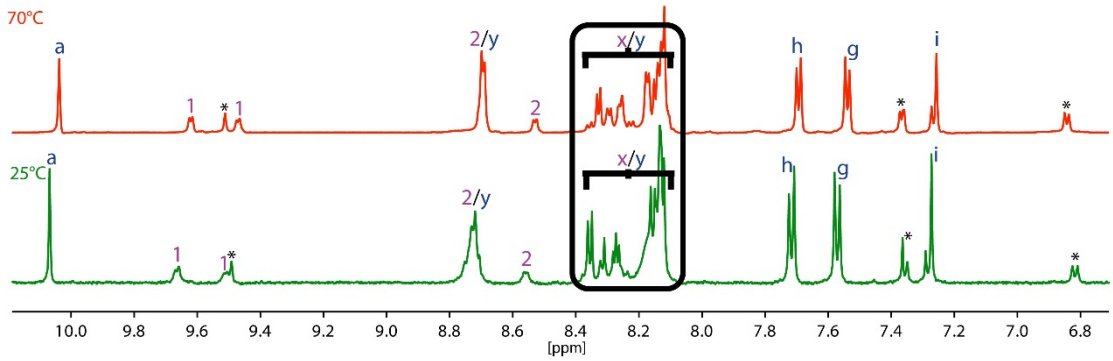

Figure 2.72 ^{1}H NMR spectra (500 MHz, DMSO-d_6) of $[Pd_2L^{OMe}_2L^{SP}_2](BF_4)_4$ at 298 K (25 °C, green) and 343 K (70 °C, red).

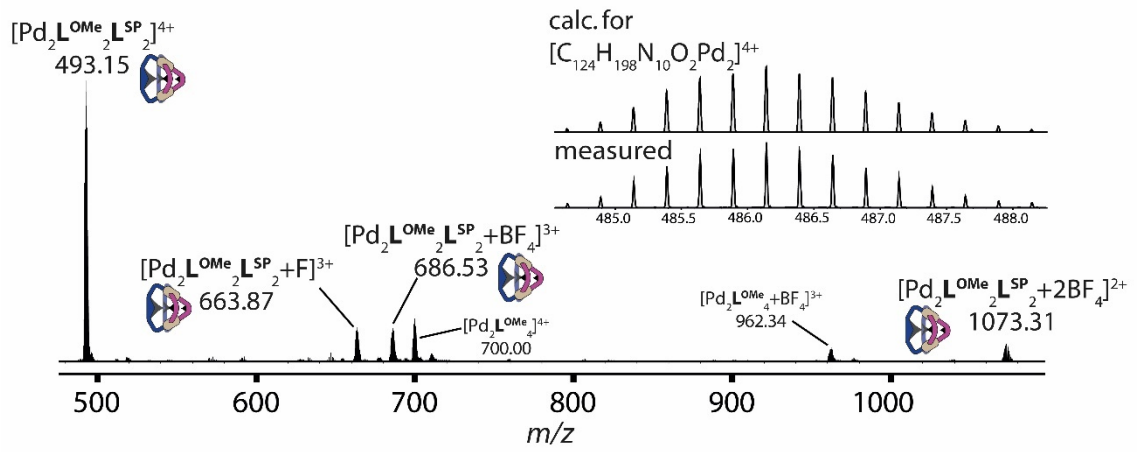

Figure 2.73 ESI mass spectrum of a $[Pd_2\mathbf{L}^{OMe}{}_2\mathbf{L}^{SP}{}_2](BF_4)_4$ sample.

ESI-MS spectrum reported in figure 2.73 displays *m/z* = 493.15 for $[Pd_2\mathbf{L}^{OMe}{}_2\mathbf{L}^{SP}{}_2]^{4+}$, *m/z* = 686.53 for $[Pd_2\mathbf{L}^{OMe}{}_2\mathbf{L}^{SP}{}_2{+}BF_4]^{3+}$, *m/z* = 663.87 for $[Pd_2\mathbf{L}^{OMe}{}_2\mathbf{L}^{SP}{}_2{+}F]^{3+}$ and *m/z* = 1073.31 for the $[Pd_2\mathbf{L}^{OMe}{}_2\mathbf{L}^{SP}{}_2{+}2BF_4]^{2+}$ charged species with fitting isotopic patterns. As already visible inside the ^{1}H NMR spectrum, minor species of $[Pd_2\mathbf{L}^{OMe}{}_4]$ is detected.

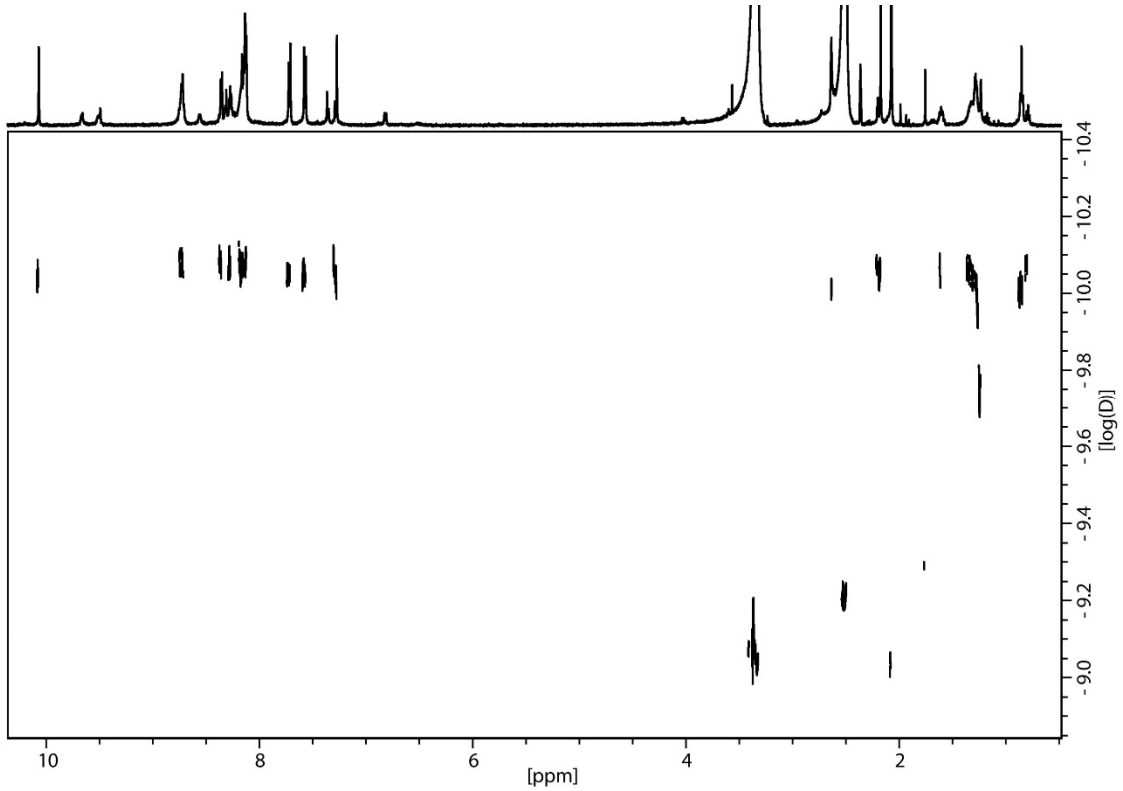

Figure 2.74 ^{1}H DOSY NMR (500 MHz, 298 K, DMSO-d_6) spectrum of the $[Pd_2\mathbf{L}^{OMe}{}_2\mathbf{L}^{SP}{}_2](BF_4)_4$ cage.

^{1}H DOSY NMR measurement shows a $[Pd_2\mathbf{L}^{OMe}{}_2\mathbf{L}^{SP}{}_2](BF_4)_4$ with a hydrodynamic radius of r_H = 12.16 Å calculated from a diffusion coefficient of $D = 9.024 \cdot 10^{-11}$ m^2·s^{-1} in figure

2.12. Again, this shows a similar size to the before reported cages of the $[Pd_2\mathbf{L}^{\mathbf{OMe}}{}_2\mathbf{L}^{\mathbf{X}}{}_2]$-type.

Since the ^{1}H NMR signals in the overlapping regions could not be separated by increasing the temperature, the areas of multiple overlapped signals corresponding to the major species $[Pd_2\mathbf{L}^{\mathbf{OMe}}{}_2\mathbf{L}^{\mathbf{SP}}{}_2](BF_4)_4$ and minor species $[Pd_2\mathbf{L}^{\mathbf{OMe}}{}_4](BF_4)_4$ are marked as x/y respectively. Signal H_a, H_h, H_g and H_i are determined due to shape, signal integration and due to similarity to the before reported cages. First notable is the already know downfield shift of a couple of $\mathbf{L}^{\mathbf{OMe}}$ indicated ^{1}H signals inside this heteroleptic cage against the upfield shift of the same proton signals for $[Pd_2\mathbf{L}^{\mathbf{OMe}}{}_4](BF_4)_4$, showing a supposed less twisted $\mathbf{L}^{\mathbf{OMe}}$. ^{1}H-^{1}H COSY NMR (figure 2.75) measured at 70 °C shows clearer separated signals and cross-peaks for H_1-H_2, with a splitting of the named signals as seen for $[Pd_2\mathbf{L}^{\mathbf{OMe}}{}_2\mathbf{L}^{\mathbf{SNH2}}{}_2](BF_4)_4$ before. This behaviour seems to support a magnetically difference of the H_1 and H_2 protons of the pyridyl groups inside the cage, not seen for the free ligand $\mathbf{L}^{\mathbf{SP}}$. ^{1}H-^{1}H NOESY NMR in figure 2.76 confirms the positions of H_1 and H_2 and additionally the distinction between H_g and H_h.

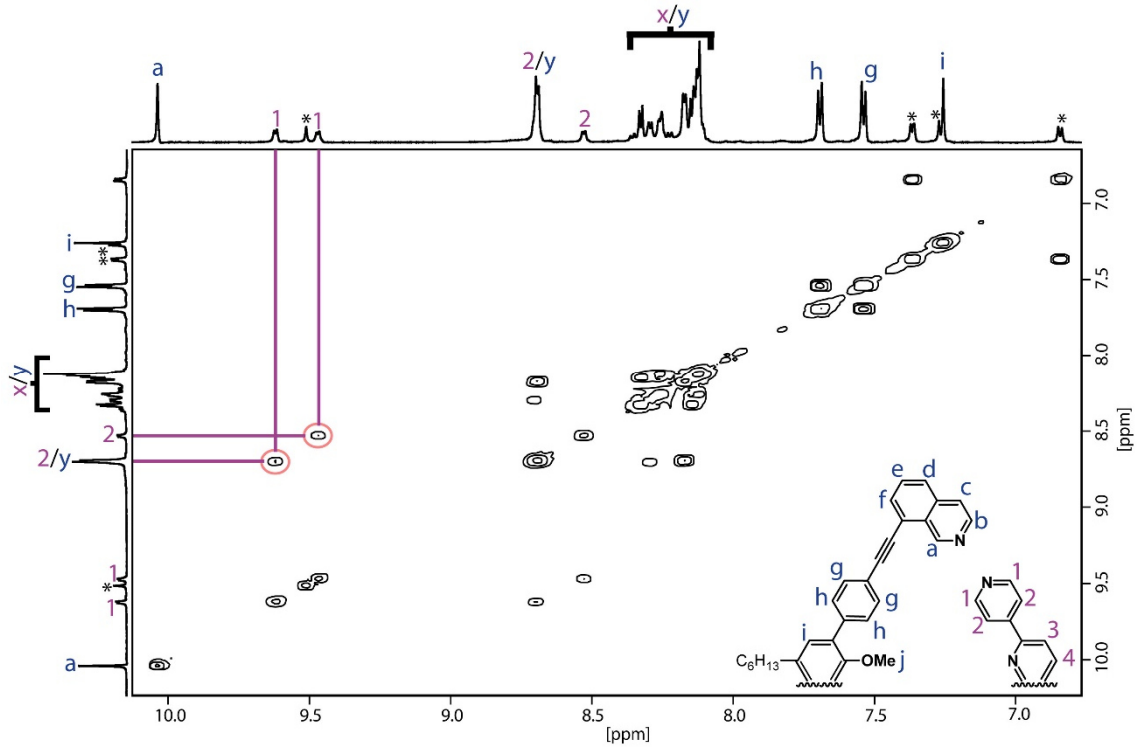

Figure 2.75 Partial ^{1}H-^{1}H COSY NMR (600 MHz, 343 K, DMSO-d_6) spectrum of the $[Pd_2\mathbf{L}^{\mathbf{OMe}}{}_2\mathbf{L}^{\mathbf{SOMe}}{}_2](BF_4)_4$ cage. Cross-peaks between $\mathbf{L}^{\mathbf{SP}}$ protons are marked purple.

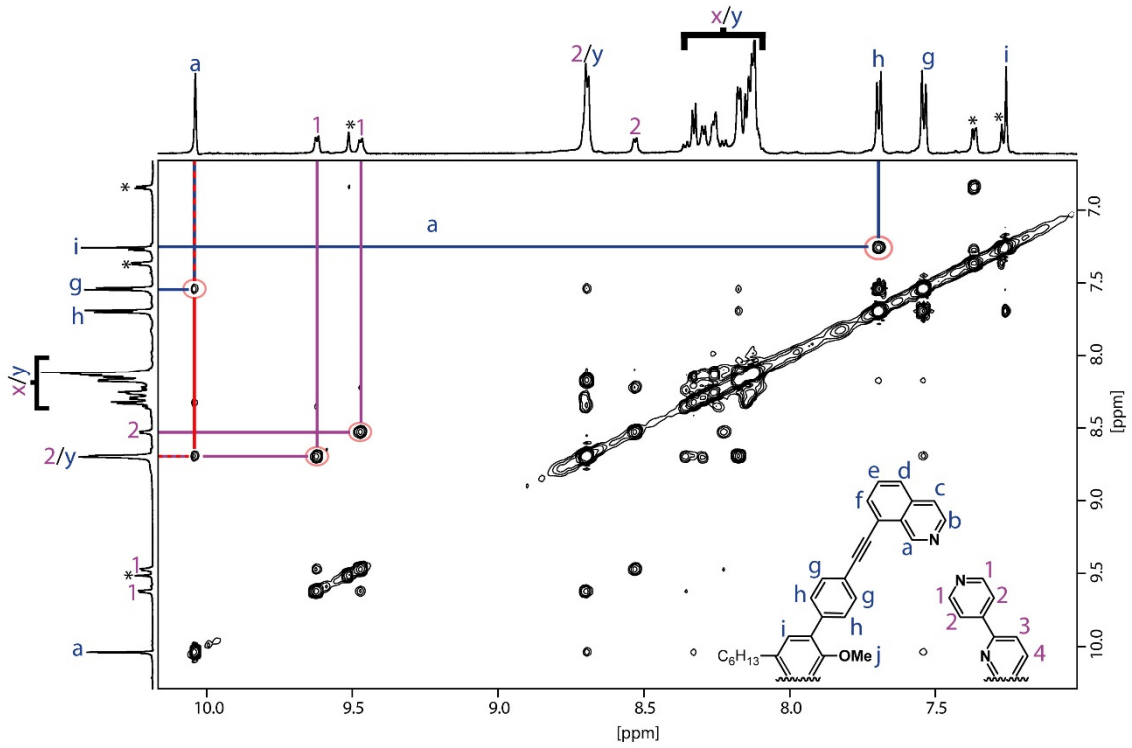

Figure 2.76 Partial ^{1}H-^{1}H NOESY NMR (700 MHz, 343 K, DMSO-d_6) spectrum of the $[Pd_2L^{OMe}{}_2L^{SP}{}_2](BF_4)_4$ cage. Cross-peaks between L^{OMe} protons are marked dark blue; cross-peaks between L^{SP} protons are marked purple; interligand cross-peaks with red.

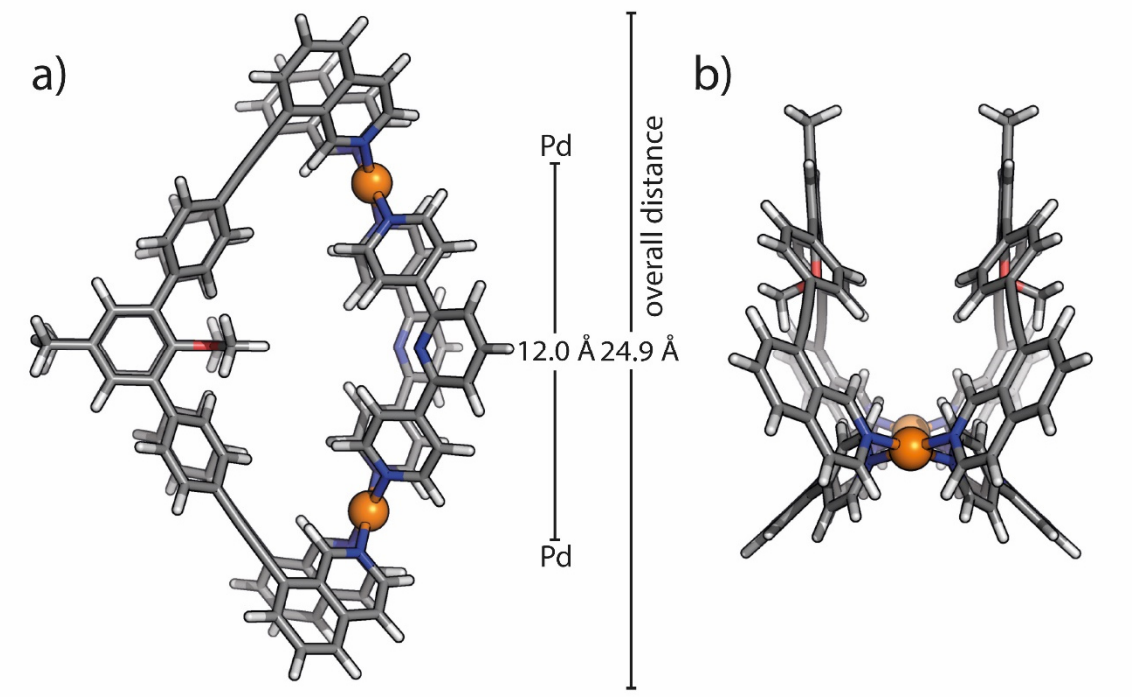

Figure 2.77 DFT (BP86-D4/def2-SVP (def2-TZVP for Pd)) optimized structure of $[Pd_2L^{OMe}{}_2L^{SP}{}_2]^{4+}$ in DMSO with a) top view and b) side view. Sidechains are scaled down to a methyl group to simplify the calculation. Colour scheme: C = dark grey, H = light grey, O = red, N = blue, Pd = orange.

The DFT calculated Pd•••Pd distance of 12.0 Å and 24.9 Å distance for the most distal protons are comparable to structurally related cages (figure 2.77). The calculated r_H = 12.16 Å from the ^{1}H DOSY NMR is in the same magnitude as the calculated size. The different bite angles **L^{SP}** with θ =112° against the θ = 120° angles of other pyridyl ligands (resulting from the heterocyclic pyridine backbone of **L^{SP}** against the phenyl-based backbones of the other used **L^{SX}** ligands) seems not to interfere with the formation of heteroleptic cages. However, the smaller angle of **L^{SP}** could be a reason for a more strained heteroleptic cage with free lone pairs of the pyridine backbone pointing at each other without a chance of turning apart like for other substituent groups (**-OMe** / **-NH$_2$**). This could conclude a hindered free rotation along the pyridyl-phenyl axis (leading to split ^{1}H NMR signals for H_1 and H_2).

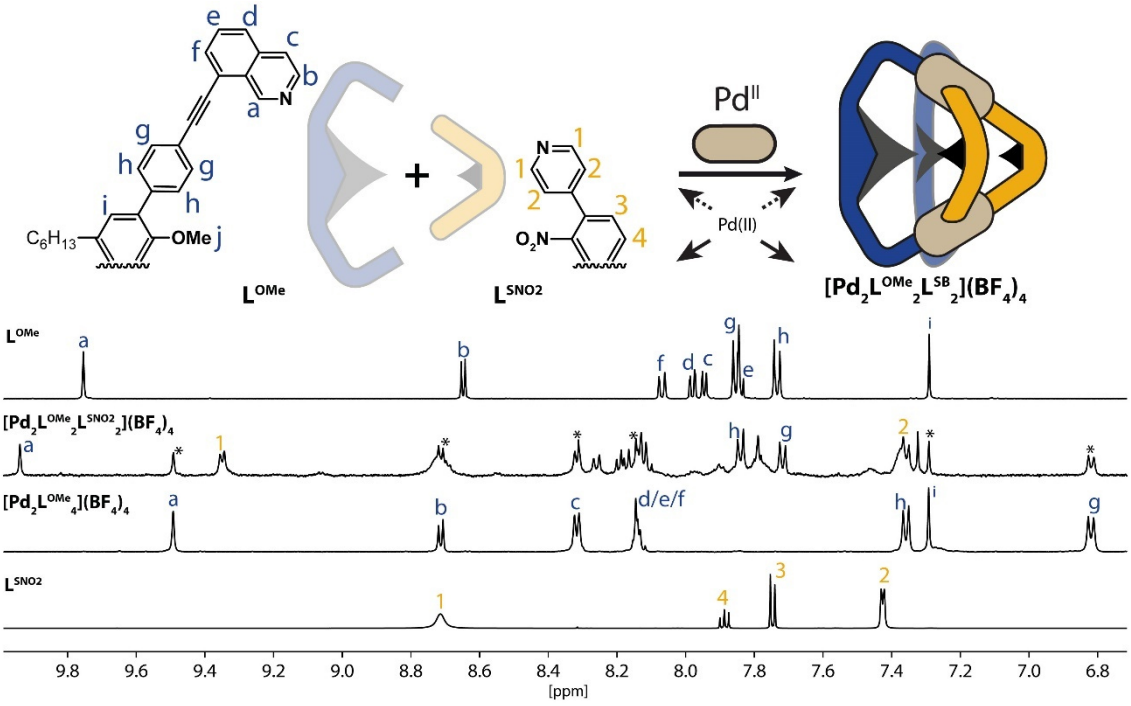

Figure 2.78 Schematic formation of the heteroleptic [Pd$_2$L$^{OMe}_2$L$^{SP}_2$](BF$_4$)$_4$ cage and comparison of the partial ^{1}H NMR spectra (500 MHz, 298 K, DMSO-d$_6$) of the free ligands L^{OMe} and L^{SNO2} with resulted mixture of supramolecular structures after adding Pd^{2+}.

As the last modification **L^{SNO2}** was synthesized and investigated for the formation of [Pd$_2$**L$^{OMe}_2$L$^{SNO2}_2$**](BF$_4$)$_4$. The ^{1}H NMR spectrum is shown in figure 2.78, presenting an incomplete formation. Adding more **L^{SNO2}**, longer heating and an exact ligand titration for an 1:1 ratio before Pd(II) addition did not lead to a clean species without [Pd$_2$**L$^{OMe}_4$**]-cage. However, new signals like the **L^{OMe}** signals in the related heteroleptic cages can be identified, leading to already many times mentioned less twisting of **L^{OMe}** inside the cage.

ESI-MS measurements in figure 2.79 clearly shows the formation of [Pd$_2$**L$^{OMe}_2$L$^{SNO2}_2$**] cage with *m/z* = 515.14 for [Pd$_2$**L$^{OMe}_2$L$^{SNO2}_2$**]$^{4+}$ and *m/z* = 1117.29 for

$[Pd_2\mathbf{L}^{OMe}{}_2\mathbf{L}^{SNO2}{}_2+2BF_4]^{2+}$. In addition, prominent peaks at *m/z* = 700.00, 962.34 and 1487.00 corresponding to $[Pd_2\mathbf{L}^{OMe}{}_4]^{4+}$, $[Pd_2\mathbf{L}^{OMe}{}_4+BF_4]^{3+}$ and $[Pd_2\mathbf{L}^{OMe}{}_4+2BF_4]^{2+}$ are observed.

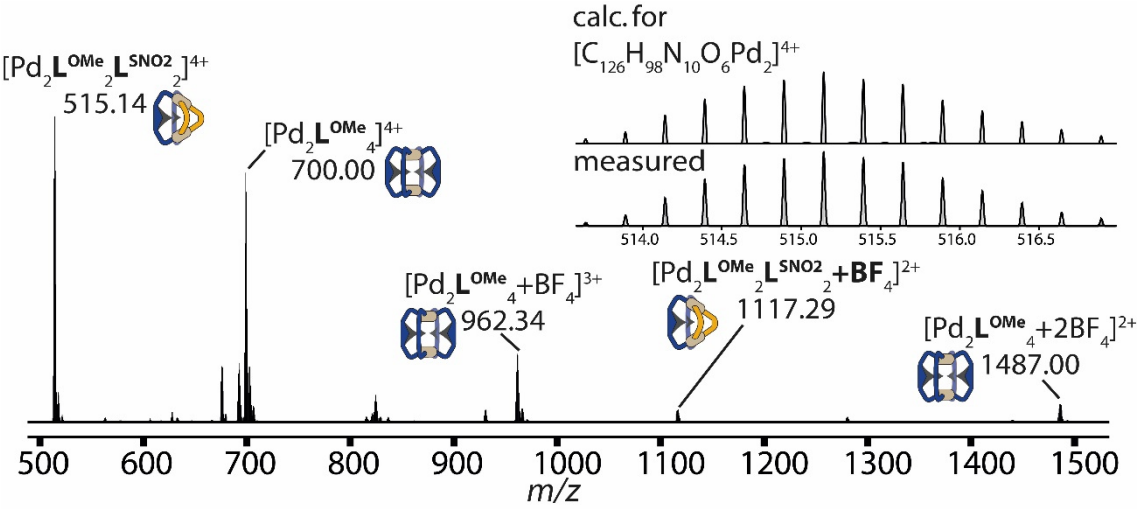

Figure 2.79 ESI mass spectrum of a $[Pd_2\mathbf{L}^{OMe}{}_2\mathbf{L}^{SNO2}{}_2](BF_4)_4$ sample.

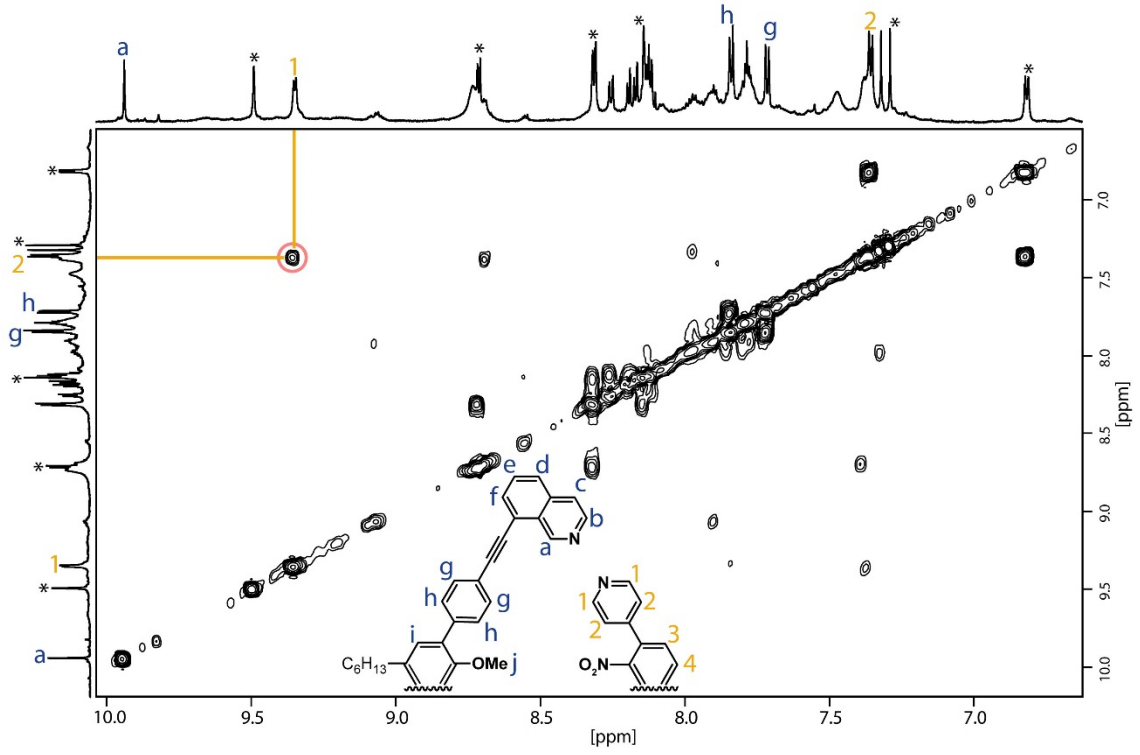

Figure 2.80 Partial ^{1}H-^{1}H COSY NMR (600 MHz, 298 K, DMSO-d_6) spectrum of the resulted mixture of supramolecular structures after adding Pd^{2+}. Cross-peaks between $\mathbf{L}^{SNO2}$ protons are marked purple.

^{1}H-^{1}H COSY and ^{1}H-^{1}H NOESY NMR experiments (figure 2.80 and figure 2.81) are hindered by strong signal overlaps. The most important recognition is given by the ^{1}H-^{1}H NOESY NMR with H_1-H_2 and H_1-H_a / H_1-H_G interligand cross-peaks.

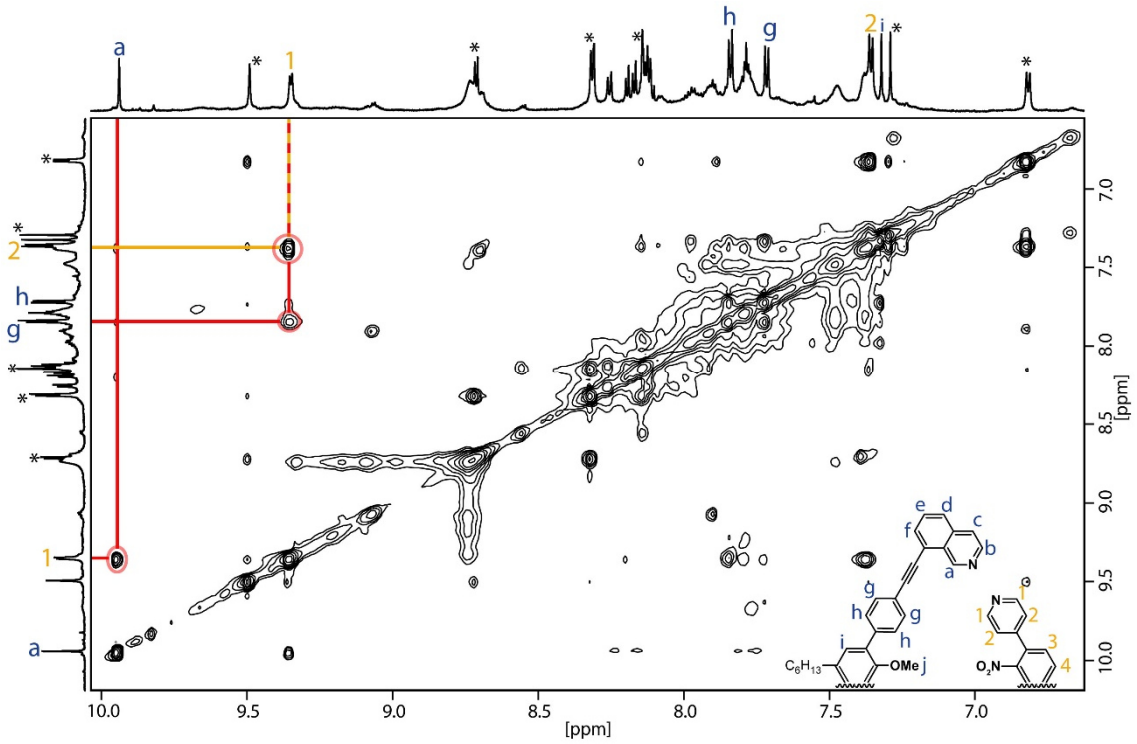

Figure 2.81 Partial ^{1}H-^{1}H NOESY NMR (700 MHz, 343 K, DMSO-d_6) spectrum of the resulted mixture of supramolecular structures after adding Pd^{2+}. Cross-peaks between L^{SNO2} protons are marked purple; interligand cross-peaks with red.

The DFT calculation shown in figure 2.81 gives a visualization of the geometric optimized structure. The Pd•••Pd distance of 12.5 Å, with a distance of 24.4 Å for the most distal protons, is comparable with the calculated values for the related heteroleptic cages. Most interestingly, the **-NO_2** groups of the L^{SNO2} ligand are pointing to each other, leading to a 'turn away movement' of the ligands induced by the repulsion of the numerous lone electron pairs. This structural feature could be responsible for the worst [$Pd_2L^{OMe}{}_2L^{SX}{}_2$]-type cage formation by the combination of L^{OMe} with L^{SNO2} seen in this work. This is indicating the steric limitations for the modification of a geometric mostly identic but chemical different system. Nevertheless, the [$Pd_2L^{OMe}{}_2L^{SNO2}{}_2$]-cage can be formed and is found to be in equilibrium between the correspondent homoleptic species similar to what was observed for the [$Pd_2L^{OMe}{}_2L^{SC4}{}_2$]-cage.

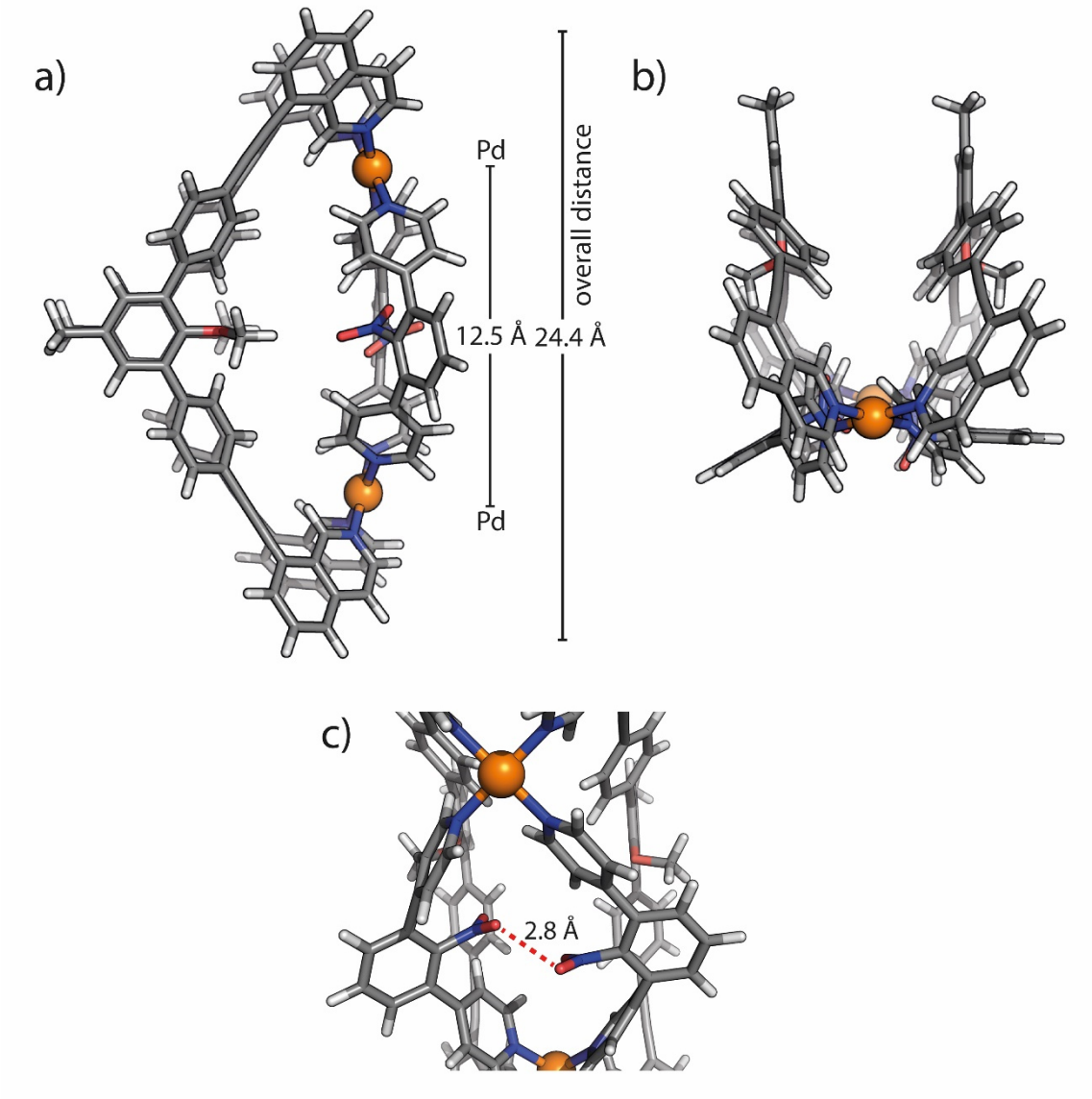

Figure 2.82 DFT (BP86-D4/def2-SVP (def2-TZVP for Pd)) calculated geometry optimization of $[Pd_2L^{OMe}{}_2L^{SNO2}{}_2]^{4+}$ in DMSO with a) top view, b) side view and, c) closer view on the nitro groups. Sidechains are scaled down to a methyl group to simplify the calculation. Colour scheme: C = dark grey, H = light grey, O = red, N = blue, Pd = orange.

Additionally, ion mobility was measured for all $[Pd_2L^{OMe}{}_2L^{SX}{}_2]$-type cages and their similar size and structural properties was shown. To obtain comparable data, for all cages the peak corresponding to the 3+ charged species was analysed and the dynamic behaviour of the cage assemblies in the gas phase could be highlighted.

Table 1 Calculated collisional cross sections tCCS with standard deviation σ and measrued eCCS in Å².

Measured species	tCCS (Å²)	σ (Å²)	eCCS (Å²)
$[Pd_2L^{OMe}{}_2L^{SB}{}_2+BF_4]^{3+}$	581	10	605.1, 617.1
$[Pd_2L^{OMe}{}_2L^{SNH2}{}_2+BF_4]^{3+}$	584	11	613.7
$[Pd_2L^{OMe}{}_2L^{SOMe}{}_2+BF_4]^{3+}$	588	11	593.6, 604.0, 611.1
$[Pd_2L^{OMe}{}_2L^{SOH}{}_2+BF_4]^{3+}$	587	8	606.5, 615.7
$[Pd_2L^{OMe}{}_2L^{SP}{}_2+BF_4]^{3+}$	584	9	613.9

2.6 Heteroleptic $[Pd_2L^{OMe}{}_2L^{SB}L^{SNO2}]$-Cage

Until now it was discussed how structural modifications of the chosen substituents effect the cages properties. From all the reported observations came the idea of combining two differently substituted pyridyl ligands in trans position to two L^{OMe} ligands in the same heteroleptic assembly to combine the approach of shape complementarity and endohedral modifications. Indeed, $[Pd_2L^{OMe}{}_2L^{SX}L^{SY}]$-type cage could be achieved. In this chapter, the most successful attempt will be discussed.

The used ligands, besides L^{OMe}, are L^{SNO2} and L^{SB}. This combination was chosen because of the described effect of lone pair repulsion between two L^{SNO2} inside $[Pd_2L^{OMe}{}_2L^{SB}{}_2](BF_4)_4$, leading to the least favourable formation of heteroleptic species reported in this work. However, the **$-NO_2$** group is also the most sterically demanding moiety in the cage environment and L^{SB} is the best counterpart since it only has a hydrogen atom pointing inside the cavity and can give to the **$-NO_2$** group in close proximity enough space inside the cavity.

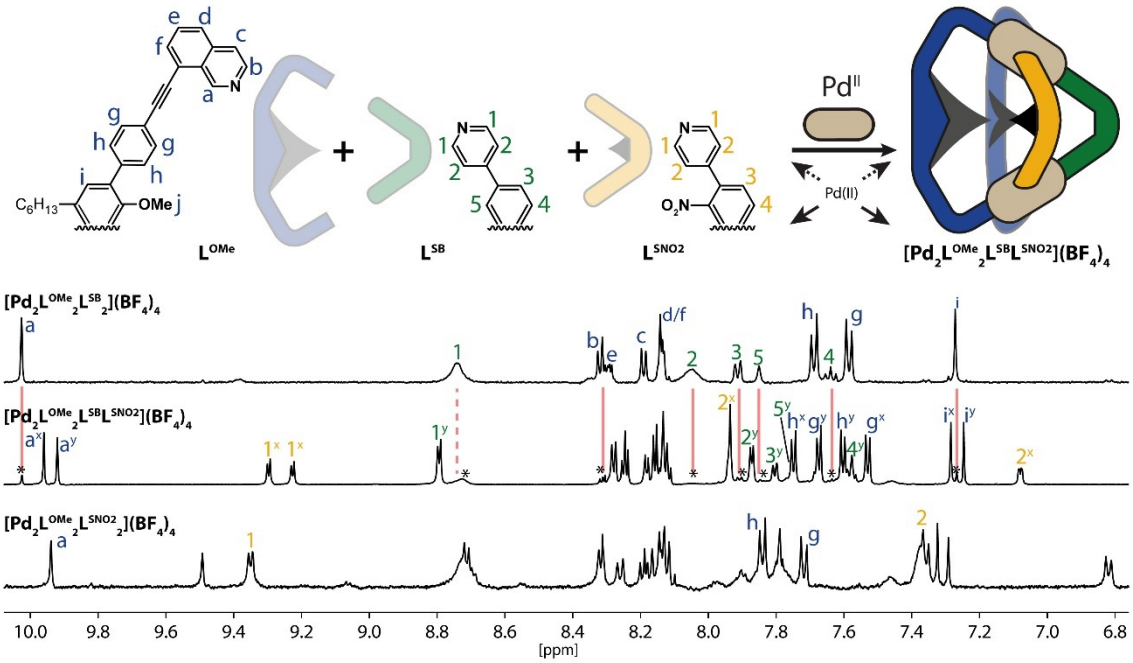

Figure 2.83 Schematic formation of the heteroleptic $[Pd_2L^{OMe}{}_2L^{SB}L^{SNO2}](BF_4)_4$ cage and comparison of the partial ^1H NMR spectra (500 MHz, 298 K, DMSO-d_6) of $[Pd_2L^{OMe}{}_2L^{SB}L^{SNO2}](BF_4)_4$ with $[Pd_2L^{OMe}{}_2L^{SB}{}_2](BF_4)_4$ and the mixture of supramolecular species resulting after trying to synthesise $[Pd_2L^{OMe}{}_2L^{SNO}{}_2](BF_4)_4$.

The cage preparation was carried out similarly to the ones reported for $[Pd_2L^{OMe}{}_2L^{SX}{}_2]$-type cages, but in a 1:0.5:0.5:1 ratio of L^{OMe}:L^{SB}: L^{SNO2}: $[Pd(CH_3CN)_4(BF_4)_2]$ to give solutions in the aimed 0.7 mM concentration of $[Pd_2L^{OMe}{}_2L^{SB}L^{SNO2}](BF_4)_4$. After heating for 10 min, the ^1H NMR spectrum was measured. It shows nicely defined new signals

differing from the respective $[Pd_2\mathbf{L}^{\mathbf{OMe}}{}_2\mathbf{L}^{\mathbf{SX}}{}_2]$-type cages, in figure 2.83. Nevertheless, small signals of $[Pd_2\mathbf{L}^{\mathbf{OMe}}{}_2\mathbf{L}^{\mathbf{SB}}{}_2](BF_4)_4$ are visible but no specific ^{1}H signals for $[Pd_2\mathbf{L}^{\mathbf{OMe}}{}_2\mathbf{L}^{\mathbf{SNO2}}{}_2](BF_4)_4$ or $[Pd_2\mathbf{L}^{\mathbf{OMe}}{}_4](BF_4)_4$, showing the more favourable combination of $[Pd_2\mathbf{L}^{\mathbf{OMe}}{}_2\mathbf{L}^{\mathbf{SB}}\mathbf{L}^{\mathbf{SNO2}}](BF_4)_4$ over $[Pd_2\mathbf{L}^{\mathbf{OMe}}{}_2\mathbf{L}^{\mathbf{SNO2}}{}_2](BF_4)_4$ due to the predicted less steric hinderance. Like for other cages, it was tried to reduce the proportion of $[Pd_2\mathbf{L}^{\mathbf{OMe}}{}_2\mathbf{L}^{\mathbf{SB}}{}_2](BF_4)_4$ to zero or at least to a minimum by longer heating or fine tuning of the ligand to ligand ratio. Unfortunately and like for other reported cases, this does not lead to a cleaner species, giving constant 8 % by ^{1}H signal integration of $[Pd_2\mathbf{L}^{\mathbf{OMe}}{}_2\mathbf{L}^{\mathbf{SB}}{}_2](BF_4)_4$ inside every sample as an equilibrium.

To make sure that the new ^{1}H signals belong to one new species and in best case to the desired $[Pd_2\mathbf{L}^{\mathbf{OMe}}{}_2\mathbf{L}^{\mathbf{SB}}\mathbf{L}^{\mathbf{SNO2}}](BF_4)_4$ cage, an ESI-MS measurement was carried out, leading to a promising clean spectrum shown in figure 2.84. The analysis ultimately indicates the $[Pd_2\mathbf{L}^{\mathbf{OMe}}{}_2\mathbf{L}^{\mathbf{SB}}\mathbf{L}^{\mathbf{SNO2}}]$ arrangement as $[Pd_2\mathbf{L}^{\mathbf{OMe}}{}_2\mathbf{L}^{\mathbf{SB}}\mathbf{L}^{\mathbf{SNO2}}]^{4+}$ with *m/z* = 503.89, $[Pd_2\mathbf{L}^{\mathbf{OMe}}{}_2\mathbf{L}^{\mathbf{SB}}\mathbf{L}^{\mathbf{SNO2}}{+}F]^{3+}$ with *m/z* = 678.19, $[Pd_2\mathbf{L}^{\mathbf{OMe}}{}_2\mathbf{L}^{\mathbf{SB}}\mathbf{L}^{\mathbf{SNO2}}{+}BF_4]^{3+}$ with *m/z* = 700.86 and $[Pd_2\mathbf{L}^{\mathbf{OMe}}{}_2\mathbf{L}^{\mathbf{SB}}\mathbf{L}^{\mathbf{SNO2}}{+}2BF_4]^{2+}$ with *m/z* = 1094.79. Fluoride counterions are detected as already seen before for $[Pd_2\mathbf{L}^{\mathbf{OMe}}{}_2\mathbf{L}^{\mathbf{SOMe}}{}_2{+}2BF_4]^{2+}$, due to decomposition of BF_4^- anions. Only a small mass peak for $[Pd_2\mathbf{L}^{\mathbf{OMe}}{}_2\mathbf{L}^{\mathbf{SB}}{}_2]^{4+}$ with *m/z* = 492.65 as a minor species is visible.

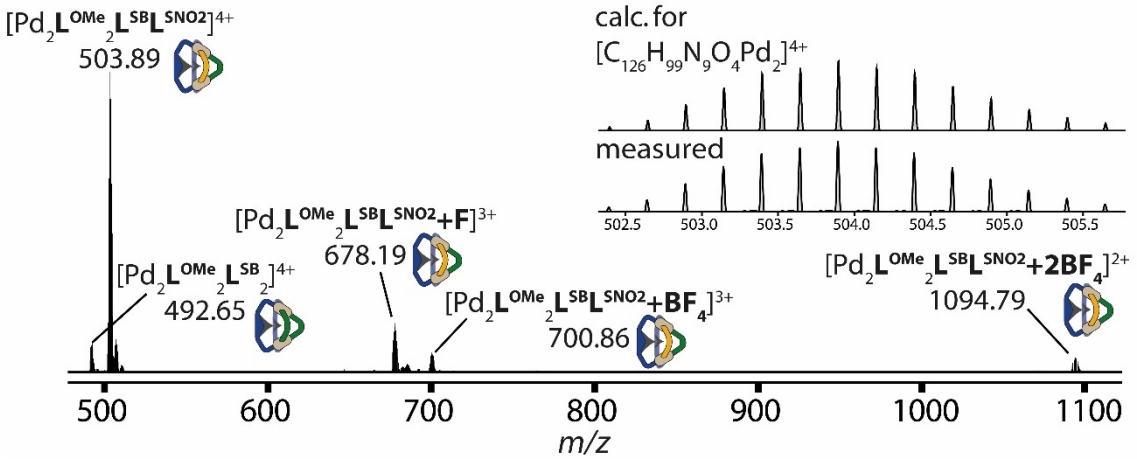

Figure 2.84 ESI mass spectrum of a $[Pd_2\mathbf{L}^{\mathbf{OMe}}{}_2\mathbf{L}^{\mathbf{SB}}\mathbf{L}^{\mathbf{SNO2}}](BF_4)_4$ sample.

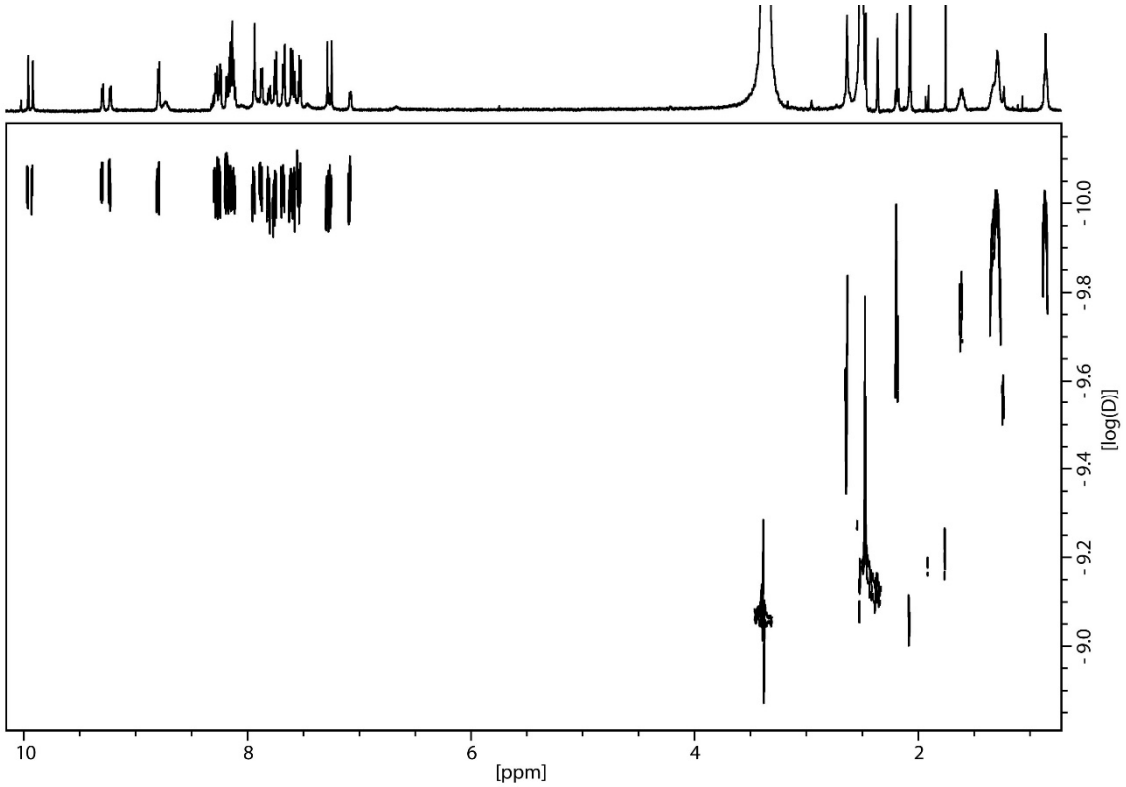

Figure 2.85 ^{1}H DOSY NMR (500 MHz, 298 K, DMSO-d_6) spectrum of the $[Pd_2L^{OMe}{}_2L^{SB}L^{SNO2}](BF_4)_4$.

^{1}H DOSY NMR measurement was performed to obtain better insight into the present cage solution. The spectra in figure 2.85 shows a nice defined main species with a diffusion coefficient of D = 8.9312 · 10^{-11} $m^2 \cdot s^{-1}$ giving a hydrodynamic radius of r_H = 12.28 Å, indicating the same size as measured for the $[Pd_2\mathbf{L}^{OMe}{}_2\mathbf{L}^{SX}{}_2]$-type cages.

With the proof of the formation for the $[Pd_2\mathbf{L}^{OMe}{}_2\mathbf{L}^{SB}\mathbf{L}^{SNO2}]$-cage, the demanding ^{1}H signal assignment needs to be done. Not only two different pyridyl based ligands with a respective ^{1}H signal set are included in this cage. Additionally, the chemical environment of each $\mathbf{L}^{OMe}$ is different, leading to ^{1}H signal series of two distinguishable $\mathbf{L}^{OMe}$ ligands. In total, signals of four magnetic different ligands need to be assigned. Fortunately, the before made experiences are helping. Similarities of the spectra are helping through this process, with estimated shift and the shape of specific proton signals.

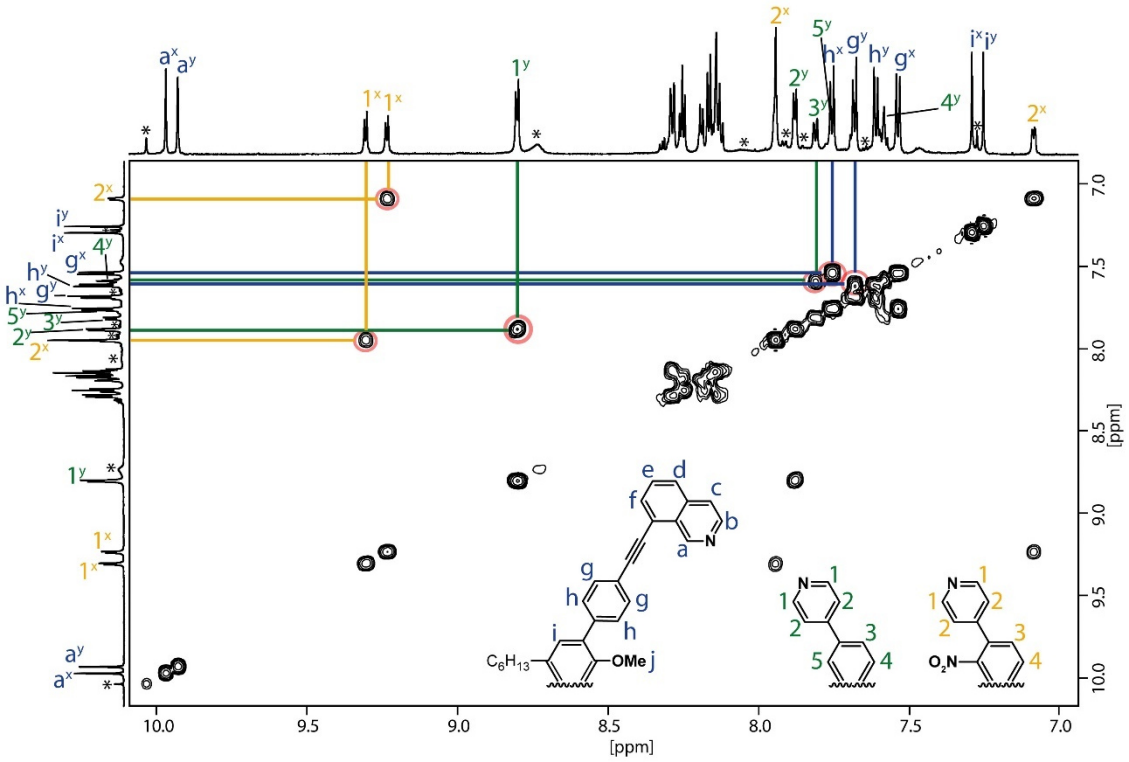

Figure 2.86 Partial ^{1}H-^{1}H COSY NMR (700 MHz, 298 K, DMSO-d_6) spectrum of the $[Pd_2L^{OMe}{}_2L^{SB}L^{SNO2}](BF_4)_4$ cage. *-marked signals indicate $[Pd_2L^{OMe}{}_2L^{SB}{}_2](BF_4)_4$ as a minor species. L^{OMe} ligands are distinguished with superscript x and y; L^{SNO2} yellow with superscript x; L^{SB} with superscript y.

The assignment starts with the ^{1}H-^{1}H COSY NMR experiment presented in figure 2.86. $\mathbf{L^{OMe}}$ ligands are marked with a superscript x or y, both in the same dark blue colour. As before, $\mathbf{L^{SNO2}}$ is labelled in yellow with superscript x for writing the analysis down and $\mathbf{L^{SB}}$ in dark green with superscript y in the same way to distinguish both ligands inside the spectra and written text. Cross-peaks for H_{gx}-H_{hx} and H_{gy}-H_{hy} are visible, with H_g and H_h determinate by shape, signal integration, shift and experience from before analysed heteroleptic structures in this work. Nevertheless, these signals are only distinguishable by ^{1}H-^{1}H NOESY NMR. The division to x or y will lead to distinguishable $\mathbf{L^{OMeX}}$ and $\mathbf{L^{OMeY}}$ ligands. ^{1}H-^{1}H COSY NMR cross-peaks are given two times for split H_{1x}-H_{2x} signals of $\mathbf{L^{SNO2}}$, within the assumption of a hindered pyridyl-phenyl axis due to the steric hinderance of the **-NO_2** and later completed assignment of the ^{1}H system of the $\mathbf{L^{SB}}$ ligand, where H_{1x}-H_{2x} is not a part of. H_{1y}-H_{2y} and H_{3y}-H_{4y} cross-peaks are retrospective assigned by ^{1}H-^{1}H NOESY NMR cross-peaks (figure 2.87) of these signals with additional H_{2y}-H_{5y} cross-peak to address all $\mathbf{L^{SB}}$ protons inside the ^{1}H spectra (figure 2.87). The H_{2y}-H_{5y} cross-peak could be easily seen as a crow-peak of H_{2y} with H_{hx}. However, H_{2x} signal shows a small shoulder and a signal integration of 5 instead of 4 H_{2x} protons for $\mathbf{L^{OMeX}}$. Only this little hint makes it possible to assign as many protons as possible. Clear determination of H_h and H_g for the $\mathbf{L^{OMeX}}$ and $\mathbf{L^{OMeY}}$ systems are given by

H_{hx}-H_{ix} / H_{hy}-H_{iy} and H_{gx}-H_{ax} / H_{gy}-H_{ay}. By ^{1}H-^{1}H COSY NMR **L^{SNO2}** assigned signals are verified by ^{1}H-^{1}H NOESY NMR. Due to multiple overlapping, it is not possible to address the signals between 8.10-8.30 ppm. Finally, interligand cross-peaks of H_{1x}-H_{ay} indicates the direct neighbouring of **L^{SNO2}** to **L^{OMeY}** and H_{1y}-H_{ax} of **L^{SB}** to **L^{OMeX}**.

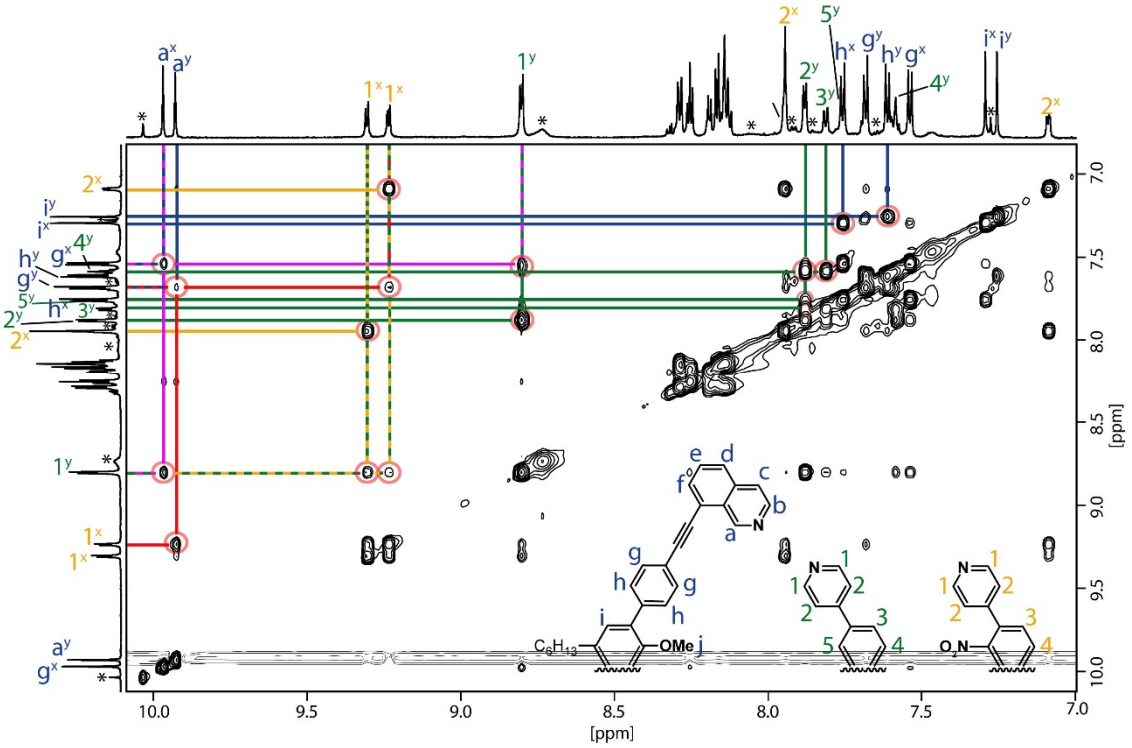

Figure 2.87 Partial ^{1}H-^{1}H NOESY NMR (700 MHz, 289 K, DMSO-d_6) spectrum of the [Pd$_2$L$^{OMe}_2$L^{SB}L^{SNO2}](BF$_4$)$_4$ cage. *-marked signals indicate [Pd$_2$L$^{OMe}_2$L$^{SB}_2$](BF$_4$)$_4$ as a minor species. L^{OMe} ligands are distinguished with superscript x and y; L^{SNO2} yellow with superscript x; L^{SB} with superscript y. Interligand cross-peaks are marked in red and pink.

Due to the lack of an X-ray structure determination of [Pd$_2$**L$^{OMe}_2$L^{SB}L^{SNO2}**](BF$_4$)$_4$ cage, a DFT model was calculated to estimate the structural arrangement of the cage and is reported in figure 2.88. The Pd•••Pd distance of 12.6 Å and a distance of the most distal hydrogen atoms of 25.2 Å is in the same order of magnitude as for [Pd$_2$**L$^{OMe}_2$L$^{SX}_2$**]-cages as expected. Most interestingly, the arrangement of the **L^{SNO2}** looks nice aligned with an inner pointing -**NO$_2$** group, showing enough cavity space thanks to the phenyl substituent as part of the backbone of **L^{SB}**. The arrangement of the cage corresponds to the arrangements of the [Pd$_2$**L$^{OMe}_2$L$^{SB}_2$**]-, [Pd$_2$**L$^{OMe}_2$L$^{SNH2}_2$**]- and [Pd$_2$**L$^{OMe}_2$L$^{SOMe}_2$**]-cages, indicating a less strained system due to the ability of the ligands to distort along the ligand axis as seen in the DFT calculations.

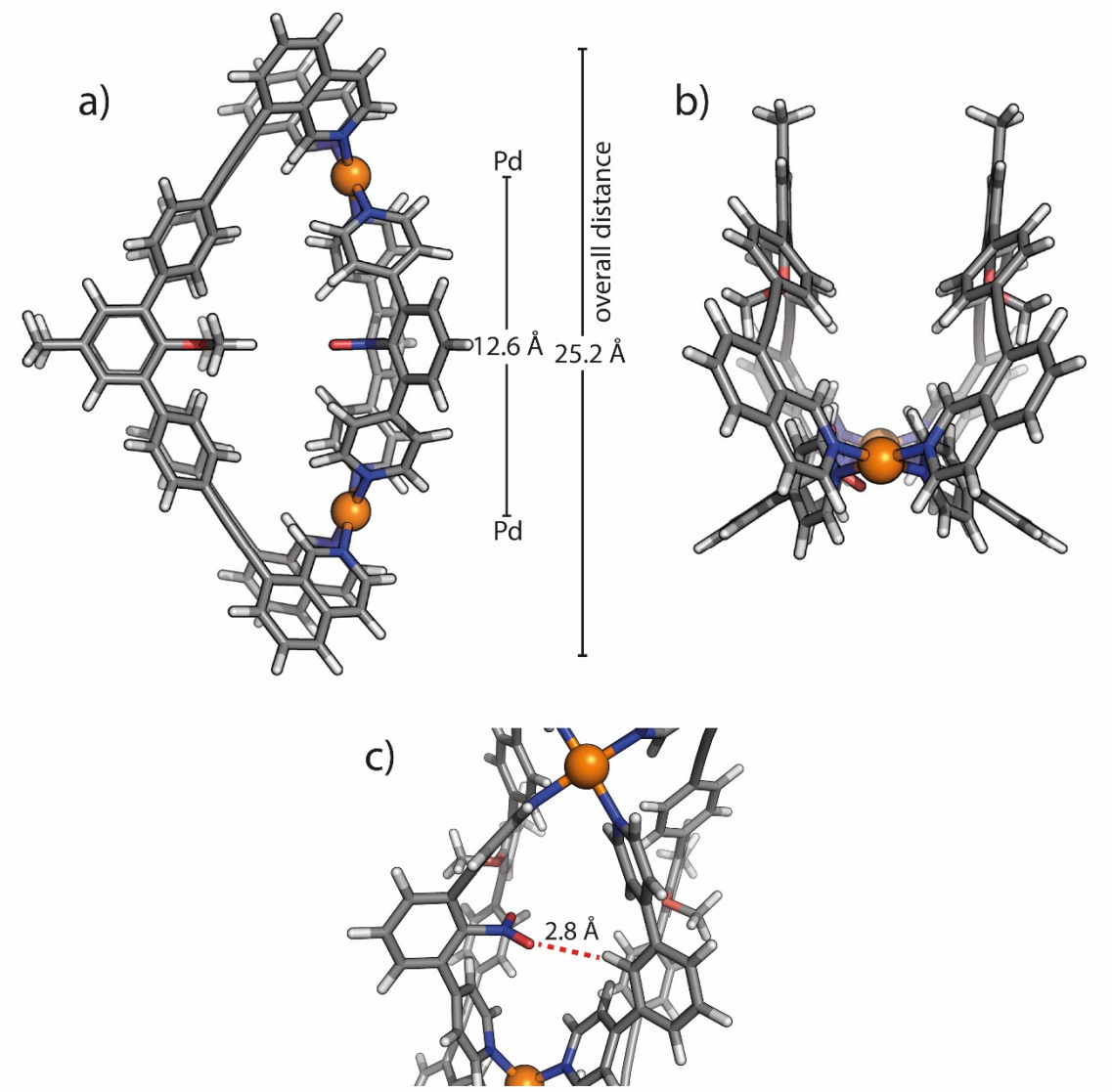

Figure 2.88 DFT (BP86-D4/def2-SVP (def2-TZVP for Pd)) calculated structure of $[Pd_2L^{OMe}{}_2L^{SB}L^{SNO2}]^{4+}$ in DMSO with a) top view, b) side view and, c) closer view on the nitro group. Sidechains are scaled down to a methyl group to simplify the calculation. Colour scheme: C = dark grey, H = light grey, O = red, N = blue, Pd = orange.

2.7 Elongated Quinoline-based Ligand

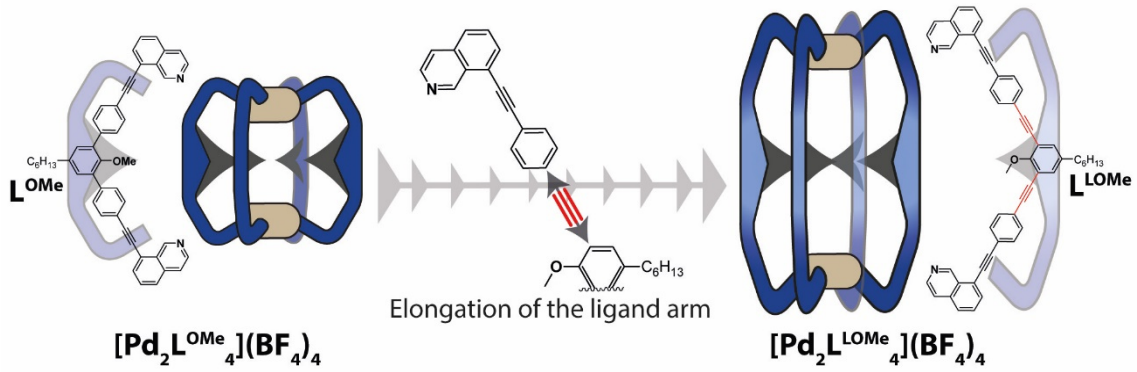

Figure 2.89 Schematic description of the elongation of the L^{OMe} ligand to form L^{LOMe} and the respective homoleptic cage.

As discussed, the small distance between the inner pointing ligands substituents can have a great influence on the overall cage structure and cage formation. Moreover, the choice of the solvent plays an important role to determine the outcome structure. By increasing the length of linker between the backbone and donor groups of a ligand, a proof of the relative importance of the ligand-ligand interaction over the solvent influence could be addressed. As a first step, an elongated $\mathbf{L^{OMe}}$ ligand is introduced by adding one additional alkynyl bridge on each side of the backbone to give $\mathbf{L^{LOMe}}$ (**L**igand **L**onger with **-OMe** group; figure 2.89).

The synthesis of $\mathbf{L^{LOMe}}$ (figure 2.90) started with compound **7** (8-((4-ethynylphenyl)ethynyl) isoquinoline) which was already introduced as a part of the $\mathbf{L^{OMe}}$ synthesis. Sonogashira coupling with ethynyltrimethylsilane gave 8-((4-((trimethylsilyl)ethynyl)phenyl) ethynyl)isoquinoline in a 89 % yield and a deprotection with 86 % yield gave 8-((4-ethynylphenyl)ethynyl)isoquinoline. The final Sonogashira coupling was carried out with N,N-Diisopropylethylamine (DIPEA) and DMF at 120 °C overnight, to give $\mathbf{L^{LOMe}}$ in a 18 % yield. The ligand was purified by GPC before further usage.

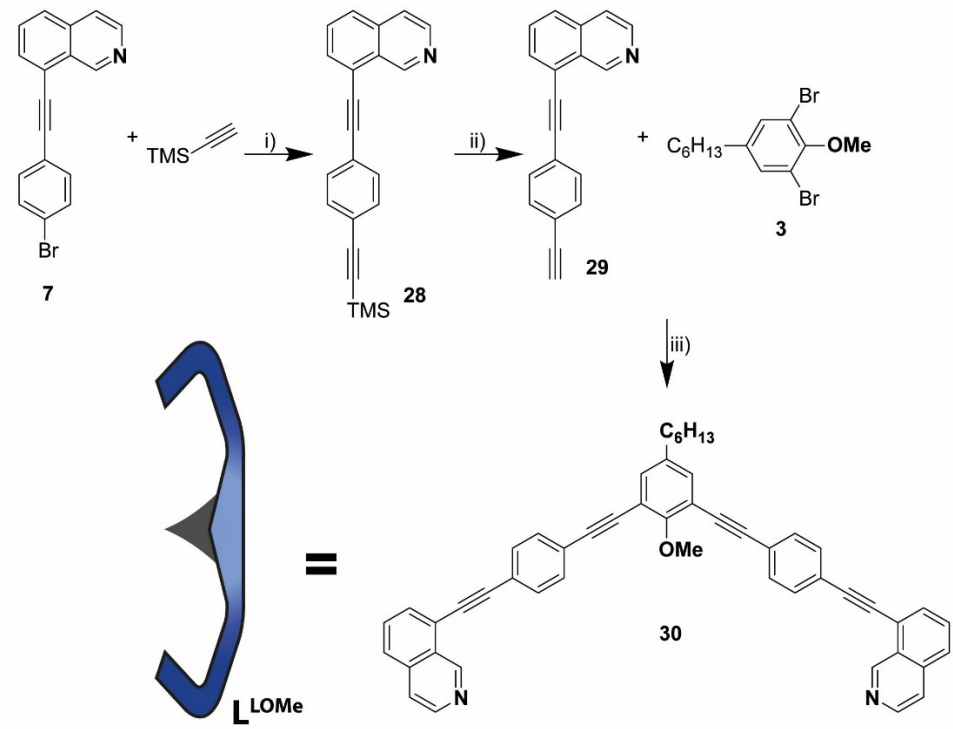

Figure 2.90 Synthesis of L^{LOMe} beginning with already for L^{OMe} synthesised compound 7$Pd(PPh_3)_2Cl_2$, CuI, Et_3N, THF, 65 °C, overnight; ii) K_2CO_3, MeOH, rt, 4 h; iii) $Pd(PPh_3)_2Cl_2$, CuI, DIPEA, DMF, 120 °C, overnight.

Cage formation was performed as already reported for the homoleptic cages in the previous sections, mixing 240 µl of 7 mM $\mathbf{L^{LOMe}}$ stock solution in CD_3CN or DMSO-d_6 with 300 µl pure solvent and 60 µl 15 mM $[Pd(CH_3CN)_4(BF_4)_2]$ stock solution in respective solvent. The mixtures were heated for 10 min to give a 0.7 mM cage solution for both solvents.

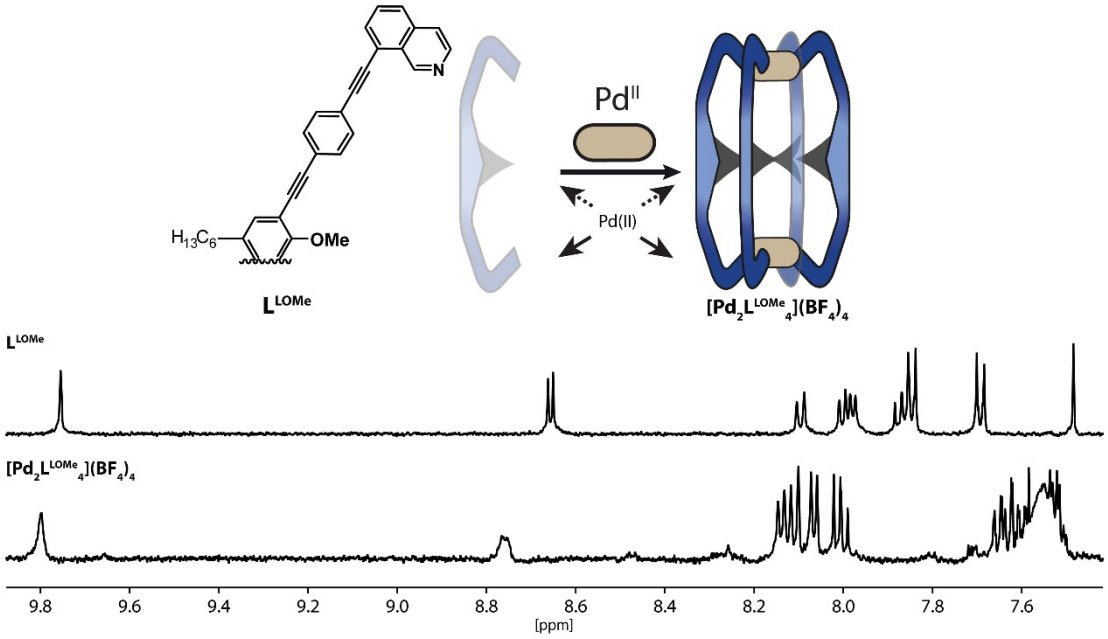

Figure 2.91 Schematic formation of the homoleptic $[Pd_2L^{LOMe}_4](BF_4)_4$ cage and partial ^1H NMR spectra (500 MHz, 298 K, CD_3CN) of the free ligand L^{LOMe}.

Figure 2.91 shows the ^1H spectra of the pure ligand and the formed homoleptic cage in CD_3CN. The well-defined ligand spectra turns by Pd(II) addition into a good defined spectra, indicating the possible formation of one supramolecular species.

To prove the existence of a homoleptic $[Pd_2\mathbf{L}^{\mathbf{LOMe}}_4](BF_4)_4$ cage, an ESI-MS spectrum was measured. Figure 2.92 shows a nice mass spectrum of $[Pd_2\mathbf{L}^{\mathbf{LOMe}}_4]^{4+}$, $[Pd_2\ \mathbf{L}^{\mathbf{LOMe}}_4+BF_4]^{3+}$ and $[Pd_2\ \mathbf{L}^{\mathbf{LOMe}}_4+2BF_4]^{2+}$ with peaks at *m/z* = 747.99, *m/z* = 1026.00 and *m/z* = 1582.49, respectively. The isotopic pattern fits perfectly.

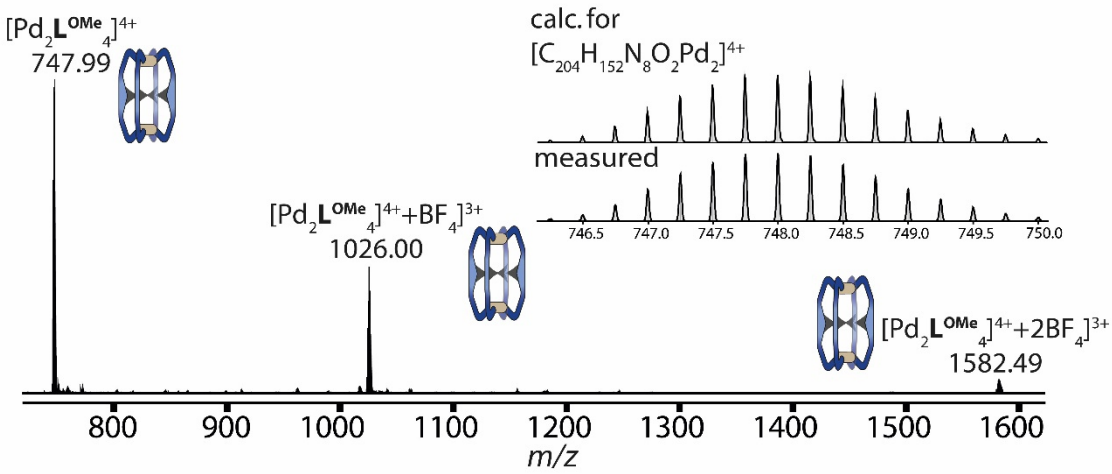

Figure 2.92 ESI mass spectrum of a $[Pd_2L^{LOMe}_4](BF_4)_4$ sample.

To have an impression of the arrangement of the ligands inside the cage, a DFT calculation for an optimized structure was carried out, leading to figure 2.93. The Pd•••Pd

distance of 24.9 Å and a distance the most distal hydrogen atoms of 32.0 Å makes the homoleptic cage slightly bigger than the $[Pd_2\mathbf{L}^{OMe}{}_4]$-cage with 19.4 Å and 24.8 Å, respectively. More interestingly, the twisted helical structure and calculated alkyne angle different to the ideal 180° (between 174° and 177°) induces a strain, making a heteroleptic assembly favourable for the $[Pd_2\mathbf{L}^{LOMe}{}_4](BF_4)_4$. Unfortunately, it was not possible to synthesize pyridyl-based ligands for a heteroleptic cage formation due to running out research time.

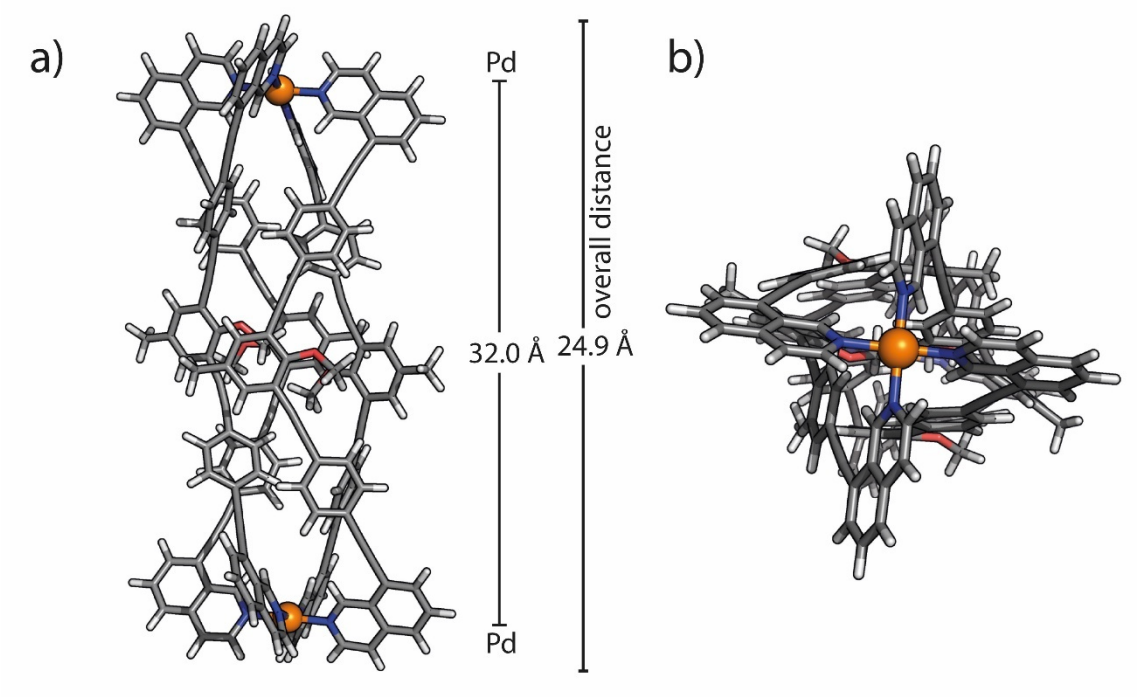

Figure 2.93 DFT (BP86-D4/def2-SVP (def2-TZVP for Pd)) calculated structure of $[Pd_2L^{LOMe}{}_4]^{4+}$ in DMSO with a) top view and b) side view. Sidechains are scaled down to a methyl group to simplify the calculation. Colour scheme: C = dark grey, H = light grey, O = red, N = blue, Pd = orange.

2.8 Host-Guest Titrations

With the formed series of topologic similar $[Pd_2\mathbf{L}^{OMe}{}_2\mathbf{L}^{SX}{}_2]$-cages differing in their endohedral environment, it is interesting to observe a possible difference in the guest-uptake. As well-known guest molecules of the Clever lab, a selection of bis-sulfonate guests as their TBA salts (tetrabutylammonium) was used for ^{1}H NMR titrations (figure 2.94).

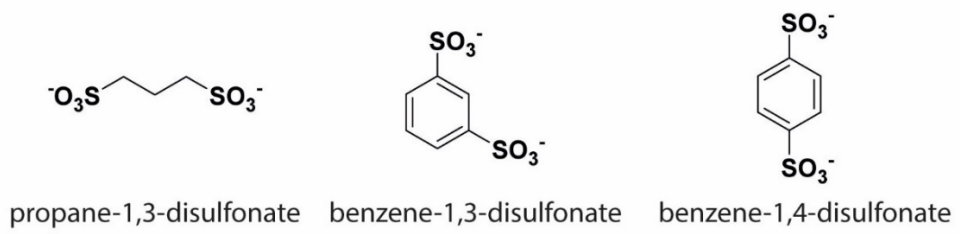

Figure 2.94 Selected sulfonate guests for titration experiments of [$Pd_2L^{OMe}{}_2L^{SX}{}_2$]-cages.

Unfortunately, in case of propane-1,3-disulfonate and benzene-1,3-disulfonate immediately resulted a precipitation of the sample already after addition of the first 0.2 eq-steps of guest molecules. Benzene-1,4-disulfate titrations (see experimental part) showed first a better behaviour but ended with quick occurring precipitation. Due to the even more bent character of [$Pd_2\mathbf{L}^{\mathbf{OMe}}{}_2\mathbf{L}^{\mathbf{SX}}{}_2$] cages against the archetype [$Pd_2\mathbf{L}^{\mathbf{A}}{}_2\mathbf{L}^{\mathbf{P}}{}_2$] cage, a guest uptake of dianionic guests seems to be less favourable for all kinds of modified [$Pd_2\mathbf{L}^{\mathbf{OMe}}{}_2\mathbf{L}^{\mathbf{SX}}{}_2$] cages. The Pd(II) metal centres cannot act as anchors for the double charged anionic molecules with a shape specific binding ability.

An interesting new type of guests are mono anionic and double substituted organophosphate guests (figure 2.95). Due to their single charge, linear structure and to some extend present, flexibility, they resulted to be more suitable for the [$Pd_2\mathbf{L}^{\mathbf{OMe}}{}_2\mathbf{L}^{\mathbf{SX}}{}_2$]-cage cavities than the sulfonates. Furthermore, phosphate compounds are of a high interest in biochemistry[135–137] and therefore interesting study objects for host-guest chemistry.

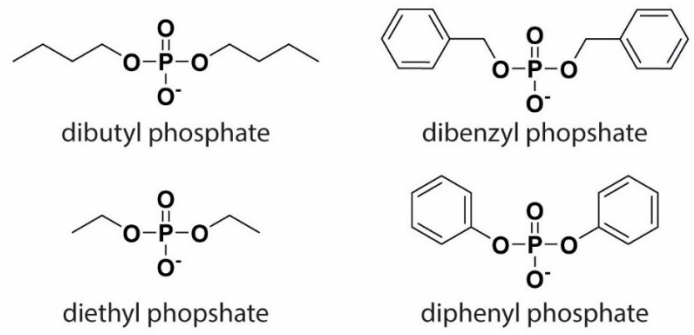

Figure 2.95 Selection of phosphate guests for titration experiments of [$Pd_2L^{OMe}{}_2L^{SX}{}_2$]-cages.

The prepared phosphate guests were used for ^{1}H NMR titrations with [$Pd_2\mathbf{L}^{\mathbf{OMe}}{}_2\mathbf{L}^{\mathbf{SB}}{}_2$]-, [$Pd_2\mathbf{L}^{\mathbf{OMe}}{}_2\mathbf{L}^{\mathbf{SNH2}}{}_2$]-,[$Pd_2\mathbf{L}^{\mathbf{OMe}}{}_2\mathbf{L}^{\mathbf{SOMe}}{}_2$]-,[$Pd_2\mathbf{L}^{\mathbf{OMe}}{}_2\mathbf{L}^{\mathbf{SOH}}{}_2$]- and [$Pd_2\mathbf{L}^{\mathbf{OMe}}{}_2\mathbf{L}^{\mathbf{SP}}{}_2$]-cages and the full titrations are listed up in the experimental part of this thesis. The described observations that follow, are similar for all **HG**-systems and are exemplified on [$Pd_2\mathbf{L}^{\mathbf{OMe}}{}_2\mathbf{L}^{\mathbf{SB}}{}_2$]- and [$Pd_2\mathbf{L}^{\mathbf{OMe}}{}_2\mathbf{L}^{\mathbf{SOMe}}{}_2$]-cages with dibutyl phosphate (DButP)and dibenzyl phosphate (DBenzP). Starting with DButP@[$Pd_2\mathbf{L}^{\mathbf{OMe}}{}_2\mathbf{L}^{\mathbf{SB}}{}_2$] (figure 2.96), the titration

shows directly new signals after addition of 0.2 eq guest and decreasing intensity of the single host signals starting from 1 eq with increase of the intensity of the new appeared signals and visible number of new signals. The shift of the signals belong to the free guest molecule is small but recognizable. A similar behaviour is observed for the DBenzP@[$Pd_2\mathbf{L}^{\mathbf{OMe}}{}_2\mathbf{L}^{\mathbf{SB}}{}_2$] titration, with new signals occuring at 0.3 eq guest addition but with a notable intensity starting over 1.0 eq. As before, the transformation of the system accelerates over 1.0 eq guest addition, leading to decreasing host signal intensities. In this case, the guest signal shift differs more from the free guest in solution than for DButP. Especially the aromatic benzyl-signals and -CH_2-group indicate a difference in DButP@[$Pd_2\mathbf{L}^{\mathbf{OMe}}{}_2\mathbf{L}^{\mathbf{SB}}{}_2$] against free guest. ^{1}H DOSY NMR experiments (figure 2.97) show multiple species with the main one consisting of mostly new appeared signals for each titration. The bad signal-to-noise ratio do not allow an analysis of the radius of the species in a qualitative analytic way. However, a correlation of the new signals is given.

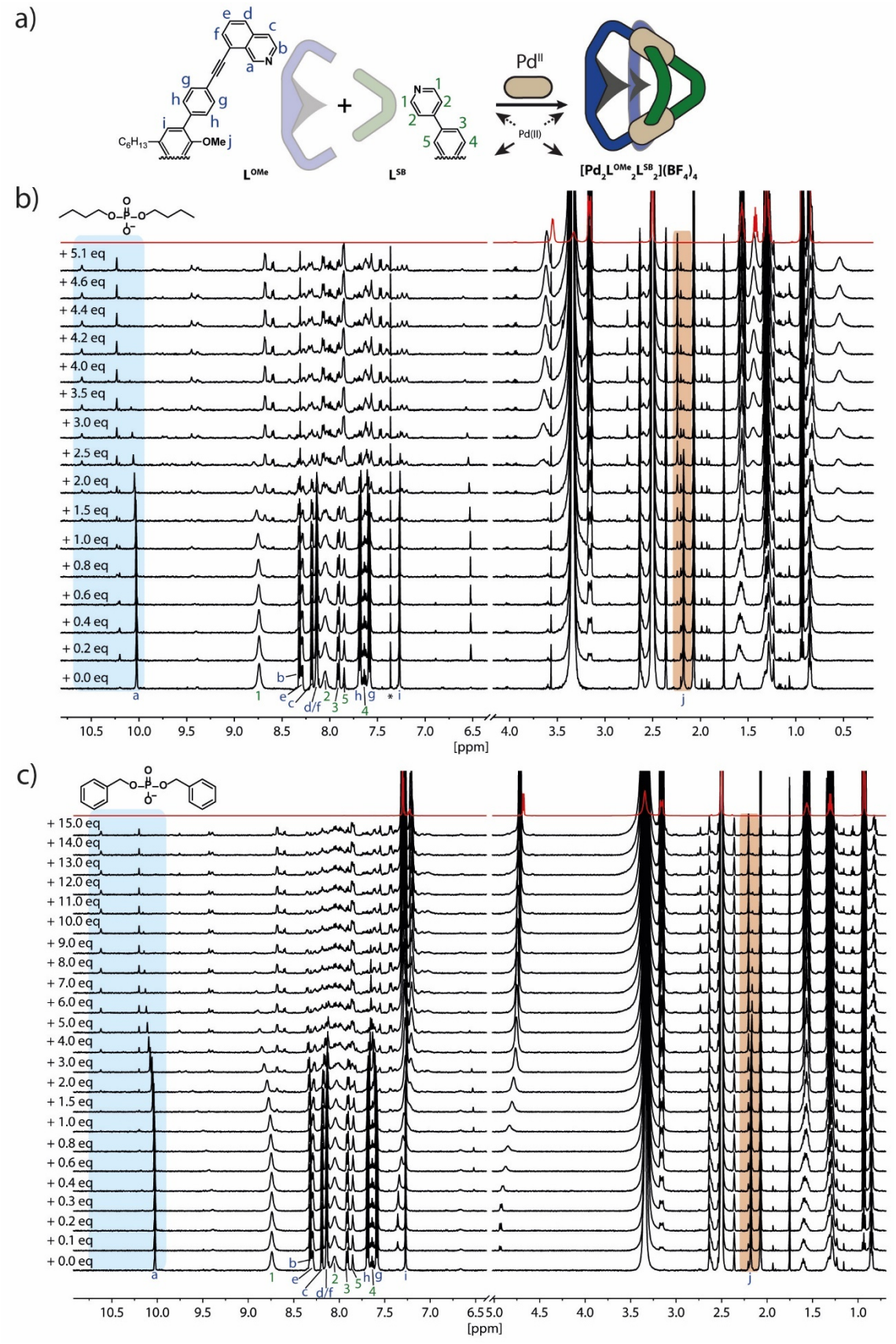

Figure 2.96 a) Scheme of the formation and proton numbering of $[Pd_2L^{OMe}{}_2L^{SB}{}_2](BF_4)_4$; b) ^1H titration (500 MHz, 298 K, DMSO-d_6) DButP@$[Pd_2L^{OMe}{}_2L^{SB}{}_2]$; c) ^1H titration (500 MHz, DMSO-d_6, 298 K) DBenzP@$[Pd_2L^{OMe}{}_2L^{SB}{}_2]$ titration.

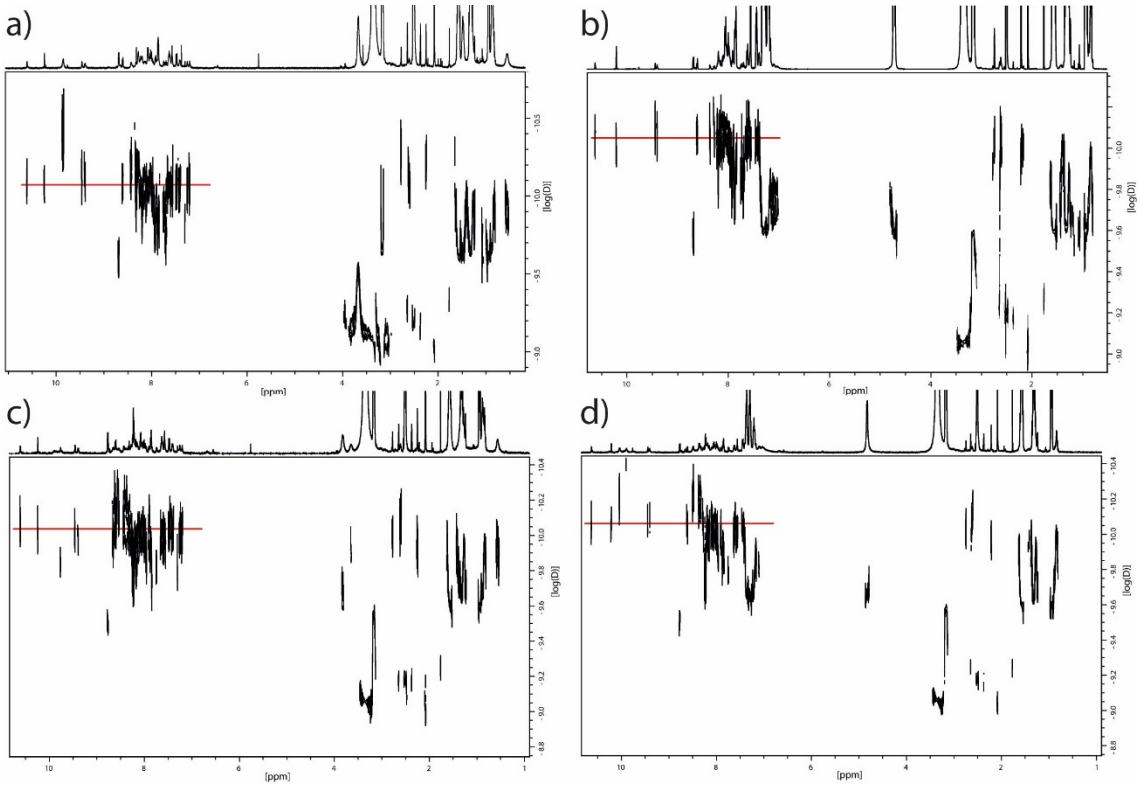

Figure 2.97 ^{1}H DOSY NMR (500 MHz, 298 K, DMSO-d_6) experiments at the end of each titration. a) DButP@[$Pd_2L^{OMe}{}_2L^{SB}{}_2$]; b) DBenzP@[$Pd_2L^{OMe}{}_2L^{SB}{}_2$]; c) DButP@[$Pd_2L^{OMe}{}_2L^{SOMe}{}_2$]; d) DBenzP@[$Pd_2L^{OMe}{}_2L^{SOMe}{}_2$].

Titration of DButP@[$Pd_2\mathbf{L}^{\mathbf{OMe}}{}_2\mathbf{L}^{\mathbf{SOMe}}{}_2$] and DBenzP@[$Pd_2\mathbf{L}^{\mathbf{OMe}}{}_2\mathbf{L}^{\mathbf{SOMe}}{}_2$] (figure 2.98) show a similar behaviour like the titrations for [$Pd_2\mathbf{L}^{\mathbf{OMe}}{}_2\mathbf{L}^{\mathbf{SOMe}}{}_2$]-cage (and others not here listened). For DButP@[$Pd_2\mathbf{L}^{\mathbf{OMe}}{}_2\mathbf{L}^{\mathbf{SOMe}}{}_2$], new signals appear at 0.6 eq addition of guest with an decreasing of free host signals over 1 eq. Signals of dibutyl phosphate, especially at lower guest concentration, show a significant shift against free guest. DBenzP@[$Pd_2\mathbf{L}^{\mathbf{OMe}}{}_2\mathbf{L}^{\mathbf{SOMe}}{}_2$] titration shows new signals with the addition of 0.4 eq guest and again a decreasing of free host signals over 1 eq. Dibenzyl phosphate signals are clearly shifted against free guest.

For all titrations, H_a (quinoline singlet of $\mathbf{L}^{\mathbf{OMe}}$) and H_j (methoxy-groups of $\mathbf{L}^{\mathbf{OMe}}$) for both cages and H_5 for [$Pd_2\mathbf{L}^{\mathbf{OMe}}{}_2\mathbf{L}^{\mathbf{SOMe}}{}_2$]$(BF_4)_4$ (methoxy-group of $\mathbf{L}^{\mathbf{SOMe}}$) are clearly indicatable, with no overlapping of other signals. All H_j and H_5 signals of the host molecule show a decreasing (while guest addition) with an occurring adjacent and increasing new signal. This could indicate a slow exchange of the guest. For H_a, two new signals appear in each case while a decreasing of the host signal. An indication of a chemical different environment for this part of the supramolecular assembly. Unfortunately, it was not possible to measure **HG**-complexes with ESI-MS due to their instability upon a dilution in acetonitrile. ^{1}H DOSY NMR spectra (figure 2.97) shows multiply new species with one main species.

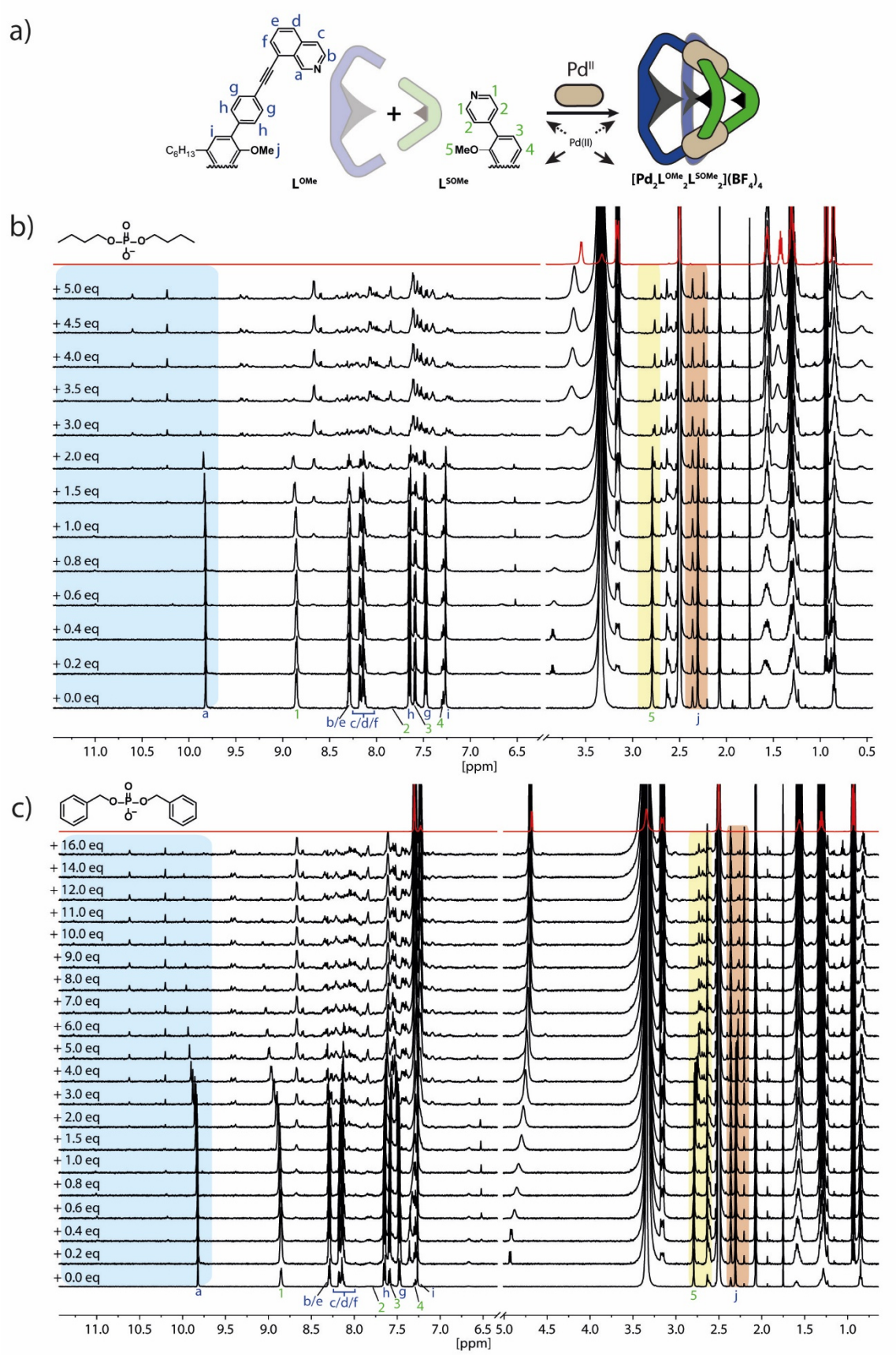

Figure 2.98 a) Scheme of the formation and proton numbering of $[Pd_2L^{OMe}_2L^{SOMe}_2](BF_4)_4$; b) ^1H titration (500 MHz, 298 K, DMSO-d_6) DButP@$[Pd_2L^{OMe}_2L^{SOMe}_2]$; c) ^1H titration (500 MHz, DMSO-d_6, 298 K) DBenzP@$[Pd_2L^{OMe}_2L^{SOMe}_2]$ titration.

In addition to the reported experiments, ^{1}H-^{1}H NOESY NMR measurements were performed, but did not reveal cross-peaks between host and guest and low intensity for other cross-peaks due to the bad signal-to-noise ratio.

A possible explanation for the discussed signal changes could be given by considering the structure of the phosphate guest. With the phosphate part of the guest molecules hosted in the middle of the cavity, the chemical proximity of the endohedral methoxy-groups of the [Pd_2**L**$^{OMe}{}_2$**L**$^{SB}{}_2$]- and [Pd_2**L**$^{OMe}{}_2$**L**$^{SOMe}{}_2$]-hosts is the same and end up in a slow exchange behaviour visible at the ^{1}H signals. The organic chains of the phosphates are flexible and could stick between the ligands not in a centred linear way, leading to doubling for some of the ligand signals (figure 2.99). Also, an uptake of two guests in a crossed position could be possible and would lead to the splitting of ligand signals inside a **HG**-complex. Both would lead to a rotaxane like structures, making a further investigation interesting and could lead to a novel supramolecular assembly. However, more analytic needs to be done for a clear scientific addressing of the visible behaviour, crystallizations for X-ray analysis are on the way.

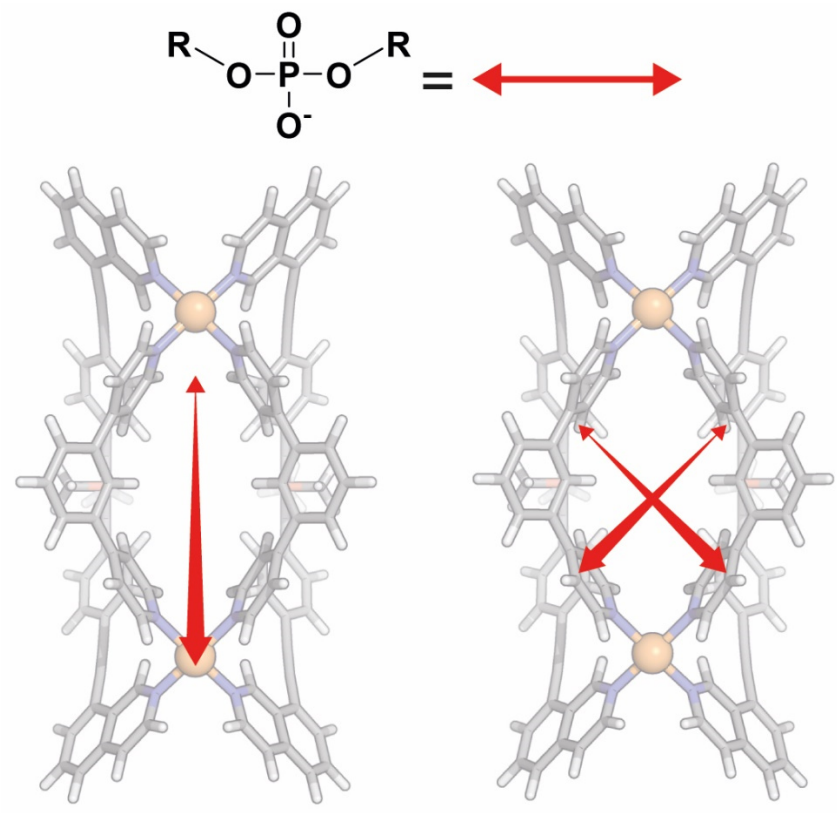

Figure 2.99 Schematic representation of possible arrangements of one or two phosphate guests inside a [Pd_2L$^{OMe}{}_2$L$^{SB}{}_2$]-cage.

2.9 Conclusions and Outlook

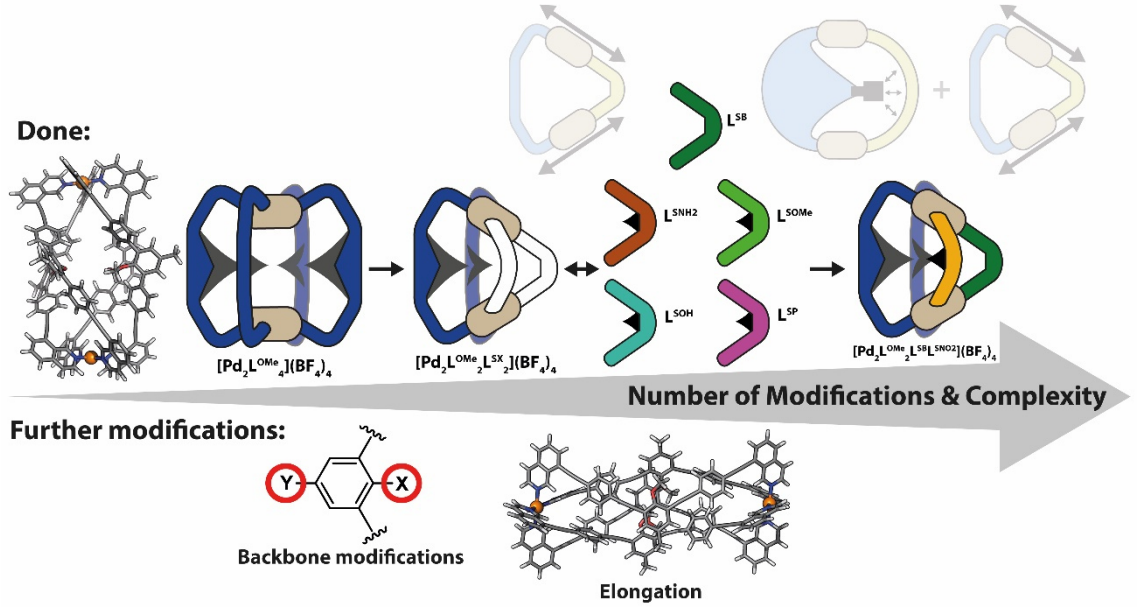

Figure 2.100 Reached goals and possible further modification possibilities.

The first aim of this thesis was to transfer the before reported ligand and homoleptic cage $\mathbf{L^A}$/$[Pd_2\mathbf{L^A}_4]$ from the previous work[116,127] of the Clever group into a system which is open for possible endohedral modifications. This goal was reached by the synthesis of ligand $\mathbf{L^{OMe}}$ and the respective cage $[Pd_2\mathbf{L^{OMe}}_4]$, which shows, similarly to the before reported coordination cage, a twisted structure. The release of strain of the structure is thought to be the driving force to form a more energetically favoured heteroleptic cages at the expense of the homoleptic ones. By deprotection of the **-OMe** group, a phenol-based ligand $\mathbf{L^{OH}}$ was synthesised showing the same behaviour when reacted with Pd(II) cations to give the homoleptic $[Pd_2\mathbf{L^{OH}}_4]$ cage structure. Nevertheless, due to better accessibility of $\mathbf{L^{OMe}}$, the heteroleptic cage formation studies concentrate on $\mathbf{L^{OMe}}$. The first attempt to introduce a clean $[Pd_2\mathbf{L^{OMe}}_2\mathbf{L^{SC4}}_4]$ cage by shape complementarity failed and led to a mixture of homo- and heteroleptic cages because of strain brought in by $\mathbf{L^{SC4}}$ due to the rigid backbone, not perfect ligand bend angle and a slightly to long -**N•••N**- distance. Fortunately, the second attempt for heteroleptic cage formation with ligand $\mathbf{L^{SB}}$ showed a clean $[Pd_2\mathbf{L^{OMe}}_2\mathbf{L^{SB}}_2]$ cage by a fitting bend angle, shorter -**N•••N**- distance and the by DFT calculations shown ability of both $\mathbf{L^{OMe}}$ ligands to distort along the ligand axis to overcome unfavourable conformeric conditions. Based on the easier synthesis because of less synthetic steps, the $\mathbf{L^{SB}}$ ligand motif instead of the $\mathbf{L^{OMe}}$ ligand was further modified to give variations with $\mathbf{L^{SNH2}}$ (aniline-), $\mathbf{L^{SOMe}}$ (methoxy-), $\mathbf{L^{SOH}}$ (phenol-), $\mathbf{L^{SP}}$ (pyridine-) and $\mathbf{L^{SNO2}}$ (nitro-) based ligands. The aniline-based ligand $\mathbf{L^{SNH2}}$ showed a perfect formation of $[Pd_2\mathbf{L^{OMe}}_2\mathbf{L^{SNH2}}_2](BF_4)_4$ with a splitting effect of the pyridyl

proton signals inside an ^{1}H NMR spectrum. DFT calculations indicate a **-H_2N•••NH_2-** distance in the range of hydrogen bonds and due to that, a stabilisation of two different pyridyl positions of $\mathbf{L^{SNH2}}$ inside the cage with no free rotation visible on the NMR time scale. Clean formation of [$Pd_2\mathbf{L^{OMe}_2L^{SOMe}_2}$]-cage with a second methoxy-functionalised ligand did not show this behaviour due the impossibility of forming hydrogen bonds inside the cavity. The formation of a [$Pd_2\mathbf{L^{OMe}_2L^{SOH}_2}$]-cage also did not led to a splitting of the pyridyl ^{1}H NMR signals, the distance for **-OH•••OH-** is calculated with 3.8 Å and thus larger than the calculated **-NH2•••NH2-** distance for [$Pd_2\mathbf{L^{OMe}_2L^{SNH2}_2}$]$(BF_4)_4$ with 2.9 Å and therefore weaker. Additionally the formation of [$Pd_2\mathbf{L^{OMe}_2L^{SOH}_2}$]$(BF_4)_4$ was not perfectly clean with a small amount of [$Pd_2\mathbf{L^{OMe}_4}$]-cage. A possible explanation could be the repulsion of the free lone pairs of the hydroxy group, leading to some sort of a homoleptic/heteroleptic equilibrium. A similar equilibrium was observed for [$Pd_2\mathbf{L^{OMe}_2L^{SP}_2}$]$(BF_4)_4$ with the [$Pd_2\mathbf{L^{OMe}_4}$]-cage. In this case, the bend angle of $\mathbf{L^{SP}}$ with 112° is smaller than 120° for the other pyridyl-based ligands, introducing a new strain in the heteroleptic assembly. However, it was possible to introduce a series of differently modified cages with the same topology and different influences of the endohedral modifications were observed. The limit of relative clean heteroleptic cage assemblies is the implementation of two neighbouring nitro-functions, leading to a heteroleptic/homoleptic ratio of nearly 1:1. Nevertheless, this was used to additionally implement (to the shape complementary formation of heteroleptic cages) an endohedral effect, resulting in the [$Pd_2\mathbf{L^{OMe}_2L^{SB}L^{SNO2}}$]$(BF_4)_4$ cage in a not perfectly clean but promising cage formation. As all [$Pd_2\mathbf{L^{OMe}_2L^{X}_2}$] cages could only be formed in DMSO-d_6, CD_3CN only gave cage mixtures with higher amounts of [$Pd_2\mathbf{L^{OMe}_4}$]$(BF_4)_4$, a remarkable influence of the chosen solvent seems to play an additional role and should be investigated in further studies. Also, different counter ions like NO_3^- or PF_6^- could be chosen to investigated better conditions for perfectly clean cage formations. To reduce the influence of the endohedral substituents on each other, an elongation of the system and resulting bigger distances between the functionalities could be introduced, a promising [$Pd_2\mathbf{L^{LOMe}_4}$] cage was already synthesised as a starting point. Further modifications inside and outside the cavity are possible, they could lead to a water soluble heteroleptic coordination cage by exchange of the hexyl chains of the $\mathbf{L^{OMe}}$ ligand with zwitterion-based side chains. Host-guest chemistry of the [$Pd_2\mathbf{L^{OMe}_2L^{X}_2}$]-cages does not seem to be trivial like for other reported cages, due to the bent topology of the Pd(II)-centres in relation to the ligands. But the variability of the introduced motif is not at its end and the foundation is given to use these first understandings to create a high number of interesting supramolecular coordination-cages based on the same topology.

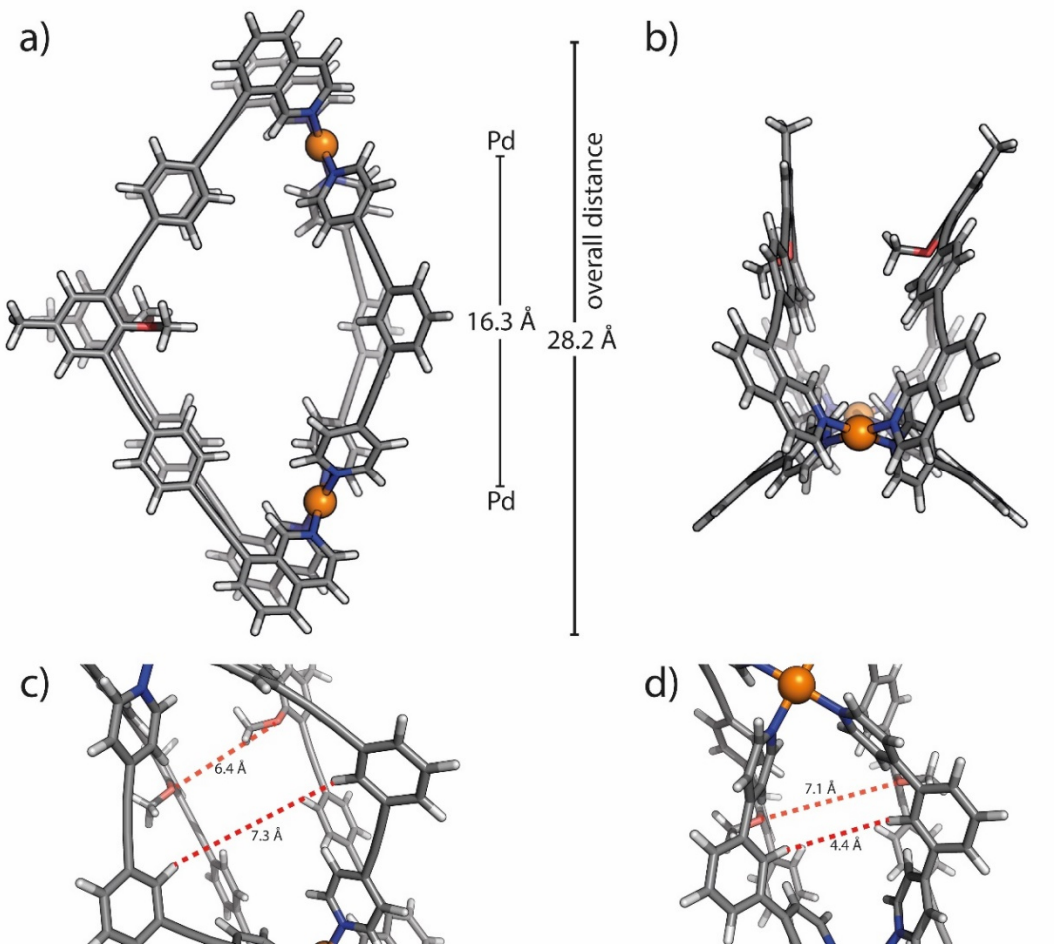

Figure 2.101 a)-c) Images of the DFT calculated structure of a possible elongated heteroleptic cage based on the introduced topology, leading to bigger distances between the endohedral functionalities in contrast to $[Pd_2L^{OMe}{}_2L^{SB}{}_2]^{4+}$ distances in d).

3 Experimental Section

General Information

Analytical Devices

Nuclear Magnetic Resonance Spectroscopy (NMR)

The NMR spectroscopic data was measured on the spectrometers *Bruker AV 500 Avance NEO, Bruker AV 400 Avance III HD NanoBay, AV 500 Avance III HD, AV 600 Avance III HD, AV 700 Avance III HD.* The chemical shifts were calibrated on tetramethylsilane (^{1}H, 0 ppm), $CFCl_3$ (^{19}F, 0 ppm), 85 % phosphoric acid (^{31}P, 0 ppm). For the ^{13}C NMR spectra the signals of the solvents were used as the internally standard (CD_3CN: 1.32, 118.26 ppm, C_6D_6: 128.06 ppm, CD_2Cl_2: 54.00 ppm, $CDCl_3$: 77.00 ppm, CD_3OD: 49.00 ppm). The chemical shift δ is given in ppm, the coupling constants J in Hz. All spectra were recorded in standard 5 mm NMR tubes at 25 °C if not stated otherwise.

Elektrospray Ionisation Mass Spectrometry (ESI-MS)

Measurement of ESI mass spectrometry data has been performed at a *Bruker ESI-timsTOF*, equipped with and electron spray ionization (ESI) source (positive/negative mode). The timsTOF consists of a time-of-flight analyser with upstream trapped ion mobility spectrometry. An Agilent ESI low concentration tuning mix has been used for calibration of tims and TOF units. Mass spectrometry data is given as mass/charge ratio (*m/z*) as well as the relative intensity regarding to the base peak (I = 100).

X-Ray Analysis

Bruker D8 venture (in-house)

The data were collected from a shock-cooled single crystal at 100(2) K on a Bruker D8 Venture CMOS with Photon 2 [No measurement device given] with an INCOATEC microfocus sealed tube, Iys 3.0 using multilayer optics as monochromator and a [No detector type given] detector. The diffractometer was equipped with a low temperature device and used CuK_α radiation (λ = 1.54178 Å). All data were integrated with SAINT and a multi-scan absorption correction using sadabs was applied. The structure was solved by direct methods using SHELXT 2014/5 (Sheldrick, 2014) and refined by full-matrix least-squares methods against F^2 by SHELXL-2014/7 (Sheldrick, 2014). All non-

hydrogen atoms were refined with anisotropic displacement parameters. The hydrogen atoms were refined isotropically on calculated positions using a riding model with their U_{iso} values constrained to 1.5 times the U_{eq} of their pivot atoms for terminal sp^3 carbon atoms and 1.2 times for all other carbon atoms. Disordered moieties were refined using bond lengths restraints and displacement parameter restraints.

The data collection and solving of crystal structures was performed by Dr. Julian Holstein and Dr. Haeri Lee.

Computational studies

Models were constructed using Wavefunction SPARTAN V 14.0 or V 18.0. All structures were optimized on PM6 by SPARTAN or DFT with BP86-D4/def2-SVP (def2-TZVP for Pd) level of theory using ORCA V 4.2.1.[138] Simulated structures for CCS calculations were optimized by GFN2-xTB 6.3.2.[139] CCS calculations were performed by Collidoscope V 1.4.[140]

3.1 Ligand Synthesis

All starting materials, salts, catalysts, and solvents were obtained from commercial sources. All reaction performed in a Schlenk tube were carried out under Argon atmosphere with standard Schlenk techniques. A GS GLOVEBOX Systemtechnik GmbH Solvent Purifications System (SPS) were used to receive dry THF. Dry DMF was purchased from Acros Organics. All reactions were monitored by thin layer chromatography (TLC), with the use of silica coated aluminium plates (Merck, silica 60, fluorescence indicator F254, thickness 0.25 mm). Silica 60, 0.02 – 0.063 mesh ASTM from Merck KGaA (Darmstadt) was used as stationary phase for column chromatography. Flash chromatography was performed on a Biotage Isolera One fraction collector with Biotage SNAP Ultra columns. Further purifications by gel permeation chromatography (GPC) were performed on Japan Analytical Industry NEXT and LaboACE with attached JAIGEL 1-HH and 2-HH 20 mm x 600 mm columns with a flowrate of 7 mL/min.

3.1.1 Synthesis of Ligand L^{OMe}

8-((trimethylsilyl)ethynyl)isoquinoline

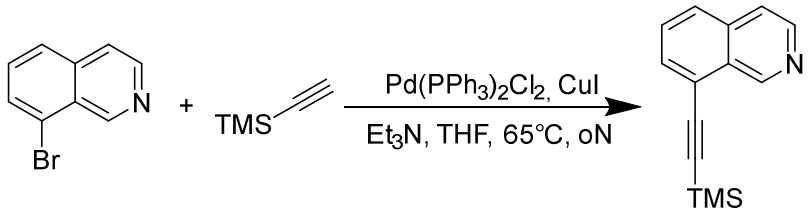

8-bromoisoquinoline (2.00 g, 9.61 mmol, 1 eq,), ethynyltrimethylsilane (1.73 ml, 12.50 mmol, 1.3 eq) , $Pd(PPh_3)_2Cl_2$ (377 mg, 0.48 mmol, 5 mol%) and CuI (366 mg, 1.92 mmol, 20 mol%) were placed into a dried 200 ml schlenk tube under inert conditions. 20 ml TEA_{dry} and 20 ml THF_{dry} were added and degassed immediately. The schlenk flask was sealed and heated up to 65 °C under stirring overnight. The reaction was controlled by TLC (Et_2O/n-Pentane = 1:1). After finished reaction and cooling down to rt, the organic solvents were removed *via vacuo* schlenk technique. The crude material was taken up in 100 ml TCM_{HPLC} and washed with 100 ml brine and 100 ml deionized water. Further purification was performed by column chromatography (SiO_2, Et_2O/n-Pentane = 1:1) to give an orange-brown oil. Yield: 1.99 g (8.83 mmol, 92 %).

^{1}H NMR (500 MHz, $CDCl_3$) δ 9.73 (s, 1H), 8.58 (d, *J* = 5.8 Hz, 1H), 7.81 – 7.74 (m, 2H), 7.67 – 7.59 (m, 2H), 0.34 (s, 9H).

MS (ESI(+)): *m/z* measured = 226.1002 $[M+H]^+$

m/z calculated = 226.1047 $[M+H]^+$

8-ethynylisoquinoline

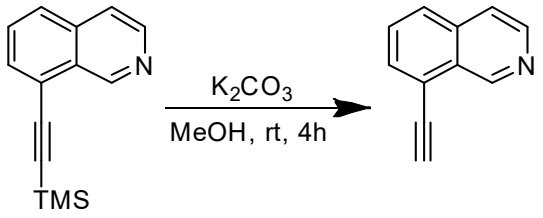

8-((trimethylsilyl)ethynyl)isoquinoline (1.99 g, 8.83 mmol, 1 eq) was placed into a 250 ml single-neck round-bottom flask and dissolved in 100 ml $MeOH_{HPLC}$. 1.6 g K_2CO_3 (11.53 mmol, 1.3 eq) were added and stirred at rt for 4 h. Afterwards, the organic solvent was removed via rotary evaporator. The occurring solid was taken up in 100 ml TCM_{HPLC} and washed three times with 200 ml deionized water. After drying over $MgSO_4$, the organic solvent was removed by rotary evaporator and the product was obtained as a brown solid. Yield: 1.34 g (8.80 mmol, 99 %).

^{1}H NMR (500 MHz, $CDCl_3$) δ 9.75 (s, 1H), 8.60 (d, *J* = 5.7 Hz, 1H), 7.87 – 7.79 (m, 2H), 7.71 – 7.63 (m, 2H), 3.56 (s, 1H).

MS (ESI(+)): *m/z* measured = 154.0703 $[M+H]^+$

m/z calculated = 154.0651 $[M+H]^+$

8-((4-bromophenyl)ethynyl)isoquinoline

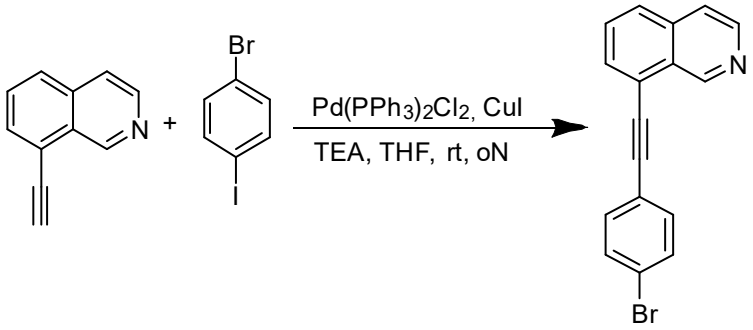

8-Ethynylisoquinoline (800 mg, 5.22 mmol, 1eq), 1-bromo-4-iodobenzene (1.77 g, 6.27 mmol, 1.2 eq), $Pd(PPh_3)_2Cl_2$ (293.3 mg, 0.42 mmol, 8 mol%) and CuI (198.92 mg, 1.04 mmol, 20 mol%) were placed in a dried 100 ml schlenk tube. Dry THF (20 ml) and TEA_{dry} (20 ml) were added to the solids and degassed immediately. The reaction mixture was stirred at room temperature overnight and controlled via TLC (n-pentane/EtOAc = 1:1). The organic solvents were removed *via vacuo* schlenk technique. The occurred solid was taken up in 100 ml TCM_{HPLC} and washed with 100 ml brine and 100 ml

deionized water before the organic phase was dried over $MgSO_4$. After removing of the organic solvents via rotary evaporator, the crude material was purified by column chromatography (SiO_2, n-pentane/EtOAc = 1:1) to give a yellow-orange solid. Yield: 1.61 g (3.57 mmol, 68 %).

^{1}H NMR (500 MHz, 298 K, $CDCl_3$) δ 9.80 (s, 1H), 8.62 (d, 1H), 7.82 (d, *J* = 7.7 Hz, 2H), 7.68 (m, *J* = 7.6 Hz, 2H), 7.58 – 7.49 (dd, 4H).

MS (ESI(+)): *m/z* measured = 308.0071 $[M+H]^+$

m/z calculated = 308.0069 $[M+H]^+$

8-((4-(4,4,5,5-tetramethyl-1,3,2-dioxaborolan-2- yl)phenyl)ethynyl)isoquinoline

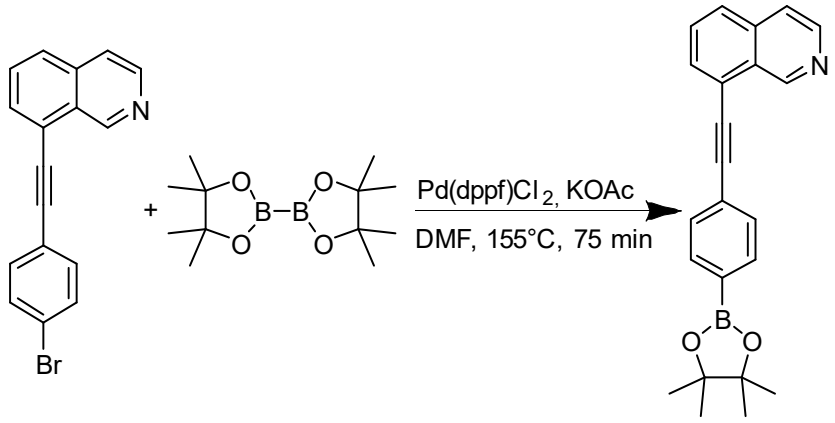

8-((4-bromophenyl)ethynyl)isoquinoline (800 mg, 2.60 mmol, 1 eq), Bis(pinacolato)diboron (857 mg, 3.37 mmol, 1.3 eq), $Pd(dppf)Cl_2$ (76 mg, 0.1 mmol, 4 mol%) and KOAc (1.53 g, 15.58 mmol, 6 eq) were placed in a dried 100 ml schlenk tube. 20 ml DMF_{dry} was added via syringe and the suspension was immediately degassed. Afterwards, the reaction mixture was heated at 155 °C for 75 min and cooled down. The mixture was transferred in a 100 ml single-necked round-bottom flask and the DMF was removed via rotary evaporator. The solid was taken up in 100 ml chloroform and washed with 100 ml brine and 100 ml water. The over $MgSO_4$ dried solvent was removed by rotary evaporator and the crude material was purified by column chromatography (SiO_2 neutralized with TEA, n-pentane/EtOAc = 1:1) to give a brown oil. Yield: 785 mg (2.21 mmol, 85 %).

^{1}H NMR (500 MHz, 298 K, $CDCl_3$) δ 9.83 (s, 1H), 8.61 (d, 1H), 7.88 – 7.78 (m, 4H), 7.72 – 7.63 (m, 2H), 7.41 (m, *J* = 5.2, 2.1 Hz, 2H), 1.27 (s, 12H).

MS (ESI(+)): *m/z* measured = 356.1856 $[M+H]^+$

m/z calculated = 356.1820 $[M+H]^+$

2,6-dibromo-4-hexylphenol

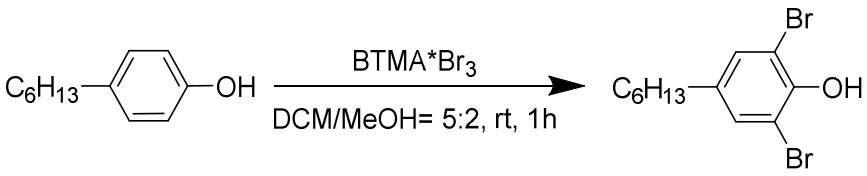

4-n-Hexylphenol (400 mg, 2.24 mmol, 1 eq) was placed in a 250 ml single-necked round-bottom flask and solved in 50 ml DCM/MeOH = 5:2. $BTMA^*Br_3$ (1.84 g, 4.71 mmol, 2.1 eq) was added and stirred at rt for 1 h. After complete consumption of 4n-hexylphenol (controlled by TLC, n-pentane/EtOAc = 1:1) the solvents were removed by rotary evaporator and the crude material was again solved in 50 ml TCM_{HPLC} and washed with 50 ml brine and 50 ml water. The organic phase was dried over $MgSO_4$ and the crude material was purified by column chromatography (SiO_2, n-pentane/EtOAc = 1:1). A colourless viscous oil was obtained as a product. Yield: 749 mg (2.23 mmol, 99 %).

^{1}H NMR (500 MHz, 298 K, DMSO-d_6) δ 9.61 (s, 1H), 7.35 (s, 2H), 2.46 (t, *J* = 7.8 Hz, 2H), 1.49 (m, *J* = 7.5 Hz, 2H), 1.25 (m, *J* = 6.1, 3.8 Hz, 6H), 0.88 – 0.82 (t, 3H).

MS (ESI(+)): *m/z* measured = 336.9689 $[M+H]^+$

m/z calculated = 336.9621 $[M+H]^+$

1,3-dibromo-5-hexyl-2-methoxybenzene

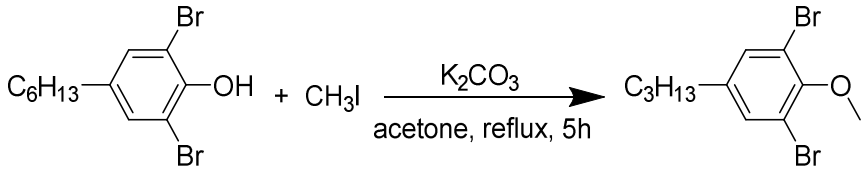

In a 100 ml single-neck round-bottom flask 2,6-dibromo-4-hexylphenol (749 mg, 2.23 mmol, 1 eq) and potassium carbonate (1.85 g, 13.37 mmol, 6 eq) were added to 30 ml $acetone_{HPLC}$. Under stirring, iodomethane (833 µl, 13.37 mmol, 6 eq) was added via syringe. The reaction was refluxed overnight. After cooling down, the solution was quenched with 50 ml 10 % sodium thiosulfate. The aqueous solution was extracted three times with 50 ml TCM_{HPLC} and the separated organic phase was dried over $MgSO_4$. Chloroform was evaporated by a rotary evaporator and no further purification was needed to give the product as a yellowish oil. Yield: 756 mg (2.16 mmol, 97 %).

1H NMR (500 MHz, 298 K, DMSO-d_6) δ 7.49 (s, 2H), 3.76 (s, 3H), 2.53 (t, *J* = 9.1 Hz, 2H), 1.52 (m, *J* = 7.7 Hz, 2H), 1.33 – 1.21 (m, 6H), 0.86 (t, *J* = 6.3 Hz, 3H).

MS (ESI(+)): *m/z* measured = 350.9764 $[M+H]^+$

m/z calculated = 350.9777 $[M+H]^+$

Final Suzuki-Miyaura coupling to form L^{OMe}

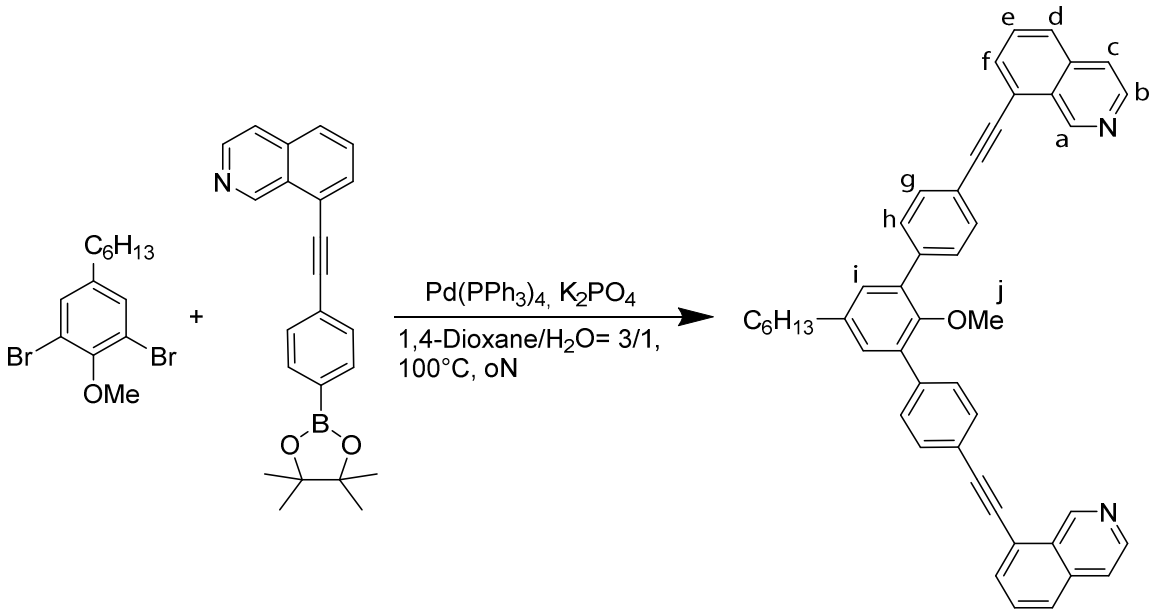

In a 200 ml schlenk tube 1,3-dibromo-5-hexyl-2-methoxybenzene (50 mg, 143 µmol, 1eq), 8-((4-(4,4,5,5-tetramethyl-1,3,2- dioxaborolan-2-yl)phenyl)ethynyl)isoquinoline (152 mg, 429 µmol, 3 eq) and K_3PO_4 (91 mg, 429 µmol, 3 eq) were solved in 15 ml 1,4-dioxane/water = 4:1 and carefully degassed. Tetrakis(triphenylphosphine)palladium(0) (8.3 mg, 7.14µmol, 5 mol%) was suspended in 10 ml dioxane/water = 4:1 and degassed directly. Afterwards, the $Pd(PPh_3)_4$ suspension was taken up by a syringe and added to first prepared schlenk tube. At 100 °C oil bath temperature, the reaction was stirred for 48 h with controlling of the reaction by TLC (n-pentane/EtOAc = 1:1). After cooling down, the occurring suspension was transferred with 70 ml chloroform to a separation funnel and washed with each time 80ml brine and deionized water. The dried organic phase ($MgSO_4$) was evaporated by rotary evaporator and the crude material was purified by column chromatography (n-pentane/EtOAc = 1:1). Yield: 46 mg (71.12 µmol, 50 %). For of cage synthesis, $\mathbf{L^{OMe}}$ was additional purified with GPC.

^{1}H NMR (500 MHz, 298 K, CD_3CN) δ 9.82 (s, *J* = 1.0 Hz, 2H), 8.61 (d, *J* = 5.7 Hz, 2H), 7.96 (d, *J* = 8.3 Hz, 2H), 7.92 (dd, *J* = 7.2, 1.1 Hz, 2H), 7.83 – 7.79 (m, 6H), 7.78 (t, *J* = 8.3, 7.2 Hz, 2H), 7.74 – 7.71 (dd, 4H), 7.29 (s, 2H), 2.73 – 2.67 (q, 2H), 1.68 (p, *J* = 7.6 Hz, 2H), 1.43 – 1.31 (m, 6H), 0.93 – 0.85 (m, 3H).

^{13}C NMR (151 MHz, 298 K, DMSO-d_6) δ 152.98, 150.54, 144.33, 139.52, 135.89, 134.44, 132.34, 132.16, 130.85, 130.82, 129.98, 128.16, 127.55, 121.26, 121.11, 120.62, 95.98, 86.48, 60.87, 35.03, 31.59, 31.54, 28.98, 22.55, 14.46.

MS (ESI(+)): *m/z* measured = 647.3086 $[M+H]^+$

m/z calculated = 647.3057 $[M+H]^+$

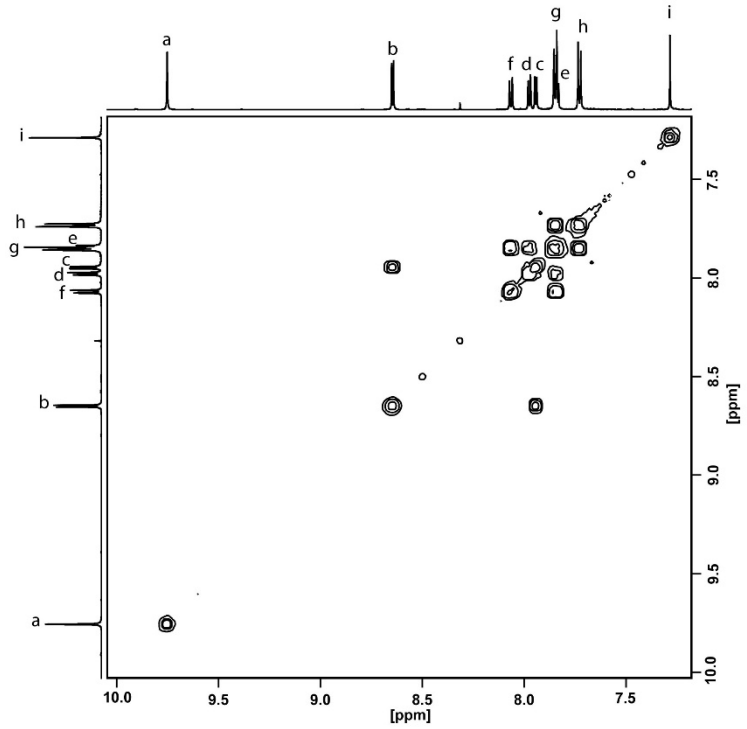

Figure 3.1 Partial ^{1}H-^{1}H COSY NMR (500MHz/DMSO-d_6) spectrum of ligand L^{OMe}.

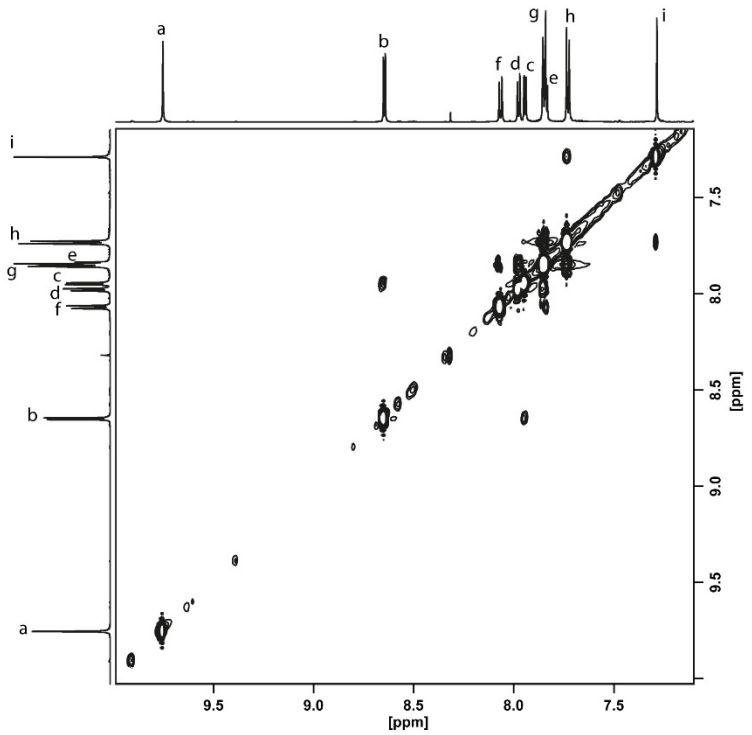

Figure 3.2 Partial ^{1}H-^{1}H NOESY NMR (700 MHz/DMSO-d_6) spectrum of ligand L^{OMe}.

3.1.2 Synthesis of Ligand L^{OH}

Deprotection of L^{OMe} with BBr_3 to give L^{OH}

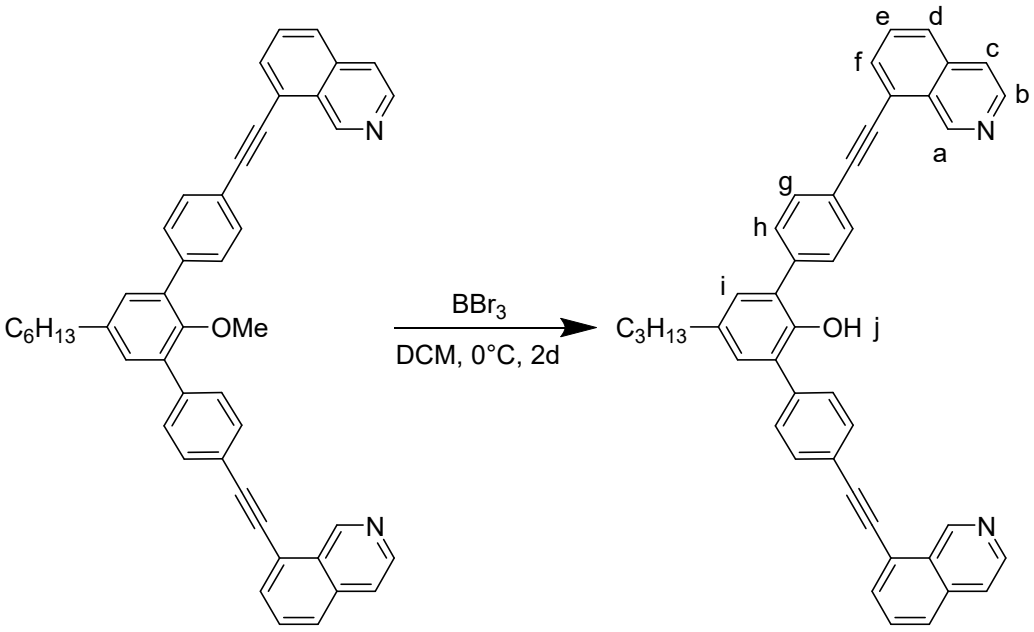

In a dried 100 ml schlenk tube, **L^{OMe}** (100 mg, 178 µmol, 1 eq) was taken up in 30 ml DCM_{dry} and cooled to 0 °C. Fresh and good quality BBr_3 (1M DCM solution, 534 µl, 534 µmol, 3 eq) was added dropwise via syringe over 20 min under stirring. Afterwards,

the reaction was slowly warmed up and carried out for two days. The reaction was quenched with ice and extracted three times with 50 ml TCM_{HPLC}. The solution was dried over $MgSO_4$ and the solvents were removed by rotary evaporator. The deprotected ligand was purified by column chromatography (SiO_2, n-pentane/EtOAc = 1:1). Yield: 44 mg (71.11 µmol, 46 %). For of cage synthesis, L^{OH} was additional purified with GPC.

^{1}H NMR (500 MHz, 298 K, DMSO-d_6) δ 9.75 (s, 2H), 8.65 (d, *J* = 5.7 Hz, 2H), 8.44 (s, 1H), 8.06 (d, *J* = 8.3 Hz, 2H), 7.96 (dd, *J* = 15.5, 6.3 Hz, 4H), 7.87 – 7.81 (m, 6H), 7.72 – 7.68 (m, 4H), 2.61 (t, *J* = 7.8 Hz, 2H), 1.62 (m, *J* = 7.5 Hz, 2H), 1.30 (m, *J* = 7.6, 3.5 Hz, 6H), 0.91 – 0.84 (t, 3H).

^{13}C NMR (151 MHz, 298 K, CD_3CN) δ 151.16, 148.57, 144.29, 139.95, 136.43, 136.08, 132.42, 132.33, 130.77, 130.72, 130.50, 129.56, 128.21, 128.00, 121.88, 121.59, 121.22, 86.39, 35.16, 32.02, 29.92, 29.29, 22.94, 13.97.

MS (ESI(+)): *m/z* measured = 632.2798 $[M+H]^+$

m/z calculated = 632.2822 $[M+H]^+$

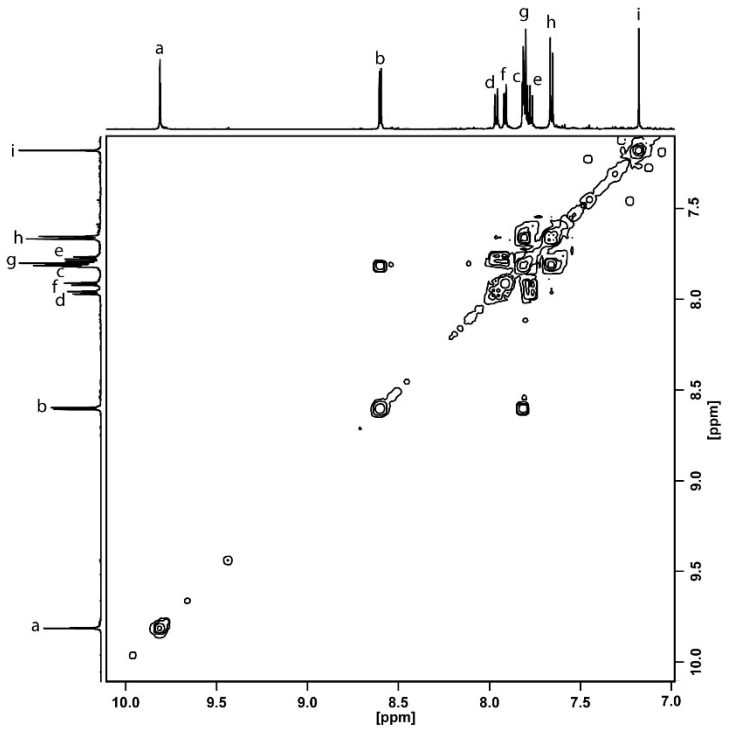

Figure 3.3 ^{1}H-^{1}H COSY NMR (500MHz/DMSO-d_6) spectrum of ligand L^{OH}.

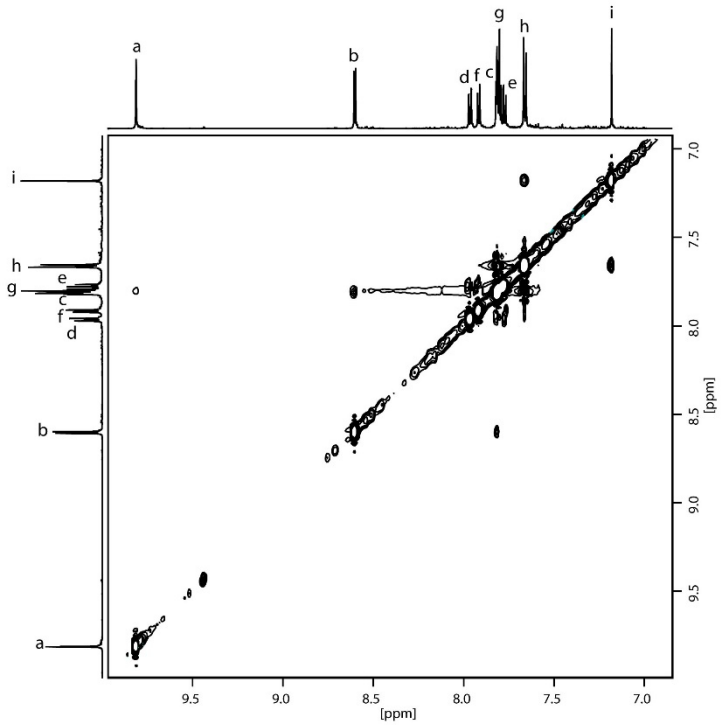

Figure 3.4 Partial ^{1}H-^{1}H NOESY NMR (700 MHz/DMSO-d_6) spectrum of ligand L^{OH}.

3.1.3 Synthesis of Ligand L^{P}

3,6-dibromo-9,10-dimethoxyphenanthrene.

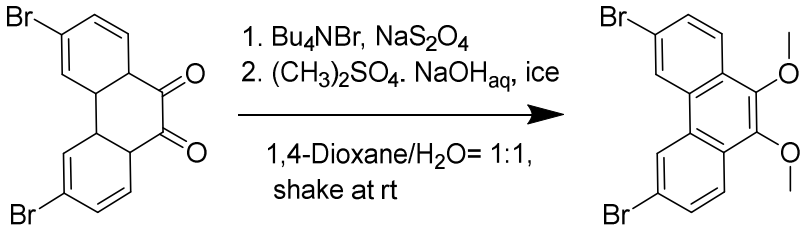

In a 25 ml separation funnel 3,6-dibromophenanthrene-9,10-dione (1.5 mg, 4.11 mmol, 1 eq), tetra-*n*-butylammonium bromide (400 mg, 1.23 mmol, 0.3 eq) and sodium dithionite (2.1 g, 11.92 mmol, 2.9 eq) were put into 40 ml 1,4-dioxane/water = 1:1. The reaction was shaken for 5 min before dimethyl sulphate (2 ml, 20.55 mmol, 5 eq.), 15 g ice and 5 ml of an aqueous 14 M NaOH solution were added. The mixture was shaken for another 15 min before it was extracted with three times 30 ml ethyl acetate. The combined organic phases were washed with three times 30 ml water, two times 30 ml NH_4OH solution and 30 ml brine. Afterwards, the organic phase was dried over $MgSO_4$ and the solvent were removed by rotary evaporator *in vacuo*. The crude material was

purified by column chromatography (SiO2, n-pentane/EtOAc = 10:1) to get a yellow powder as a product. Yield: 345 mg (1.72 mmol, 21 %).

^{1}H NMR (500 MHz, 298 K, $CDCl_3$) 8.6 (d, *J* = 1.9 Hz, 2H), 8.12 (d, *J* = 8.7 Hz, 2H), 7.73 (dd, *J* = 8.7 Hz, *J* = 1.8 Hz, 2H), 4.07 (s, 3H).

MS (ESI(+)): *m/z* measured = 403.9732 $[M+H]^+$

m/z calculated = 403.9727 $[M+H]^+$

Final synthesis step of L^P

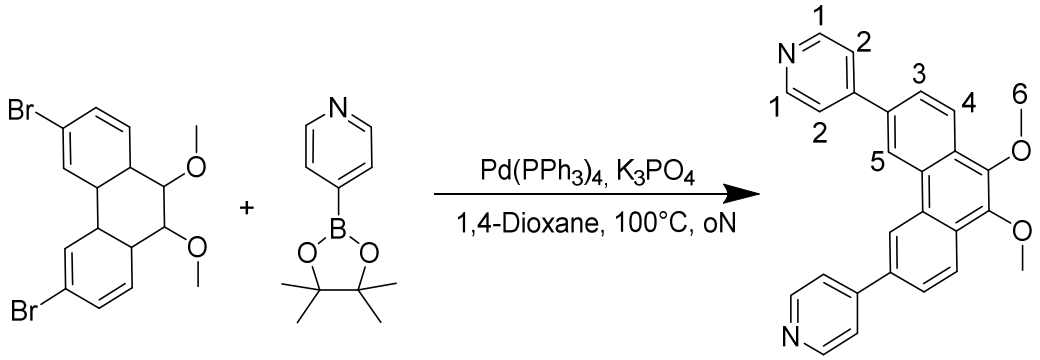

In a 100 ml Schlenk tube 3,6-dibromo-9,10-dimethoxyphenanthrene (160 mg, 0.4 mmol, 1 eq), 4-(4,4,5,5-tetramethyl-1,3,2-dioxaborolan-2-yl)pyridine (250 mg, 1.2 mmol, 3 eq) K_3PO_4 (700 mg, 3.3 mmol, 8.3 eq) and $Pd(PPh_3)_4$ (5 mg, 41 µmol, 3 mol%) were suspended in 25 ml 1,4-dioxane and degassed immediately. The reaction was heated to 100 °C overnight. After cooling down, 40 ml water were added, and the product was extracted with three times 30 ml chloroform. The combined organic solvents were dried over $MgSO_4$ and removed after filtration by rotary evaporator. The crude material was purified by column chromatography (SiO2, $CHCl_3$/MeOH = 10:1) and GPC to yield a brown crystalline solid. Yield (before GPC): 75 mg, 0.19 mmol, 47 %).

^{1}H NMR (500 MHz, 298 K, $CDCl_3$) 8.92 (d, *J* = 1.7Hz, 2H), 8.76 (m, 4H), 8.39 (d, J= 8.5 Hz, 2H), 7.93 (dd, J= 8.5, 1.7 Hz, 2H), 7.78 - 7.63 (m, 4H), 4.16 (s, 6H).

^{13}C NMR (151 MHz, 298 K, DMSO-d_6) *δ* 150.59, 148.58, 144.55, 136.12, 130.04, 129.01, 126.14, 123.62, 122.21, 121.38, 61.26.

MS (ESI(+)): *m/z* measured = 393.1632 $[M+H]^+$

m/z calculated = 393.1598 $[M+H]^+$

3.1.4 Synthesis of Ligand L^{SAc4}

10-hexylacridin-9(10H)-one

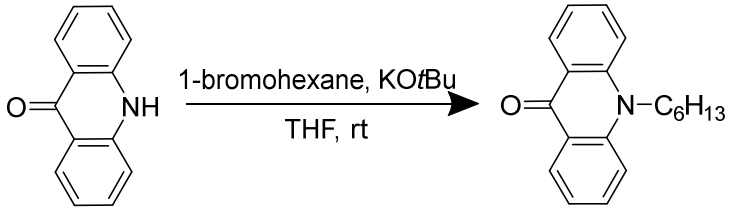

In a 250 ml one-necked flask 9(10*H*)-acridone (5.0 g, 25.6 mmol, 1 eq) was dissolved in 80 ml THF. Potassium-*tert*-butanolat (3.2 g, 28.2 mmol, 1.1 eq) was added and the reaction mixture was stirred at room temperature for 1.5 h. Afterwards, 1-Bromohexane (8.5 g/ 7.6 ml, 51.2 mmol, 2 eq) were added dropwise over 20 min to the solution before the reaction was refluxed for 10 h. After cooling down, the mixture was filtered over celite and washed with EtOAc. The organic solvents were removed by rotary evaporator and the crude product was purified by column chromatography (SiO2, $CHCl_3$ (100 %) to $CHCl_3$/MeOH = 10:1) to give a solid bright yellow powder. Yield: 3.45 g, 25.61 mmol, 69 %).

^{1}H NMR (500 MHz, 298 K, $CDCl_3$) 8.60 (dd, *J* = 7.95 Hz, *J* = 1.45 Hz, 2H, a), 7.74 (m, *J* = 8.65, 7.05 Hz, *J* = 1.65 Hz, 2H, c), 7.51 (d, *J* = 8.70 Hz, a'), 7.30 (t, *J* = 7.44 Hz, 2H, b), 4.37 (t, 2H), 1.98 (p, *J* = 7.7 Hz, 2H), 1.59 (p, *J* = 7.4 Hz, 2H), 1.50 (m, *J* = 26.2, 7.5 Hz, 4H), 0.95 (t, *J* = 7.1 Hz, 3H).

MS (ESI(+)): *m/z* measured = 195.0710 $[M+H]^+$

m/z calculated = 195.0679 $[M+H]^+$

2,7-dibromo-10-hexylacridin-9(10H)-one.

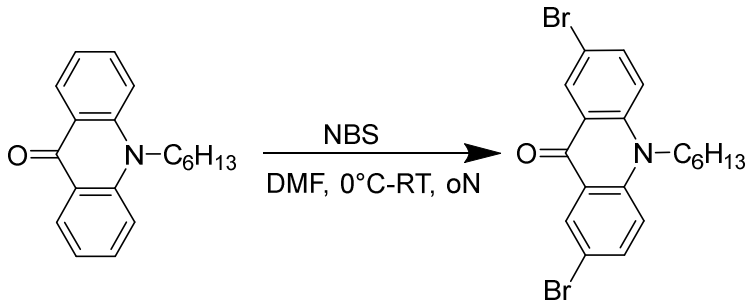

In a 250 ml one-necked flask, 10-hexylacridin-9(10H)-one (3.45 g, 25.61 mmol, 1 eq) was dissolved in DMF and cooled down to 0 °C. N-Bromosuccinimide (12.8 g, 71.71 mmol, 2.8 eq) was added over 30 min followed by slowly warming up and stirring at room temperature overnight. Afterwards, the reaction was quenched with 50 ml water and filtered through a paper filter. The product was purified by column chromatography

(SiO2, $CHCl_3$ (100 %) to $CHCl_3$/MeOH = 20:1) to give a bright yellow powder. Yield: 5.01 g, 15.45 mmol, 74 %.

^{1}H NMR (500 MHz, 298 K, $CDCl_3$): *δ* (ppm) = 8.65 (dd, *J* = 7.95 Hz, *J* = 1.45 Hz, 2H), 7.79 (m, *J* = 8.65, 7.05 Hz, *J* = 1.65 Hz, 2H) 7.37 (t, *J* = 7.44 Hz, 2H), 4.28 (t, 2H), 1.90 (p, *J* = 7.7 Hz, 2H), 1.53 (p, *J* = 7.4 Hz, 2H), 1.43-1.28 (m, *J* = 26.2, 7.5 Hz, 4H), 0.92 (t, *J* = 7.1 Hz, 3H).

MS (ESI(+)): *m/z* measured = 352.8887 $[M+H]^+$

m/z calculated = 352.8869 $[M+H]^+$

Final synthesis step of L^{SAc4}

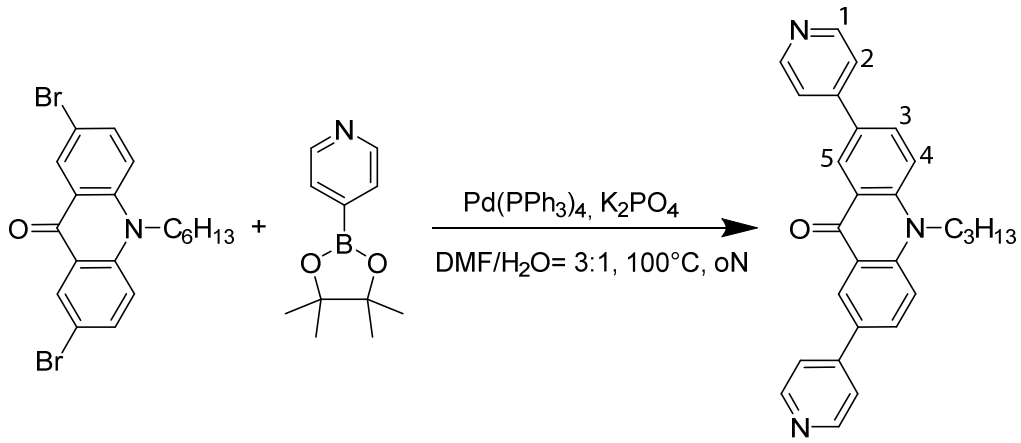

A 250ml Schlenk tube is filled with 100 mg 2,7-dibromo-10-hexylacridin-9(10H)-one (0.23 mmol, 1 eq), 4-(4,4,5,5-tetramethyl-1,3,2-dioxaborolan-2-yl)pyridine (141 mg, 0.69 mmol, 3 eq), potassium phosphate (146 mg, 0.69 mmol, 3 eq) and $Pd(Ph_3)_4$ (13 mg, 0.011 mmol, 11 µmol, 5 mol%). A mixture of 25 ml DMF/water = 3:1was added and immediately degassed. Afterwards, the suspension was heated up to 100 °C and stirred overnight. 20 ml water was added to the cooled down reaction and the product was extracted with 3x 80 ml chloroform. The united organic phases were washed with 100 brine and 100 ml deionized water before they were dried over $MgSO_4$. The organic phase was removed by a rotary evaporator and the crude material was purified by column chromatography (SiO2, $CHCl_3$/MeOH = 10:1) and GPC to give a bright yellow powder. Yield (before GPC): 78 mg, 0.18 mmol, 79 %.

^{1}H NMR (500 MHz, 298 K, DMSO-d_6) δ 8.96 (d, *J* = 2.4 Hz, 2H), 8.73 (d, *J* = 5.3 Hz, 4H), 8.10 (dd, *J* = 9.0, 2.5 Hz, 3H), 7.76 (d, *J* = 5.3 Hz, 4H), 7.69 (d, *J* = 9.1 Hz, 2H), 4.50 – 4.42 (t, 2H), 2.02 (p, *J* = 7.7 Hz, 2H), 1.63 (p, *J* = 7.4 Hz, 2H), 1.45 (m, *J* = 26.2, 7.5 Hz, 4H), 0.97 (t, *J* = 7.1 Hz, 3H).

^{13}C NMR (151 MHz, 298 K, DMSO-d_6) δ 176.73, 150.80, 146.11, 142.21, 132.99, 130.48, 125.18, 122.37, 121.34, 117.84, 46.01, 31.52, 27.43, 26.12, 22.62, 14.39.

MS (ESI(+)): *m/z* measured = 349.1202 $[M+H]^+$

m/z calculated = 349.1210 $[M+H]^+$

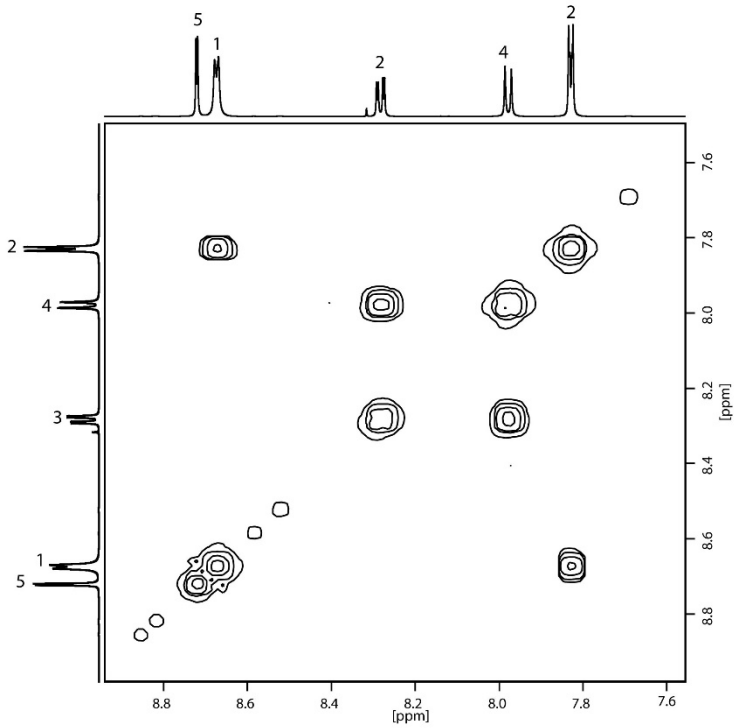

Figure 3.5 Partial ^{1}H-^{1}H COSY NMR (500MHz/DMSO-d_6) spectrum of ligand L^{SAc4}.

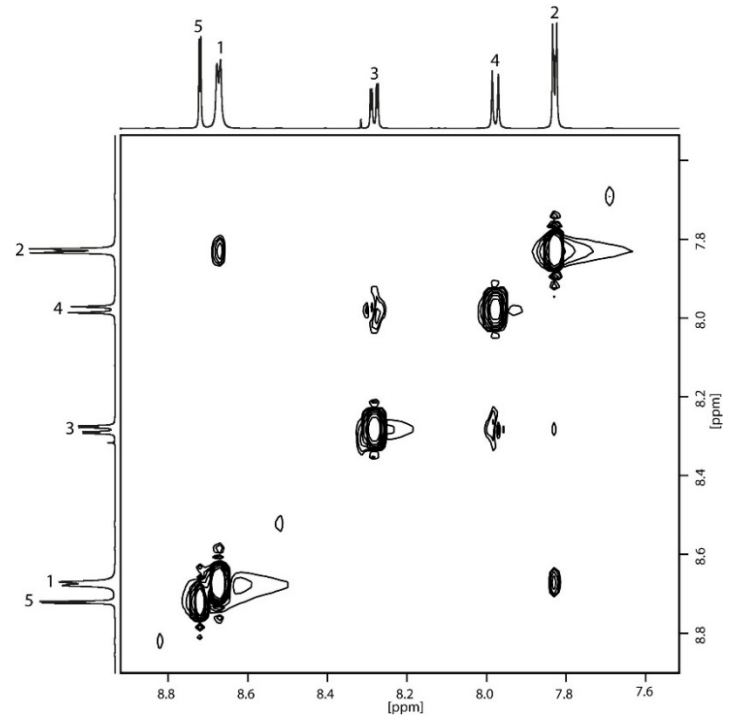

Figure 3.6 Partial ^{1}H-^{1}H NOESY NMR (700 MHz/DMSO-d_6) spectrum of ligand L^{SAc4}.

3.1.5 Synthesis of Ligand L^{SC4}

3,6-dibromo-9H-carbazole synthesis

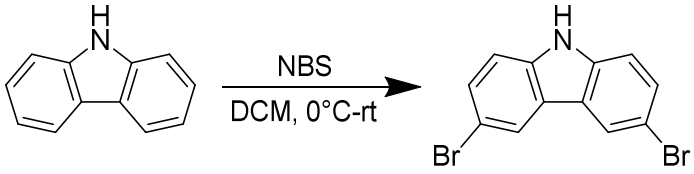

9*H*-carbazole (5 g, 29,9 mmol, 1 eq) was placed in a 250 ml one-necked flask and dissolved in 100 ml CH_2Cl_2. After cooling down to 0 °C, N-Bromosuccinimide (10.7 g, 59.8mmol, 2.1 eq) was added over 30 min followed by slowly warming up over hours and stirring overnight at rt. Afterwards, 80 g ice were added to quench the reaction and the mixture was washed with three times 80 ml chloroform. The combined organic solvents were dried over $MgSO_4$ and removed by rotary evaporator. The product was purified by recrystallisation in ethanol. Yield: 3.6 g, 11.06 mmol, 36 %.

^{1}H NMR (500 MHz, 298 K, $CDCl_3$): δ (ppm) = 8.13 (d, *J* = 1.9 Hz, 2H), 7.52 (dd, *J* = 8.6 Hz, *J* = 1.9 Hz, 2H), 7.31 (d, *J* = 8.6 Hz, 2H).

MS (ESI(+)): *m/z* measured = 352.9001 $[M+H]^+$

m/z calculated = 352.8998 $[M+H]^+$

3,6-dibromo-9-hexyl-9H-carbazole

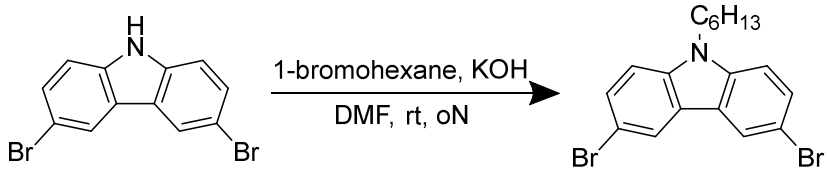

In a 250 ml round-bottom flask with 80 ml DMF 3,6-dibromo-9H-carbazole (2 g, 6.2 mmol, 1 eq) and KOH (2 g, 11.1 mmol, 1.8 eq) were dissolved and stirred at rt for 1 h. Over 20 min, 1-Bromohexane was added dropwise via syringe and the mixture was stirred overnight. The mixture was then poured into 300 g ice and after complete melting of the ice extracted with three times 100 ml chloroform. The combined organic phases were removed by rotary evaporator and the crude material was purified by column chromatography (SiO_2, pentane/acetone = 2:1) to give a white crystalline powder. Yield: 2.21 g, 6.15 mmol, 88 %).

^{1}H NMR (400 MHz, 298 K, $CDCl_3$): *δ* (ppm) = 8.13 (d, *J* = 1.9 Hz, 2H), 7.55 (dd, *J* = 8.7, *J* = 2.0 Hz, 2H), 7.26 (d, ^3J = 8.6 Hz, 2H), 4.22 (t, *J* = 7.2 Hz, 2H), 1.81 (p, *J* = 7.3 Hz, 2H), 1.29 (m, *J* = 10.0, 6.4, 3.5 Hz, 6H), 0.87 (t, *J* = 8.7, 1H).

MS (ESI(+)): *m/z* measured = 324.8899 $[M+H]^+$

m/z calculated = 324.8920 $[M+H]^+$

Final synthesis step of L^{SC4}

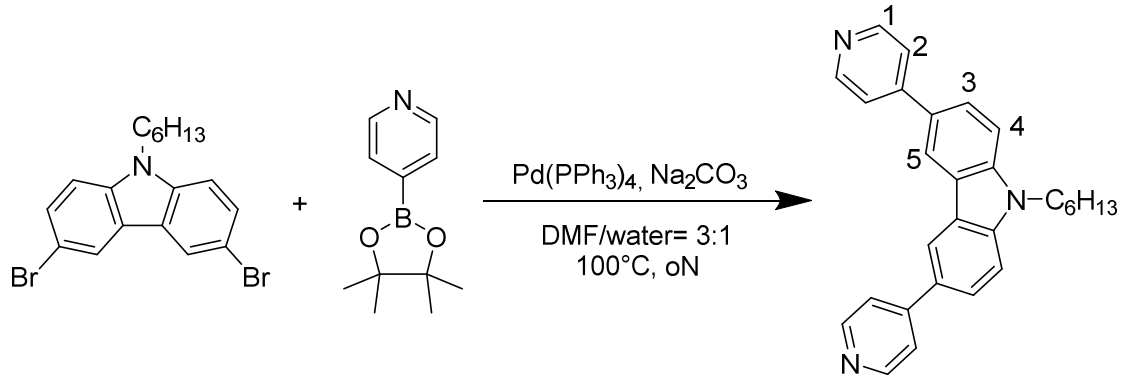

3,6-dibromo-9-hexyl-9H-carbazole (80 mg, 0.2 mmol, 1 eq), 4-(4,4,5,5-tetramethyl-1,3,2-dioxaborolan-2-yl)pyridine (160.4 mg, 0.78 mmol, 4 eq) Na_2CO_3 (62.2 mg, 0.59 mmol, 3 eq) and $Pd(Ph_3)_4$ (9 mg, 7.8 µmol, 4 mol%) were dissolved in 15 ml DMF/water (3:1) and immediately degassed. The stirring reaction took place at 100 °C overnight. After cooling down, 80 ml deionized water were added to the reaction vessel. It was extracted three times with 80 ml chloroform and the united organic phases were washed with 80 ml brine, 80 ml saturated aqueous NH_4Cl solution and 80 ml deionized water before drying over $MgSO_4$. The organic solvents were removed by rotary evaporator and the crude material was purified by column chromatography (SiO_2, acetone/n-pentane = 1:1) and GPC. Yield (before GPC): 26 mg, 0.06 mmol, 33 %).

^{1}H NMR (500 MHz, 298 K, DMSO-d_6) δ 8.87 (d, *J* = 1.8 Hz, 2H), 8.66 (d, *J* = 5.2 Hz, 4H), 7.99 (dd, *J* = 8.6, 1.9 Hz, 2H), 7.87 (dd, 4H), 7.79 (d, *J* = 8.6 Hz, 2H), 4.50 (t, *J* = 7.1 Hz, 2H), 1.82 (p, *J* = 7.1 Hz, 2H), 1.38 – 1.19 (m, 6H), 0.82 (t, *J* = 7.1 Hz, 3H).

^{13}C NMR (151 MHz, 298 K, $CDCl_3$) δ 149.11, 147.91, 140.42, 128.38, 124.23, 122.48, 118.09, 108.65, 42.49, 30.53, 27.97, 25.94, 21.51, 12.98.

MS (ESI(+)): *m/z* measured = 406.2293 $[M+H]^+$

m/z calculated = 406.2278 $[M+H]^+$

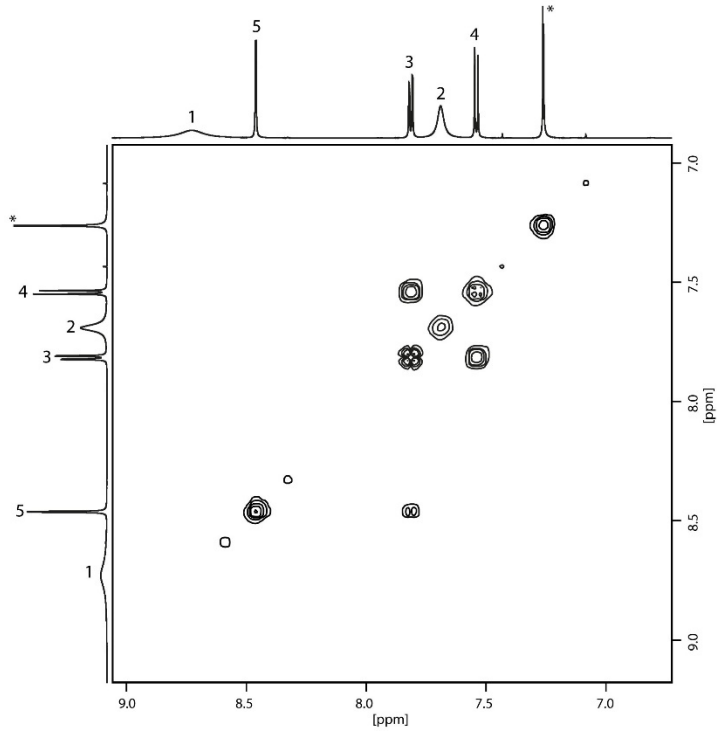

Figure 3.7 ^{1}H-^{1}H COSY NMR (500MHz/DMSO-d_6) NMR of ligand L^{SC4}. * marks $CHCl_3$, broadening of signal a lead to no ^{1}H-^{1}H COSY NMR cross-peak to b.

3.1.6 Synthesis of Ligand L^{SB}

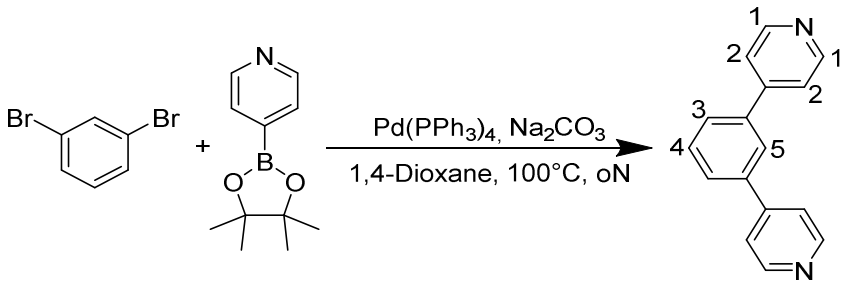

In a 200 ml Schlenk tube, 1,3-dibromobenzene (500 mg, 2.21 mmol, 1 eq), 4-(4,4,5,5-tetramethyl-1,3,2-dioxaborolan-2-yl) pyridine (1.3 g, 6.36 mmol, 3 eq), Na_2CO_3 (674 mg, 6.36 mmol, 3 eq) and $Pd(PPh_3)_4$ (74 mg, 64 µmol, 3 mol%) were suspended in 25 ml 1,4-dioxane and immediately degassed. Afterwards, the sealed vessel was heated up to 100 °C overnight and the reaction progress was controlled by TLC (pure acetone). The cooled down mixture was transferred to a separation funnel and 100 ml deionized water was added. The product was extracted three times with 80 ml chloroform and the united organic phases were washed with 100 brine and 100 ml deionized water before drying over $MgSO_4$. After removing the organic solvents with a rotary evaporator, the crude material was purified by column chromatography (SiO_2, pure acetone). GPC purification was performed before the ligand was used for further synthesis. White powder, Yield (before GPC): 381 mg (1.64 mmol, 77 %).

^{1}H NMR (500 MHz, 298 K, DMSO-d_6) δ 8.71 – 8.66 (dd, 4H), 8.20 (t, *J* = 1.9 Hz, 1H), 7.92 (dd, *J* = 7.7, 1.8 Hz, 2H), 7.88 – 7.85 (dd, 4H), 7.70 (t, *J* = 7.7 Hz, 1H).

^{13}C NMR (176 MHz, 298 K, DMSO-d_6) δ 150.73, 147.08, 138.69, 130.60, 128.14, 125.89, 122.02.

MS (ESI(+)): *m/z* measured = 233.1065 $[M+H]^+$

m/z calculated = 233.1073 $[M+H]^+$

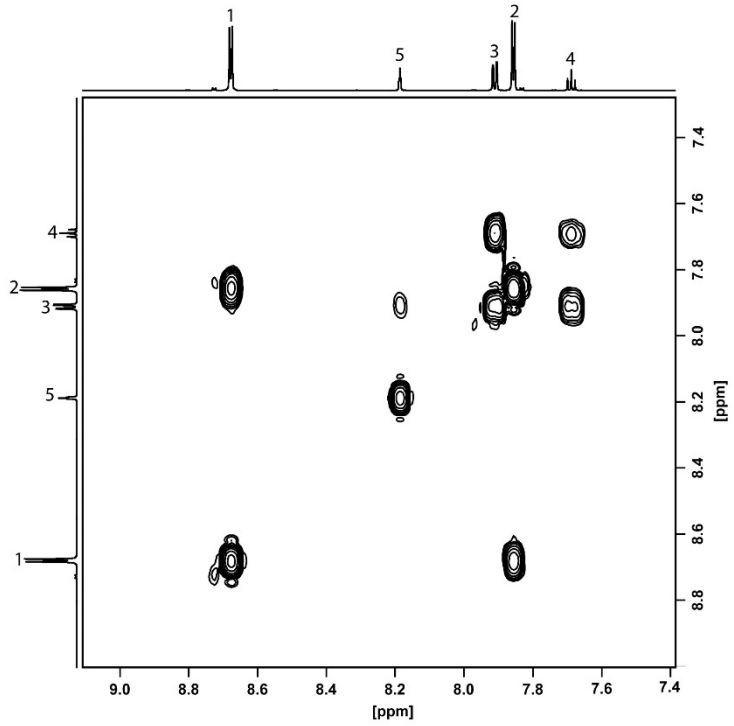

Figure 3.8 Partial ^{1}H-^{1}H COSY NMR (500MHz/DMSO-d_6) spectrum of ligand L^{SB}.

3.1.7 Synthesis of Ligand L^{SP}

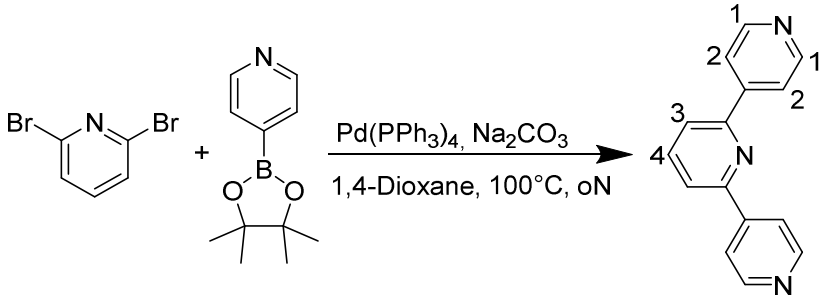

2,6-dibromopyridine (500 mg, 2.11 mmol, 1 eq), 4-(4,4,5,5-tetramethyl-1,3,2-dioxaborolan-2-yl) pyridine (1.3 g, 6.33 mmol, 3 eq), Na_2CO_3 (671 mg, 6.33 mmol, 3 eq) and $Pd(PPh_3)_4$ (73 mg, 63 µmol, 3 mol%) were added to a 200ml Schlenk tube. After addition of 25 ml 1,4-dioxane the vessel was directly degassed. The reaction was stirred overnight at 100 °C and controlled by TLC (pure acetone). After cooling down, the

suspension was transferred to a separation funnel and 100 ml deionized water was added. The suspension was extracted three times with 80 ml chloroform and the organic phase was washed with brine and deionized water (100 ml each). The dried solvent (over $MgSO_4$) was removed by rotary evaporator and the crude material was purified by column chromatography (SiO2, pure acetone) and GPC before the ligand was used for further synthesis. White powder, Yield (before GPC): 312 mg (1.34 mmol, 63 %).

^{1}H NMR (500 MHz, 298 K, DMSO-d_6) δ 8.78 – 8.76 (dd, 4H), 8.25 (d, *J* = 1.1 Hz, 1H), 8.24 – 8.21 (m, 5H), 8.16 (t, *J* = 8.6, 6.9 Hz, 1H).

^{13}C NMR (176 MHz, 298 K, DMSO-d_6) δ 154.05, 150.94, 145.63, 139.69, 121.92, 121.36.

MS (ESI(+)): *m/z* measured = 234.0985 $[M+H]^+$

m/z calculated = 234.1026 $[M+H]^+$

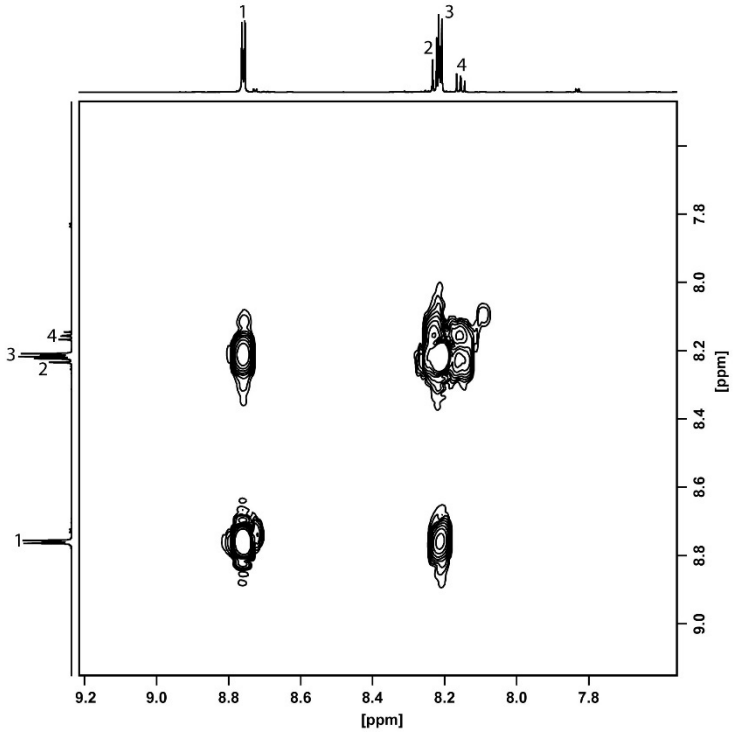

Figure 3.9 Partial ^{1}H-^{1}H COSY NMR (500MHz/DMSO-d_6) spectrum of ligand L^{SP}.

3.1.8 Synthesis of Ligand L^{SA}

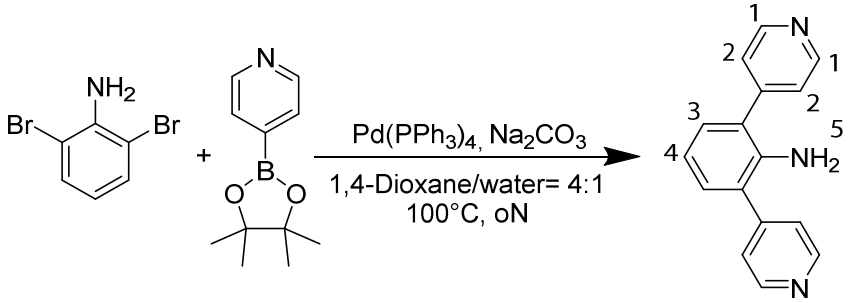

A 200 ml Schlenk tube was filled with 2,6-dibromoaniline (400 mg, 1.59 mmol, 1 eq), 4-(4,4,5,5-tetramethyl-1,3,2-dioxaborolan-2-yl) pyridine (981 mg, 4.78 mmol, 3 eq), Na_2CO_3 (507 mg, 4.78 mmol, 3 eq) and $Pd(PPh_3)_4$ (48 mg, 48 µmol, 3 mol%) and 20ml 1,4-dioxane/water = 4:1 and immediately degassed. The reaction took place at 100 °C overnight and was controlled by TLC (pure acetone). After cooling down, the suspension was transferred to a separation funnel and 80 ml deionized water was added. It was extracted three times with 70 ml chloroform and the united organic phases were washed with 80 ml brine and 80 ml deionized water before drying over $MgSO_4$. Purification was performed by column chromatography (SiO_2, pure acetone) and GPC before the synthesised ligand was used for cage synthesis. Greyish powder, Yield (before GPC): (1.43 mmol, 90 %).

^{1}H NMR (500 MHz, 298 K, $CDCl_3$) δ 8.73 (s, 4H), 7.55 (s, 4H), 7.13 (d, *J* = 7.6 Hz, 2H), 6.85 (t, *J* = 7.6 Hz, 1H), 4.60 (s, 2H).

^{13}C NMR (151 MHz, 298 K, DMSO-d_6) δ 150.57, 147.30, 141.82, 130.93, 125.19, 125.19, 118.08.

MS (ESI(+)): *m/z* measured = 248.1154 $[M+H]^+$

m/z calculated = 248.1182 $[M+H]^+$

Comment: Aniline-Group leads to extreme broadening of the aromatic signals of the pyridyl groups. No ^{1}H-^{1}H-COSY NMR.

3.1.9 Synthesis of Ligand L^{SOMe}

1,3-dibromo-2-methoxybenzene

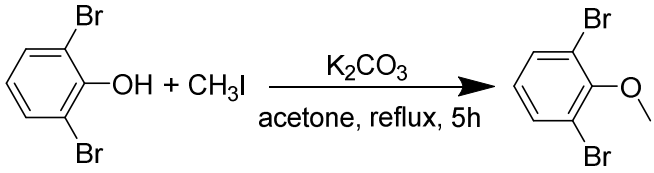

2,6-dibromophenol (1 g, 3.97 mmol, 1 eq) and K_2CO_3 was weight in a 100 ml single-neck round-bottom flask and solved in 50ml $acetone_{HPLC}$. Iodomethane (3.38 g, 3.1 ml, 23.82 mmol, 6 eq) was added dropwise via syringe. The reaction was refluxed for 5 hours and after cooling down, the solution was quenched with 50 ml of 10 % sodium thiosulfate. The suspension was extracted with chloroform (HPLC grade,3x50ml) and the organic phase was dried over $MgSO_4$ before the solvent was removed by rotary evaporator. The product was given as a colourless oil and was used for coupling reaction without further purification. Yield: 386 mg (1.45 mmol, 37 %).

^{1}H NMR (400 MHz, 298 K, DMSO-d_6) δ 7.67 (d, *J* = 8.0 Hz, 2H), 7.04 (t, *J* = 8.0 Hz, 1H), 3.80 (s, 3H).

MS (ESI(+)): *m/z* measured = 266.8824 $[M+H]^+$

m/z calculated = 266.8838 $[M+H]^+$

Final synthesis step of L^{SOMe}

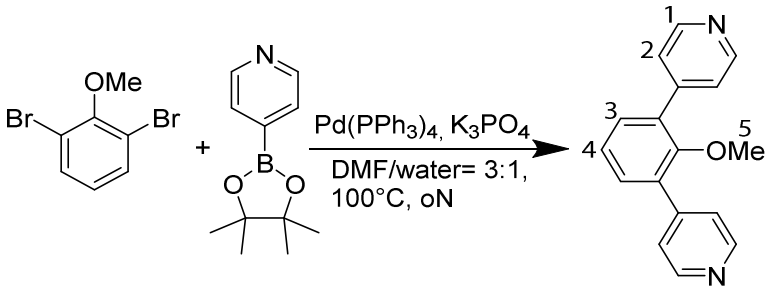

In a 200 ml Schlenk tube 1,3-dibromo-2-methoxybenzene (386 mg, 1.45 mmol, 1 eq), 4-(4,4,5,5-tetramethyl-1,3,2-dioxaborolan-2-yl)pyridine (893 mg, 4.35 mmol, 3 eq), K_3PO_4 (602 mg, 4.35 mmol, 3 eq) and $Pd(PPh_3)_4$ (50 mg, 44 µmol, 3 mol%) were placed and dissolved in 20ml DMF/water = 3:1 before it was immediately degassed. The reaction was stirred at 100 °C overnight and controlled by TLC. After cooling down, 80 ml deionized water were added to the into a separation funnel transferred reaction mixture. It was extracted three times with 80 chloroform and the united organic phases were washed with 80 brine and 80 ml deionized water before drying over $MgSO_4$. After removing the organic solvents by rotary evaporator, the crude material was purified by column chromatography (SiO_2, pure acetone). For further use, it was also necessary to purify the ligand by GPC to give a white powder. Yield (before GPC): 201 mg (0.77 mmol, 53 %).

^{1}H NMR (500 MHz, 298 K, $CDCl_3$) δ 8.71 – 8.68 (dd, 4H), 7.57 – 7.54 (dd, 4H), 7.43 (d, *J* = 7.6 Hz, 2H), 7.33 (t, *J* = 8.2, 7.0 Hz, 1H), 3.19 (s, 3H).

^{13}C NMR (151 MHz, 298 K, DMSO-d_6) δ 155.24, 150.21, 145.79, 133.17, 131.87, 125.59, 124.32, 61.42.

MS (ESI(+)): *m/z* measured = 263.1158 $[M+H]^+$

m/z calculated = 263.1179 $[M+H]^+$

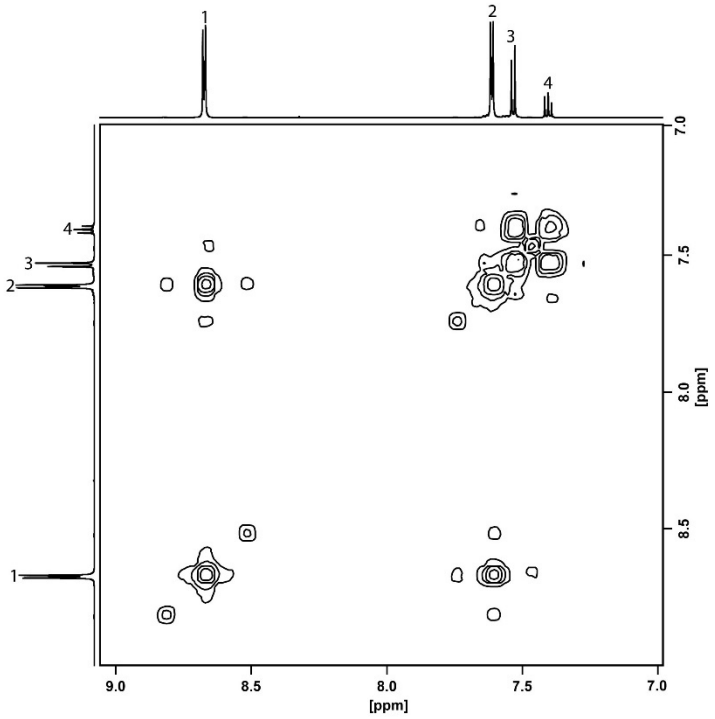

Figure 3.10 Partial ^{1}H-^{1}H COSY NMR (500MHz/DMSO-d_6) spectrum of ligand L^{SOMe}.

3.1.10 Synthesis of Ligands L^{SOH}

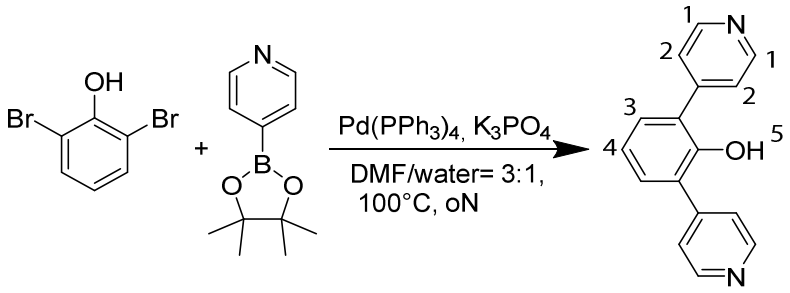

2,6-di(pyridin-4-yl)phenol (700 mg, 2.78 mmol, 1 eq), 4-(4,4,5,5-tetramethyl-1,3,2-dioxaborolan-2-yl)pyridine (1.71 g, 8.34 mmol, 3 eq), K_3PO_4 (1.15 g, 8.34 mmol, 3 eq) and $Pd(PPh_3)_4$ (96 mg, 83 µmol, 3 mol%) were placed in a 200 ml Schlenk tube and 20 ml DMF/water = 3:1 were added before the Schlenk tube was carefully degassed. The reaction was carried out at 100 °C under stirring overnight and controlled by TLC. After cooling down, the reaction mixture was transferred to a separation funnel and 80 ml deionized water were added. The aqueous suspension was three times extracted with 80 ml chloroform which was washed with brine, saturated aqueous NH_4Cl solution and 80 ml deionized water (each time 80 ml). After evaporating of the organic solvents, the crude material was purified by column chromatography and GPC for further use. White powder. Yield (before GPC): 251 mg (1.01 mmol, 36 %).

^{1}H NMR (500 MHz, 298 K, $CDCl_3$) δ 8.76 – 8.71 (dd, 4H), 7.55 – 7.50 (dd, 4H), 7.38 (d, *J* = 7.6 Hz, 2H), 7.21 – 7.15 (t, 1H), 5.58 (s, 1H).

^{13}C NMR (151 MHz, 298 K, DMSO-d_6) δ 151.39, 150.00, 146.47, 131.38, 129.27, 124.73, 121.74.

MS (ESI(+)): *m/z* measured = 252.8655 $[M+H]^+$

m/z calculated = 252.8681 $[M+H]^+$

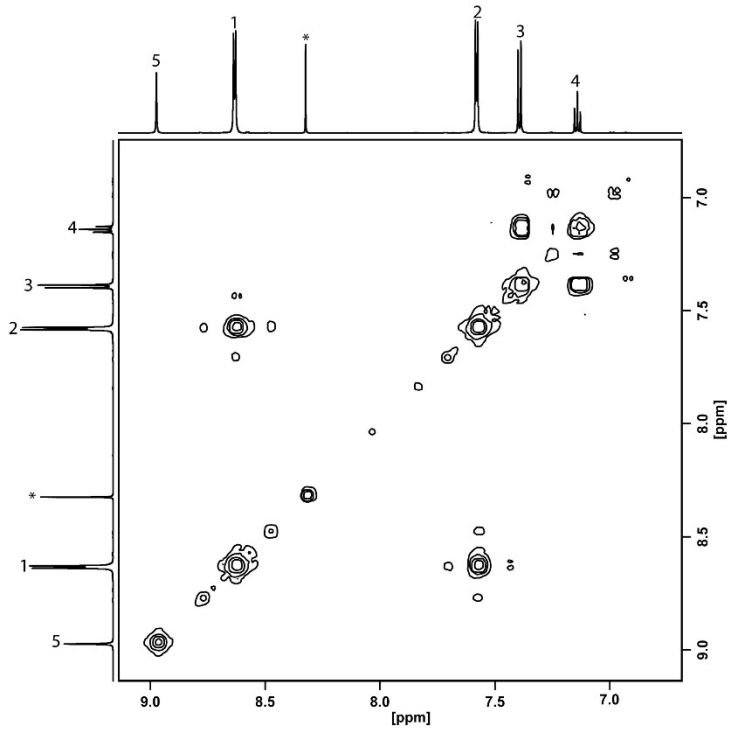

Figure 3.11 Partial ^{1}H-^{1}H COSY NMR (500MHz/DMSO-d_6) spectrum of ligand L^{SOH}. *-marked signal = Chloroform.

3.1.11 Synthesis of Ligand L^{SNO2}

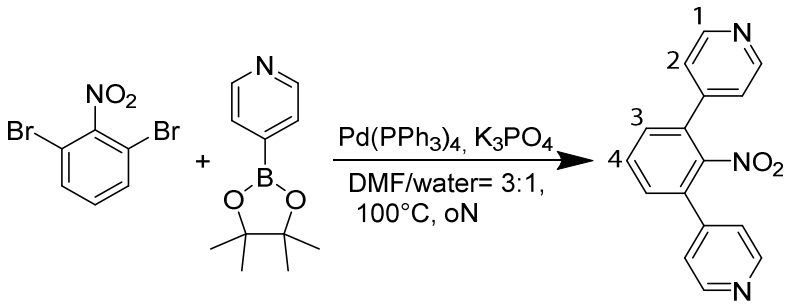

A 200 ml Schlenk tube with 2,6-di(pyridin-4-yl)phenol (700 mg, 2.49 mmol, 1 eq), 4-(4,4,5,5-tetramethyl-1,3,2-dioxaborolan-2-yl)pyridine (1.53 g, 7.48 mmol, 3 eq), K_3PO_4 (1.03 g, 7.48 mmol, 3 eq) and $Pd(PPh_3)_4$ (86 mg, 75 µmol, 3 mol%) and 20 ml DMF/water = 3:1 inside was prepared and immediately degassed. After no further

change of educts/product ratio occurred (TLC; pure acetone), the cooled down mixture was transferred into a separation funnel and mixed with 80 ml deionized water. The suspension was extracted three times with 80 ml chloroform. Brine and deionized water (each 80 ml) were successive used to wash the organic solvents before drying over $MgSO_4$. With removed solvents (rotary evaporator), the crude material was purified by column chromatography (SiO_2, pure acetone). For further synthetic use, the ligand was purified by GPC. Yellowish powder. Yield (before GPC): 385 mg (1.39 mmol, 56 %).

^{1}H NMR (500 MHz, 298 K, $CDCl_3$) δ 8.74 – 8.68 (dd, 4H), 7.70 (t, *J* = 8.1, 7.5 Hz, 1H), 7.51 (d, *J* = 7.7 Hz, 2H), 7.34 – 7.30 (dd, 4H).

^{13}C NMR (151 MHz, 298 K, DMSO-d_6) δ 150.68, 148.42, 143.93, 132.41, 132.12, 131.84, 123.22.

MS (ESI(+)): *m/z* measured = 278.0921 $[M+H]^+$

m/z calculated = 278.0924 $[M+H]^+$

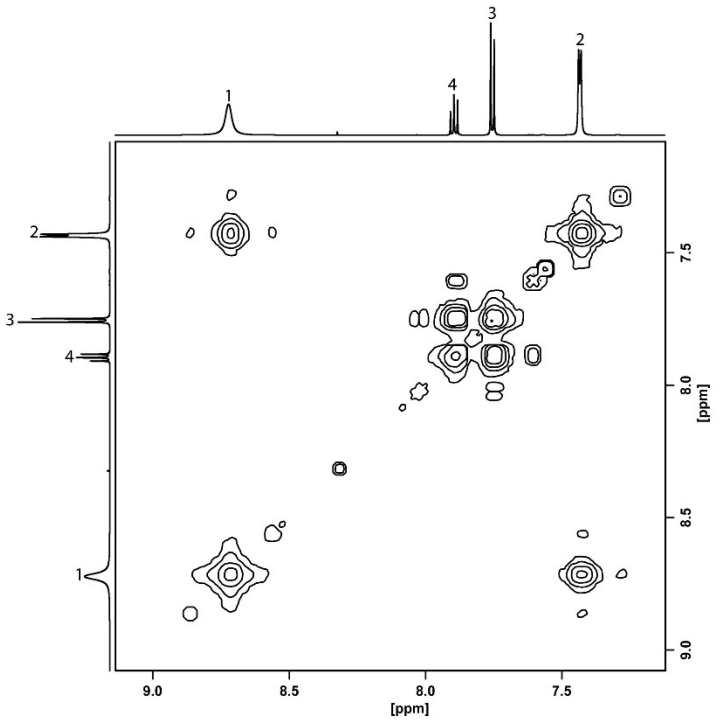

Figure 3.12 Partial ^{1}H-^{1}H COSY NMR (500MHz/DMSO-d_6) spectrum of ligand L^{SNO2}.

3.1.12 Synthesis of Ligand L^{LOMe}

8-((4-bromophenyl)ethynyl)isoquinoline was prepared like in chapter 6.2.2.1. descripted.

8-((4-((trimethylsilyl)ethynyl)phenyl)ethynyl)isoquinoline

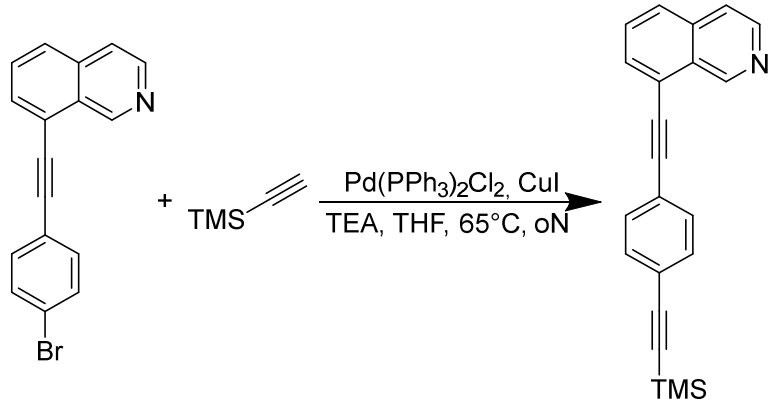

In a 200 ml Schlenk tube were given 8-((4-bromophenyl)ethynyl)isoquinoline (1.2 g, 3.89 mmol, 1 eq), ethynyltrimethylsilane (2.8 ml, 19.47 mmol, 5 eq), $Pd(PPh_3)_4Cl_2$ (137 mg, 195 µmol, 5 mol%) and CuI (148 mg, 779 µmol, 20 mol%). After adding 20 ml TEA_{dry} and 20 ml DMF_{dry} and carefully degassing, the reaction was heated up to 65 °C and stirred overnight. The reaction was controlled by TLC (n-pentane/EtOAc = 2:1) and after finishing and cooling down, the organic solvents were removed *via vacuo* Schlenk technique. The occurring solid was taken up in 100 ml TCM_{HPLC} and washed with 100 ml brine and 100 ml deionized water. Afterwards, the combined organic phases were dried over $MgSO_4$ and the solvent was removed via rotary evaporator. The crude material was purified by flash chromatography (SiO_2, n-pentane/EtOAc = 2:1) to give a brown oil. Yield: 1.1 g (3.46 mmol, 89 %).

^{1}H NMR (500 MHz, 298 K, DMSO-d_6) δ 9.75 (s, 1H), 8.67 (d, 1H), 8.06 (d, *J* = 8.3 Hz, 1H), 7.96 (d, *J* = 7.2 Hz, 2H), 7.84 (t, *J* = 7.7 Hz, 1H), 7.75 (d, *J* = 8.0 Hz, 2H), 7.56 (d, *J* = 7.9 Hz, 2H), 0.26 (s, 9H).

MS (ESI(+)): *m/z* measured = 326.1350 $[M+H]^+$

m/z calculated = 326.1360 $[M+H]^+$

8-((4-ethynylphenyl)ethynyl)isoquinoline

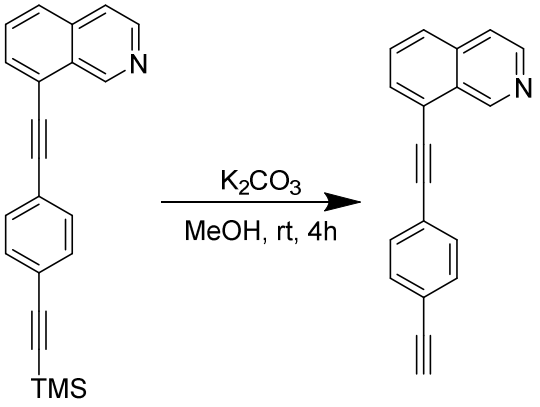

8-((4-((trimethylsilyl)ethynyl)phenyl)ethynyl)isoquinoline (1.1 g, 3.46 mmol, 1 eq) was placed in a 250 ml single-neck round-bottom flask and solved 100 ml $MeOH_{HPLC}$ before 622 mg K_2CO_3 (4.50 mmol, 1.3 eq) was added. The reaction took place under stirring for 4 hours. Afterwards, the methanol was removed by rotary evaporator before 100 ml TCM_{HPLC} was added and washed with three times 200 ml deionized water. After drying over $MgSO_4$, the organic solvent was removed by rotary evaporator and the product was obtained as a yellow solid. Yield: 751 mg (2.96 mmol, 86 %).

^{1}H NMR (500 MHz, 298 K, DMSO-d_6) δ 9.71 (s, 1H), 8.64 (d, *J* = 5.7 Hz, 1H), 8.07 (d, *J* = 8.3 Hz, 1H), 7.97 (d, *J* = 7.2 Hz, 1H), 7.94 (d, *J* = 5.6 Hz, 1H), 7.84 (t, *J* = 7.7 Hz, 1H), 7.77 (d, *J* = 7.9 Hz, 2H), 7.59 (d, *J* = 8.0 Hz, 2H), 4.42 (s, 1H).

MS (ESI(+)): *m/z* measured = 254.0943 $[M+H]^+$

m/z calculated = 254.0964 $[M+H]^+$

Final Sonogashira coupling to give L^{LOMe}

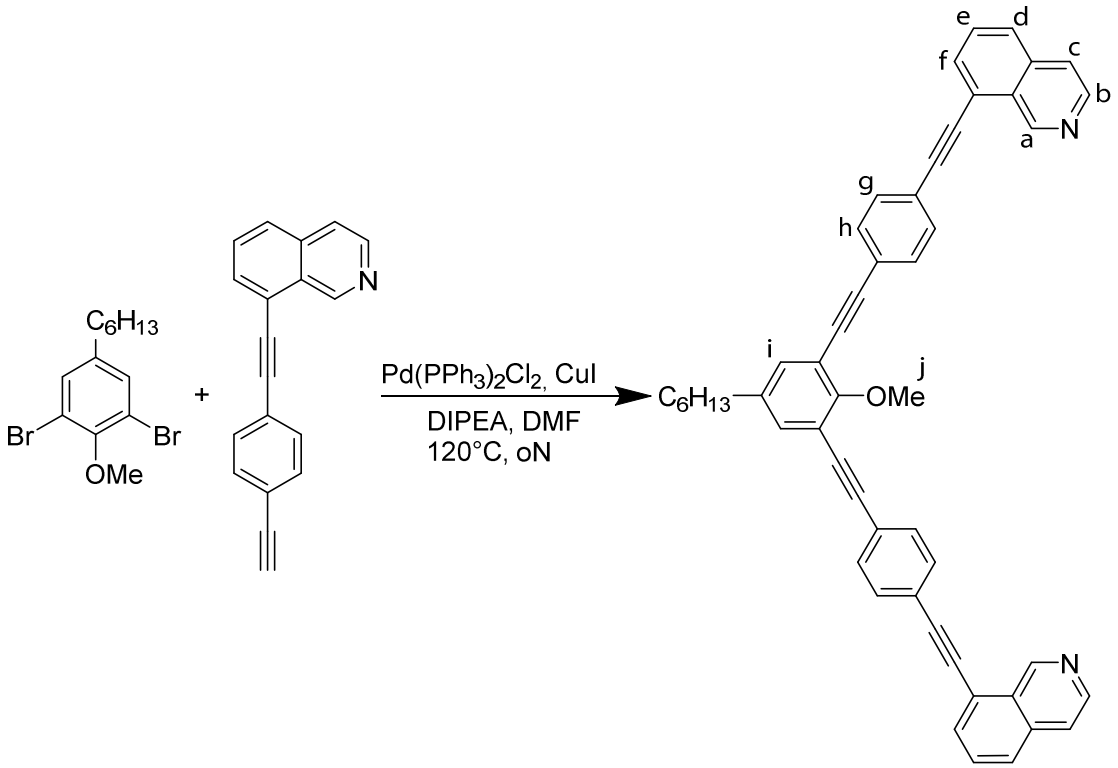

A 200 ml Schlenk tube was filled with 1,3-dibromo-5-hexyl-2-methoxybenzene (130 mg, 371 µmol, 1 eq), 8-((4-ethynylphenyl)ethynyl)isoquinoline (235 mg, 928 µmol, 2.5 eq), $Pd(PPh_3)_4Cl_2$ (26 mg, 37 µmol, 10 mol%) and CuI (14 mg, 74 µmol, 20 mol%). The solids were suspended in 20 ml DIPEA and 20 ml DMF and directly degassed. At 120 °C, the reaction was stirred for two days and controlled by TLC (n-pentane/EtOAc = 1:1). After removing of the solvents by *vacuo* Schlenk technique, the crude solid was taken up in 100 chloroform and washed with 100 brine and 100 ml deionized water. The organic solvent was dried over $MgSO_4$, removed by rotary evaporator and further purification by column chromatography (SiO_2, n-pentane/EtOAc = 1:1) and GPC took place.

^{1}H NMR (500 MHz, 298 K, DMSO-d_6) δ 9.75 (s, 2H), 8.66 (d, *J* = 5.6 Hz, 2H), 8.10 (d, *J* = 8.3 Hz, 2H), 8.02 – 7.95 (m, 6H), 7.90 – 7.82 (m, 6H), 7.72 – 7.67 (d, 2H), 7.48 (s, 2H), 4.10 (s, 3H), 2.59 (t, 2H), 1.60 (t, 2H), 1.18 (m, 6H), 0.92 – 0.84 (t, 3H).

^{13}C NMR (151 MHz, 298 K, DMSO-d_6) δ 159.99, 150.50, 144.33, 139.03, 135.89, 134.37, 132.60, 132.58, 132.19, 130.84, 128.44, 127.51, 123.40, 122.65, 121.30, 120.31, 116.63, 95.48, 93.47, 88.08, 61.82, 34.32, 31.55, 31.14, 28.72, 22.52, 14.46.

MS (ESI(+)): *m/z* measured = 695.3034 $[M+H]^+$

m/z calculated = 695.3057 $[M+H]^+$

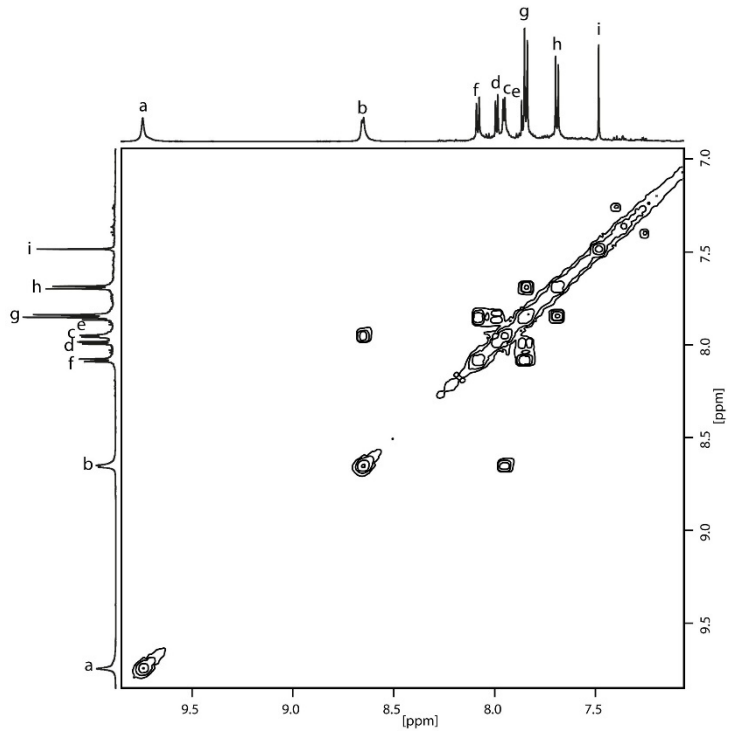

Figure 3.13 3.14 Partial ^{1}H-^{1}H COSY NMR (500MHz/DMSO-d_6) spectrum of ligand L^{LOMe}.

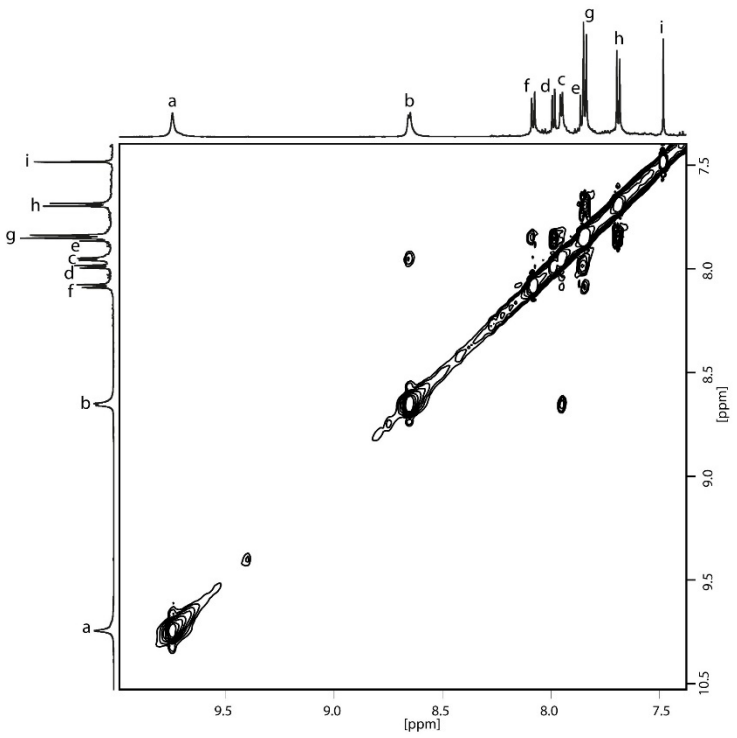

Figure 3.15 Partial ^{1}H-^{1}H NOESY NMR (700 MHz/DMSO-d_6) spectrum of ligand L^{LOMe}.

3.2 Formation of supramolecular Structures

3.2.1 Formation of homoleptic quinoline-based Cages

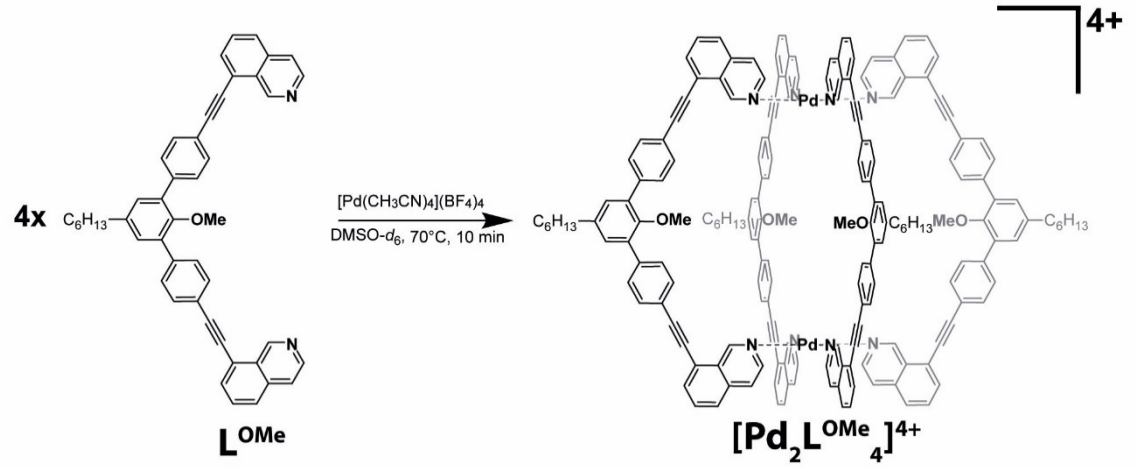

Schematic formation of homoleptic $[Pd_2\mathbf{L}^{\mathbf{OMe}}{}_4](BF_4)_4$. Exemplary for $[Pd_2\mathbf{L}^{\mathbf{OH}}{}_4](BF_4)_4$ and $[Pd_2\mathbf{L}^{\mathbf{LOMe}}{}_4](BF_4)_4$, too.

3.2.1.1 Synthesis of $[Pd_2L^{OMe}{}_4](BF_4)_4$

A 7 mM stock solution of ligand $\mathbf{L}^{\mathbf{OMe}}$ (240 µl, 1.68 µmol, CD_3CN or DMSO-d_6) and a 15 mM stock solution of $[Pd(CH_3CN)_4(BF_4)_2]$ (60 µl, 0.9 µmol, CD_3CN or DMSO-d_6) were placed into an NMR-tube and 300 µl CD_3CN/DMSO-d_6 were added. The sealed NMR-Tube was placed into a heating block for 2 hours to give a 0.7 mM $[Pd_2\mathbf{L}^{\mathbf{OMe}}{}_4](BF_4)_4$ slightly yellow cage solution.

^{1}H NMR (500 MHz, 298 K, CD_3CN) δ 9.75 (s, *J* = 0.9 Hz, 8H), 8.62 (d, *J* = 6.7 Hz, 8H), 8.10 (d, *J* = 8.1 Hz, 8H), 8.06 (d, *J* = 6.5 Hz, 8H), 8.02 (dd, *J* = 7.3, 1.3 Hz, 8H), 8.00 – 7.96 (t, 8H), 7.39 – 7.32 (d, 16H), 7.26 (s, 8H), 7.20 – 7.14 (d, 16H), 2.77 (q, *J* = 8.0 Hz, 8H), 2.02 (s, 12H), 1.81 – 1.73 (p, 8H), 1.46 – 1.23 (m, 24H), 0.86 (t, *J* = j7.1 Hz, 12H).

^{1}H NMR (500 MHz, 298 K, DMSO-d_6) δ 9.49 (s, 8H), 8.71 (d, *J* = 6.6 Hz, 8H), 8.32 (d, *J* = 6.8 Hz, 8H), 8.17 – 8.11 (m, 24H), 7.36 (d, *J* = 8.0 Hz, 16H), 7.29 (s, 8H), 6.82 (d, *J* = 7.9 Hz, 16H), 2.72 (q, *J* = 7.8 Hz, 8H), 2.07 (s, 12H), 1.69 (p, *J* = 7.5 Hz, 8H), 1.38 – 1.15 (m, 24H), 0.79 (t, *J* = 7.1 Hz, 12H).

^{13}C NMR (176 MHz, 298 K, CD_3CN) δ 173.18, 152.51, 144.39, 140.83, 140.37, 137.74, 135.02, 134.77, 131.56, 131.25, 130.55, 128.91, 128.50, 126.33, 121.91, 120.76, 97.05, 85.30, 60.49, 35.29, 32.08, 31.95, 29.18, 22.96, 14.00.

MS (ESI(+)): $[C_{188}H_{152}N_8O_4Pd_2]^{4+}$ *m/z* measured = 700.0001 $[M+H]^+$

m/z calculated = 700.0016 $[M+H]^+$

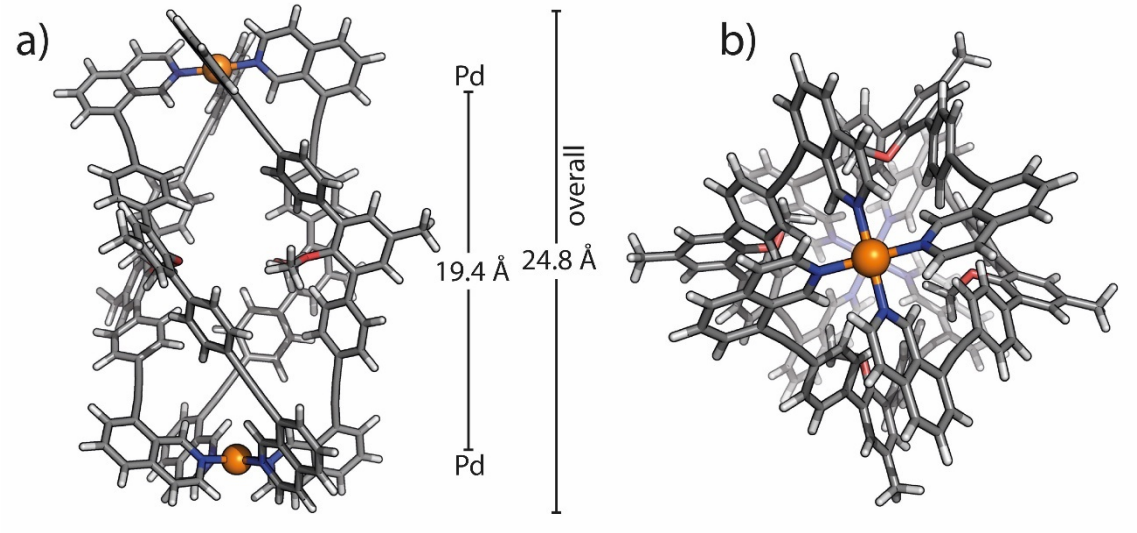

Figure 3.16 DFT (BP86-D4/def2-SVP (def2-TZVP for Pd)) calculated structure of (M)-$[Pd_2L^{OMe}{}_4]^{4+}$ in DMSO with a) top view and b) side view. Colour scheme: C = dark grey, H = light grey, O = red, N = blue, Pd = orange.

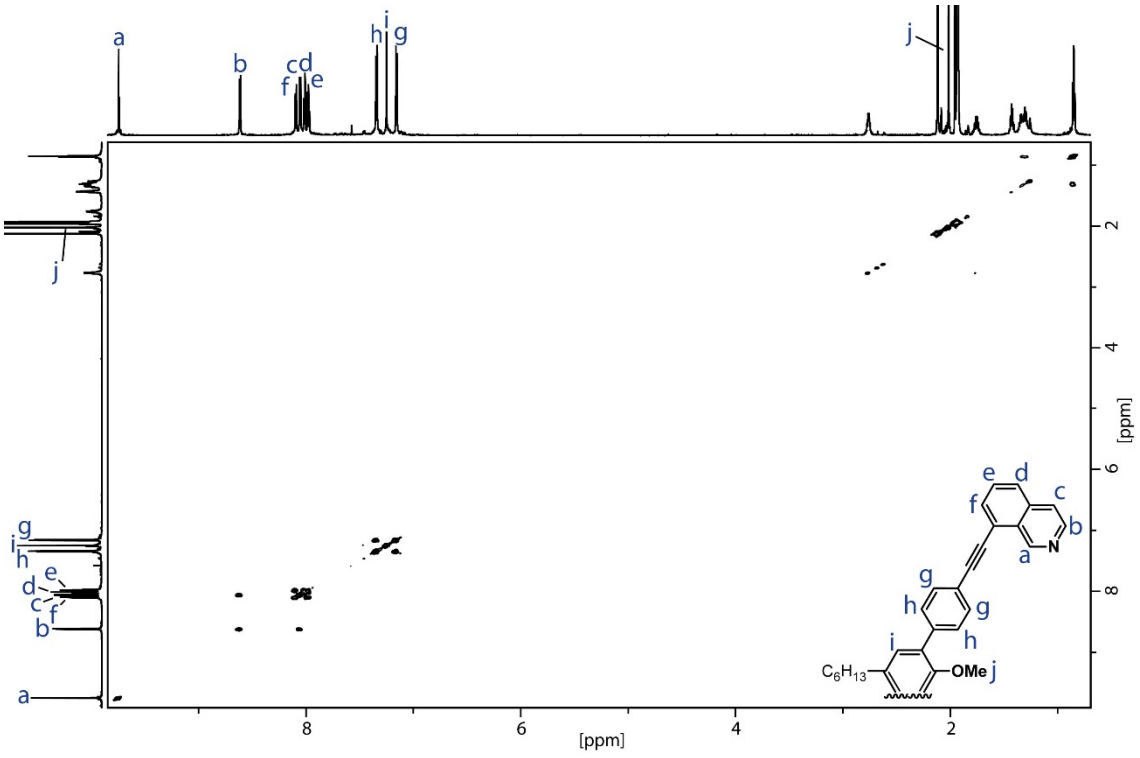

Figure 3.17 ^{1}H-^{1}H COSY NMR (700 MHz, 298 K, CD_3CN) spectrum of $[Pd_2L^{OMe}{}_4](BF_4)_4$.

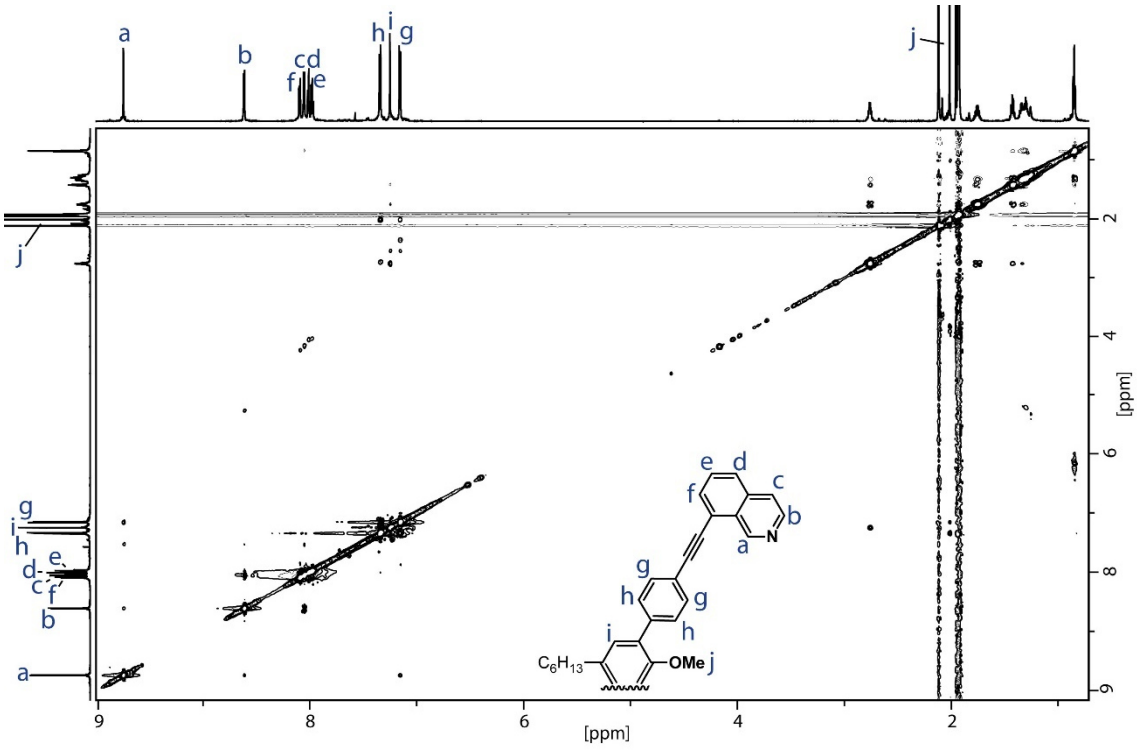

Figure 3.18 ^{1}H-^{1}H NOESY (700 MHz, 298 K, CD_3CN) spectrum of homoleptic $[Pd_2L^{OMe}_4](BF_4)_4$.

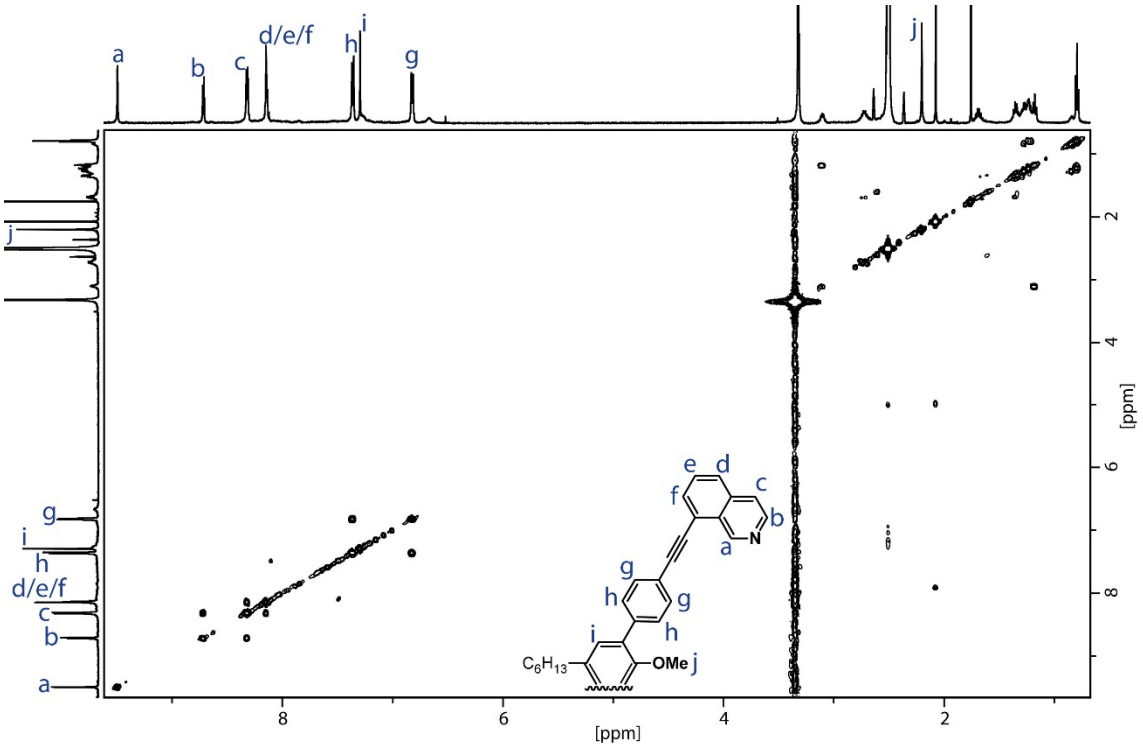

Figure 3.19 ^{1}H-^{1}H COSY NMR (700 MHz, 298 K, DMSO-d_6) spectrum of $[Pd_2L^{OMe}_4](BF_4)_4$.

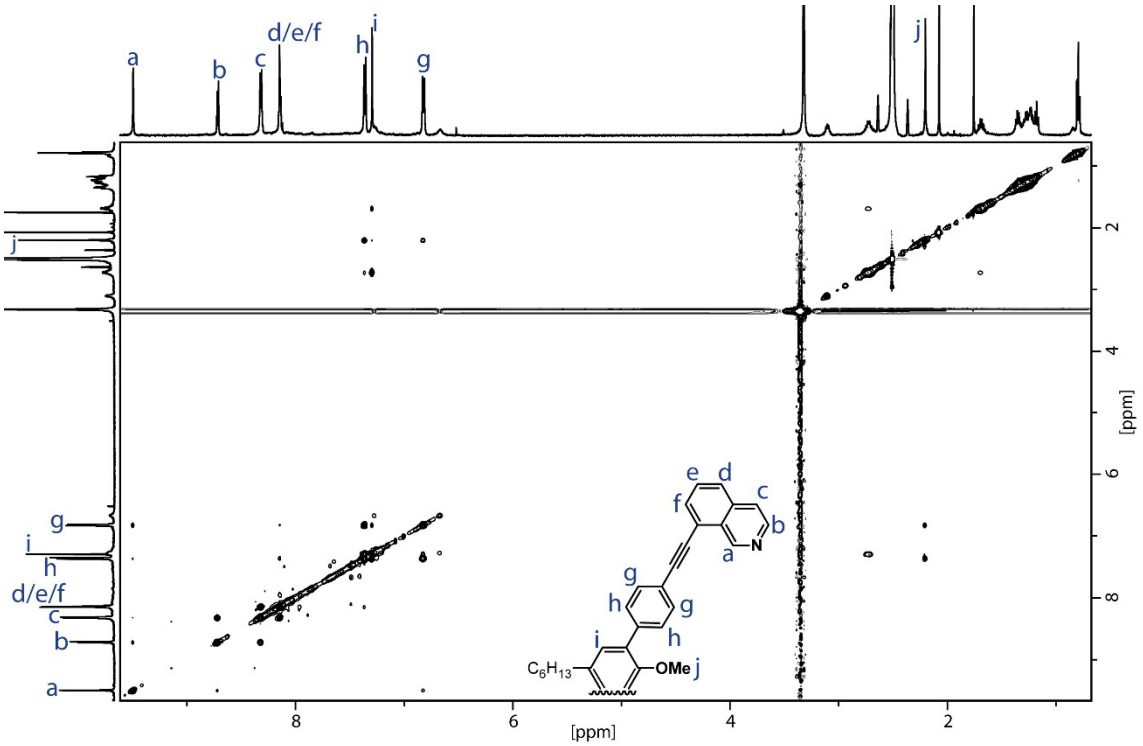

Figure 3.20 ^{1}H-^{1}H NOESY NMR (700 MHz, 298 K, DMSO-d_6) spectrum of $[Pd_2L^{OMe}{}_4](BF_4)_4$.

X-ray analysis

Single crystals were grown out of 200 µl 0.7 mM cage solutions placed in a tube with a diameter of 0.8 mm. This tube was closed with a cab in which a 1 mm wide hole was made. Afterwards, the tube was placed in a 5 ml vial containing 2 ml pure ethyl acetate of HPLC grade. The vial was closed and placed in a fridge at 4 °C for three weeks to get the single crystals. The sample was measured as described at the general procedures.

Table 2 Crystallographic data of $[Pd_2L^{OMe}{}_4](BF_4)_4$

CCDC number	/
Identifications code	rr45c
Empirical formula	$C_{760}H_{620}B_{16}F_{64}N_{36}O_{16}Pd_8$
Formula weight	12753.04
Temperature [K]	100(2)
Crystal system	triclinic
Space group (number)	$P\bar{1}$ (2)
a [Å]	17.6831(11)

b [Å]	22.9969(14)
c [Å]	43.681(3)
α [Å]	93.753(2)
β [Å]	90.399(2)
γ [Å]	99.232(2)
Volume [Å^3]	17492.9(19)
Z	1
ρ_{calc} [g/cm^3]	1.211
μ [mm^{-1}]	2.252
F(000)	6584
Crystal size [mm^3]	0.05×0.05×0.05
Crystal colour	yellow
Crystal shape	block
Radiation	CuK_α (λ =1.54178 Å)
2Θ range [°]	4.05 to 83.29 (1.16 Å)
Index ranges	-15 ≤ h ≤ 15 -19 ≤ k ≤ 19 -37 ≤ l ≤ 37
Reflections collected	165382
Independent reflections	23463 R_{int} = 0.0541 R_{sigma} = 0.0327
Completeness to θ = 41.647°	100.0 %
Data / Restraints / Parameters	23463/8414/4118
Goodness-of-fit on F^2	1.995
Final *R* indexes [*I*≥2σ(*I*)]	R_1 = 0.1272 wR_2 = 0.4061

Final *R* indexes [all data]	R_1 = 0.1445	wR_2 = 0.4227
Largest peak/hole [eÅ^3]	1.26/-0.82	

3.2.1.2 Synthesis of $[Pd_2L^{OH}_4](BF_4)_4$

In an NMR tube, 240 µl of a 7 mM $\mathbf{L^{OH}}$ stock solution (1.68 µmol) were combined with a 15 mM stock solution of $[Pd(CH_3CN)_4(BF_4)_2]$ (60 µl, 0.9 µmol, CD_3CN) and 300 µl pure CD_3CN. After sealing of the tube, the mixture was heated for 18 h to give a yellow cage solution of 0.7 mM $[Pd_2\mathbf{L^{OH}}_4](BF_4)_4$.

^{1}H NMR (500 MHz, 298 K, CD_3CN) δ 9.85 (s, 8H), 8.67 (d, *J* = 6.6 Hz, 8H), 8.09 (d, *J* = 8.2 Hz, 8H), 8.06 (d, *J* = 6.5 Hz, 8H), 8.02 (dd, *J* = 7.2, 1.3 Hz, 8H), 7.97 (dd, *J* = 8.1, 7.2 Hz, 8H), 7.42 – 7.38 (m, 16), 7.26 (d, *J* = 7.9 Hz, 16H), 7.17 (s, 8H),2.74 (q, *J* = 7.5 Hz, 8H), 1.77 (p, *J* = 11.2, 7.5, 3.7 Hz, 8H), 1.40 – 1.19 (m, 24H), 0.86 (t, *J* = 7.2 Hz, 12H).

^{13}C NMR (151 MHz, 298 K, CD_3CN) δ 153.78, 144.13, 137.76, 134.89, 134.49, 132.26, 132.23, 131.24, 130.62, 130.55, 130.42, 129.11, 128.81, 128.43, 126.28, 121.92, 97.39, 74.05, 35.03, 32.11, 32.05, 29.17, 22.98, 14.01.

MS (ESI(+)): $[C_{184}H_{144}N_8O_4Pd_2]^{4+}$ *m/z* measured = 685.9890 $[M+H]^+$

m/z calculated = 685.9859 $[M+H]^+$

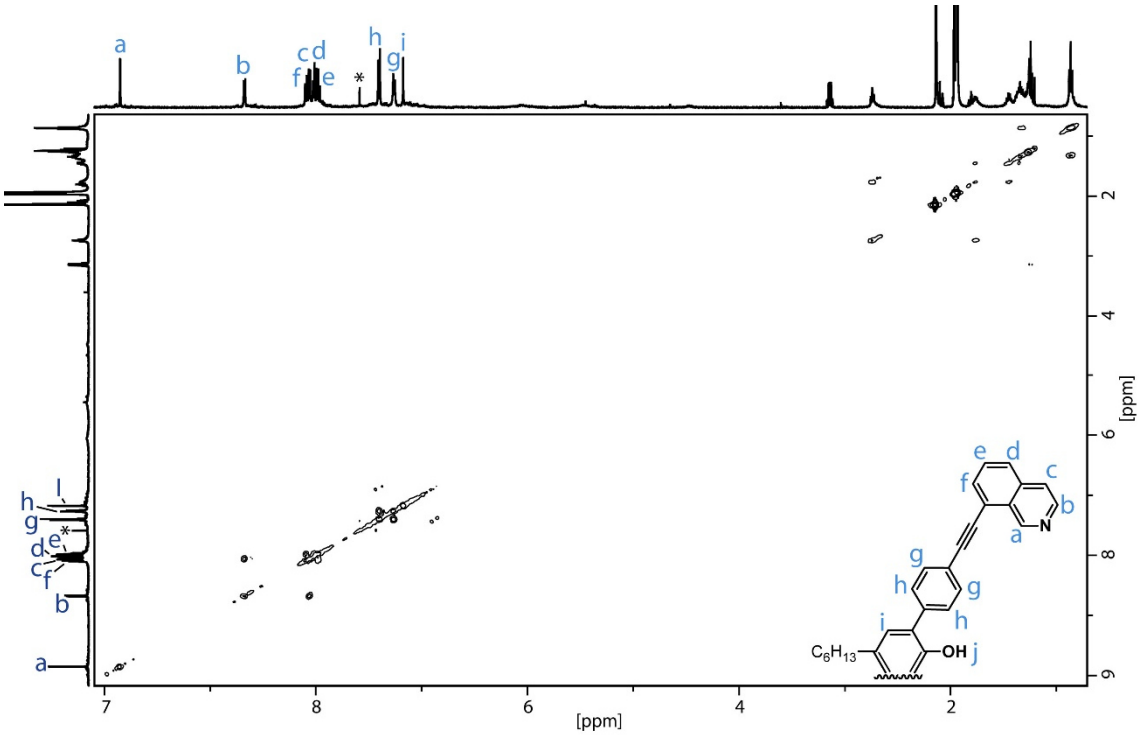

Figure 3.21 ^{1}H-^{1}H COSY NMR (600 MHz, 298 K, CD_3CN) spectrum of $[Pd_2L^{OH}_4](BF_4)_4$.

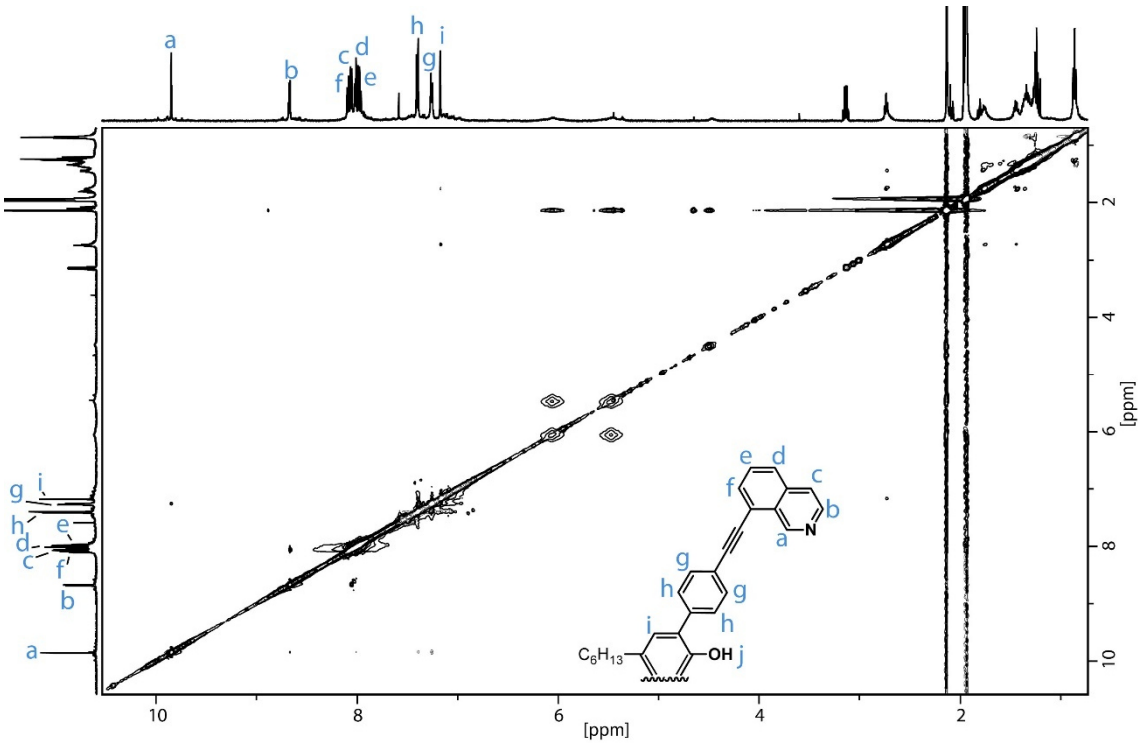

Figure 3.22 ^{1}H-^{1}H NOESY NMR (600 MHz, 298 K, DMSO-d_6) spectrum of $[Pd_2L^{OH}_4](BF_4)_4$.

3.2.1.3 Synthesis of $[Pd_2L^{LOMe}_4](BF_4)_4$

A 7 mM stock solution of $\mathbf{L^{LOMe}}$ was prepared and 240 µl (1.68 µmol) of this solution were combined with $[Pd(CH_3CN)_4(BF_4)_2]$ (60 µl, 0.9 µmol, CD_3CN) and 300 µl pure

CD_3CN. After sealing, the NMR tube was placed in a 70 °C hot heating block for 2 h to give a yellow $[Pd_2\mathbf{L}^{\mathbf{LOMe}}{}_4](BF_4)_4$ cage solution of 0.7 mM.

^{1}H NMR (500 MHz, 298 K, CD_3CN) shows less clean separated signals.

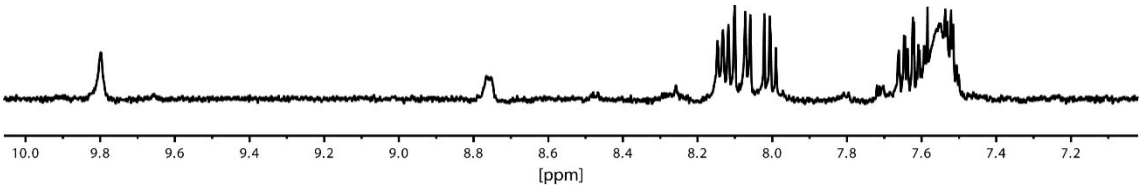

Figure 3.23 Partial ^{1}H NMR 500 MHz spectra at 298 K in CD_3CN. Measuring at higher temperatures lead to broadening of all signals. A clean signal assignment by 2D-NMR techniques was not possible.

MS (ESI(+)): $[C_{204}H_{152}N_8O_4Pd_2]^{4+}$ *m/z* measured = 747.9998 $[M+H]^+$

m/z calculated = 748.0017 $[M+H]^+$

3.2.2 Synthesis of heteroleptic $[Pd_2\mathbf{L}^{\mathbf{OMe}}{}_2\mathbf{L}^{\mathbf{X}}{}_2](BF_4)_4$ cages.

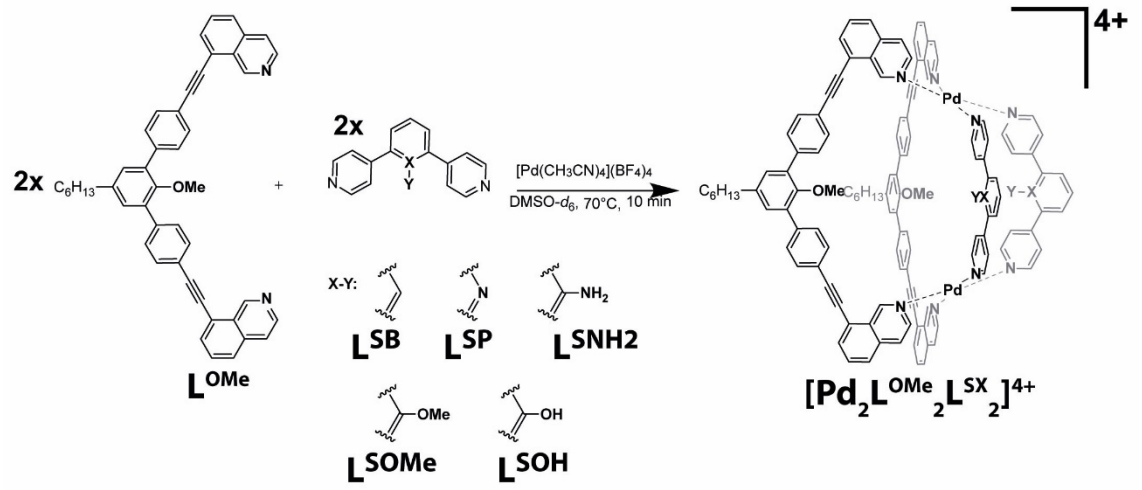

All heteroleptic Cages of the $[Pd_2\mathbf{L}^{\mathbf{OMe}}{}_2\mathbf{L}^{\mathbf{SX}}{}_2](BF_4)_4$ type are prepared as followed: In an NMR tube, 120 µl of a 7 mM stock solution of $\mathbf{L}^{\mathbf{OMe}}$ (1.68 µmol, DMSO-d_6) were combined with 120 µl of $\mathbf{L}^{\mathbf{SB}}$ $\mathbf{L}^{\mathbf{SP}}$, $\mathbf{L}^{\mathbf{SNH2}}$, $\mathbf{L}^{\mathbf{SOMe}}$, $\mathbf{L}^{\mathbf{SOH}}$ or $\mathbf{L}^{\mathbf{SNO2}}$ (7 mM, 1.68 µmol, DMSO-d_6), respectively. To each different ligand mixture, 60 µl of a 15 mM $[Pd(CH_3CN)_4(BF_4)_2]$ stock solution (0.9 µmol, DMSO-d_6) and 300 µl pure DMSO-d_6 were added. The sealed NMR tubes were heated for 10 min in a 70 °C warm heating block to give yellow but different shaded 0.7 mM cage solutions.

3.2.2.1 $[Pd_2L^{OMe}{}_2L^{SB}{}_2](BF_4)_4$

^{1}H NMR (700 MHz, 298 K, DMSO-d_6) δ 10.02 (s, 8H), 8.74 (s, 8H), 8.32 (d, *J* = 6.4 Hz, 4H), 8.29 (dd, *J* = 6.3, 3.2 Hz, 4H), 8.19 (d, *J* = 6.5 Hz, 4H), 8.15 – 8.11 (m, 8H), 8.04 (s, 8H), 7.91 (d, *J* = 7.7 Hz, 4H), 7.85 (s, 2H), 7.69 (d, *J* = 7.9 Hz, 8H), 7.64 (t, *J* = 7.6 Hz, 2H), 7.58 (d, *J* = 7.9 Hz, 8H), 7.27 (s, 4H), 2.61 (t, *J* = 7.8 Hz, 4H), 2.18 (s, 6H), 1.60 (t, *J* = 7.5 Hz, 4H), 1.35 – 1.26 (m, 12H), 0.87 – 0.83 (t, 6H).

^{13}C NMR (151 MHz, 298 K, DMSO-d_6) δ 169.81, 153.25, 150.51, 150.16, 142.60, 137.67, 137.62, 135.04, 132.52, 132.50, 131.73, 130.98, 129.95, 129.27, 128.73, 128.04, 127.74, 127.36, 126.43, 126.10, 123.27, 122.03, 119.48, 118.05, 116.44, 95.82, 83.68, 56.77, 29.42, 26.83, 20.85, 20.39, 12.32, -0.50.

MS (ESI(+)): $[C_{126}H_{100}N_8O_2Pd_2]^{4+}$ *m/z* measured = 492.6533 $[M+H]^+$

m/z calculated = 492.6517 $[M+H]^+$

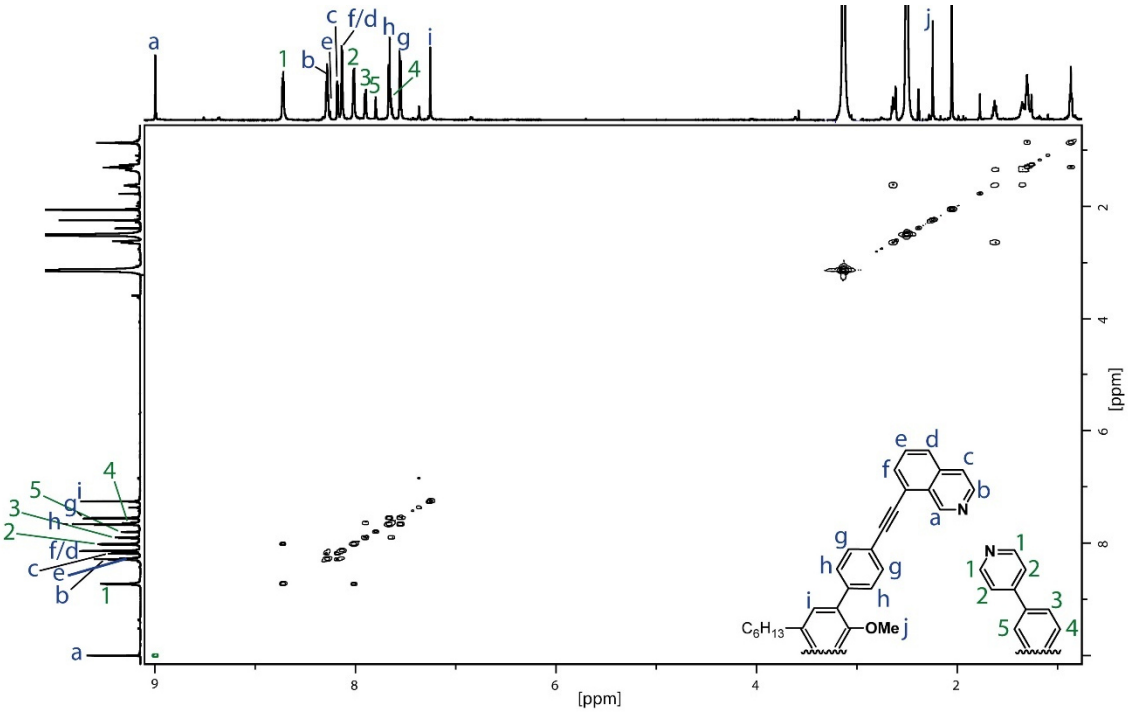

Figure 3.24 ^{1}H-^{1}H COSY NMR (700 MHz, 343 K, DMSO-d_6) spectrum of $[Pd_2L^{OMe}{}_2\ L^{SB}{}_2](BF_4)_4$.

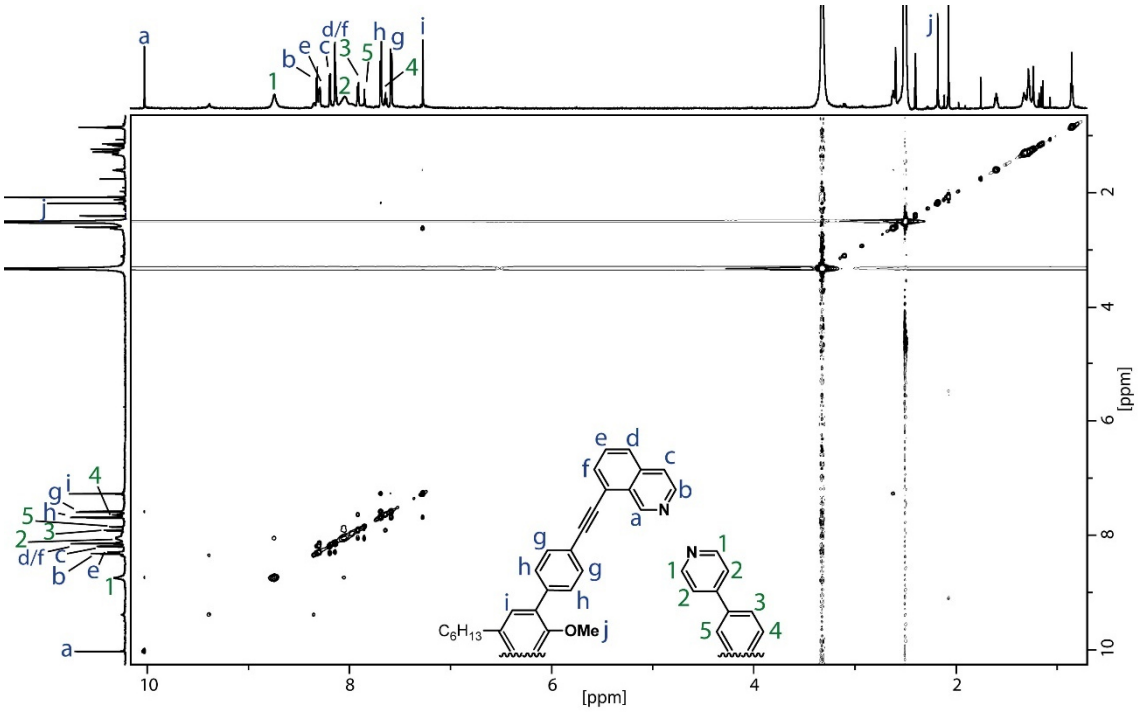

Figure 3.25 ^{1}H-^{1}H NOESY NMR (600 MHz, 298 K, DMSO-d$_6$) spectrum of [Pd$_2$L$^{OMe}_2$ L$^{SB}_2$](BF$_4$)$_4$.

3.2.2.2 [Pd$_2$L$^{OMe}_2$L$^{SP}_2$](BF$_4$)$_4$

Aromatic 1H signals not all clear to separate.

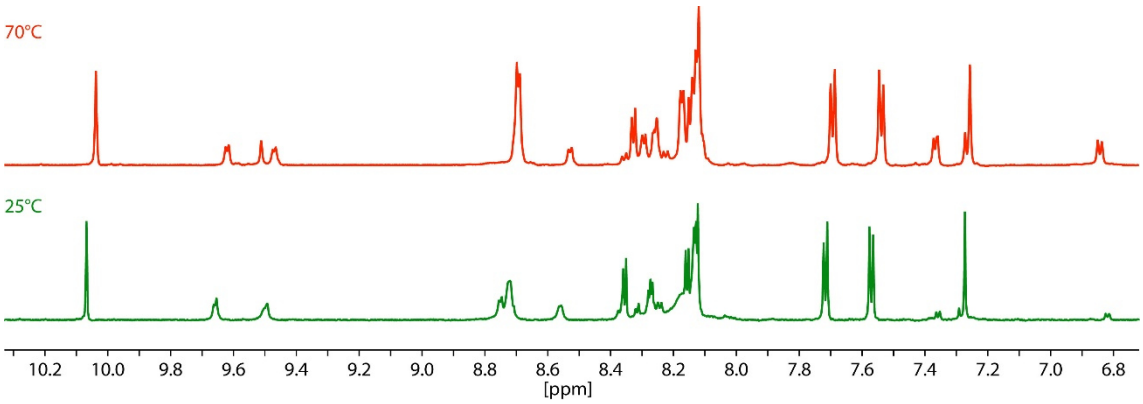

Figure 3.26 Aromatic signals of [Pd$_2$L$^{OMe}_2$L$^{SP}_2$](BF$_4$)$_4$. Not all signals are separated either at 25 °C or 70 °C.

^{13}C NMR (176 MHz, 298 K, DMSO-d$_6$) δ 165.82, 165.13, 163.61, 163.42, 161.67, 160.87, 157.84, 157.38, 155.79, 154.38, 149.93, 146.83, 143.97, 141.13, 140.26, 136.93, 133.26, 132.06, 131.39, 129.26, 127.28, 119.40, 117.82, 97.83, 89.55, 54.12, 34.24, 30.82, 28.23, 21.78, 13.71, 0.90.

MS (ESI(+)): [C$_{124}$H$_{98}$N$_{10}$O$_2$Pd$_2$]$^{4+}$ *m/z* measured = 493.1505 [M+H]$^+$

m/z calculated = 493.1493 [M+H]$^+$

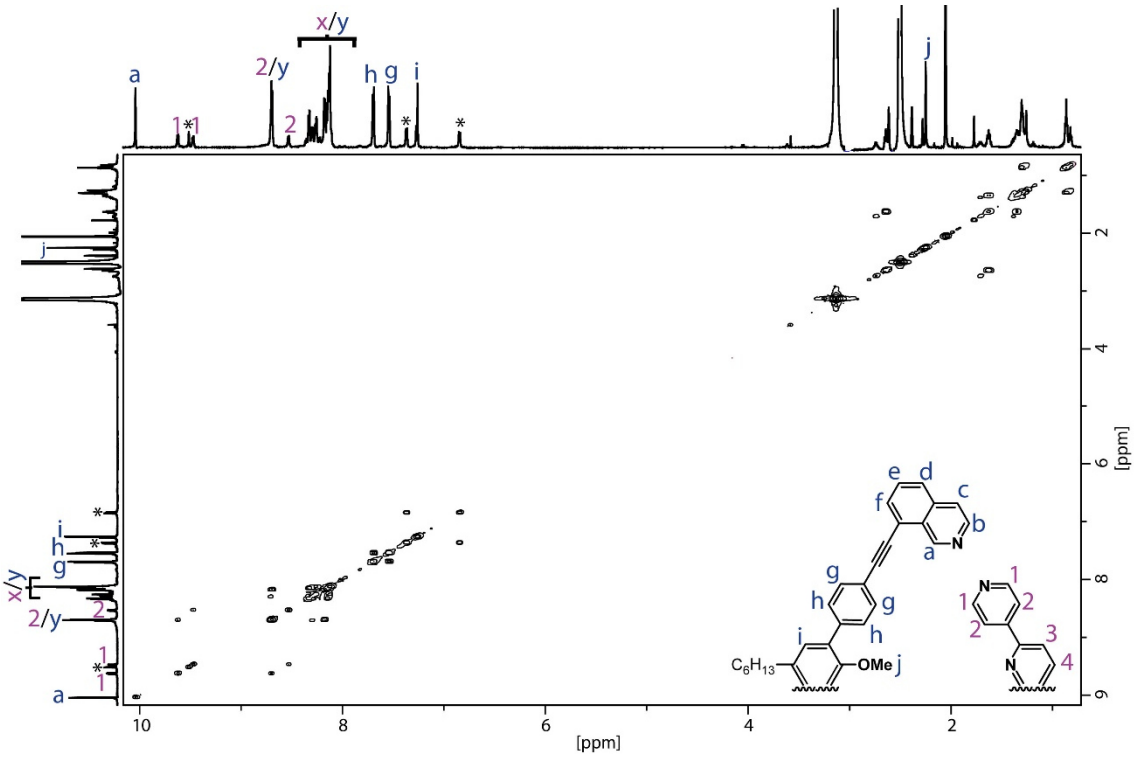

Figure 3.27 ^{1}H-^{1}H COSY NMR (600 MHz, 343 K, DMSO-d_6) spectrum of $[Pd_2L^{OMe}{}_2\ L^{SP}{}_2](BF_4)_4$.

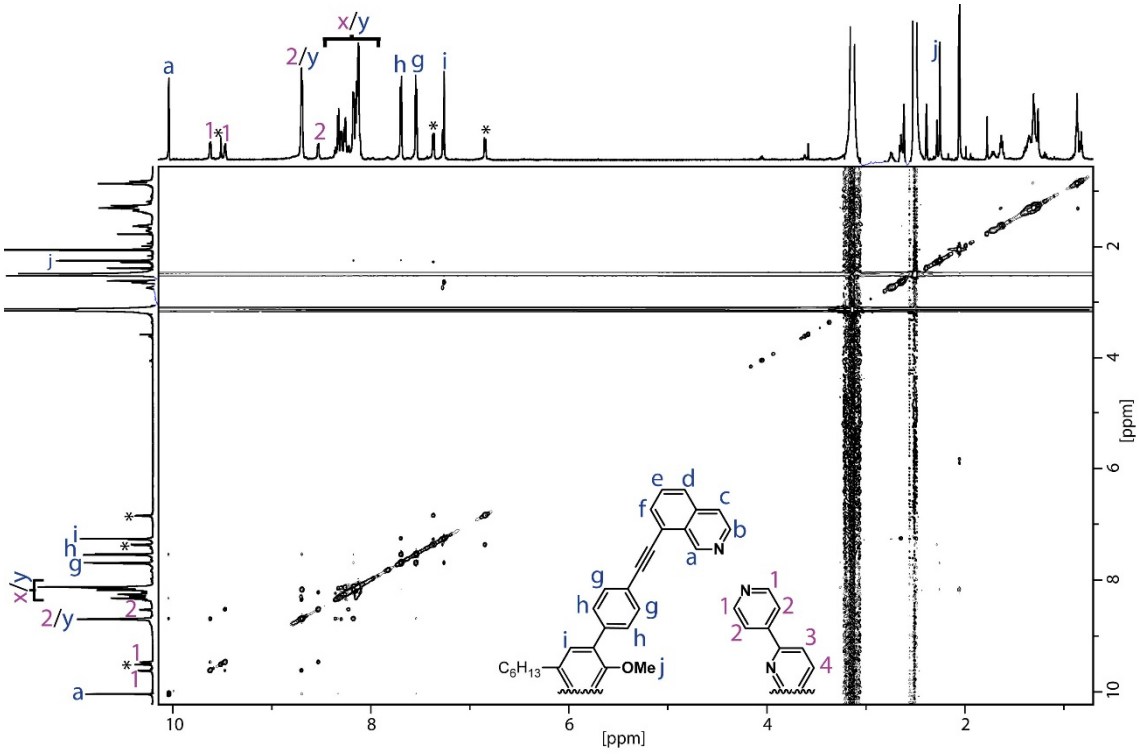

Figure 3.28 ^{1}H-^{1}H NOESY NMR (700 MHz, 343 K, DMSO-d_6) spectrum of $[Pd_2L^{OMe}{}_2\ L^{SP}{}_2](BF_4)_4$.

3.2.2.3 $[Pd_2L^{OMe}{}_2L^{SNH2}{}_2](BF_4)_4$

^{1}H NMR (700 MHz, 298 K, DMSO-d_6) δ 10.08 (s, 4H), 9.22 (d, *J* = 5.8 Hz, 4H), 9.06 (d, *J* = 5.9 Hz, 4H), 8.28 (d, *J* = 8.1 Hz, 4H), 8.25 (d, *J* = 6.4 Hz, 4H), 8.19 – 8.15 (m, 8H), 8.12 (t, *J* = 7.7 Hz, 4H), 7.79 (d, *J* = 7.8 Hz, 8H), 7.67 (d, *J* = 7.9 Hz, 8H), 7.63 (d, *J* = 5.9 Hz, 4H), 7.31 (s, 4H), 7.29 – 7.24 (d, 4H), 7.14 (d, *J* = 7.5 Hz, 4H), 6.71 (t, *J* = 7.5 Hz, 2H), 3,63 (s, 4H), 2.66 (t, *J* = 7.8 Hz, 4H), 2.33 (s, 6H), 1.63 (t, *J* = 7.6 Hz, 4H), 1.37 – 1.25 (m, 12H), 0.89 – 0.85 (t, 6H).

^{13}C NMR (151 MHz, 298 K, DMSO-d_6) δ 169.82, 152.76, 151.52, 150.36, 149.24, 149.08, 142.46, 139.26, 137.77, 134.97, 132.50, 131.98, 131.34, 129.99, 128.89, 127.89, 126.60, 126.17, 126.07, 125.46, 123.16, 122.38, 119.43, 118.17, 116.78, 116.44, 95.57, 83.56, 57.06, 29.44, 26.89, 20.85, 20.41, 12.34, -0.50.

MS (ESI(+)): $[C_{126}H_{102}N_{10}O_2Pd_2]^{4+}$ *m/z* measured = 500.1582 $[M+H]^+$

m/z calculated = 500.1572 $[M+H]^+$

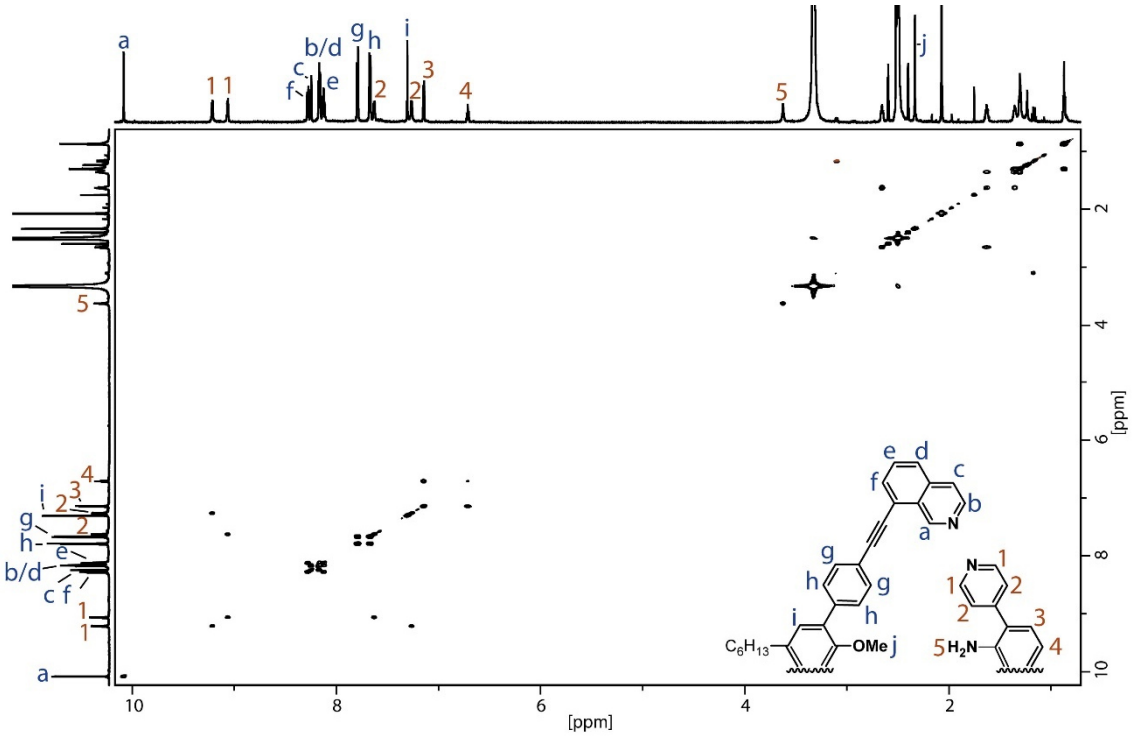

Figure 3.29 ^{1}H-^{1}H COSY NMR (700 MHz, 298 K, DMSO-d_6) spectrum of $[Pd_2L^{OMe}{}_2L^{SNH2}{}_2](BF_4)_4$.

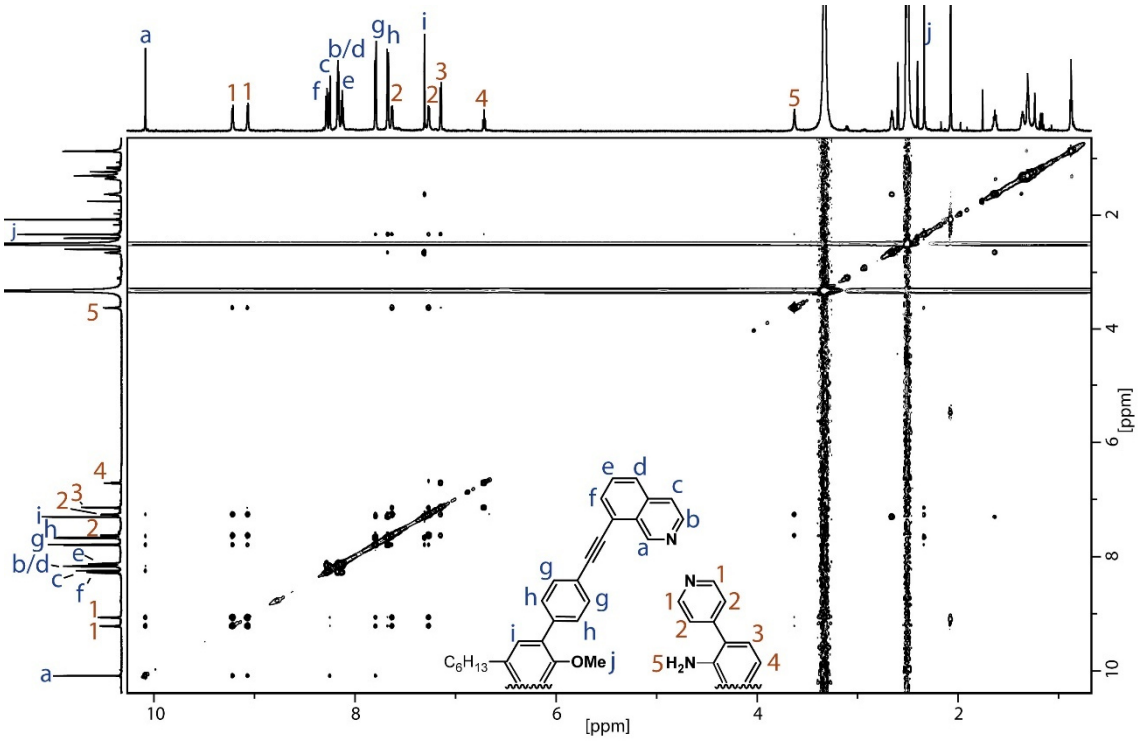

Figure 3.30 ^{1}H-^{1}H NOESY NMR (700 MHz, 298 K, DMSO-d$_6$) spectrum of [Pd$_2$L$^{OMe}_2$ L$^{SNH2}_2$](BF$_4$)$_4$.

3.2.2.4 [Pd$_2$L$^{OMe}_2$L$^{SOMe}_2$](BF$_4$)$_4$

^{1}H NMR (700 MHz, 298 K, DMSO-d$_6$) δ 9.84 – 9.81 (s, 8H), 8.85 (d, *J* = 5.4 Hz, 8H), 8.31 – 8.28 (d, 8H), 8.18 (d, *J* = 6.5 Hz, 4H), 8.16 – 8.12 (m, 8H), 7.83 (s, 8H), 7.65 (d, *J* = 8.1 Hz, 8H), 7.59 (d, *J* = 7.5 Hz, 4H), 7.49 – 7.46 (m, 8H), 7.29 (t, *J* = 7.6 Hz, 3H), 7.26 (s, 4H), 2.62 (t, 4H), 2.31 (s, 6H), 1.63 – 1.57 (p, 4H), 1.34 – 1.25 (m, 12H), 0.87 – 0.83 (t, 6H).

^{13}C NMR (151 MHz, 298 K, DMSO-d$_6$) δ 169.80, 152.93, 150.69, 147.71, 142.87, 137.50, 135.03, 132.51, 131.60, 131.25, 130.15, 129.81, 128.96, 128.70, 127.71, 127.16, 127.08, 126.25, 126.16, 123.85, 123.04, 119.43, 117.90, 116.44, 95.70, 83.37, 57.45, 29.41, 26.78, 20.85, 20.39, 12.30, -0.50.

MS (ESI(+)): $[C_{128}H_{104}N_8O_4Pd_2]^{4+}$ *m/z* measured = 507.6561 $[M+H]^+$

m/z calculated = 507.6570 $[M+H]^+$

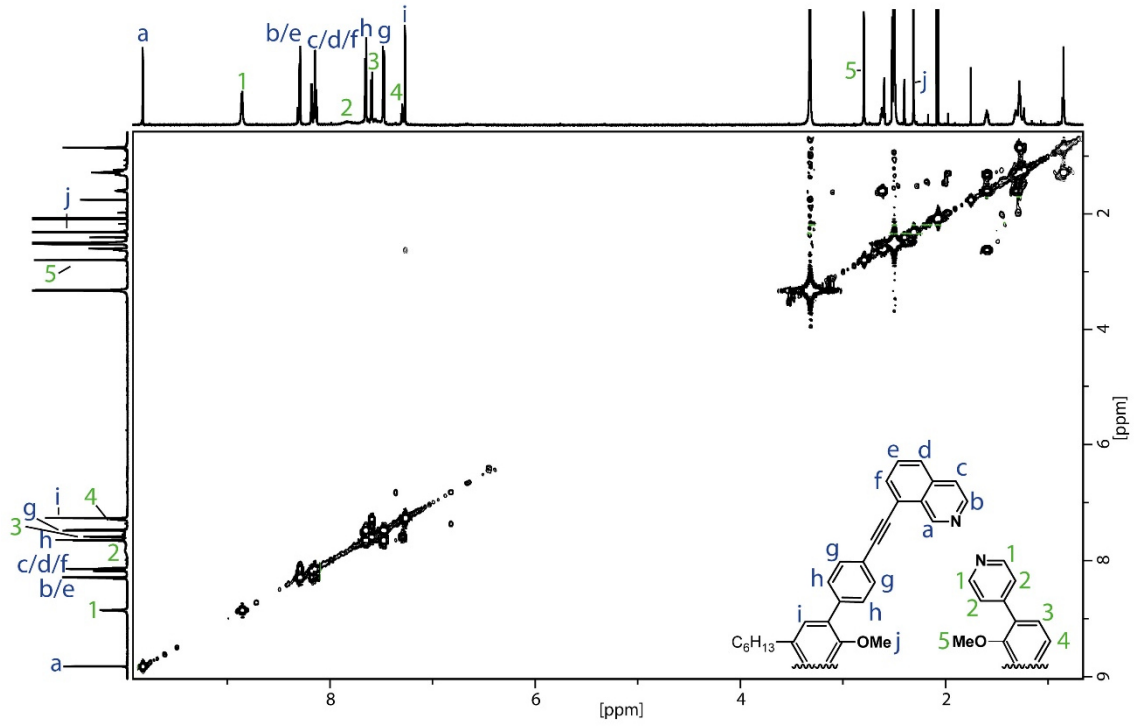

Figure 3.31 ^{1}H-^{1}H COSY NMR (700 MHz, 298 K, DMSO-d$_6$) spectrum of [Pd$_2$L$^{OMe}_2$ L$^{SOMe}_2$](BF$_4$)$_4$.

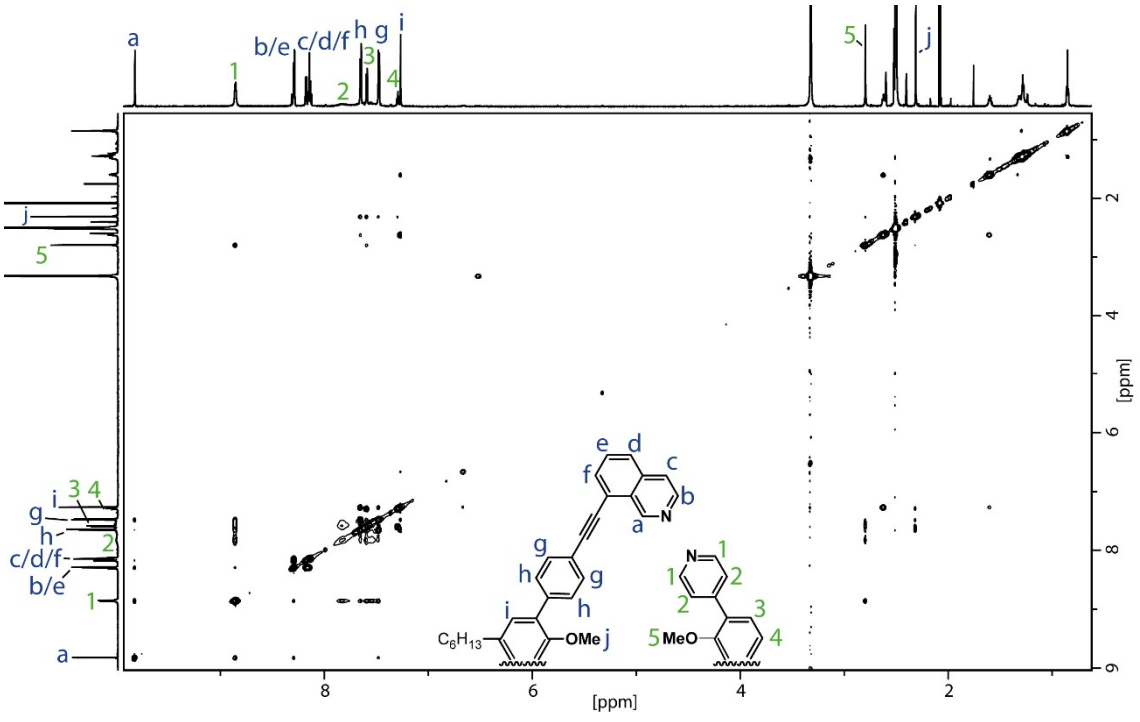

Figure 3.32 ^{1}H-^{1}H NOESY NMR (700 MHz, 298 K, DMSO-d$_6$) spectrum of [Pd$_2$L$^{OMe}_2$ L$^{SNH2}_2$](BF$_4$)$_4$.

3.2.2.5 [Pd$_2$L$^{OMe}_2$L$^{SOH}_2$](BF$_4$)$_4$

^{1}H NMR (400 MHz, 343 K, DMSO-d$_6$) δ 10.03 (s, 4H), 8.96 (d, *J* = 6.2 Hz, 8H), 8.31 – 8.24 (m, 6H), 8.19 – 8.09 (m, 14H), 7.71 (d, *J* = 8.4 Hz, 8H), 7.64 (d, *J* = 8.3 Hz, 8H),

7.58 (d, *J* = 5.8 Hz, 8H), 7.44 (d, *J* = 7.5 Hz, 4H), 7.27 (d, *J* = 2.3 Hz, 4H), 7.07 (t, *J* = 7.7 Hz, 2H), 2.67 (t, *J* = 3.8, 2.0 Hz, 4H), 2.33 (s, *J* = 3.8 Hz, 6H), 1.64 (p, *J* = 7.4 Hz, 4H), 1.42 – 1.28 (m, 12H), 0.91 – 0.85 (t, 6H).

^{13}C NMR (151 MHz, 298 K, DMSO-d_6) δ 169.80, 152.94, 152.92, 150.39, 147.98, 147.88, 142.48, 137.83, 137.70, 134.98, 132.48, 131.93, 131.19, 130.01, 128.90, 127.83, 126.32, 126.15, 125.98, 123.19, 119.79, 119.45, 118.15, 116.44, 95.65, 83.63, 56.78, 29.44, 26.88, 20.86, 20.41, 12.34, -0.50.

MS (ESI(+)): $[C_{126}H_{100}N_8O_4Pd_2]^{4+}$ *m/z* measured = 500.6488 $[M+H]^+$

m/z calculated = 500.6492 $[M+H]^+$

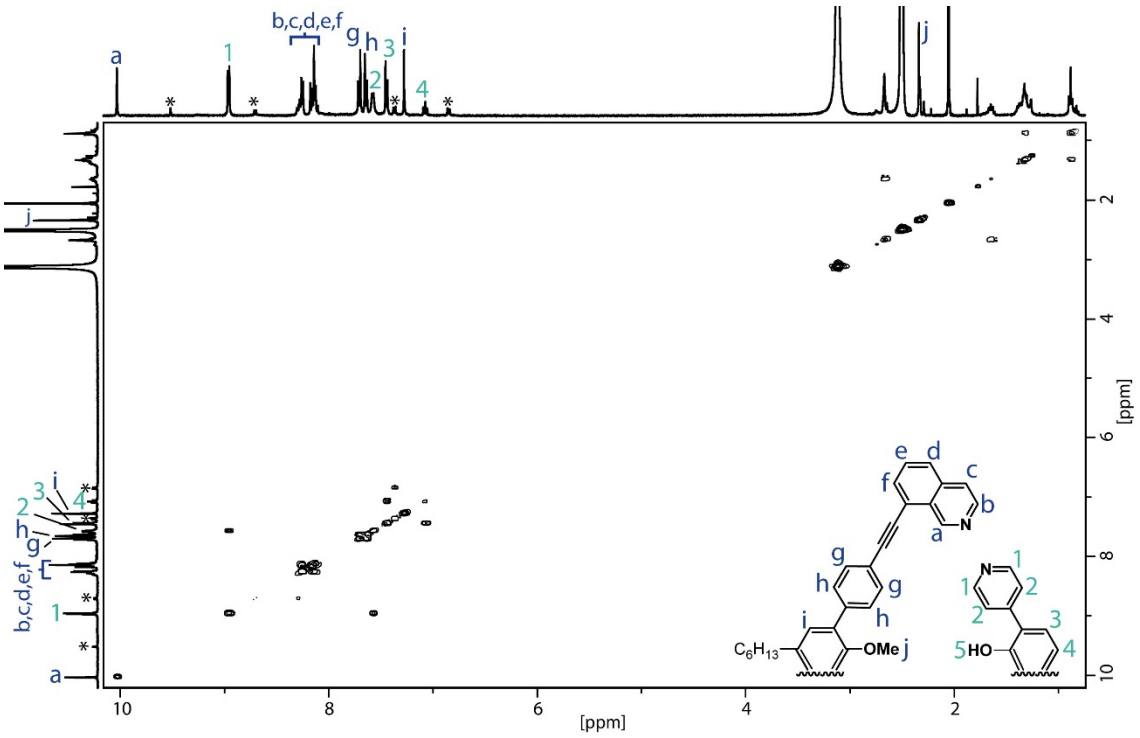

Figure 3.33 ^{1}H-^{1}H COSY NMR (400 MHz, 343 K, DMSO-d_6) spectrum of $[Pd_2L^{OMe}{}_2L^{SOH}{}_2](BF_4)_4$.

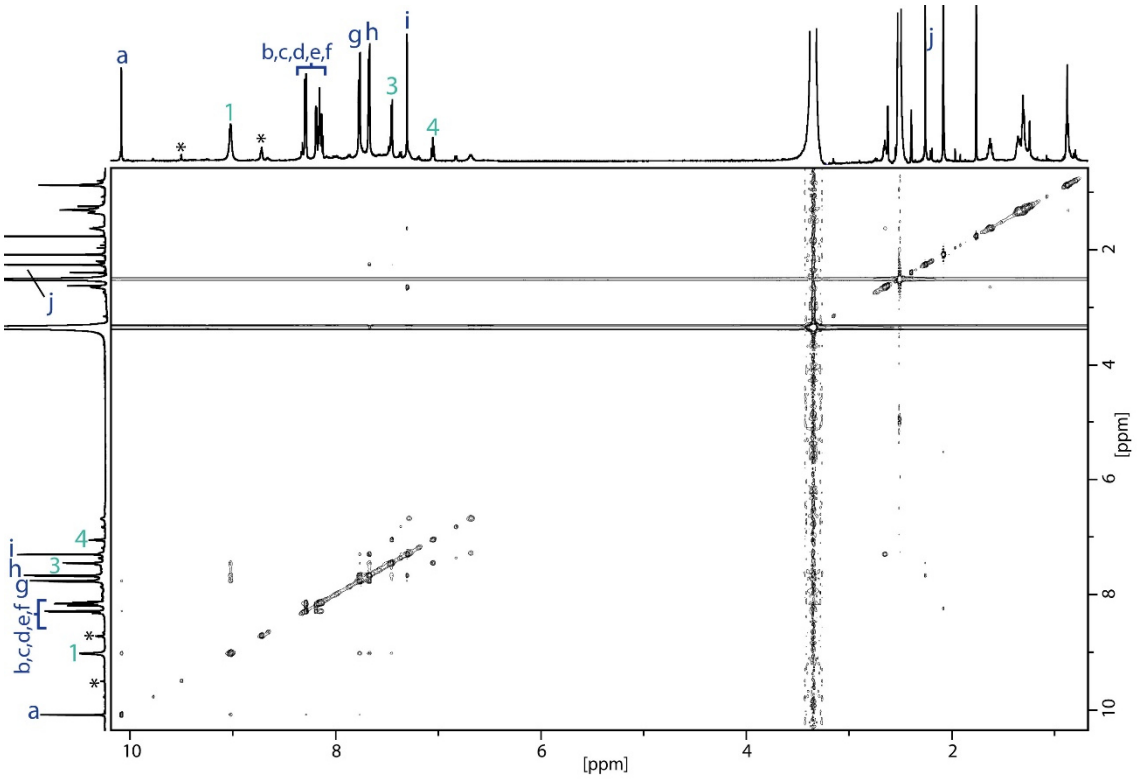

Figure 3.34 ^{1}H-^{1}H NOESY NMR (600 MHz, 298 K, DMSO-d_6) spectrum of $[Pd_2L^{OMe}_2L^{SOH}_2](BF_4)_4$.

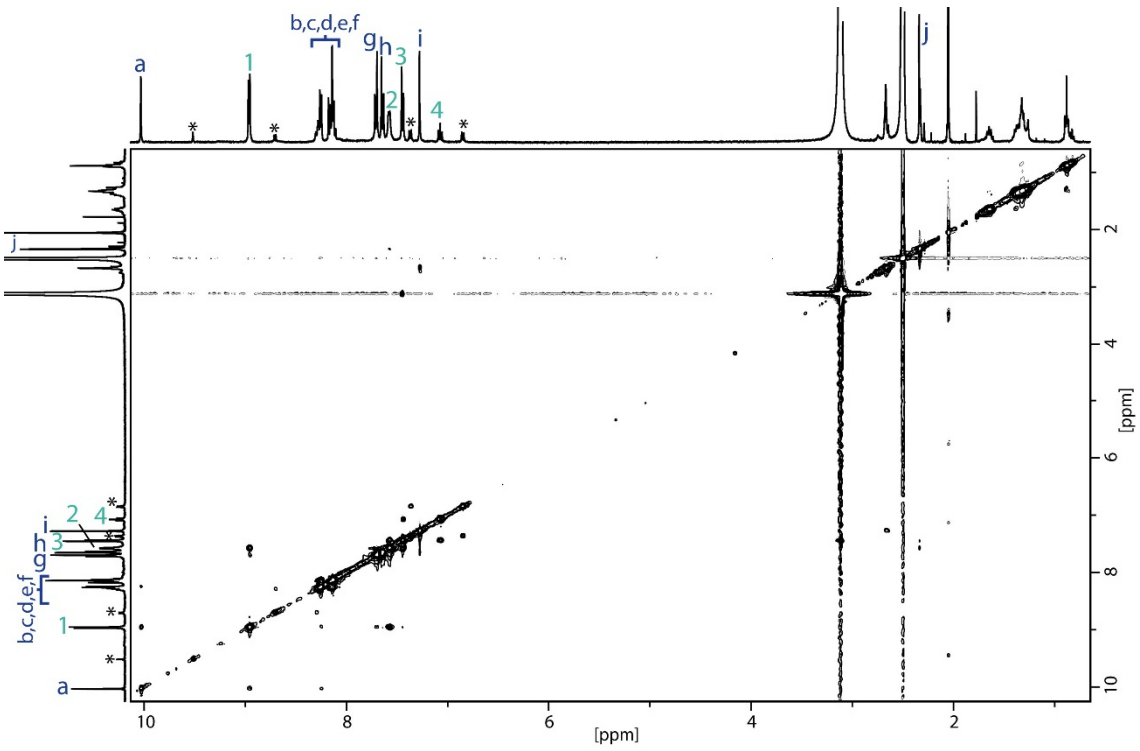

Figure 3.35 ^{1}H-^{1}H NOESY NMR (400 MHz, 343 K, DMSO-d_6) spectrum of $[Pd_2L^{OMe}_2L^{SOH}_2](BF_4)_4$.

3.2.3 Synthesis of the $[Pd_2L^{OMe}{}_2L^{SB}L^{SNO2}](BF_4)_4$.

$[Pd_2L^{OMe}{}_2L^{SB}L^{SNO2}](BF_4)_4$ and similar were prepared as followed: In an NMR tube, 120 µl of a 7 mM L^{OMe} stock solution (1.68 µmol, DMSO-d_6) was combined with 60 µl of L^{SB} and 60 µl L^{SNO2} (0.84 µmol, DMSO-d_6). 60 µl (0.9 µmol) of a 15 mM stock solution of $[Pd(CH_3CN)_4(BF_4)_2]$ in DMSO-d_6 and 300 µl pure DMSO-d_6 were added. The sealed NMR tubes were heated for 10 min inside a heating block at 70 °C to give a slightly yellow solution.

3.2.3.1 $[Pd_2L^{OMe}{}_2L^{SB}L^{SNO2}](BF_4)_4$

^{1}H NMR (700 MHz, 298 K, DMSO-d_6) δ 9.96 (s, 2H), 9.92 (s, 2H), 9.30 (d, *J* = 5.8 Hz, 2H), 9.23 (d, *J* = 5.9 Hz, 2H), 8.79 (d, *J* = 6.0 Hz, 4H), 8.28 (d, *J* = 7.9 Hz, 4H), 8.25 (t, *J* = 6.1 Hz, 4H), 8.18 (d, *J* = 6.6 Hz, 2H), 8.16 (d, *J* = 6.8 Hz, 4H), 8.14 – 8.11 (m, 6H), 7.94 (d, *J* = 3.2 Hz, 4H), 7.87 (d, 4H), 7.80 (d, *J* = 7.6, 1.7 Hz, 2H), 7.75 (d, *J* = 8.1 Hz, 4H), 7.69 – 7.66 (m, 5H), 7.60 (d, *J* = 8.1 Hz, 4H), 7.59 – 7.57 (m, 2H), 7.53 (d, *J* = 8.1 Hz, 4H), 7.28 (s, 2H), 7.25 (s, 2H), 7.08 (dd, *J* = 5.9, 2.2 Hz, 2H), 2.63 (q, 4H), 2.47 (s, 3H), 2.19 (s, 3H), 1.61 (p, *J* = 7.1 Hz, 4H), 1.31 – 1.26 (m, 12H), 0.87 – 0.84 (m, 6H).

MS (ESI(+)): $[C_{126}H_{99}N_9O_4Pd_2]^{4+}$ *m/z* measured = 503.8941 $[M+H]^+$

m/z calculated = 503.8980 $[M+H]^+$

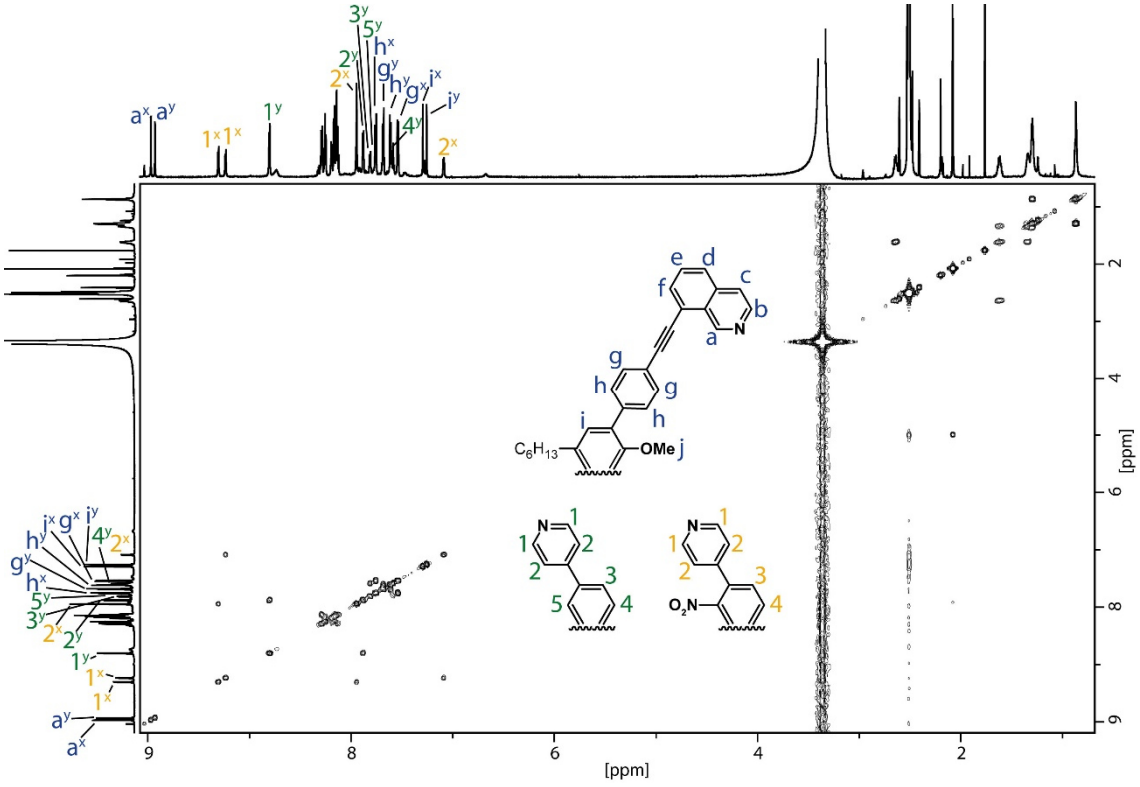

Figure 3.36 ^{1}H-^{1}H COSY NMR (700 MHz, 343 K, DMSO-d_6) spectrum of $[Pd_2L^{OMe}{}_2L^{SOH}{}_2](BF_4)_4$.

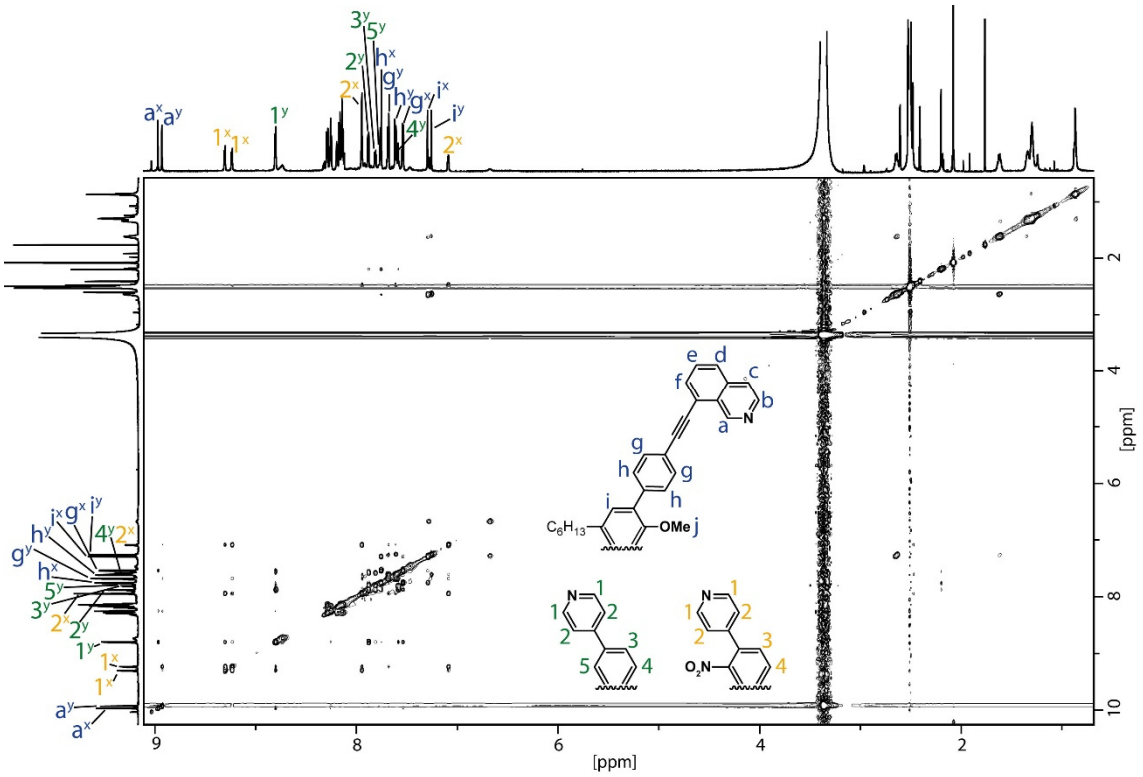

Figure 3.37 ^{1}H-^{1}H NOESY NMR (700 MHz, 298 K, DMSO-d_6) spectrum of $[Pd_2L^{OMe}{}_2L^{SB}L^{SNO2}](BF_4)_4$.

3.2.4 Formation of homoleptic Species with L^{SX} Ligands

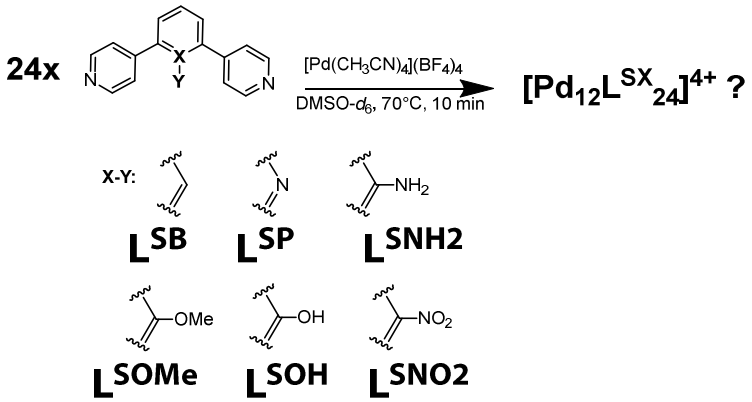

All supramolecular Spezies with L^{SX} were tried to prepare as followed: A 7 mM stock solution of ligand L^{SX} (L^{SB}, L^{SP}, L^{SNH2}, L^{SOMe}, L^{SOH} or L^{SNO2}) (240 µl, 1.68 µmol, DMSO-d_6) and a 15 mM stock solution of $[Pd(CH_3CN)_4(BF_4)_2]$ (60 µl, 0,9 µmol, DMSO-d_6) were placed into an NMR-tube and 300 µl DMSO-d_6 were added. The sealed NMR-Tube was placed into a heating block for 2 hours to give the supramolecular species.

3.2.4.1 $[Pd_{12}L^{SB}_{24}](BF_4)_{24}$

Extended broadening and overlaying of the ^1H signals.

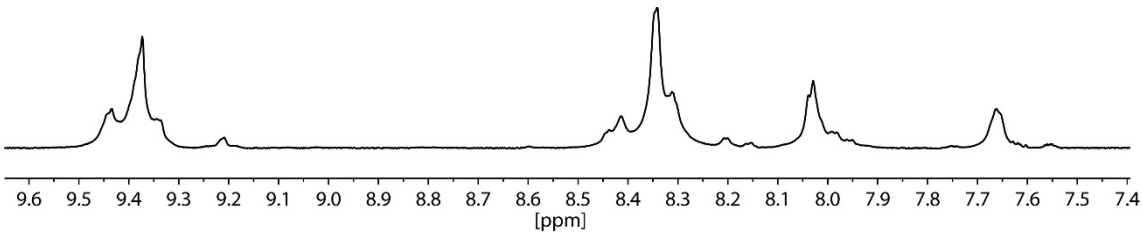

Figure 3.38 ^1H spectrum with 700 MHz spectrometer frequency at 298 K of $[Pd_{12}L^{SB}_{24}](BF_4)_{24}$ in DMSO-d_6 (aromatic area).

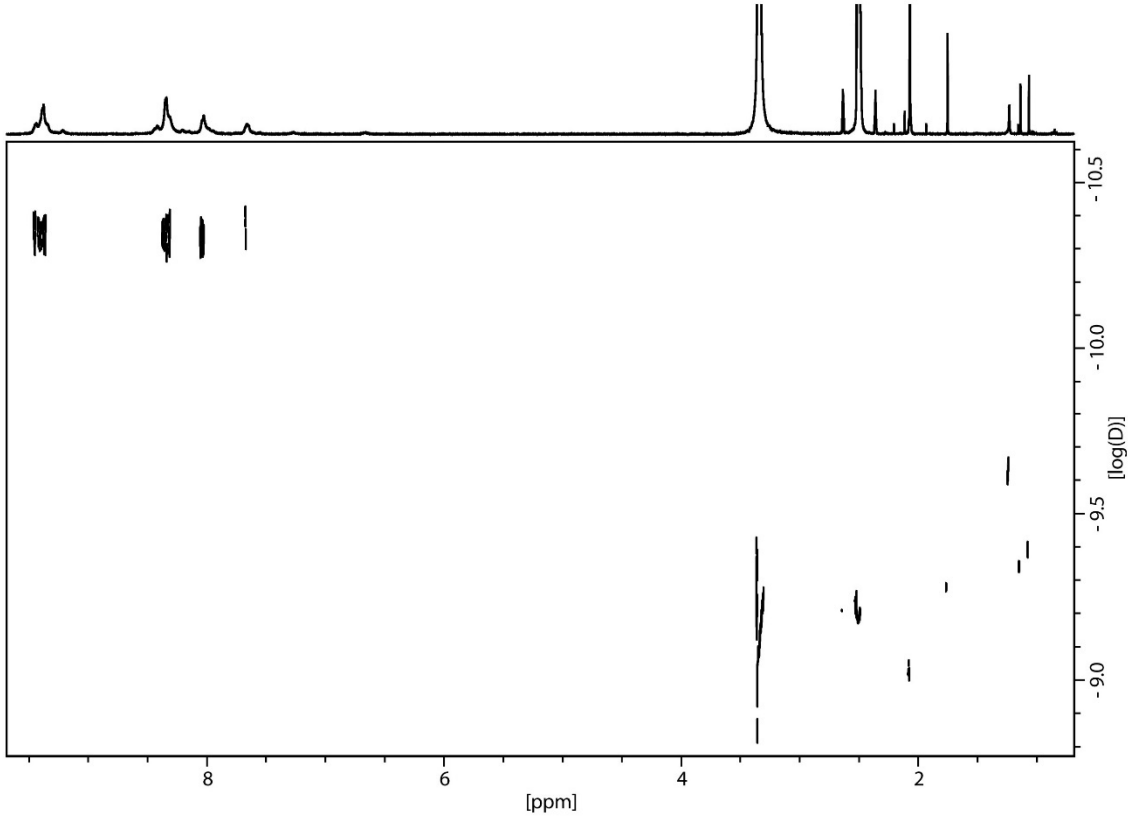

Figure 3.39 ^1H DOSY NMR (500 MHz, 298 K, DMSO-d_6) spectrum of $[Pd_{12}L^{SB}_{24}](BF_4)_{24}$.

^{13}C NMR (176 MHz, 298 K, DMSO-d_6) δ 169.80, 149.44, 147.59, 133.34, 128.95, 127.84, 122.55.

3.2.4.2 $[Pd_{12}L^{SP}_{24}](BF_4)_{24}$

Extended broadening and overlaying of the ^1H signals.

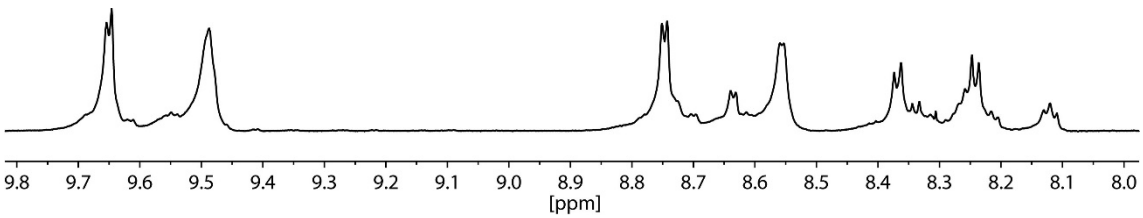

Figure 3.40 ^{1}H spectrum with 700 MHz spectrometer frequency at 298 K of $[Pd_{12}L^{SP}{}_{24}](BF_4)_{24}$ in DMSO-d_6 (aromatic area).

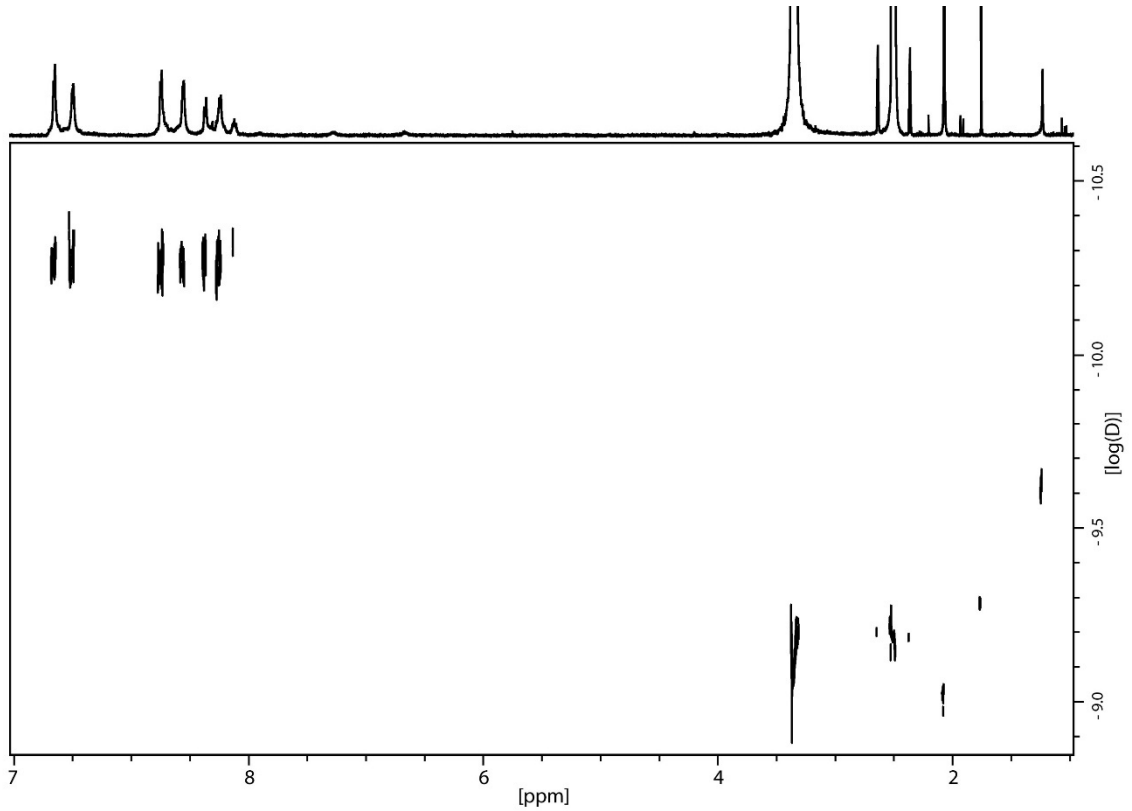

Figure 3.41 ^{1}H DOSY NMR (500 MHz, 298 K, DMSO-d_6) spectrum of $[Pd_{12}L^{SP}{}_{24}](BF_4)_{24}$

^{13}C NMR (176 MHz, 298 K, DMSO-d_6) δ 169.82, 150.01, 149.60, 148.36, 122.63, 121.90.

3.2.4.3 $[Pd_{12}L^{SNH2}{}_{24}](BF_4)_{24}$

Extended broadening and overlaying of the ^{1}H signals.

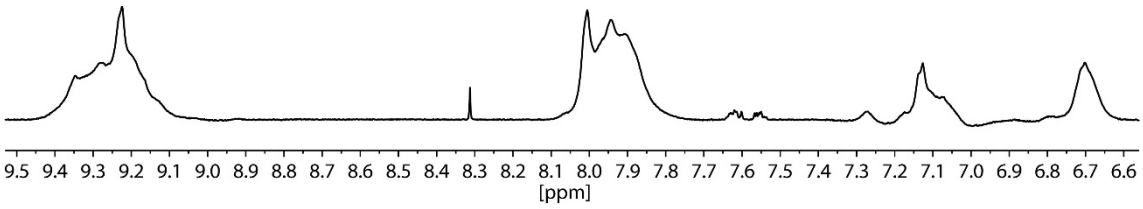

Figure 3.42 ^{1}H spectrum with 600 MHz spectrometer frequency at 298 K of $[Pd_{12}L^{SNH2}{}_{24}](BF_4)_{24}$ in DMSO-d_6 (aromatic area).

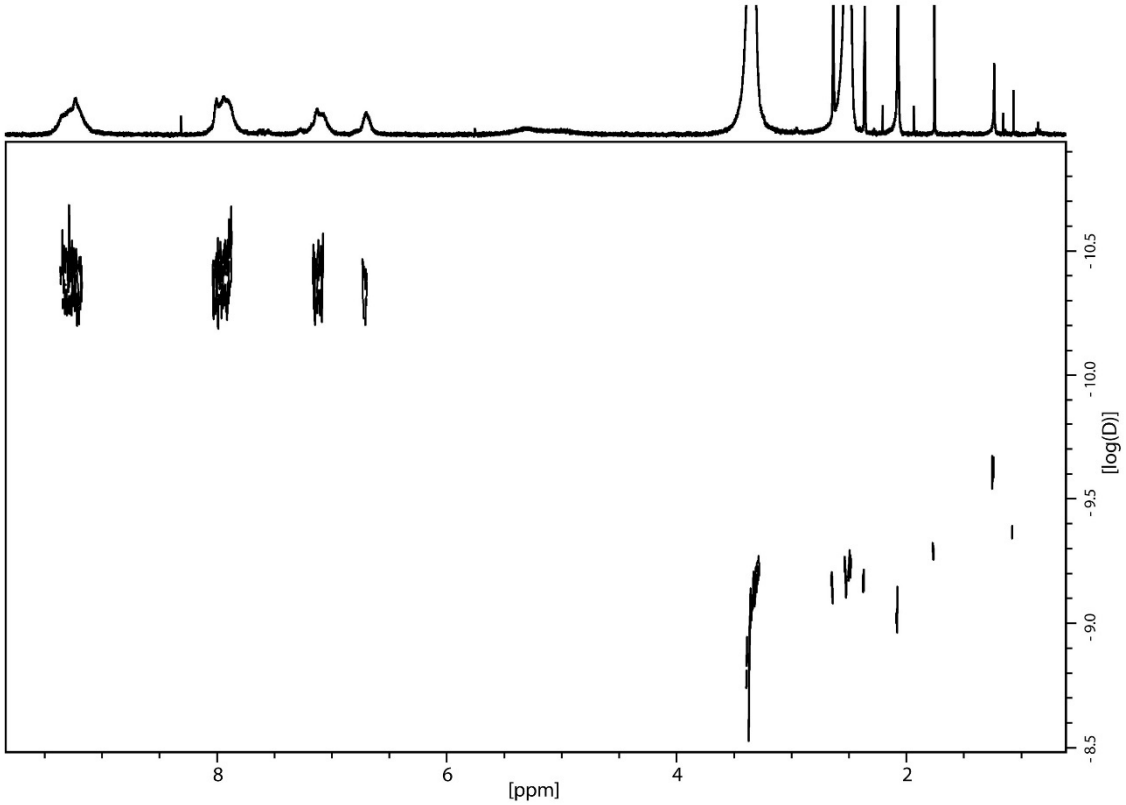

Figure 3.43 ^{1}H DOSY NMR (500 MHz, 298 K, DMSO-d_6) spectrum of $[Pd_{12}L^{SNH2}{}_{24}](BF_4)_{24}$.

^{13}C NMR (151 MHz, 298 K, DMSO-d_6) δ 169.79, 149.45, 149.26, 147.44, 129.87, 124.58, 121.15.

3.2.4.4 L^{SOMe} + $[Pd(CH_3CN)_4(BF_4)_2]$

Extended broadening and overlaying of the ^{1}H signals.

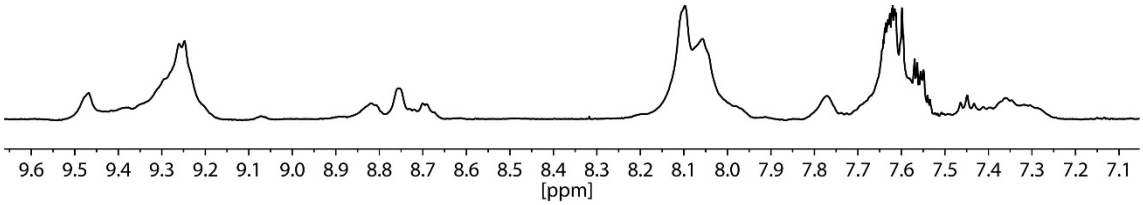

Figure 3.44 ^{1}H spectrum with 500 MHz spectrometer frequency at 298 K of L^{SOMe} + $[Pd(CH_3CN)_4(BF_4)_2]$ in DMSO-d_6 (aromatic area).

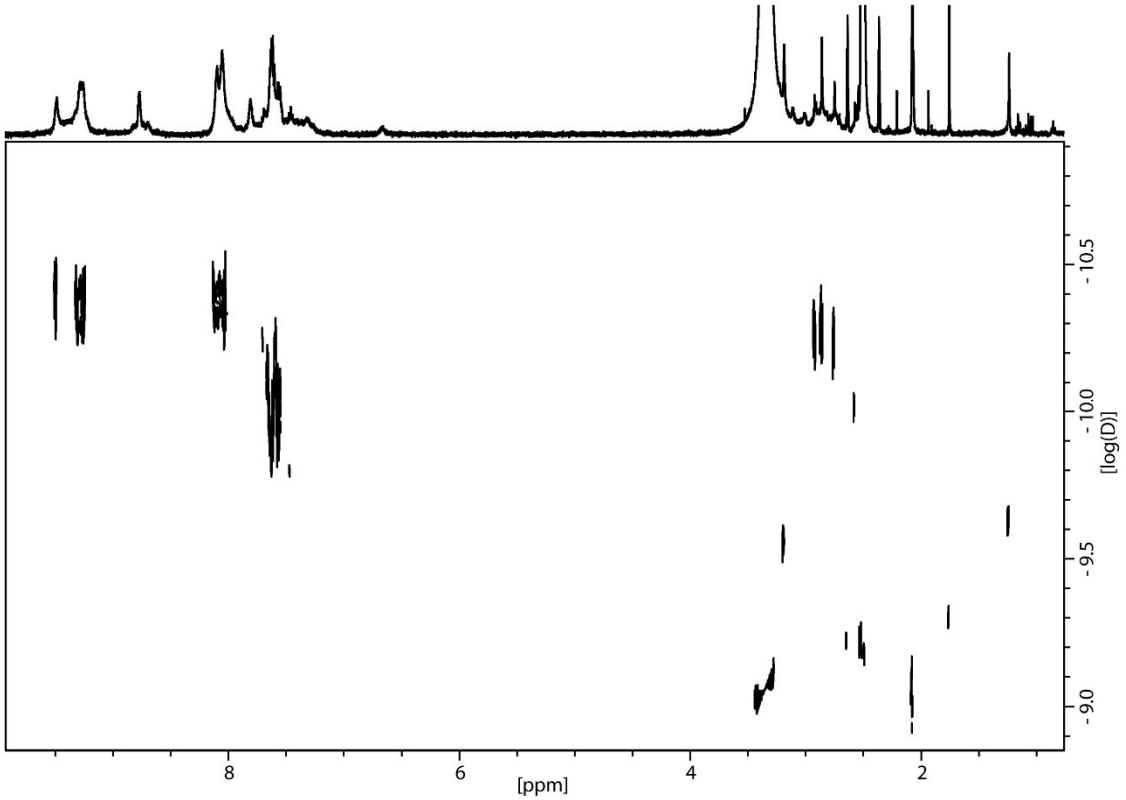

Figure 3.45 1H DOSY NMR (500 MHz, 298 K, DMSO-d_6) spectrum of L^{SOMe} + $[Pd(CH_3CN)_4(BF_4)_2]$ indicating two species.

^{13}C NMR (151 MHz, 298 K, DMSO-d_6) δ 169.78, 149.32, 149.05, 146.81, 131.42, 130.40, 125.09, 59.60.

3.2.4.5 $[Pd_{12}L^{SOH}_{24}](BF_4)_{24}$

Extended broadening and overlaying of the ^{1}H signals.

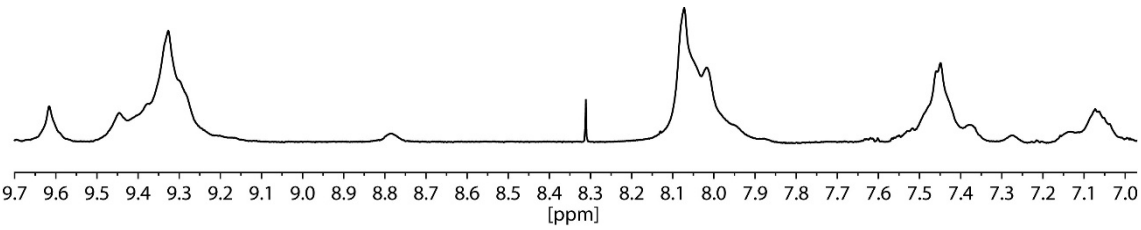

Figure 3.46 ^{1}H spectrum with 600 MHz spectrometer frequency at 298 K of $[Pd_{12}L^{SOH}_{24}](BF_4)_{24}$ in DMSO-d_6 (aromatic area).

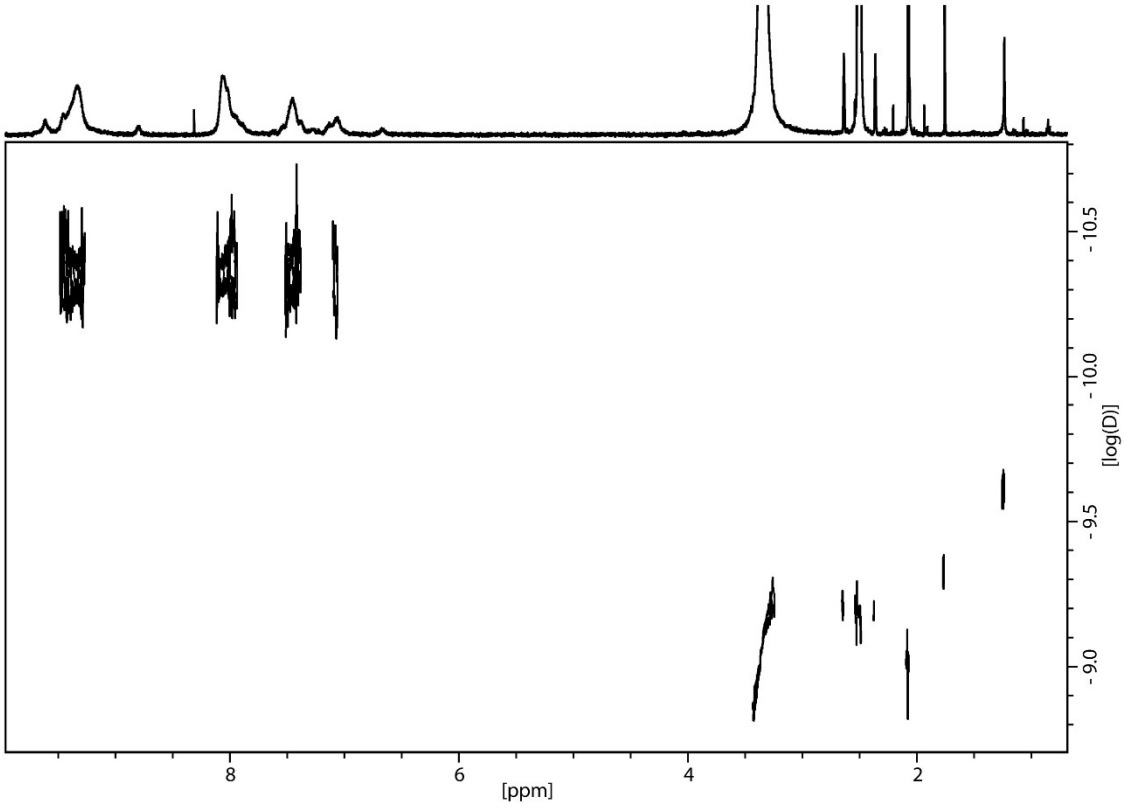

Figure 3.47 ^{1}H DOSY NMR (500 MHz, 298 K, DMSO-d_6) spectrum of $[Pd_{12}L^{SOH}_{24}](BF_4)_{24}$.

^{13}C NMR (151 MHz, 298 K, DMSO-d_6) δ 169.80, 148.90, 148.00, 130.64, 129.80, 125.31, 120.09.

3.2.4.6 L^{SNO2} + $[Pd(CH_3CN)_4(BF_4)_2]$

Extended broadening and overlaying of the ^{1}H signals.

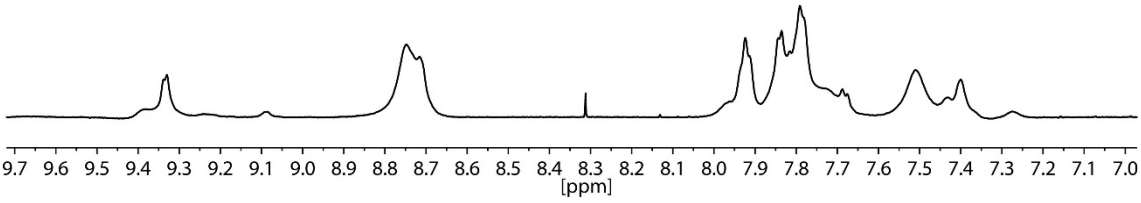

Figure 3.48 ^{1}H spectrum with 600 MHz spectrometer frequency at 298 K of L^{SNO2} + $[Pd(CH_3CN)_4(BF_4)_2]$ in DMSO-d_6 (aromatic area).

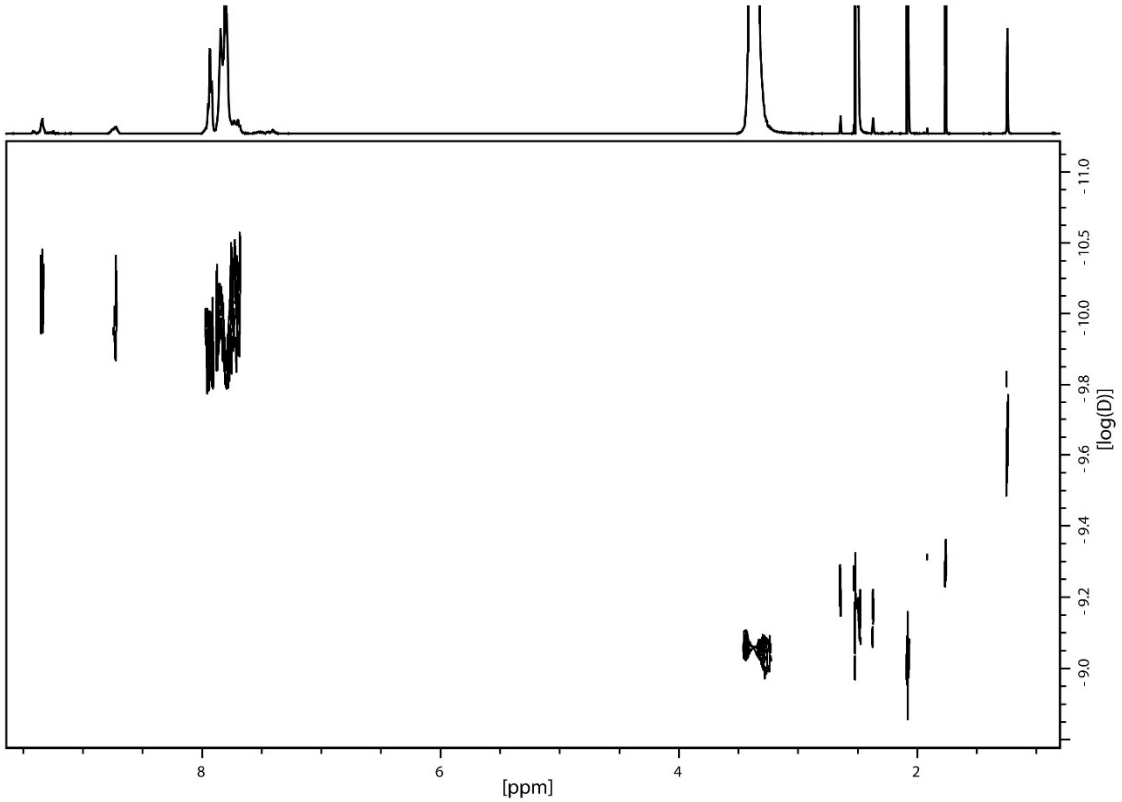

Figure 3.49 ^{1}H DOSY NMR (500 MHz, 298 K, DMSO-d_6) spectrum of L^{SNO2} + $[Pd(CH_3CN)_4(BF_4)_2]$ indicating two species.

^{13}C NMR (151 MHz, 298 K, DMSO-d_6) δ 169.79, 149.86, 148.38, 147.92, 130.54, 129.96, 121.49.

3.3 ^{1}H NMR Spectroscopy Titrations

3.3.1 Preparation of the Guest Salts

All guests were prepared as tetrabutylammonium salts and obtained by reported procedures.[123][141] All starting materials were commercially available with the sulphonate guest as a sodium salt and all phosphate guests as free acids. All used solvents were in HPLC-grade.

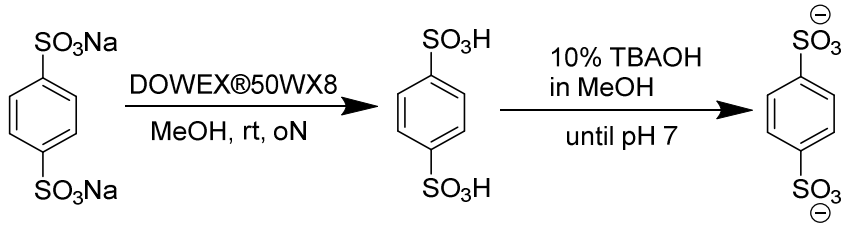

Figure 3.50 Synthesis path for anionic for tetrabutylammonium beneze-1,1-disulfonate (tetrabutylammonium counter cations missing for clarity).

Sodium benzene-1,4-disulfonate (300 mg, 1.06 mmol, 1 eq) was placed in a 50 ml one-necked round bottom flask and solved in 25 ml methanol. DOWEX®50WX8 as an acidic cation exchange agent was added and the mixture was stirred overnight. Afterwards, the mixture was filtrated to remove the solid cation exchange agent and the solvent was evaporated to obtain the free benzene-1,4-disulfonic acid (Yield: 99 %, 250 mg, 1.05 mmol). A certain amount of the free acid was placed in a 50 ml one-necked round bottom flask and solved in 20 ml methanol. Under permanent stirring, a 10 % tetrabutylammonium hydroxide solution in methanol was added slowly and dropwise until pH 7 was adjusted. The solvents were removed by rotary evaporator and the solid white powder was solved in chloroform and filtered to remove any solid impurity. After evaporation of the chloroform, tetrabutylammonium benzene-1,4-disulfonate was obtained and the purity was confirmed by ^{1}H NMR spectroscopy by showing a correct ratio of anion to cation by 1:2.

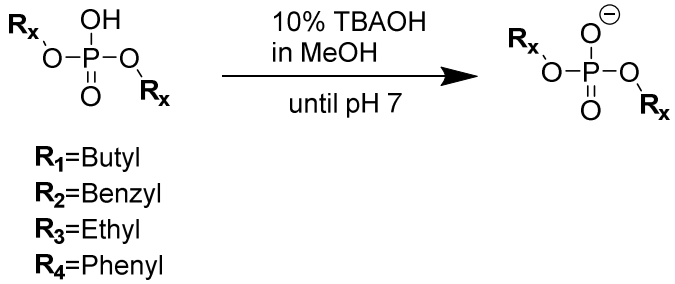

Figure 3.51 Neutralisation of the free acids to anionic phosphates (tetrabutylammonium counter cations missing for clarity).

100 mg of dialkyl phosphates as free acids were placed in a 50 ml one-necked round bottom flask and solved in 20 ml methanol, respectively. Under stirring, 10 % tetrabutylammonium hydroxide solution in methanol was added dropwise until pH 7 was adjusted. The solvent was removed by rotary evaporator and the slimy pale materials were solved in chloroform and filtered. After removing of the chloroform, the slimy products need to dry for several days in vacuo (Schlenk line) to remove all residues of organic solvents. The purities and the anion to cation ratios (1:1) were confirmed by ^{1}H NMR spectroscopy.

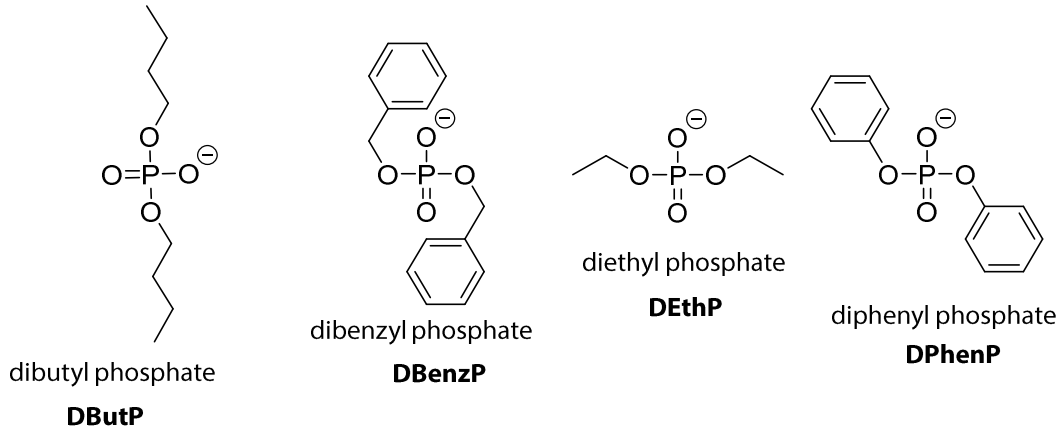

Figure 3.52 Phosphates used as guest molecules in ^{1}H NMR-titrations with $[Pd_2L^{OMe}{}_2L^{X}{}_2](BF_4)_4$-type cages. Abbreviations are shown, respectively.

3.3.2 Titration of anionic guests to $[Pd_2L^{OMe}{}_2L^{X}{}_2](BF_4)_4$-type cages

To a solution of $[Pd_2L^{OMe}{}_2L^{X}{}_2](BF_4)_4$ cages (500 µl, 0.7 mM, DMSO-d_6) placed in an NMR tube, a 15 mM DMSO-d_6 solution of the tetrabutylammonium salts of the respective guests was titrated by a volume pipette. After careful shaking of the solution, the ^{1}H NMR spectra at 298 K were recorded immediately.

3.3.2.1 Guest-Titrations of $[Pd_2L^{OMe}{}_2L^{SB}{}_2](BF_4)_4$

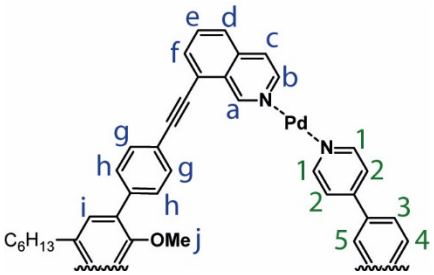

Scheme 3.1 Simplified structure of $[Pd_2L^{OMe}{}_2L^{SB}{}_2](BF_4)_4$ to show the position of the assigned protons.

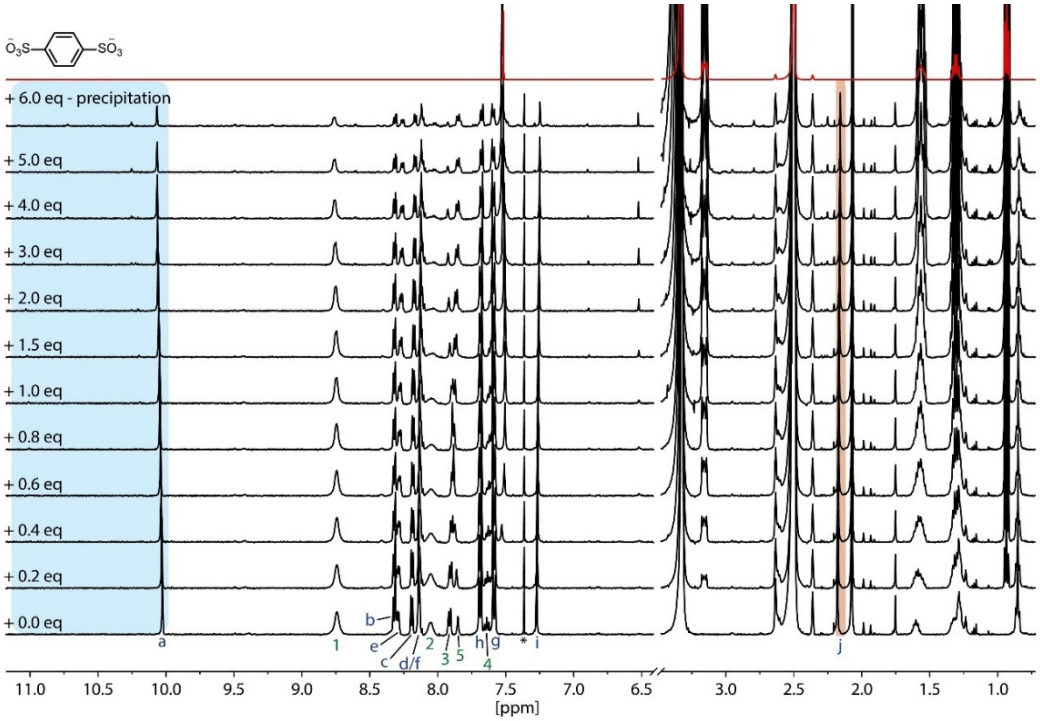

Figure 3.53 ^{1}H NMR titration (500 MHz, DMSO-d_6, 298 K) of $[Pd_2L^{OMe}{}_2L^{SB}{}_2](BF_4)_4$ with tetrabutylammonium benzene-1,4-disulfonate. During the titration, signal H_a (L^{OMe}- singlet of quinoline part of the ligand, highlighted in blue) and H_j (L^{OMe}- Methoxy group of the ligand, highlighted in red) were focused to identify the progress of the titration. For signal H_a and H_j, only a very small shift could be observed. By addition of 1.0 eq small new signal were observed, but also a decreasing of the signal intensities with a recognizable turbidity of the sample until at 6.0 eq guest addition precipitation occurred. This indicated an agglomeration of the Host with the Guest.

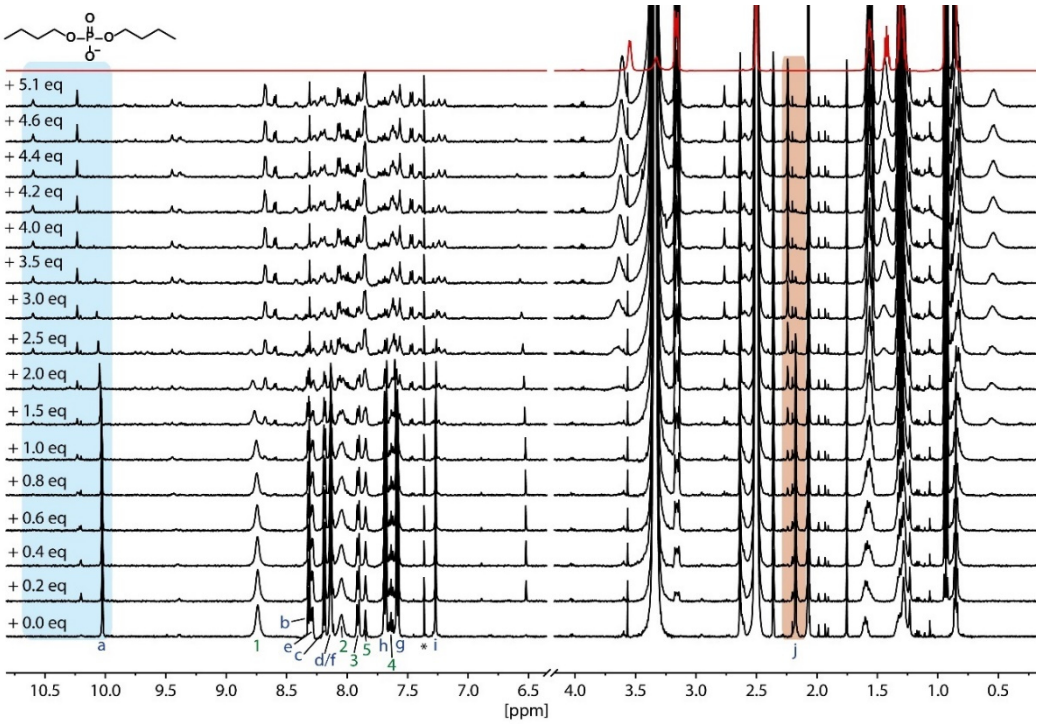

Figure 3.54 ^{1}H NMR titration (500 MHz, DMSO-d_6, 298 K) of $[Pd_2L^{OMe}{}_2L^{SB}{}_2](BF_4)_4$ with tetrabutylammonium dibutyl phosphate as a guest. During the titration, signal H_a (L^{OMe}- singlet of quinoline part of the ligand, highlighted in blue) and H_j (L^{OMe}- Methoxy group of the ligand, highlighted in red) were focused to identify the progress of the titration. 5.1 eq guest were used to form the new $[DButP@Pd_2L^{OMe}{}_2L^{SB}{}_2]$ species.

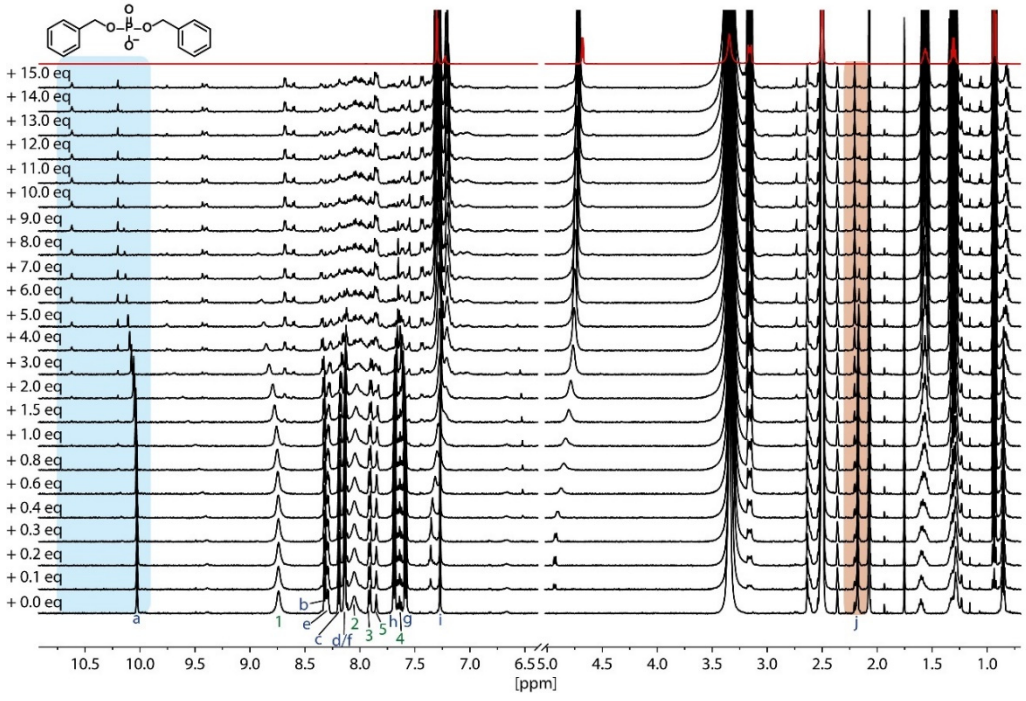

Figure 3.55 ^{1}H NMR titration (500 MHz, DMSO-d_6, 298 K) of $[Pd_2L^{OMe}{}_2L^{SB}{}_2](BF_4)_4$ with tetrabutylammonium dibenzyl phosphate as a guest. During the titration, signal H_a (L^{OMe}- singlet of quinoline part of the ligand, highlighted in blue) and H_j (L^{OMe}- Methoxy group of the ligand, highlighted in red) were focused to identify the progress of the titration. 15 eq guest were used to form the new $[DBenzP@Pd_2L^{OMe}{}_2L^{SB}{}_2]$ species.

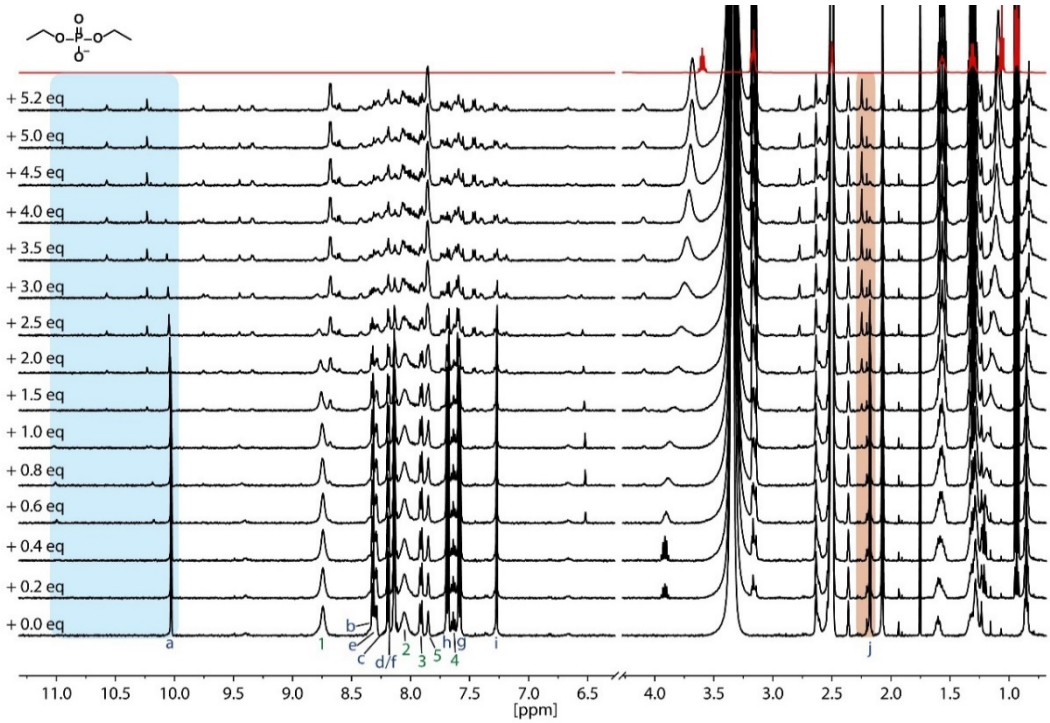

Figure 3.56 ^{1}H NMR titration (500 MHz, DMSO-d_6, 298 K) of $[Pd_2L^{OMe}{}_2L^{SB}{}_2](BF_4)_4$ with tetrabutylammonium diethyl phosphate as a guest. During the titration, signal H_a (L^{OMe}- singlet of quinoline part of the ligand, highlighted in blue) and H_j (L^{OMe}- Methoxy group of the ligand, highlighted in red) were focused to identify the progress of the titration. 5.2 eq guest were used to form the new $[DEthP@Pd_2L^{OMe}{}_2L^{SB}{}_2]$ species.

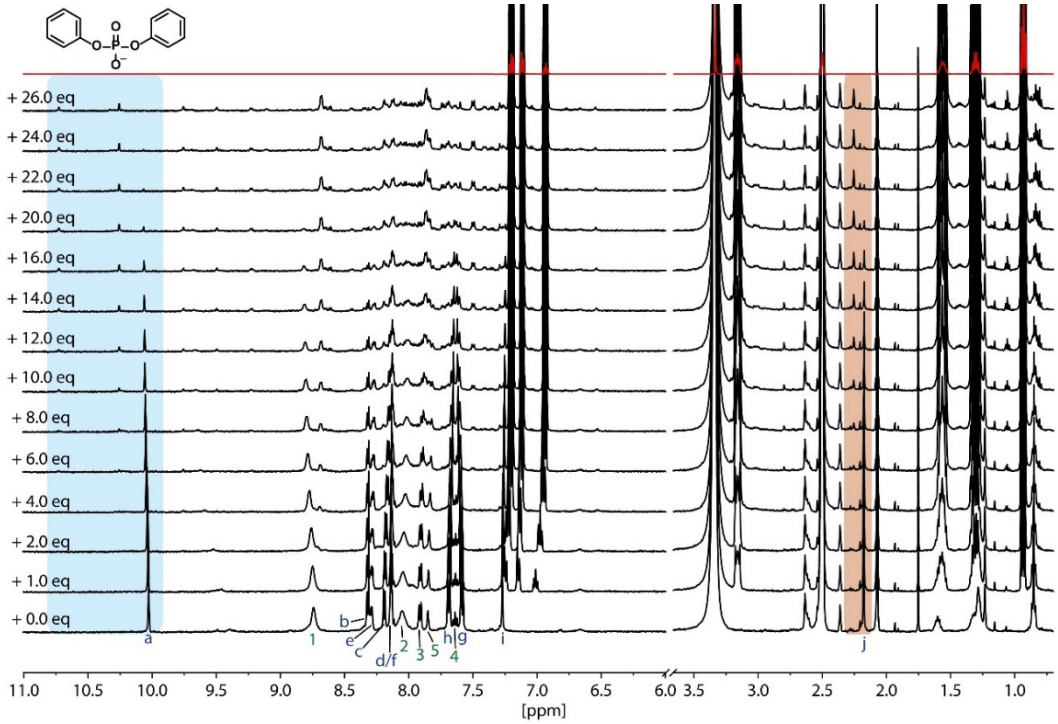

Figure 3.57 ^{1}H NMR titration (500 MHz, DMSO-d_6, 298 K) of $[Pd_2L^{OMe}{}_2L^{SB}{}_2](BF_4)_4$ with tetrabutylammonium diphenyl phosphate as a guest. During the titration, signal H_a (L^{OMe}- singlet of quinoline part of the ligand, highlighted in blue) and H_j (L^{OMe}- Methoxy group of the ligand, highlighted in red) were focused to identify the progress of the titration. 26 eq guest were used to form the new $[DPhenP@Pd_2L^{OMe}{}_2L^{SB}{}_2]$ species.

3.3.2.2 Guest-Titrations of $[Pd_2L^{OMe}{}_2L^{SNH2}{}_2](BF_4)_4$

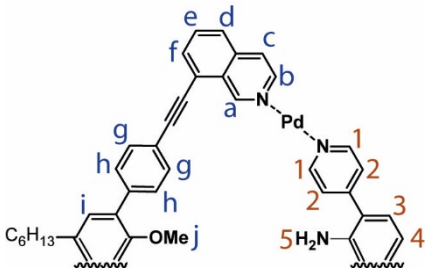

Scheme 3.2 Simplified structure of $[Pd_2L^{OMe}{}_2L^{SNH2}{}_2](BF_4)_4$ to show the position of the assigned protons. Protons of the Aniline function 5 could not be determined.

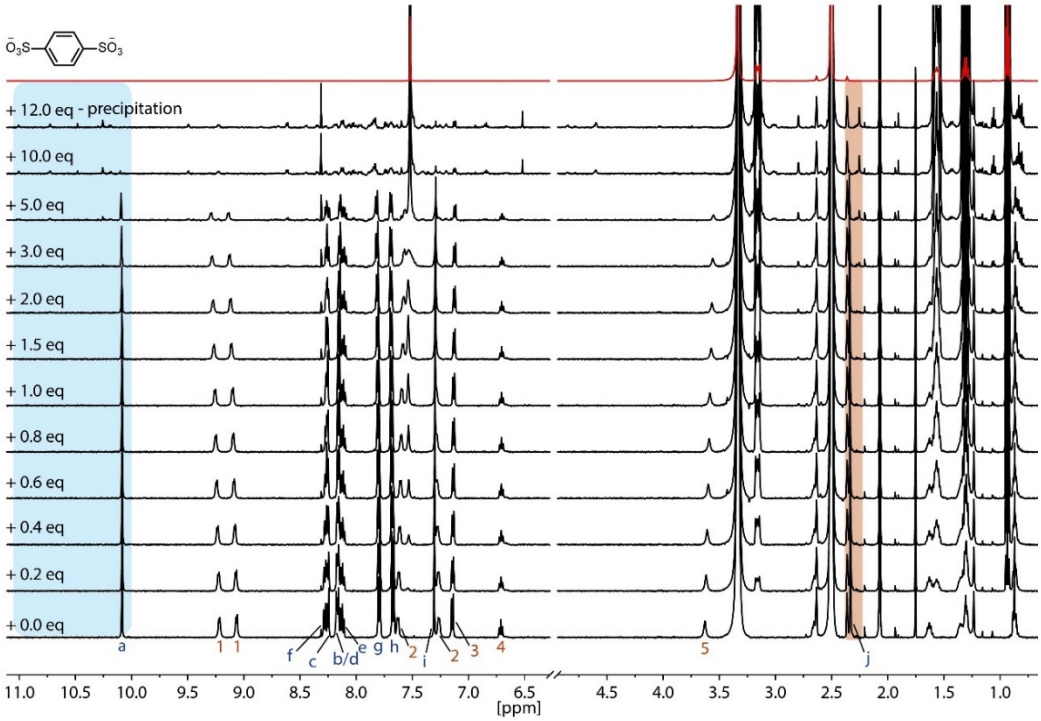

Figure 3.58 ^{1}H NMR titration (500 MHz, DMSO-d_6, 298 K) of $[Pd_2L^{OMe}{}_2L^{SNH2}{}_2](BF_4)_4$ with tetrabutylammonium benzene-1,4-disulfonate. During the titration, signal H_a (L^{OMe}- singlet of quinoline part of the ligand, highlighted in blue) and H_j (L^{OMe}- Methoxy group of the ligand, highlighted in red) were focused to identify the progress of the titration. For signal H_a and H_j, only a very small shift could be observed. By addition of 2.0 eq small new signal were observed. Until 5 eq guest addition, no turbidity occurred. After adding of 10 eq guest the sample turned turbid and with 12 eq the solution precipitated. This indicated an agglomeration of sample compounds.

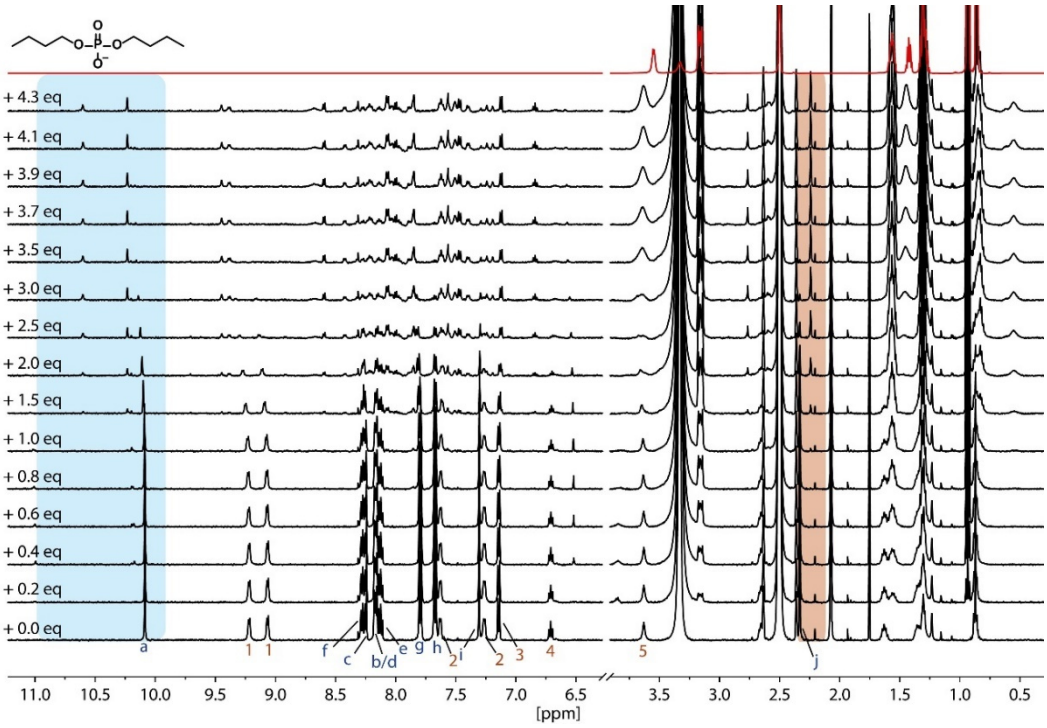

Figure 3.59 ^{1}H NMR titration (500 MHz, DMSO-d_6, 298 K) of $[Pd_2L^{OMe}{}_2L^{SNH2}{}_2](BF_4)_4$ with tetrabutylammonium dibutyl phosphate as a guest. During the titration, signal H_a (L^{OMe}- singlet of quinoline part of the ligand, highlighted in blue) and H_j (L^{OMe}- Methoxy group of the ligand, highlighted in red) were focused to identify the progress of the titration. 4.3 eq guest were used to form the new $[DButP@Pd_2L^{OMe}{}_2L^{SNH2}{}_2]$ species.

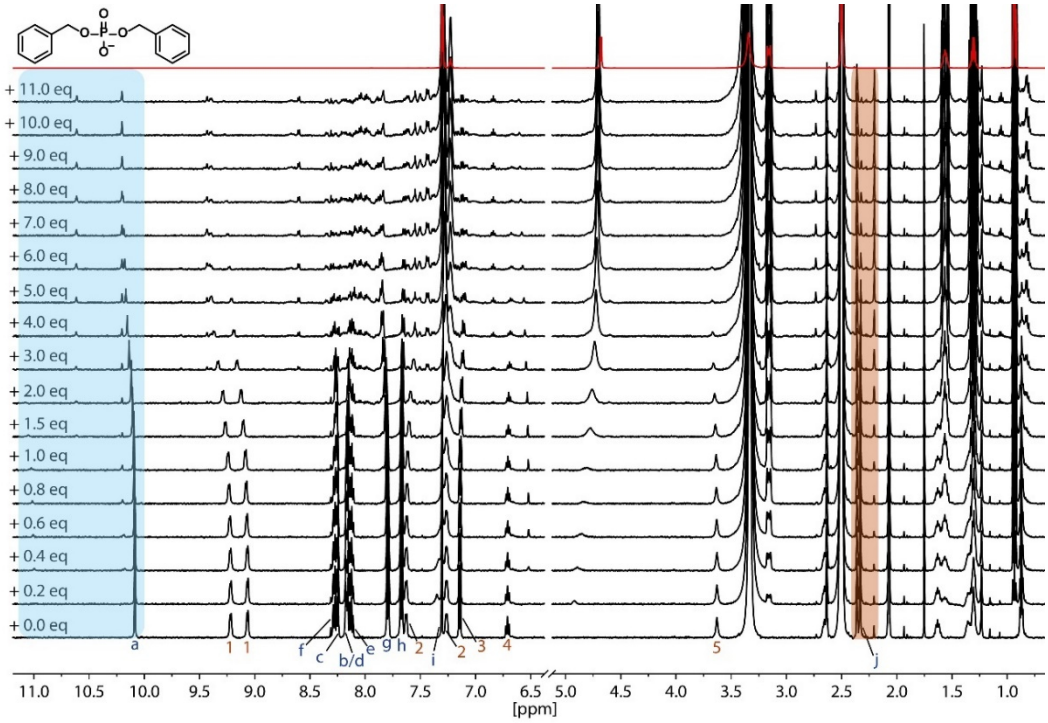

Figure 3.60 ^{1}H NMR titration (500 MHz, DMSO-d_6, 298 K) of $[Pd_2L^{OMe}{}_2L^{SNH2}{}_2](BF_4)_4$ with tetrabutylammonium dibenzyl phosphate as a guest. During the titration, signal H_a (L^{OMe}- singlet of quinoline part of the ligand, highlighted in blue) and H_j (L^{OMe}- Methoxy group of the ligand, highlighted in red) were focused to identify the progress of the titration. 11 eq guest were used to form the new $[DBenzP@Pd_2L^{OMe}{}_2L^{SNH2}{}_2]$ species.

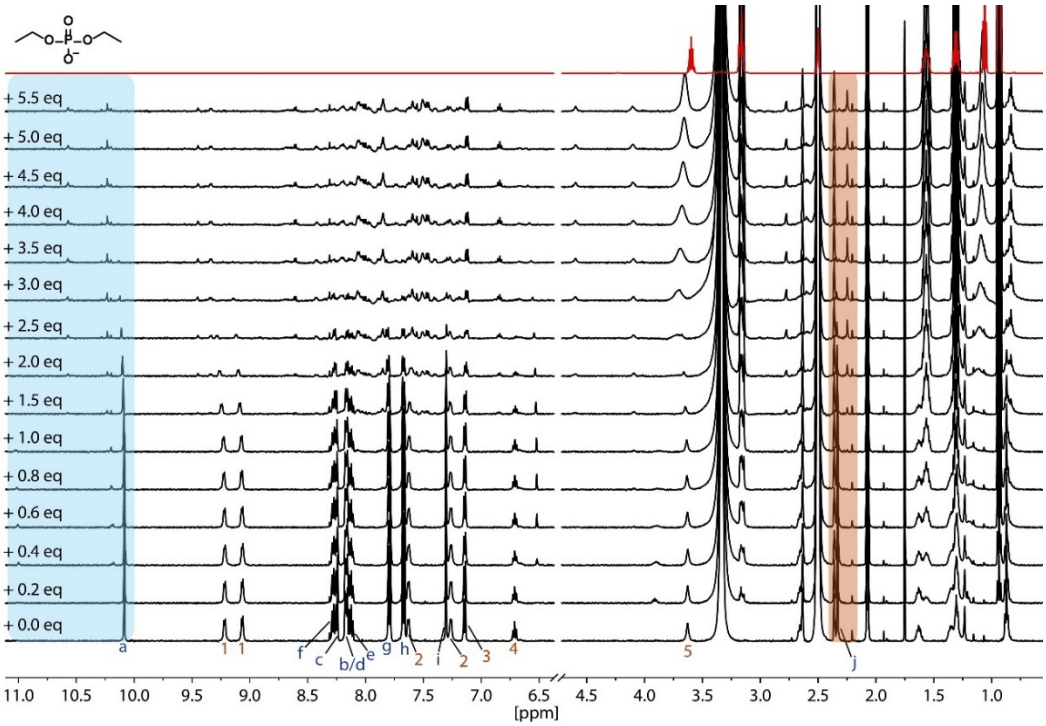

Figure 3.61 ^{1}H NMR titration (500 MHz, DMSO-d_6, 298 K) of $[Pd_2L^{OMe}{}_2L^{SNH2}{}_2](BF_4)_4$ with tetrabutylammonium diethyl phosphate as a guest. During the titration, signal H_a (L^{OMe}- singlet of quinoline part of the ligand, highlighted in blue) and H_j (L^{OMe}- Methoxy group of the ligand, highlighted in red) were focused to identify the progress of the titration. 5.5 eq guest were used to form the new $[DEthP@Pd_2L^{OMe}{}_2L^{SNH2}{}_2]$ species.

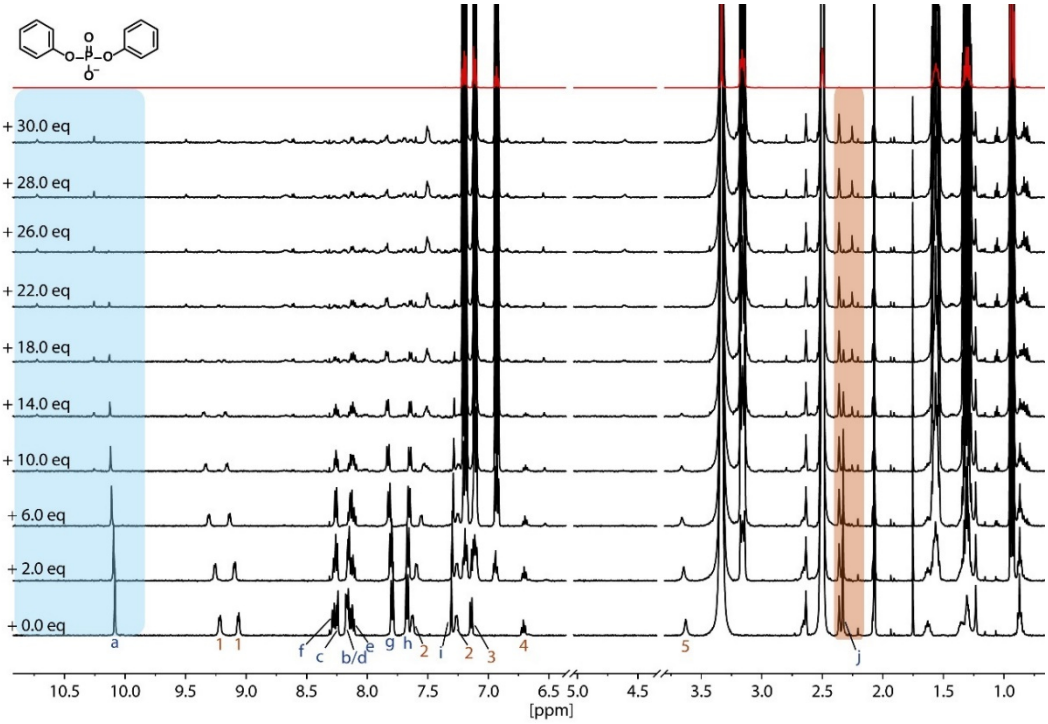

Figure 3.62 ^{1}H NMR titration (500 MHz, DMSO-d_6, 298 K) of $[Pd_2L^{OMe}{}_2L^{SNH2}{}_2](BF_4)_4$ with tetrabutylammonium diphenyl phosphate as a guest. During the titration, signal H_a (L^{OMe}- singlet of quinoline part of the ligand, highlighted in blue) and H_j (L^{OMe}- Methoxy group of the ligand, highlighted in red) were focused to identify the progress of the titration. 30 eq guest were used to form the new $[DPhenP@Pd_2L^{OMe}{}_2L^{SNH2}{}_2]$ species.

3.3.2.3 Guest-Titrations of $[Pd_2L^{OMe}{}_2L^{SOMe}{}_2](BF_4)_4$

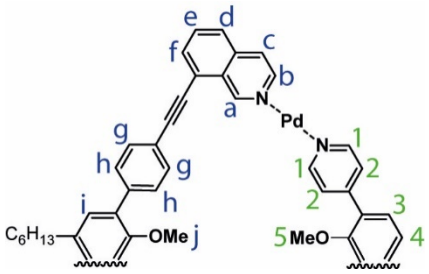

Scheme 3.3 Simplified structure of $[Pd_2L^{OMe}{}_2L^{SOMe}{}_2](BF_4)_4$ to show the position of the assigned protons.

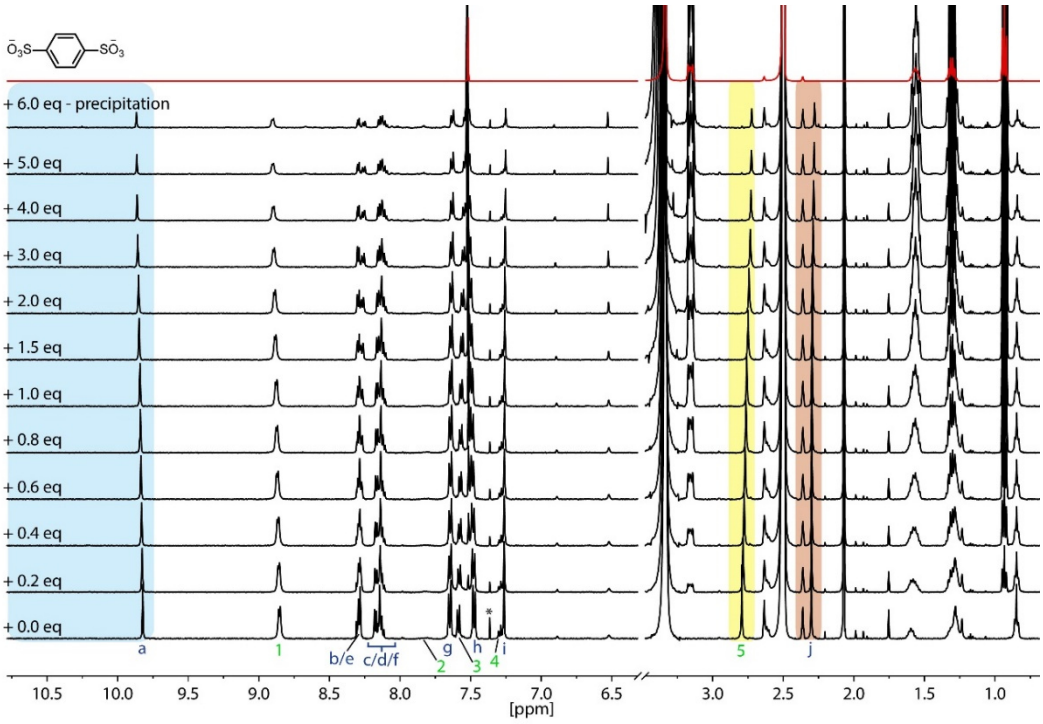

Figure 3.63 ^{1}H NMR titration (500 MHz, DMSO-d_6, 298 K) of $[Pd_2L^{OMe}{}_2L^{SOMe}{}_2](BF_4)_4$ with tetrabutylammonium benzene-1,4-disulfonate. During the titration, signal H_a (L^{OMe}- singlet of quinoline part of the ligand, highlighted in blue) and H_j (L^{OMe}- Methoxy group of the ligand, highlighted in red) and 5 (L^{SOMe}- Methoxy group of the ligand, highlighted in yellow) were focused to identify the progress of the titration. Only small shifts of the signals were observed, no new signals with additional decreasing of the signal intensities. After 6.0 eq, the sample precipitates.

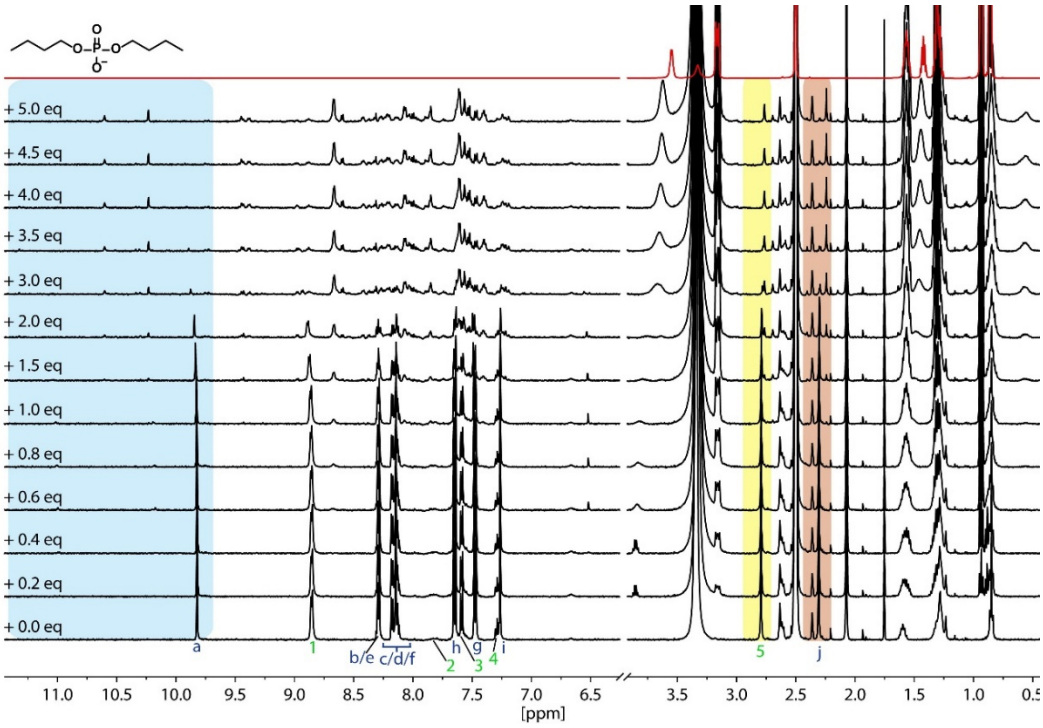

Figure 3.64 ^{1}H NMR titration (500 MHz, DMSO-d_6, 298 K) of $[Pd_2L^{OMe}{}_2L^{SOMe}{}_2](BF_4)_4$ with tetrabutylammonium dibutyl phosphate as a guest. During the titration, signal H_a (L^{OMe}- singlet of quinoline part of the ligand, highlighted in blue); H_j (L^{OMe}- Methoxy group of the ligand, highlighted in red) and H_5 (L^{SOMe}- Methoxy group of the ligand, highlighted in yellow) were focused to identify the progress of the titration. 5 eq guest were used to form the new $[DButP@Pd_2L^{OMe}{}_2L^{SOMe}{}_2]$ species.

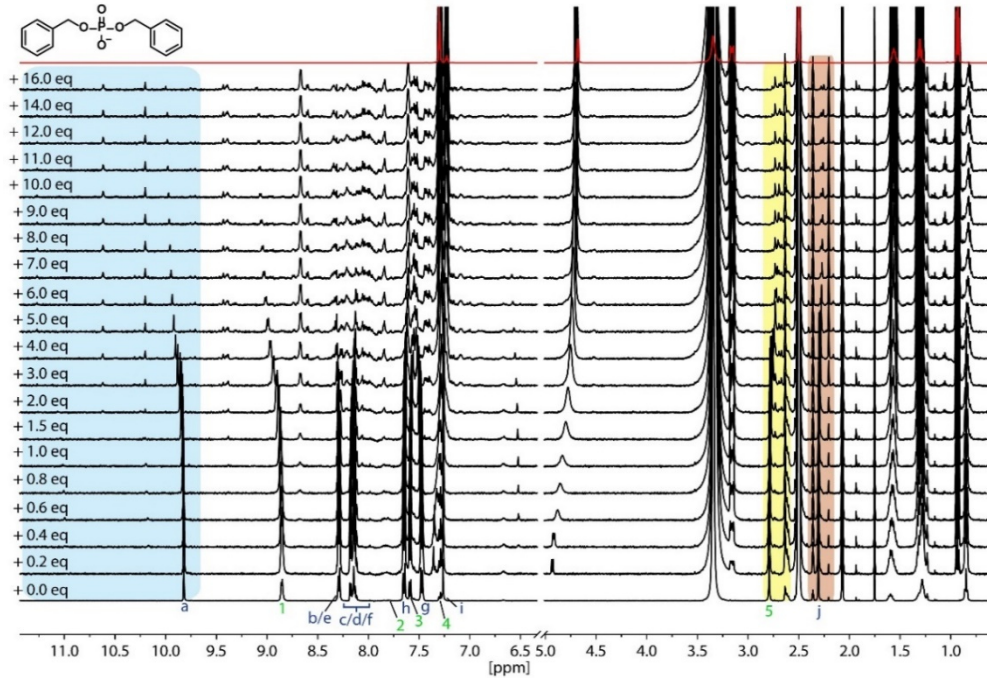

Figure 3.65 ^{1}H NMR titration (500 MHz, DMSO-d_6, 298 K) of $[Pd_2L^{OMe}{}_2L^{SOMe}{}_2](BF_4)_4$ with tetrabutylammonium dibenzyl phosphate as a guest. During the titration, signal H_a (L^{OMe}- singlet of quinoline part of the ligand, highlighted in blue); H_j (L^{OMe}- Methoxy group of the ligand, highlighted in red) and H_5 (L^{SOMe}- Methoxy group of the ligand, highlighted in yellow) were focused to identify the progress of the titration. 16 eq guest were used to form the new $[DBenP@Pd_2L^{OMe}{}_2L^{SOMe}{}_2]$ species.

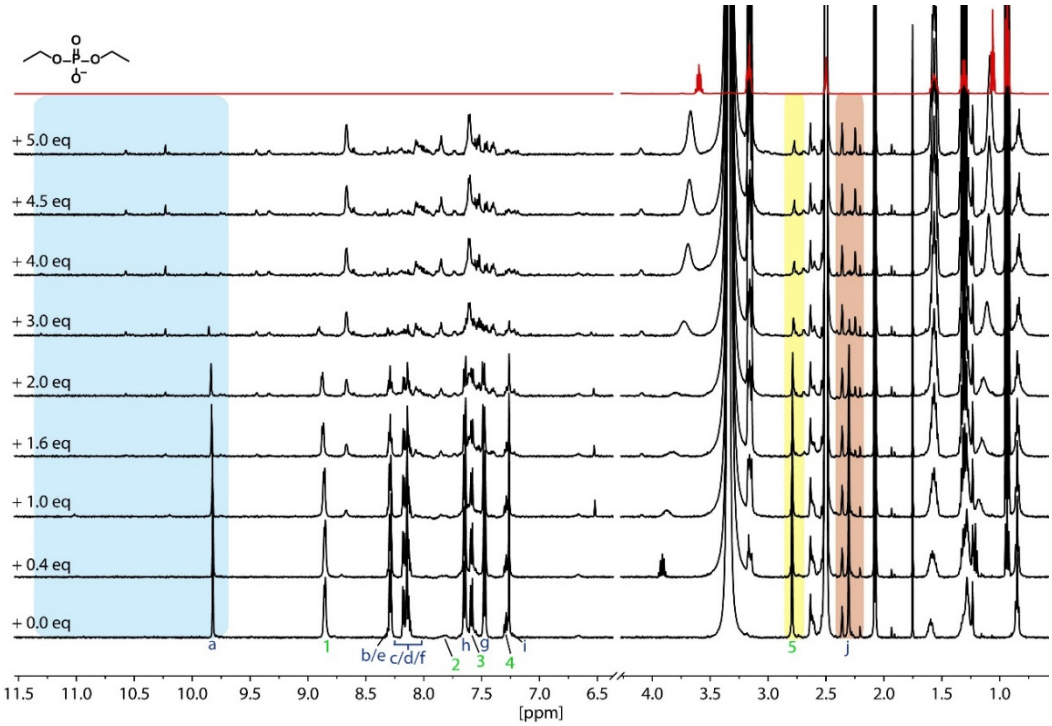

Figure 3.66 Figure 3.67 ^{1}H NMR titration (500 MHz, DMSO-d_6, 298 K) of $[Pd_2L^{OMe}{}_2L^{SOMe}{}_2](BF_4)_4$ with tetrabutylammonium diethyl phosphate as a guest. During the titration, signal H_a (L^{OMe}- singlet of quinoline part of the ligand, highlighted in blue); H_j (L^{OMe}- Methoxy group of the ligand, highlighted in red) and H_5 (L^{SOMe}- Methoxy group of the ligand, highlighted in yellow) were focused to identify the progress of the titration. 5 eq guest were used to form the new $[DEthP@Pd_2L^{OMe}{}_2L^{SOMe}{}_2]$ species.

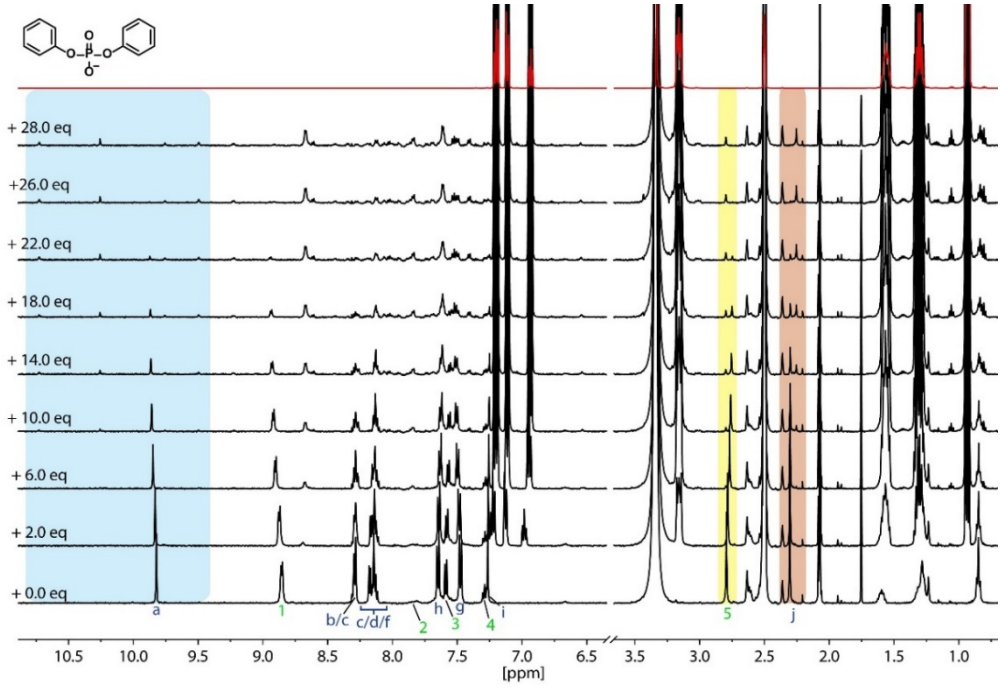

Figure 3.68 ^{1}H NMR titration (500 MHz, DMSO-d_6, 298 K) of $[Pd_2L^{OMe}{}_2L^{SOMe}{}_2](BF_4)_4$ with tetrabutylammonium diphenyl phosphate as a guest. During the titration, signal H_a (L^{OMe}- singlet of quinoline part of the ligand, highlighted in blue); H_j (L^{OMe}- Methoxy group of the ligand, highlighted in red) and H_5 (L^{SOMe}- Methoxy group of the ligand, highlighted in yellow) were focused to identify the progress of the titration. 28 eq guest were used to form the new $[DPhenP@Pd_2L^{OMe}{}_2L^{SOMe}{}_2]$ species.

3.3.2.4 Guest-Titrations of $[Pd_2L^{OMe}{}_2L^{SOH}{}_2](BF_4)_4$

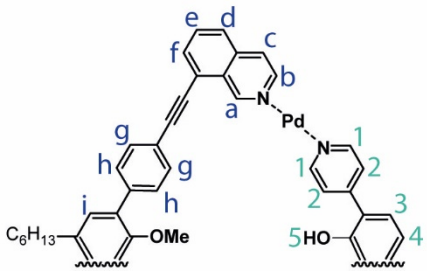

Scheme 3.4 Simplified structure of $[Pd_2L^{OMe}{}_2L^{SOH}{}_2](BF_4)_4$ to show the position of the assigned protons. Phenol proton could not be determined at 298 K.

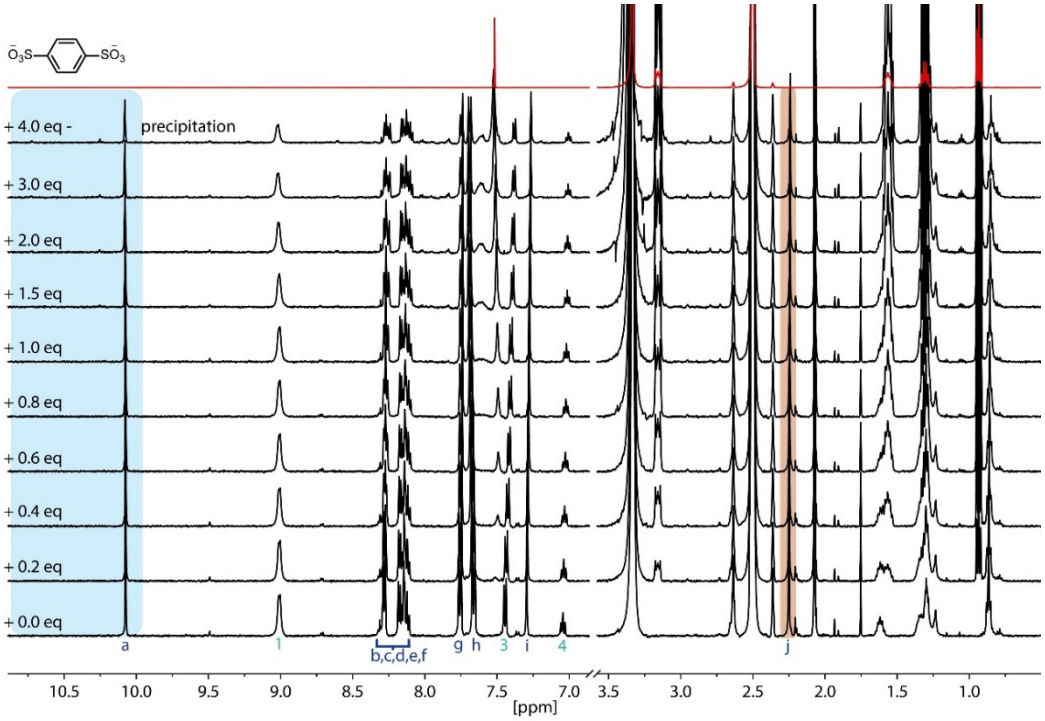

Figure 3.69 ^{1}H NMR titration (500 MHz, DMSO-d_6, 298 K) of $[Pd_2L^{OMe}{}_2L^{SOH}{}_2](BF_4)_4$ with tetrabutylammonium benzene-1,4-disulfonate. During the titration, signal H_a (L^{OMe}- singlet of quinoline part of the ligand, highlighted in blue) and H_j (L^{OMe}- Methoxy group of the ligand, highlighted in red) were focused to identify the progress of the titration. For signal H_a and H_j, only a very small shift could be observed with new signals by addition of 1.0 eq of guest. At 4.0 eq, the sample precipitated.

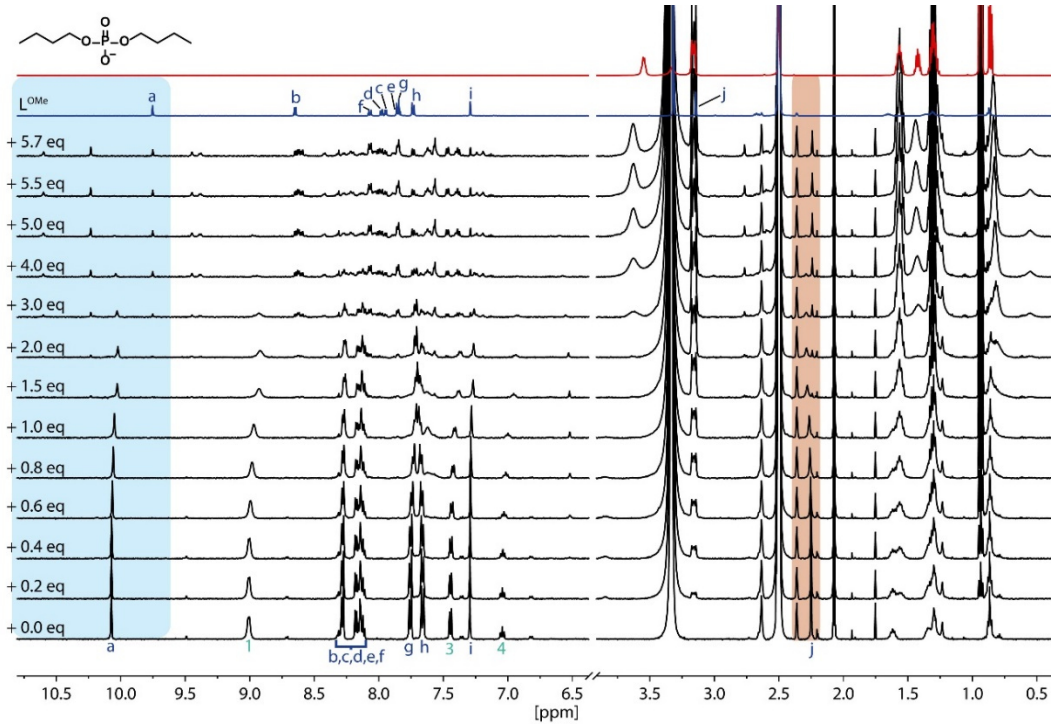

Figure 3.70 ^{1}H NMR titration (500 MHz, DMSO-d_6, 298 K) of $[Pd_2L^{OMe}{}_2L^{SOH}{}_2](BF_4)_4$ with tetrabutylammonium dibutyl phosphate as a guest. During the titration, signal H_a (L^{OMe}- singlet of quinoline part of the ligand, highlighted in blue) and H_j (L^{OMe}- Methoxy group of the ligand, highlighted in red) were focused to identify the progress of the titration. 5.7 eq guest were used to form the new $[DButP@Pd_2L^{OMe}{}_2L^{SOH}{}_2]$ species. Starting at addition of 2 eq guest, free ligand L^{OMe} is visible.

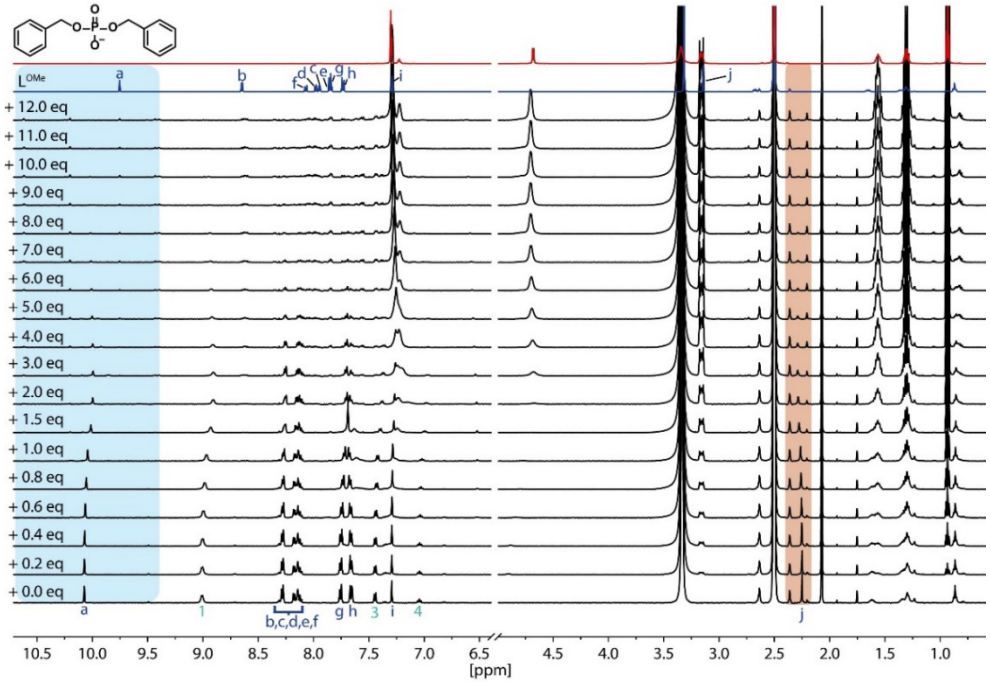

Figure 3.71 ^{1}H NMR titration (500 MHz, DMSO-d_6, 298 K) of $[Pd_2L^{OMe}{}_2L^{SOH}{}_2](BF_4)_4$ with tetrabutylammonium dibenzyl phosphate as a guest. During the titration, signal H_a (L^{OMe}- singlet of quinoline part of the ligand, highlighted in blue) and H_j (L^{OMe}- Methoxy group of the ligand, highlighted in red) were focused to identify the progress of the titration. 12 eq guest were used to form the new $[DBenzP@Pd_2L^{OMe}{}_2L^{SOH}{}_2]$ species. Starting at addition of 4 eq guest, free ligand L^{OMe} is visible.

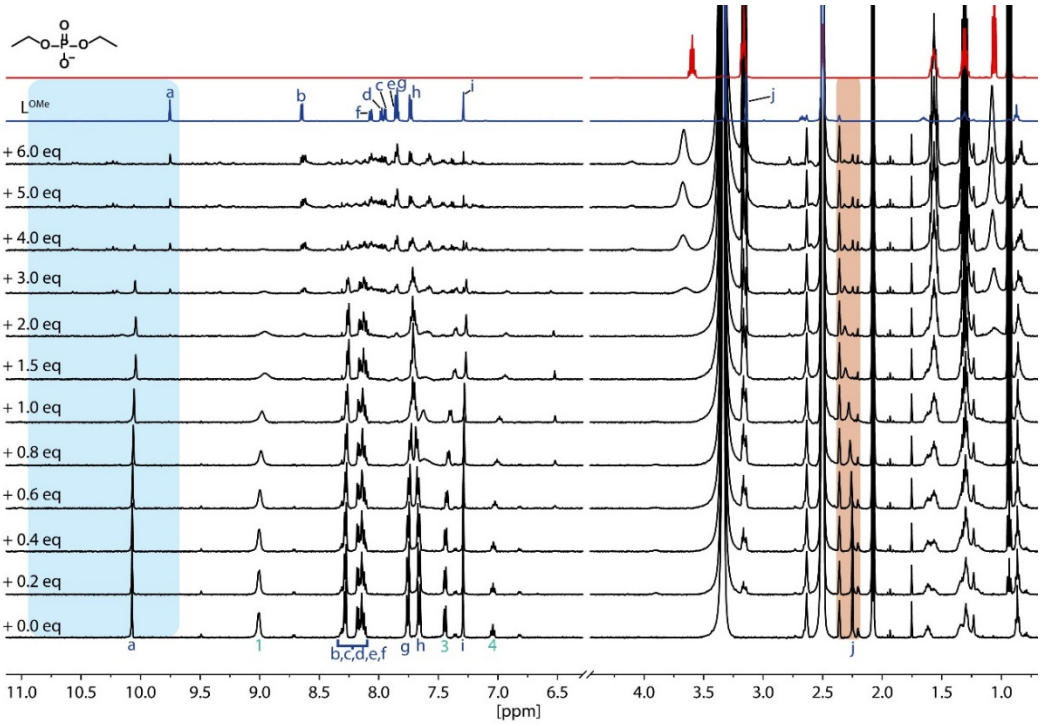

Figure 3.72 ^{1}H NMR titration (500 MHz, DMSO-d_6, 298 K) of $[Pd_2L^{OMe}{}_2L^{SOH}{}_2](BF_4)_4$ with tetrabutylammonium diethyl phosphate as a guest. During the titration, signal H_a (L^{OMe}- singlet of quinoline part of the ligand, highlighted in blue) and H_j (L^{OMe}- Methoxy group of the ligand, highlighted in red) were focused to identify the progress of the titration. 6 eq guest were used to form the new $[DEthP@Pd_2L^{OMe}{}_2L^{SOH}{}_2]$ species. Starting at addition of 2 eq guest, free ligand L^{OMe} is visible.

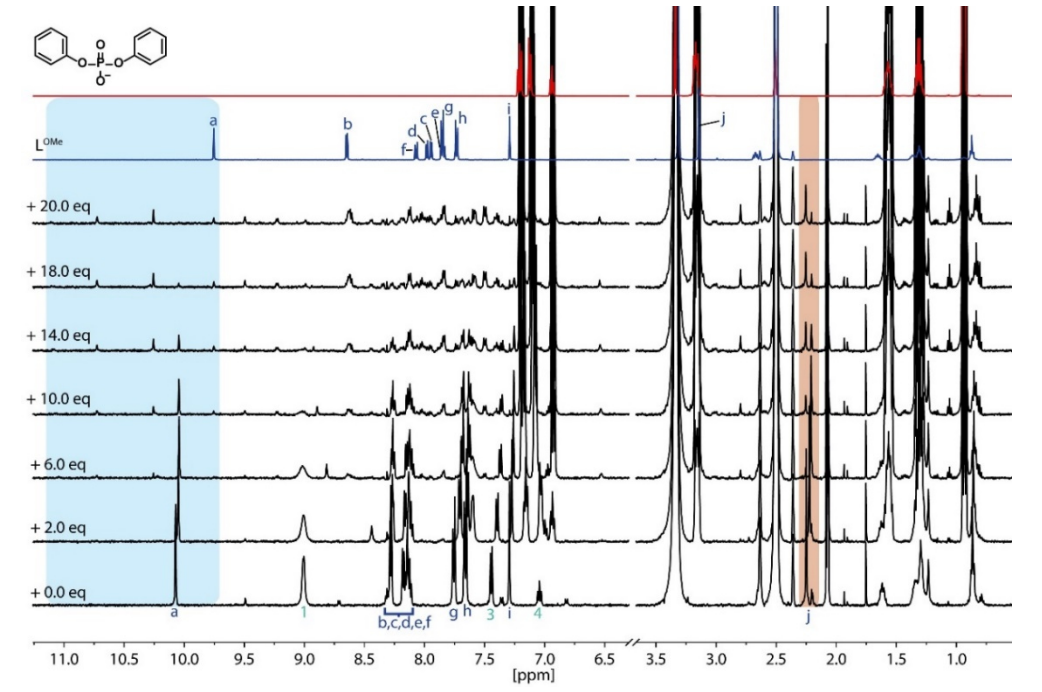

Figure 3.73 ^{1}H NMR titration (500 MHz, DMSO-d_6, 298 K) of $[Pd_2L^{OMe}{}_2L^{SOH}{}_2](BF_4)_4$ with tetrabutylammonium diphenyl phosphate as a guest. During the titration, signal H_a (L^{OMe}- singlet of quinoline part of the ligand, highlighted in blue) and H_j (L^{OMe}- Methoxy group of the ligand, highlighted in red) were focused to identify the progress of the titration. 20 eq guest were used to form the new $[DPhenP@Pd_2L^{OMe}{}_2L^{SOH}{}_2]$ species. Starting at addition of 10 eq guest, free ligand L^{OMe} is visible.

3.3.2.5 Guest-Titrations of $[Pd_2L^{OMe}_2L^{SP}_2](BF_4)_4$

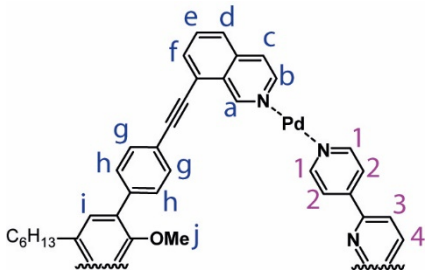

Scheme 3.5 Simplified structure of $[Pd_2L^{OMe}_2L^{SP}_2](BF_4)_4$ to show the position of the assigned protons. Not all protons could be identified in the spectrum due to multiple overlaying (via 2D NMR techniques, see results of structure determining).

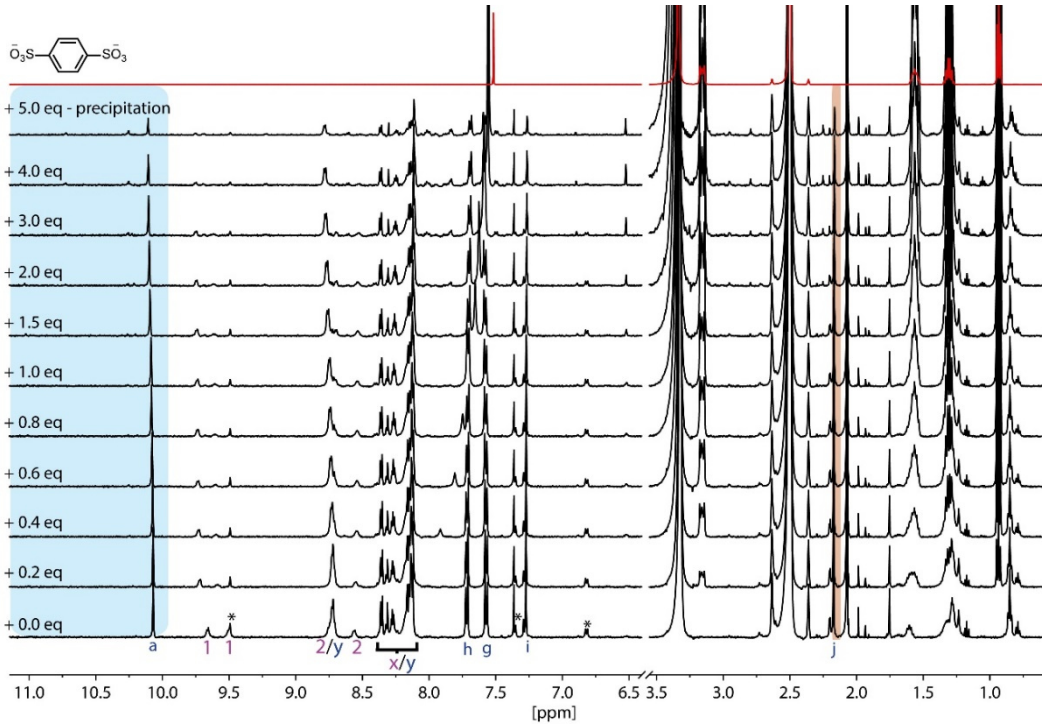

Figure 3.74 ^{1}H NMR titration (500 MHz, DMSO-d_6, 298 K) of $[Pd_2L^{OMe}_2L^{SP}_2](BF_4)_4$ with tetrabutylammonium benzene-1,4-disulfonate. During the titration, signal H_a (L^{OMe}- singlet of quinoline part of the ligand, highlighted in blue) and H_j (L^{OMe}- Methoxy group of the ligand, highlighted in red) were focused to identify the progress of the titration. For signal a and j, only a very small shift could be observed. By addition of 1.5 eq small new signal were observed, but also a decreasing of the signal intensities with a recognizable turbidity of the sample until at 6.0 eq guest addition precipitation occurred. This indicated an agglomeration of the Host with the Guest.

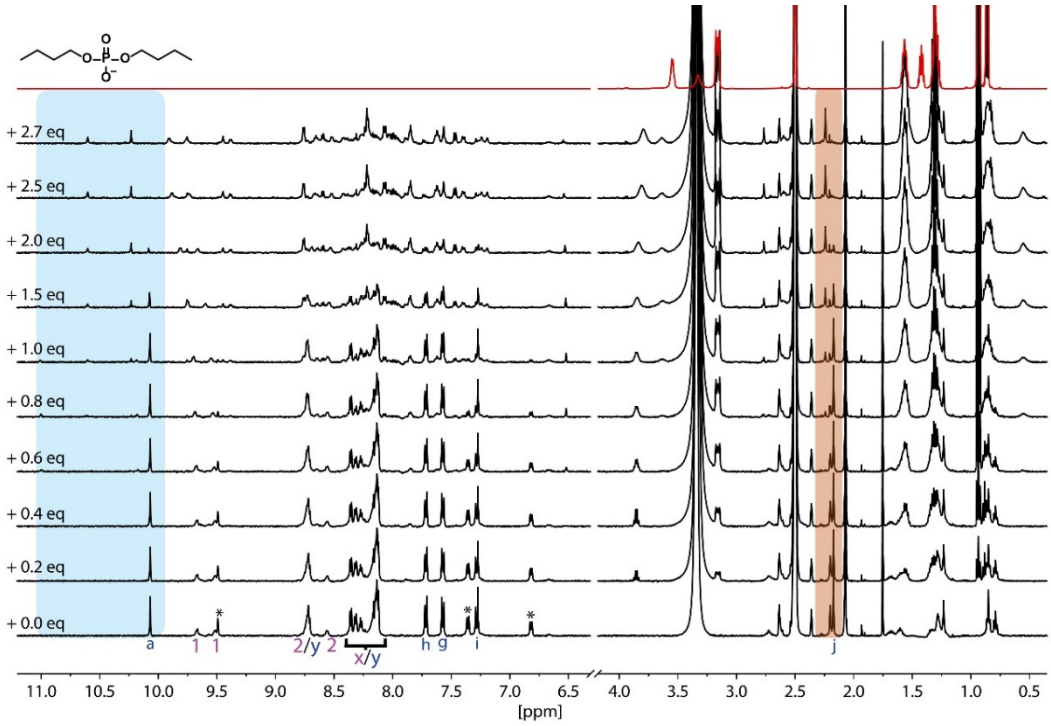

Figure 3.75 ^{1}H NMR titration (500 MHz, DMSO-d_6, 298 K) of $[Pd_2L^{OMe}{}_2L^{SP}{}_2](BF_4)_4$ with tetrabutylammonium dibutyl phosphate as a guest. During the titration, signal H_a (L^{OMe}- singlet of quinoline part of the ligand, highlighted in blue) and H_j (L^{OMe}- Methoxy group of the ligand, highlighted in red) were focused to identify the progress of the titration. 2.7 eq guest were used to form the new [DButP@$Pd_2L^{OMe}{}_2L^{SP}{}_2$] species.

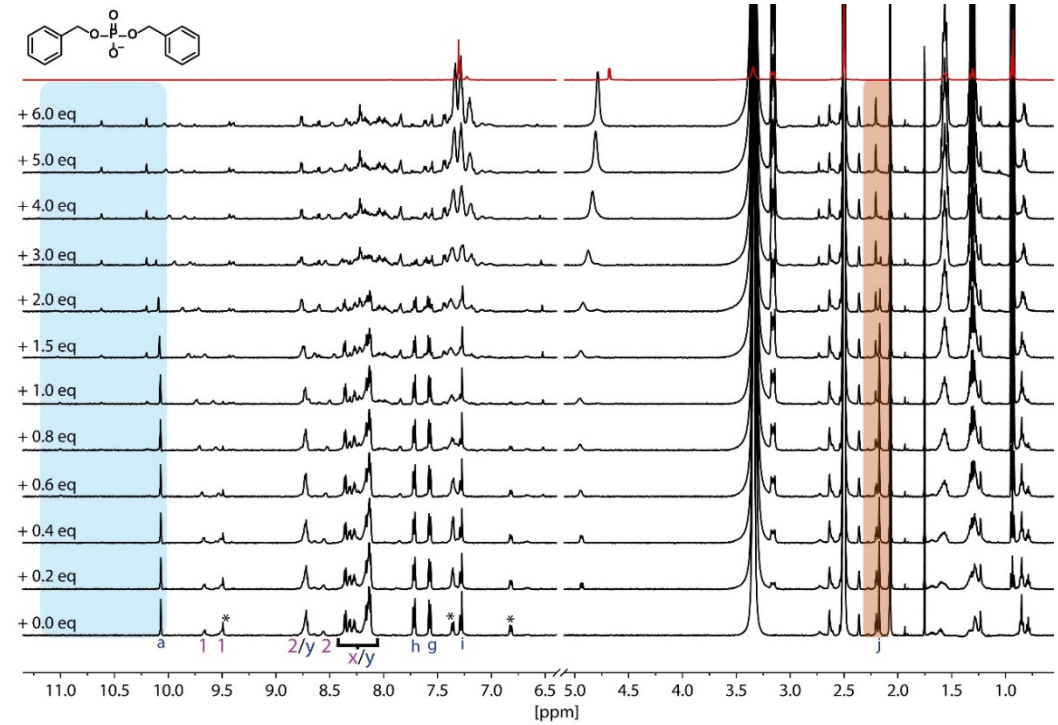

Figure 3.76 ^{1}H NMR titration (500 MHz, DMSO-d_6, 298 K) of $[Pd_2L^{OMe}{}_2L^{SP}{}_2](BF_4)_4$ with tetrabutylammonium dibenzyl phosphate as a guest. During the titration, signal H_a (L^{OMe}- singlet of quinoline part of the ligand, highlighted in blue) and H_j (L^{OMe}- Methoxy group of the ligand, highlighted in red) were focused to identify the progress of the titration. 6.0 eq guest were used to form the new [DBenzP@$Pd_2L^{OMe}{}_2L^{SP}{}_2$] species.

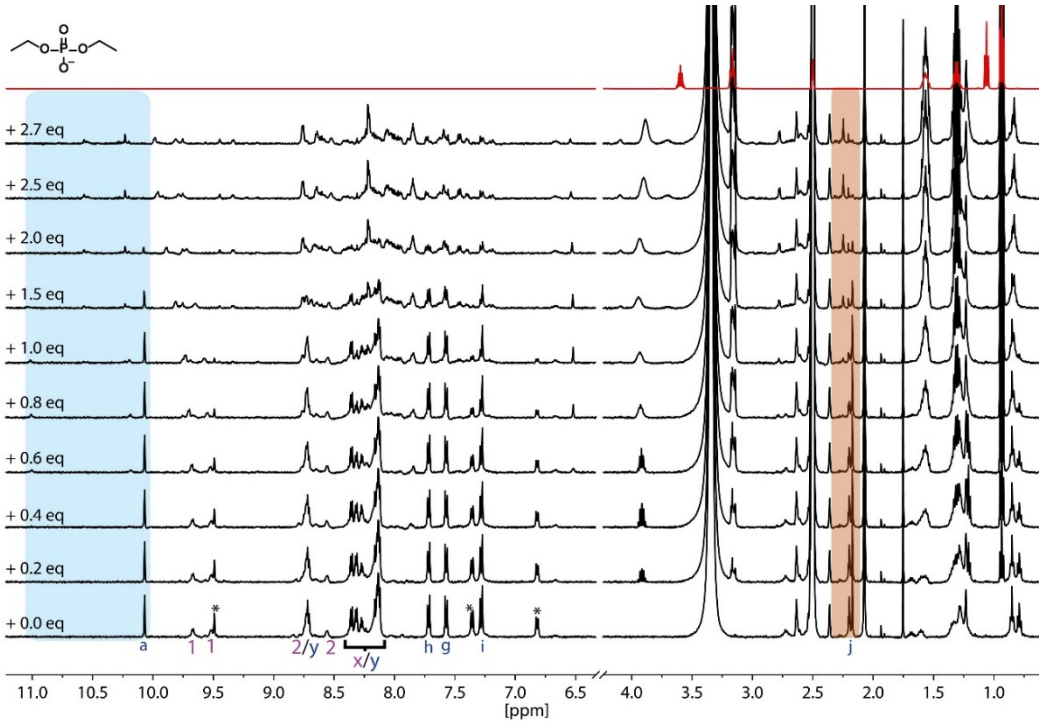

Figure 3.77 ^{1}H NMR titration (500 MHz, DMSO-d_6, 298 K) of $[Pd_2L^{OMe}{}_2L^{SP}{}_2](BF_4)_4$ with tetrabutylammonium diethyl phosphate as a guest. During the titration, signal H_a (L^{OMe}- singlet of quinoline part of the ligand, highlighted in blue) and H_j (L^{OMe}- Methoxy group of the ligand, highlighted in red) were focused to identify the progress of the titration. 2.7 eq guest were used to form the new $[DEthylP@Pd_2L^{OMe}{}_2L^{SP}{}_2]$ species.

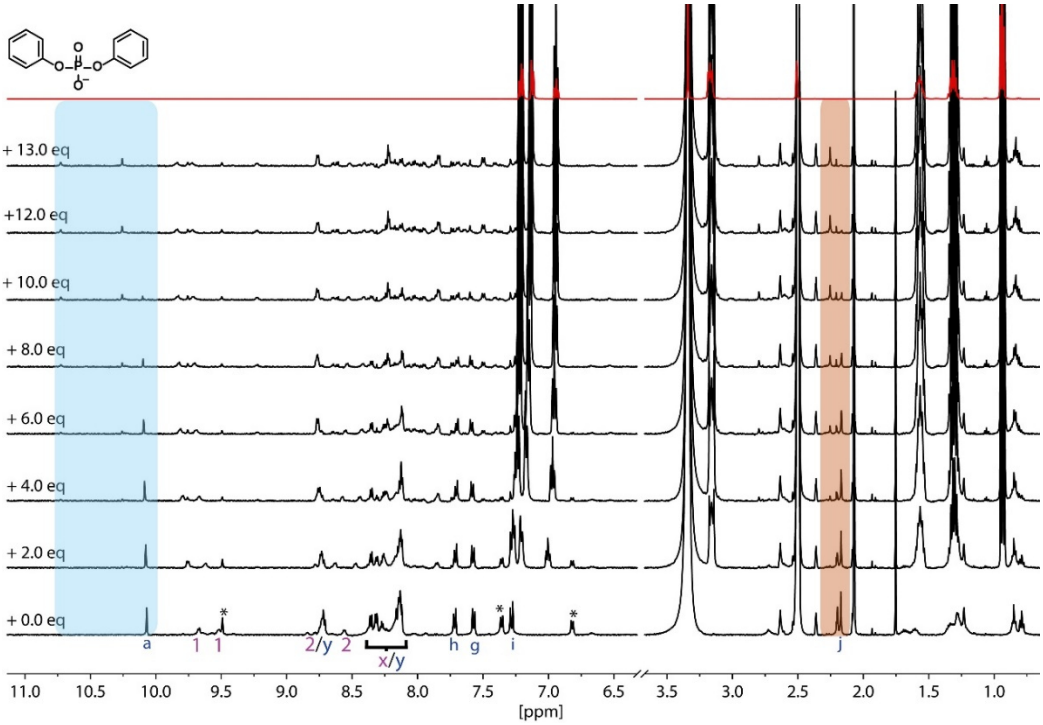

Figure 3.78 ^{1}H NMR titration (500 MHz, DMSO-d_6, 298 K) of $[Pd_2L^{OMe}{}_2L^{SP}{}_2](BF_4)_4$ with tetrabutylammonium diphenyl phosphate as a guest. During the titration, signal H_a (L^{OMe}- singlet of quinoline part of the ligand, highlighted in blue) and H_j (L^{OMe}- Methoxy group of the ligand, highlighted in red) were focused to identify the progress of the titration. 13 eq guest were used to form the new $[DPhenylP@Pd_2L^{OMe}{}_2L^{SP}{}_2]$ species.

4 List of Figures

5 References

[1] J.-M. Lehn, *Angew. Chem. Int. Ed.* **1988**, *27*, 89.

[2] J. M. Lehn, *Science* **1985**, *227*, 849.

[3] J.-M. Lehn, *Supramolecular Chemistry*, VCH, Weinheim, New York, **1995**.

[4] P. D. Beer, P. A. Gale, D. K. Smith, *Supramolecular Chemistry*, Oxford Univ. Press, Oxford, **2003**.

[5] E. Mattia, S. Otto, *Nat. Nanotechnol.* **2015**, *10*, 111.

[6] D. B. Amabilino, P. A. Gale, *Chem. Soc. Rev.* **2017**, *46*, 2376.

[7] F. H. Crick, Watson James D., *Proc. R. Soc. Lond. A* **1954**, *223*, 80.

[8] C. R. Calladine, *Understanding DNA*. *The Molecule and How it Works*, Elsevier Academic Press, San Diego, **2004**.

[9] L. Stryer, J. Berg, J. Tymoczko, G. Gatto, *Biochemistry*, Macmillan Learning, New York, **2019**.

[10] L. Backman, *Protein Chemistry*, De Gruyter, Berlin, **2020**.

[11] C. J. Pedersen, *J. Am. Chem. Soc.* **1967**, *89*, 7017.

[12] B. Dietrich, J. M. Lehn, J. P. Sauvage, *Tetrahedron Lett.* **1969**, *10*, 2885.

[13] D. J. Cram, T. Kaneda, R. C. Helgeson, G. M. Lein, *J. Am. Chem. Soc.* **1979**, *101*, 6752.

[14] C. A. Schalley, *Analytical Methods in Supramolecular Chemistry*, Wiley-VCH, Weinheim, **2012**.

[15] G. Gil-Ramírez, D. A. Leigh, A. J. Stephens, *Angew. Chem. Int. Ed.* **2015**, *54*, 6110.

[16] C. Dietrich-Buchecker, J. Sauvage, J. Kintzinger, *Tetrahedron Lett.* **1983**, *24*, 5095.

[17] E. Wasserman, *J. Am. Chem. Soc.* **1960**, *82*, 4433.

[18] C. O. Dietrich-Buchecker, J. P. Sauvage, *Chem. Rev.* **1987**, *87*, 795.

[19] C. O. Dietrich-Buchecker, J. P. Sauvage, J. M. Kern, *J. Am. Chem. Soc.* **1984**, *106*, 3043.

[20] C. Dietrich-Buchecker, J.-P. Sauvage, *Molecular catenanes, rotaxanes and knots*. *A journey through the world of molecular topology*, Wiley-VCH, Weinheim, New York, **1999**.

[21] K. S. Chichak, S. J. Cantrill, A. R. Pease, S.-H. Chiu, G. W. V. Cave, J. L. Atwood, J. F. Stoddart, *Science* **2004**, *304*, 1308.

[22] J.-F. Ayme, J. E. Beves, D. A. Leigh, R. T. McBurney, K. Rissanen, D. Schultz, *Nature Chem* **2011**, *4*, 15.

[23] C. D. Pentecost, K. S. Chichak, A. J. Peters, G. W. V. Cave, S. J. Cantrill, J. F. Stoddart, *Angew. Chem. Int. Ed.* **2007**, *46*, 2.

[24] C. Peinador, V. Blanco, J. M. Quintela, *J. Am. Chem. Soc.* **2009**, *131*, 920.

[25] J.-C. Chambron, J.-P. Sauvage, *New J. Chem.* **2013**, *37*, 49.

[26] J.-P. Sauvage, *Chem. Commun. (Camb)* **2005**, 1507.

[27] E. R. Kay, D. A. Leigh, *Pure Appl. Chem.* **2008**, *80*, 17.

[28] J. A. Bravo, F. M. Raymo, J. F. Stoddart, A. J. P. White, D. J. Williams, *European Journal of Organic Chemistry* **1998**, *1998*, 2565.

[29] I. T. Harrison, S. Harrison, *J. Am. Chem. Soc.* **1967**, *89*, 5723.

[30] K. D. Hänni, D. A. Leigh, *Chem. Soc. Rev.* **2010**, *39*, 1240.

[31] P. L. Anelli, N. Spencer, J. F. Stoddart, *J. Am. Chem. Soc.* **1991**, *113*, 5131.

[32] J. F. Stoddart, *Angew. Chem. Int. Ed.* **2017**, *56*, 11094.

[33] J. D. Badjic, V. Balzani, A. Credi, S. Silvi, J. F. Stoddart, *Science* **2004**, *303*, 1845.

[34] J. D. Badjic, C. M. Ronconi, J. F. Stoddart, V. Balzani, S. Silvi, A. Credi, *J. Am. Chem. Soc.* **2006**, *128*, 1489.

[35] N. Koumura, R. W. Zijlstra, R. A. van Delden, N. Harada, B. L. Feringa, *Nature* **1999**, *401*, 152.

[36] T. Kudernac, N. Ruangsupapichat, M. Parschau, B. Maciá, N. Katsonis, S. R. Harutyunyan, K.-H. Ernst, B. L. Feringa, *Nature* **2011**, *479*, 208.

[37] I. V. Kolesnichenko, E. V. Anslyn, *Chem. Soc. Rev.* **2017**, *46*, 2385.

[38] G. W. Gokel, L. Barbour, J. L. Atwood, *Comprehensive Supramolecular Chemistry II*, Elsevier Science, Saint Louis, **2017**.

[39] S. Saha, I. Regeni, G. H. Clever, *Coord. Chem. Rev.* **2018**, *374*, 1.

[40] T. R. Cook, Y.-R. Zheng, P. J. Stang, *Chem. Rev.* **2013**, *113*, 734.

[41] S. Pullen, G. H. Clever, *Acc. Chem. Res.* **2018**, *51*, 3052.

[42] R. Chakrabarty, P. S. Mukherjee, P. J. Stang, *Chem. Rev.* **2011**, *111*, 6810.

[43] B. H. Northrop, Y.-R. Zheng, K.-W. Chi, P. J. Stang, *Acc. Chem. Res.* **2009**, *42*, 1554.

[44] R. van Eldik, R. Puchta (Eds.) *Advances in inorganic chemistry*, *Volume 71*, AP Academic Press an imprint of Elsevier, Cambridge, MA, San Diego, CA, Oxford, London, **2018**.

[45] S. Leininger, B. Olenyuk, P. J. Stang, *Chem. Rev.* **2000**, *100*, 853.

[46] M. Fujita, J. Yazaki, K. Ogura, *J. Am. Chem. Soc.* **1990**, *112*, 5645.

[47] P. J. Stang, D. H. Cao, *J. Am. Chem. Soc.* **1994**, *116*, 4981.

[48] R. S. Forgan, J.-P. Sauvage, J. F. Stoddart, *Chem. Rev.* **2011**, *111*, 5434.

[49] J. E. Beves, B. A. Blight, C. J. Campbell, D. A. Leigh, R. T. McBurney, *Angew. Chem. Int. Ed.* **2011**, *50*, 9260.

[50] J. M. Lehn, A. Rigault, J. Siegel, J. Harrowfield, B. Chevrier, D. Moras, *Proc. Natl. Acad. Sci. U. S. A.* **1987**, *84*, 2565.

[51] B. Kersting, M. Meyer, R. E. Powers, K. N. Raymond, *J. Am. Chem. Soc.* **1996**, *118*, 7221.

[52] C. Piguet, G. Bernardinelli, G. Hopfgartner, *Chem. Rev.* **1997**, *97*, 2005.

[53] M. Albrecht, *Chem. Rev.* **2001**, *101*, 3457.

[54] D. L. Caulder, R. E. Powers, T. N. Parac, K. N. Raymond, *Angew. Chem. Int. Ed.* **1998**, *37*, 1840.

[55] N. Takeda, K. Umemoto, K. Yamaguchi, M. Fujita, *Nature* **1999**, *398*, 794.

[56] B. F. Abrahams, S. J. Egan, R. Robson, *J. Am. Chem. Soc.* **1999**, *121*, 3535.

[57] M. Eddaoudi, D. B. Moler, H. Li, B. Chen, T. M. Reineke, M. O'Keeffe, O. M. Yaghi, *Acc. Chem. Res.* **2001**, *34*, 319.

[58] B. Moulton, J. Lu, A. Mondal, M. J. Zaworotko, *Chem. Commun.* **2001**, 863.

[59] A. Ikeda, M. Yoshimura, H. Udzu, C. Fukuhara, S. Shinkai, *J. Am. Chem. Soc.* **1999**, *121*, 4296.

[60] K. Harris, D. Fujita, M. Fujita, *Chem. Commun.* **2013**, *49*, 6703.

[61] C. Eerdun, S. Hisanaga, J. Setsune, *Angew. Chem. Int. Ed.* **2013**, *52*, 929.

[62] A. P. Paneerselvam, S. S. Mishra, D. K. Chand, *J Chem Sci* **2018**, *130*, 1.

[63] S. Sato, T. Murase, M. Fujita in *Supramolecular Chemistry* (Eds.: P. A. Gale, J. W. Steed), John Wiley & Sons, Ltd, Chichester, UK, **2012**.

[64] A. M. Johnson, M. C. Young, X. Zhang, R. R. Julian, R. J. Hooley, *J. Am. Chem. Soc.* **2013**, *135*, 17723.

[65] A. Schmidt, A. Casini, F. E. Kühn, *Coord. Chem. Rev.* **2014**, *275*, 19.

[66] G. H. Clever, P. Punt, *Acc. Chem. Res.* **2017**, *50*, 2233.

[67] B. S. Pilgrim, N. R. Champness, *Chempluschem* **2020**, *85*, 1842.

[68] M. Han, D. M. Engelhard, G. H. Clever, *Chem. Soc. Rev.* **2014**, *43*, 1848.

[69] D. A. McMorran, P. J. Steel, *Angew. Chem. Int. Ed.* **1998**, *37*, 3295.

[70] L. J. Barbour, G. W. Orr, J. L. Atwood, *Nature* **1998**, *393*, 671.

[71] S. Löffler, J. Lübben, L. Krause, D. Stalke, B. Dittrich, G. H. Clever, *J. Am. Chem. Soc.* **2015**, *137*, 1060.

[72] M. Käseborn, J. J. Holstein, G. H. Clever, A. Lützen, *Angew. Chem. Int. Ed.* **2018**, *57*, 12171.

[73] B. P. Burke, W. Grantham, M. J. Burke, G. S. Nichol, D. Roberts, I. Renard, R. Hargreaves, C. Cawthorne, S. J. Archibald, P. J. Lusby, *J. Am. Chem. Soc.* **2018**, *140*, 16877.

[74] S. K. Samanta, D. Moncelet, V. Briken, L. Isaacs, *J. Am. Chem. Soc.* **2016**, *138*, 14488.

[75] F. Schmitt, J. Freudenreich, N. P. E. Barry, L. Juillerat-Jeanneret, G. Süss-Fink, B. Therrien, *J. Am. Chem. Soc.* **2012**, *134*, 754.

[76] A. Schmidt, M. Hollering, M. Drees, A. Casini, F. E. Kühn, *Dalton Trans.* **2016**, *45*, 8556.

[77] J. E. M. Lewis, E. L. Gavey, S. A. Cameron, J. D. Crowley, *Chem. Sci.* **2012**, *3*, 778.

[78] T. N. Parac, D. L. Caulder, K. N. Raymond, *J. Am. Chem. Soc.* **1998**, *120*, 8003.

[79] M. D. Pluth, K. N. Raymond, *Chem. Soc. Rev.* **2007**, *36*, 161.

[80] P. D. Beer, P. A. Gale, *Angew. Chem. Int. Ed Engl.* **2001**, *40*, 486.

[81] H.-N. Zhang, Y. Lu, W.-X. Gao, Y.-J. Lin, G.-X. Jin, *Chem. Eur. J.* **2018**, *24*, 18913.

[82] X. Han, Y.-X. Xu, J. Yang, X. Xu, C.-P. Li, J.-F. Ma, *ACS Appl. Mater. Interfaces* **2019**, *11*, 15591.

[83] Y. Liu, A. D. Gill, Y. Duan, L. Perez, R. J. Hooley, W. Zhong, *Chem. Commun.* **2019**, *55*, 11563.

[84] J. W. Steed, *Chem. Soc. Rev.* **2009**, *38*, 506.

[85] S. J. Lee, W. Lin, *J. Am. Chem. Soc.* **2002**, *124*, 4554.

[86] J. Wang, C. He, P. Wu, J. Wang, C. Duan, *J. Am. Chem. Soc.* **2011**, *133*, 12402.

[87] L.-J. Chen, Y.-Y. Ren, N.-W. Wu, B. Sun, J.-Q. Ma, Li Zhang, H. Tan, M. Liu, X. Li, H.-B. Yang, *J. Am. Chem. Soc.* **2015**, *137*, 11725.

[88] A. Chowdhury, P. Howlader, P. S. Mukherjee, *Chem. Eur. J.* **2016**, *22*, 7468.

[89] J. Rebek, *Acc. Chem. Res.* **2009**, *42*, 1660.

[90] D. M. Vriezema, M. Comellas Aragonès, J. A. A. W. Elemans, J. J. L. M. Cornelissen, A. E. Rowan, R. J. M. Nolte, *Chem. Rev.* **2005**, *105*, 1445.

[91] J. Gao, S. Ma, D. T. Major, K. Nam, J. Pu, D. G. Truhlar, *Chem. Rev.* **2006**, *106*, 3188.

[92] Y. Ueda, H. Ito, D. Fujita, M. Fujita, *J. Am. Chem. Soc.* **2017**, *139*, 6090.

[93] M. Otte, *ACS Catal.* **2016**, *6*, 6491.

[94] C. J. Brown, F. D. Toste, R. G. Bergman, K. N. Raymond, *Chem. Rev.* **2015**, *115*, 3012.

[95] P. M. Bogie, L. R. Holloway, C. Ngai, T. F. Miller, D. K. Grewal, R. J. Hooley, *Chem. Eur. J.* **2019**, *25*, 10232.

[96] C. Ngai, P. M. Bogie, L. R. Holloway, P. C. Dietz, L. J. Mueller, R. J. Hooley, *J. Org. Chem.* **2019**, *84*, 12000.

[97] J. Wei, L. Zhao, C. He, S. Zheng, J. N. H. Reek, C. Duan, *J. Am. Chem. Soc.* **2019**, *141*, 12707.

[98] B. Breiner, J. K. Clegg, J. R. Nitschke, *Chem. Sci.* **2011**, *2*, 51.

[99] R. Warmuth, *Eur. J. Org. Chem.* **2001**, *2001*, 423.

[100] V. M. Dong, D. Fiedler, B. Carl, R. G. Bergman, K. N. Raymond, *J. Am. Chem. Soc.* **2006**, *128*, 14464.

[101] D. Fujita, Y. Ueda, S. Sato, N. Mizuno, T. Kumasaka, M. Fujita, *Nature* **2016**, *540*, 563.

[102] D. Bardhan, D. K. Chand, *Chem. Eur. J.* **2019**, *25*, 12241.

[103] L. Chen, Q. Chen, M. Wu, F. Jiang, M. Hong, *Acc. Chem. Res.* **2015**, *48*, 201.

[104] C. García-Simón, M. Garcia-Borràs, L. Gómez, I. Garcia-Bosch, S. Osuna, M. Swart, J. M. Luis, C. Rovira, M. Almeida, I. Imaz et al., *Chem. Eur. J.* **2013**, *19*, 1445.

[105] C. Colomban, V. Martin-Diaconescu, T. Parella, S. Goeb, C. García-Simón, J. Lloret-Fillol, M. Costas, X. Ribas, *Inorg. Chem.* **2018**, *57*, 3529.

[106] C. García-Simón, R. Gramage-Doria, S. Raoufmoghaddam, T. Parella, M. Costas, X. Ribas, J. N. H. Reek, *J. Am. Chem. Soc.* **2015**, *137*, 2680.

[107] Y.-R. Zheng, Z. Zhao, M. Wang, K. Ghosh, J. B. Pollock, T. R. Cook, P. J. Stang, *J. Am. Chem. Soc.* **2010**, *132*, 16873.

[108] Y.-R. Zheng, H.-B. Yang, K. Ghosh, L. Zhao, P. J. Stang, *Chem. Eur. J.* **2009**, *15*, 7203.

[109] M. Yoshizawa, M. Nagao, K. Kumazawa, M. Fujita, *J. Organomet. Chem.* **2005**, *690*, 5383.

[110] R. Zhu, W. M. Bloch, J. J. Holstein, S. Mandal, L. V. Schäfer, G. H. Clever, *Chem. Eur. J.* **2018**, *24*, 12976.

[111] S. Hiraoka, Y. Kubota, M. Fujita, *Chem. Commun.* **2000**, 1509.

[112] K. Kumazawa, K. Biradha, T. Kusukawa, T. Okano, M. Fujita, *Angew. Chem. Int. Ed Engl.* **2003**, *42*, 3909.

[113] M. Yamashina, T. Yuki, Y. Sei, M. Akita, M. Yoshizawa, *Chem. Eur. J.* **2015**, *21*, 4200.

[114] A. M. Johnson, R. J. Hooley, *Inorg. Chem.* **2011**, *50*, 4671.

[115] Q.-F. Sun, S. Sato, M. Fujita, *Angew. Chem. Int. Ed.* **2014**, *126*, 13728.

[116] W. M. Bloch, Y. Abe, J. J. Holstein, C. M. Wandtke, B. Dittrich, G. H. Clever, *J. Am. Chem. Soc.* **2016**, *138*, 13750.

[117] P. J. Stang, B. Olenyuk, *Acc. Chem. Res.* **1997**, *30*, 502.

[118] T. Habereder, M. Warchhold, H. Nöth, K. Severin, *Angew. Chem. Int. Ed.* **1999**, *38*, 3225.

[119] S. Klotzbach, F. Beuerle, *Angew. Chem. Int. Ed.* **2015**, *54*, 10356.

[120] W. M. Bloch, J. J. Holstein, W. Hiller, G. H. Clever, *Angew. Chem. Int. Ed.* **2017**, *56*, 8285.

[121] P. A. Gale, J. W. Steed (Eds.) *Supramolecular Chemistry*, John Wiley & Sons, Ltd, Chichester, UK, **2012**.

[122] P. Thordarson, *Chem. Soc. Rev.* **2011**, *40*, 1305.

[123] G. H. Clever, S. Tashiro, M. Shionoya, *Angew. Chem. Int. Ed.* **2009**, *48*, 7010.

[124] Y.-H. Li, Y. Zhang, Y.-M. Legrand, A. van der Lee, J.-J. Jiang, C.-X. Chen, C.-Y. Su, M. Barboiu, *Dalton Trans.* **2017**, *46*, 15204.

[125] L. Avram, Y. Cohen, *Chem. Soc. Rev.* **2015**, *44*, 586.

[126] S. V. Kharlamov, S. K. Latypov, *Russ. Chem. Rev.* **2010**, *79*, 635.

[127] W. M. Bloch, G. H. Clever, *Chem. Commun.* **2017**, *53*, 8506.

[128] R. Zhu, J. Lübben, B. Dittrich, G. H. Clever, *Angew. Chem. Int. Ed.* **2015**, 2796.

[129] M. Fujita, H. Oka, K. Ogura, *Tetrahedron Letters* **1995**, *36*, 5247.

[130] M. Tominaga, K. Suzuki, M. Kawano, T. Kusukawa, T. Ozeki, S. Sakamoto, K. Yamaguchi, M. Fujita, *Angew. Chem. Int. Ed.* **2004**, *43*, 5621.

[131] J. B. Pollock, T. R. Cook, P. J. Stang, *J. Am. Chem. Soc.* **2012**, *134*, 10607.

[132] F. Jiang, N. Wang, Z. Du, J. Wang, Z. Lan, R. Yang, *Chem. Asian J.* **2012**, *7*, 2230.

[133] D. Fujita, H. Yokoyama, Y. Ueda, S. Sato, M. Fujita, *Angew. Chem. Int. Ed.* **2015**, *54*, 155.

[134] G. A. Jeffrey, *An introduction to hydrogen bonding*, Oxford Univ. Press, New York, **1997**.

[135] J. M. Berg, J. L. Tymoczko, G. J. Gatto jr., L. Stryer, *Stryer Biochemie*, Springer Spektrum, Berlin, **2018**.

[136] N. A. Minton, V. S. Murray, *Med. Toxicol. Adverse Drug Exp.* **1988**, *3*, 350.

[137] K. von der Saal, *Biochemie*, Springer Spektrum, Berlin, **2020**.

[138] F. Neese, *Wiley Interdiscip. Rev. Comput. Mol. Sci.* **2018**, *8*.

[139] C. Bannwarth, S. Ehlert, S. Grimme, *J. Chem. Theory Comput.* **2019**, *15*, 1652.

[140] S. A. Ewing, M. T. Donor, J. W. Wilson, J. S. Prell, *J. Am. Soc. Mass Spectrom.* **2017**, *28*, 587.

[141] G. H. Clever, W. Kawamura, M. Shionoya, *Inorg. Chem.* **2011**, *50*, 4689.

Acknowledgements

I would like to thank my supervisor Prof. Dr. Guido Clever for offering me the opportunity to work in his group and guiding me into the fascinating field of supramolecular chemistry. It was a journey I am thankful for. I also like to thank Prof. Dr. Sebastian Henke for being on my PhD examination board.

I like to thank TU Dortmund and ERC for working on the Consolidator Grant RAMSES project within my Ph.D. time. The author gratefully acknowledges the computing time provided on the Linux HPC cluster at Technical University Dortmund (LiDO3), partially funded in the course of the Large-Scale Equipment Initiative by the German Research Foundation (DFG) as project 271512359.

Thank to Birgit Thormann and Dr. Gabriele Trötscher-Kaus for all the organisational work and encouraging words during hard times. Also, I would like to note that the best coffee is made by Birgit in the morning. During the day it is getting worse (I mean you, Philip!). The technicians Kristian Surich, Laura Schneider, Alex Klauke and Maike Wolters for cover our backs with chemicals, support of devices and even more chemicals. Of course, a special thanks to Laura Schneider for ESI-Mass measurements. Thanks to Prof. Dr. Wolf Hiller, Benjamin Kissel, Jan Schonert and Bastian Grabe for supporting me and our group with first class NMR service. For X-ray data collection I would like to thank Dr. Haeri Lee and Dr. Julian Holstein. Christoph Drechsler, thank you for your support on calculations. Thanks to Dr. Sonja Pullen, Dr. Philip Punt, Dr. Irene Regeni and Andre Platzek for proofreading my thesis and brainstorming sessions through the years. Thanks to all Azubis and students for helping me in the lab.

Thanks to all members of the “boy’s office” for nerdy discussion on games, movies, fishing, and memes during the years. Thanks to my lab mates (H-LAB! PISELLI!) for having fun and tolerate my taste of music. We are all Patatas (Oma Irenes Kartoffelsalat). Thanks to Philip “Pfeffiphlipse” and Marcel “ich glaub die sind tot” for all the party nights (of course only at weekends) and concerts (“Steuerklasse 1 und keiner sagt danke”). Andre, fishing trips until we are old (only if Kristina support us with lunch boxes)? Lukas, we will win the CL in 2025, I guarantee it! Jacopo, only thing I can say is “Boopa-dee Bappa-dee”! Bo, Rujin (Ahbeiteh Häta!”) and Bin thanks for teaching me some Chinese words and learn some nonsense German from Andre and me.

There are endless stories of this Ph.D. years. It was an intense time, scientifical and personal. I thank all members of the Clever lab for everything and accepting me as a part of this group. I found friends for life. And I know how to run a Kiosk, great success.

At last, special thanks to my parents, friends, and my girlfriend Annika for motivating me and accepting my only two emotions euphoric and devasted during the years. Only a Sith deals in absolutes!